16th Machining Innovations Conference for Aerospace Industry - MIC 2016

16th Machining Innovations Conference for Aerospace Industry - MIC 2016

Laser Scored Machining of Fiber Reinforced Plastics to Prevent Delamination

Wolfgang Hintze[a],*, Marcel Cordes[a], Tobias Geis[a], Melchior Blühm[a], Claus Emmelmann[b], Marten Canisius[b]

[a] Institute of Production Management and Technology, Hamburg University of Technology, Denickestr. 17, 21073 Hamburg, Germany
[b] Institute of Laser and System Technologies, Hamburg University of Technology, Denickestr. 17, 21073 Hamburg, Germany

Abstract

Delamination is a major problem in contour milling of fiber reinforced plastics (FRP) causing scrap or rework. Today, delamination avoidance limits overall productivity and tool life. Damage of the top layer of a composite structure is initiated if fibers are not cut during first engagement of the cutting edge, but deflected. Generated cracks propagate due to recurrent contact of fibers with the rotating tool. In contrast, when laser cutting FRP, the heat input often leads to an extensive heat-affected zone (HAZ), particularly in case of large laminate thickness and high energy input. Combination of both processes is a promising approach to overcome the mentioned disadvantages. Experiments indicate that pre-scoring of the top layer is possible with negligible HAZ for FRP materials using proper laser parameters, especially low energy input per unit length. Positioning of the laser scored kerf along the contour to be manufactured by the subsequent milling tool prevents crack propagation along the fiber direction even with a heavily worn milling tool at increased feed rate. Furthermore, laser pre-scoring eliminates protruding fibers and allows for edge chamfering. The process understanding is enhanced using simulation of the laser pre-scoring, particularly considering heat conduction and forced convection, as well as by presenting a model for the mechanism of delamination prevention.

* Corresponding author. Tel.: +49-40-42878-3233; fax: +49-40-42878-2295.
  E-mail address: w.hintze@tuhh.de

1. Introduction

Carbon fiber reinforced plastics (CFRP) have become a major material for structural elements in modern aircraft design. FRP components usually have to undergo a processing step to obtain their final contour. For this purpose contour milling or laser cutting are two possible processes. Contour milling is well-established for trimming of FRP. Nevertheless, the occurrence of delamination and fiber protrusion limits the tool life and the feed rate significantly and, furthermore, causes expensive rework or even scrap. Laser cutting avoids delamination because it is a thermal and not a mechanical process. However, the key disadvantage of laser cutting FRP is the HAZ, which is mostly considered unacceptable by the aeronautical industry today.

In contour milling, the occurrence of delamination depends to a considerable degree on the fiber orientation angle ϕ and the fiber cutting angle θ [1,2,3,4,5]. A widely used failure criteria for FRP is the *Puck* inter-fiber fracture criteria. It is divided in three different failure modes A, B and C depending on the ratio between normal stress to shear stress in the material [6]. Another significant factor for the quality of the workpiece edge is the wear condition of the tool. The feed force increases significantly with increasing wear, which is accompanied by a greater degree of delamination [3]. Due to the high abrasiveness of the fibers, polycrystalline diamond (PCD) is recommended as a cutting material [3,7]. In full-groove cuts a better edge quality is achieved at the up-milled surface ply [8].

Two different process approaches for laser cutting are available to pursue either high productivity or high quality. Cutting with continuous wave laser systems with a mean power in the kilowatt range allows feed rates above 10 m/min [9,10]. The inherent HAZ and thermal damage of the laminate´s surface at the edge causes a low relevance of laser processing in commercial applications today. Higher cutting quality can be achieved with pulsed laser systems [11]. However, for typical laminates feed rates are limited to about 1 m/min. Concerning the laser wavelength, CO_2 lasers have a much better absorption behavior in FRP than solid state lasers in the range of 1 µm, especially when cutting glass fibers. A first analysis of the kerf building under the influence of the first exposures during laser remote cutting is done by Schmidt-Lehr et al. [12]. A linear relationship between the kerf depth and the number of exposures is found up to a kerf depth of about 6 mm. For continuous wave laser processes a few approaches for numerical process simulation exist [13,14,15]. 3D finite difference or finite element methods are used to predict the temperature field as well as the HAZ or the kerf geometry. Only Liebelt [13] considered all three phenomena for an orthogonal-anisotropic material with a thickness of 0.24 mm. All simulations are based on the numeric solution of the heat transfer equation that considers the isotropic or orthogonal-anisotropic heat conduction. Phase changes of the material are modeled in each study, while Liebelt included the phase changes of the polymer as well as the fiber material. The fiber reinforced material is considered as a continuum in all studies.

The laser scored machining (LSM) process combines laser cutting and milling in a way that promises to overcome the disadvantages of the individual processes. Laser cutting is used to score a kerf into the top layer of the laminate. Due to the small depth of the kerf, the thermal impact on the laminate is greatly reduced, which minimizes the size of the HAZ to an extent that can be considered negligible. In the subsequent milling process, the kerf prevents the occurrence and propagation of delamination.

2. Delamination prevention model

During milling, delamination predominantly occurs in the outside layers of the laminate due to the lack of support. Regarding the effect of scoring, two mechanisms have to be distinguished. The first one is the interruption of delamination propagation at the scored kerf. With the tool proceeding along its feed path, delamination propagates along the fiber direction. In order to interrupt the propagation, the depth of the scored kerf d_k has to be larger than the depth d_d in which the delamination is propagating, Fig. 1a. The second mechanism is the prevention of initial delamination, as shown in Fig. 1b. The cutting edge exerts a force F on the workpiece. When the cutting edge reaches the kerf, the outside layers of the laminate above point e support against the acting force.
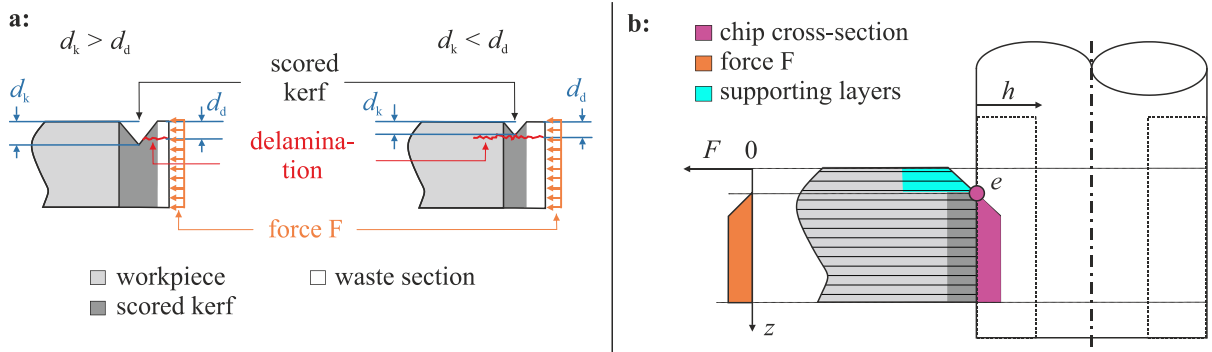
Fig. 1. (a) Interruption of the delamination at the scored kerf; (b) Support of the outside layers during milling.

To show the effect of the supporting layers, a finite element analysis (FEA) has been carried out. Therefore, the cutting force F_c and cutting normal force F_{cn} have been measured as a function of the tool engagement angle φ during machining of CFRP in full engagement. In the FEA, these forces were applied to a 2 x 2 x 1 mm³ specimen, Fig. 2a. The cutting edge is represented by an area of the width twice the cutting edge radius r_n (2 x 28 µm) and the length of the cutting edge in engagement. The material characteristics were adjusted according to the existing fiber cutting angle and fiber orientation angle. The meshing was done as an unstructured mesh of tetrahedron elements with intermediate nodes. In addition, the mesh was refined towards the contact area where the load is applied. The convergence of the resulting stresses and the node displacement was then tested with the h-method [15] to guarantee sufficient accuracy and short simulation time. In fact, the assessment of failure in case of three-axial stress state is yet only possible by experiments. As a first approach, the failure assessment using the modes of *Puck* is based on separate consideration of the stresses acting in the top layer, neglecting stress and strain interactions perpendicular to the laminate plane. The calculated stress for each element of the model was used to determine whether damage occurred based on the failure mode criteria of *Puck*. For a fiber orientation angle $\phi = 135°$ and a fiber cutting angle $\theta = 135°$, the results are shown in Fig. 2b for an unscored and a scored surface ($d_k = 300$ µm). Blue marked elements represent *Puck* mode A, yellow elements mode B and red elements mode C. Behind the cutting edge, *Puck* modus A is present due to tensile stress. In the contact area, modus B is present due to high shear stress and compressive stress. In front of the cutting edge, mode C occurs due to high compressive stress. The scored model does not show damage of the outside layer, only a few damaged elements are present at the lower edge of the kerf. The model of delamination prevention by scoring and the support of the outside layers by the kerf will be validated experimentally in Chapter 4.
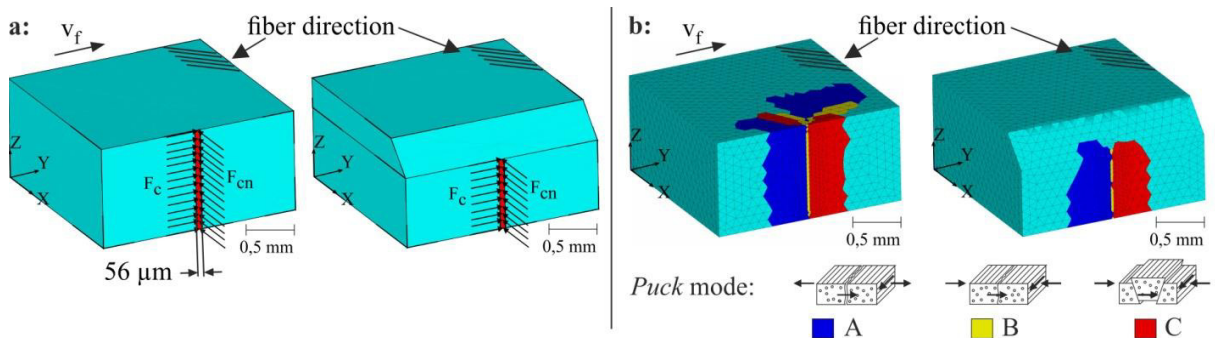

Fig. 2. (a) FEA model for simulation of the FRP material damage; (b) Simulation results for $\phi = 135°$

3. Simulation of laser pre-scoring

The minimization of the HAZ and the prediction of the kerf geometry are important goals of laser scoring process development. Due to the plurality of laser process parameters, a simulation of the laser scoring process has been carried out. For this purpose, a model has been developed which consists of a finite difference based simulation of the heat conduction in the yz-plane perpendicular to the feed direction (Fig. 3a left) and a finite volume based simulation of the transient flow of the gaseous process emissions in the kerf (xz-plane) as well as the resulting convective heat transfer (Fig. 3a right).

Regarding the finite difference simulation of heat conduction, as shown in Fig. 3a left, the explicit formulation is chosen due to robustness, stability and speed of the simulation. The transient temperature field is calculated in the yz-plane, while heat conduction in feed direction is neglected. This is admissible, because the heat conduction is very slow compared to the feed rate of the laser beam.
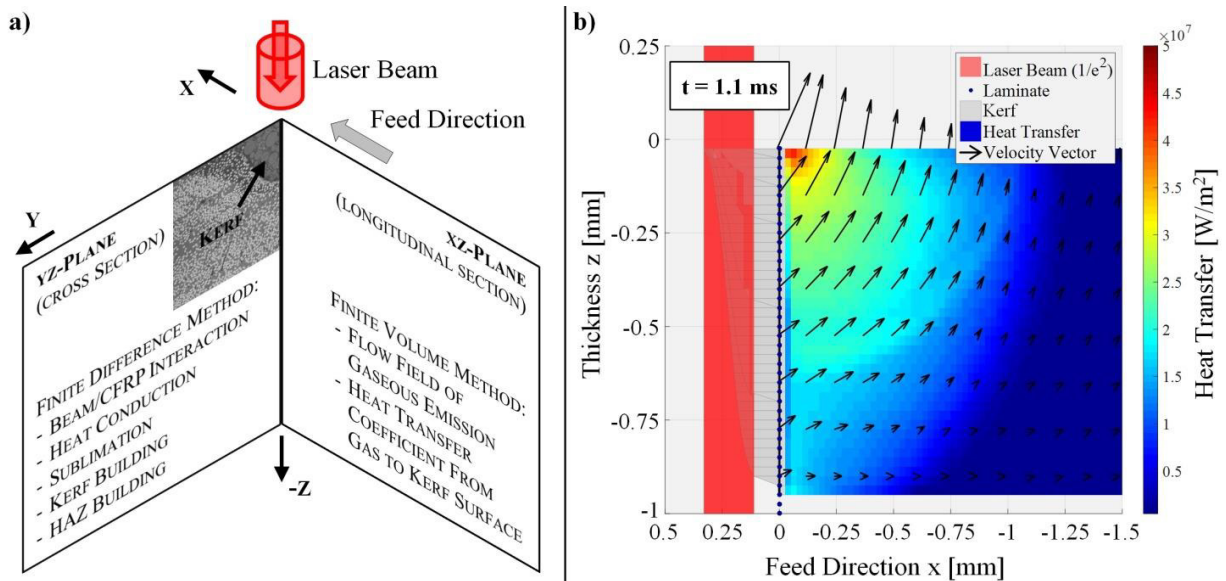

Fig. 3. (a) Coordinate system and modeled phenomena; (b) Gaseous process emission flow field and heat transfer to kerf surface

Based on the changing kerf geometry during the laser exposure, the boundary conditions and material properties of the finite difference mesh are adapted. Thus, the model includes the phenomenon of non-linear kerf depth development with further exposure repetitions. The parametrical material model considers the laminate´s setup such as number of layers, their particular thickness and fiber orientation, fiber volume fraction as well as the thermal conductivity, capacity and latent heat of matrix, fiber and the HAZ. The material properties used in the simulation are summarized in Table 1.

Table 1. Material characteristics of the examined CFRP laminate

Resin type	Epoxy	Fiber volume fraction	60 %
Carbon fiber type	HT (high tenacity)	Thermal conductivity fiber / epoxy	10 / 0.54 $Wm^{-1}K^{-1}$
Laminate structure	[135°, 45°, 135°,...]	Specific heat fiber / epoxy	710 / 1,900 $Jkg^{-1}K^{-1}$
Laminate thickness	5 mm	Latent heat fiber / epoxy	43,000 / 1,020 Jg^{-1}
Lamina thickness	250 μm (UD tape)	Sublimation temp. fiber / epoxy	3,825 / 393-497 °C

The reinforced material is considered as a continuum based on the rule of mixture with orthogonal-anisotropic properties [13]. The HAZ is treated as a combination of solid polymer and fiber with a weighting according to the local degradation of the polymer. The two phase changes during the sublimation of the polymer as well as the carbon fibers are considered [14]. The material model is based on measured data of temperature gradient analysis as well as of differential scanning calorimetry. The heat source is calculated using laser parameters such as power, feed rate, number of exposure repetitions, repetition delay and beam intensity profile.

The convective heat transfer in the xz-plane is considered (Fig. 3a right), because the gaseous process emission from sublimation transports a huge amount of thermal energy that cannot be neglected. The gas flows with very high velocity, pressure and temperature out of the kerf after passing its surface. A process simulation that just considers the heat conduction is not sufficient to calculate the temperature field and HAZ during continuous wave laser scoring or cutting of FRP properly. The convection model is formulated based on the explicit finite volume method. It considers the compressibility of the gas, the flow resistance and the heat transfer of the forced convection at the existing kerf geometry, which is known from the interaction between laser beam and material calculated in the yz-plane. The simulation enables the calculation of the transient temperature, pressure and velocity field in the kerf. The field coupling between the yz-plane and the xz-plane is realized by iterative, alternate calculation.

Based on this model, the forced convection for the entire kerf surface can be calculated, Fig. 3b. The first velocity component of the flow field is oriented opposite to the feed direction of the laser beam and its second velocity component opposite to the beam direction. Especially for high kerf depth (in the range of several beam diameters), the flow takes a long way along the kerf surface, resulting in a considerable amount of thermal energy transferred to the laminate by forced convection. Ultimately, the kerf geometry as well as the HAZ are known.

4. Experimental results and model validation of laser scored machining

4.1. Geometry of the kerf and HAZ when laser pre-scoring

The top layer of the laminate is initially scored with a CO_2 laser, which has a maximum laser output power of 650 W and a wavelength of 10.6 μm. The beam is guided by a 2D-Scanner with an F-Theta lens and a focal length of 200 mm. The resulting focus diameter was approx. 220 μm. In order to validate the above mentioned laser cutting and delamination models and to investigate the influence of the kerf geometry on the edge quality after milling, the process parameters feed rate $v_{f,l}$ of the laser, laser power P and number of exposures n_{exp} are varied. For the experiments, the same CFRP material is used as for the simulation of pre-scoring, Table 1.

The kerf geometry is characterized based on cross sections of the pre-scored specimens. Fig. 4 shows specimens with different energy input per unit length S, which is calculated as follows:

$$S = \frac{P}{v_{f,l}} \cdot n_{\mathrm{exp}} \tag{1}$$

As expected, higher energy input per unit length leads to an increase in kerf depth. The maximum resulting kerf depth is 670 μm, thus penetrates up to the third lamina (Fig. 4d). The HAZ is visible as a result of different light reflection. For maximum S, the width of the HAZ is 357 μm at the surface. Compared to laser-only cutting of such CFRP materials the HAZ width is significantly reduced [16].

The cross sections that were obtained using the simulation described in Chapter 3 are presented in the lower part of Fig. 4. In order to fit the experimental results, the simulated laser power was multiplied by a constant factor of 0.53. The discrepancies may be attributed to the self-shielding of the laser process due to emissions. Furthermore, the mesh is comparatively coarse, which causes increased accumulation of thermal energy at the grid elements at the kerf surface compared to the real process. In addition, free convection and radiation between ambience and surface are neglected.
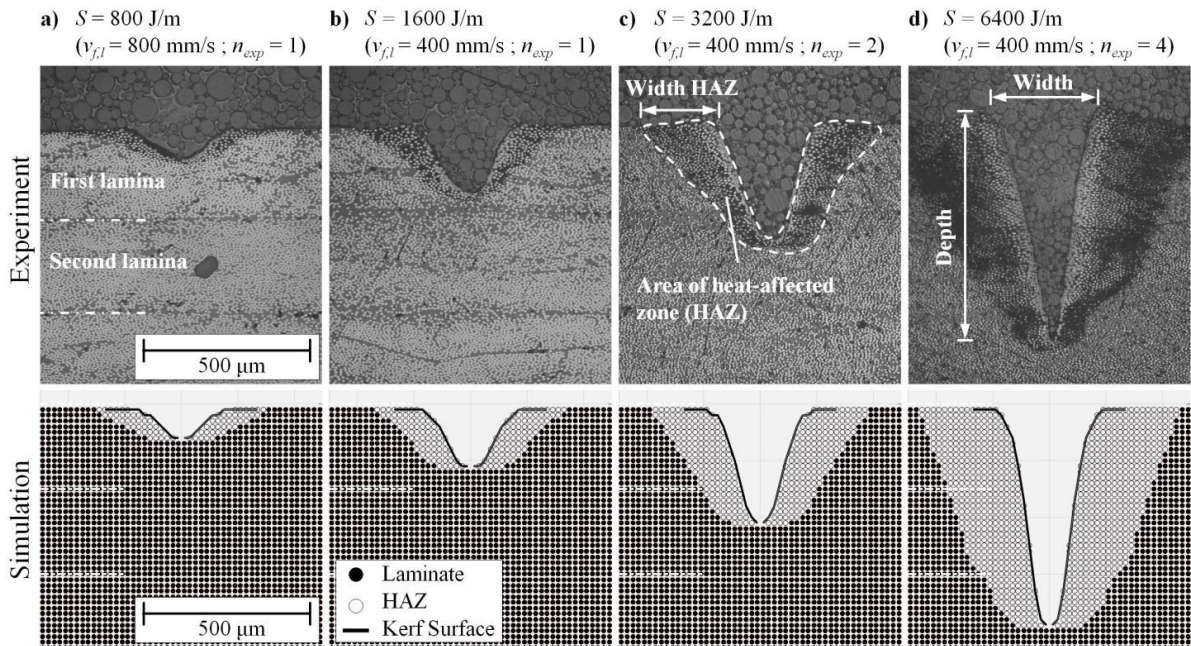
a) $S = 800$ J/m   **b)** $S = 1600$ J/m   **c)** $S = 3200$ J/m   **d)** $S = 6400$ J/m
    $(v_{f,l} = 800$ mm/s ; $n_{exp} = 1)$ $(v_{f,l} = 400$ mm/s ; $n_{exp} = 1)$ $(v_{f,l} = 400$ mm/s ; $n_{exp} = 2)$ $(v_{f,l} = 400$ mm/s ; $n_{exp} = 4)$

Fig. 4. Cross sections and simulation of CO_2-laser pre-scoring with laser power $P = 640$W

4.2. Milling of the pre-scored specimens

Afterwards, the pre-scored specimens are milled on a 5-axis-machining center. The machining is carried out in full groove cuts (slotting) with a PCD end mill, which has a cutting edge radius (CER) of 60 µm. Hence, the cutting edges are heavily worn and at the end of their industrial usage [2,17]. In contrast to the industrial practice, the feed per tooth is set high to 0.09 mm in order to show the high potential of the laser scored machining. For comparison with the conventional contour milling, reference grooves with the worn and a sharp (CER=12 µm) tool are milled without pre-scoring. The cutting parameters are summarized in Table 2. Since in general a better quality is achieved at the up-milled edge [8], only the up-milled edge of the top lamina is assessed. The relative position of the milled groove to the pre-scored kerf was chosen in a way that the trimmed edge runs in the center of the kerf. Thus, laser pre-scoring simultaneously allows for edge chamfering, which is often required for subsequent processing steps like handling or painting.

Table 2. Properties of tool and cutting conditions used in the experiments.

Diameter (mm)	12.7
Number of teeth, z	2
Helix angle (deg)	0
Cutting edge radius CER (µm)	12 (sharp); 60 (worn)
Feed per tooth, f_z (mm)	0.09
Cutting velocity, v_c (m/min)	798

Fig. 5 shows microscopic images of the resulting edge quality depending on the laser process parameters. First of all, without pre-scoring the heavy impact of tool wear in terms of CER on delamination becomes apparent. On the other hand, with increasing energy input per unit length the pre-scoring results in a complete prevention of delamination. Both, fiber protrusions and surface damage extending into the material are not evident.
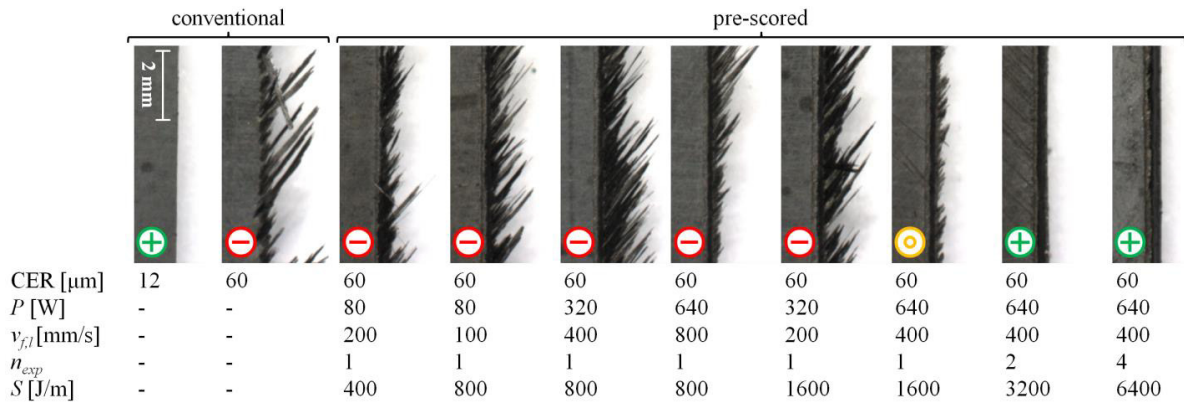
	conventional		pre-scored								
CER [µm]	12	60	60	60	60	60	60	60	60	60
P [W]	-	-	80	80	320	640	320	640	640	640
$v_{f,l}$ [mm/s]	-	-	200	100	400	800	200	400	400	400
n_{exp}	-	-	1	1	1	1	1	1	2	4
S [J/m]	-	-	400	800	800	800	1600	1600	3200	6400

Fig. 5. Comparison of edge quality after milling with and without laser pre-scoring for fiber orientation angle 135°

4.3. Influence of kerf geometry on edge quality

The influence of the kerf geometry on edge quality after milling is shown in Fig. 6. The geometrical characteristics depth and width of the kerf as well as the area of the HAZ have been extracted from the cross sections, compare Fig. 4. For each specimen, two cross sections have been prepared and the measured values averaged. The depth of the kerf is increasing virtually linear with increasing energy input per unit length, whereas the width remains almost constant. The delamination is prevented starting with a scoring depth of approximately 250 µm, which corresponds with the thickness of one lamina.
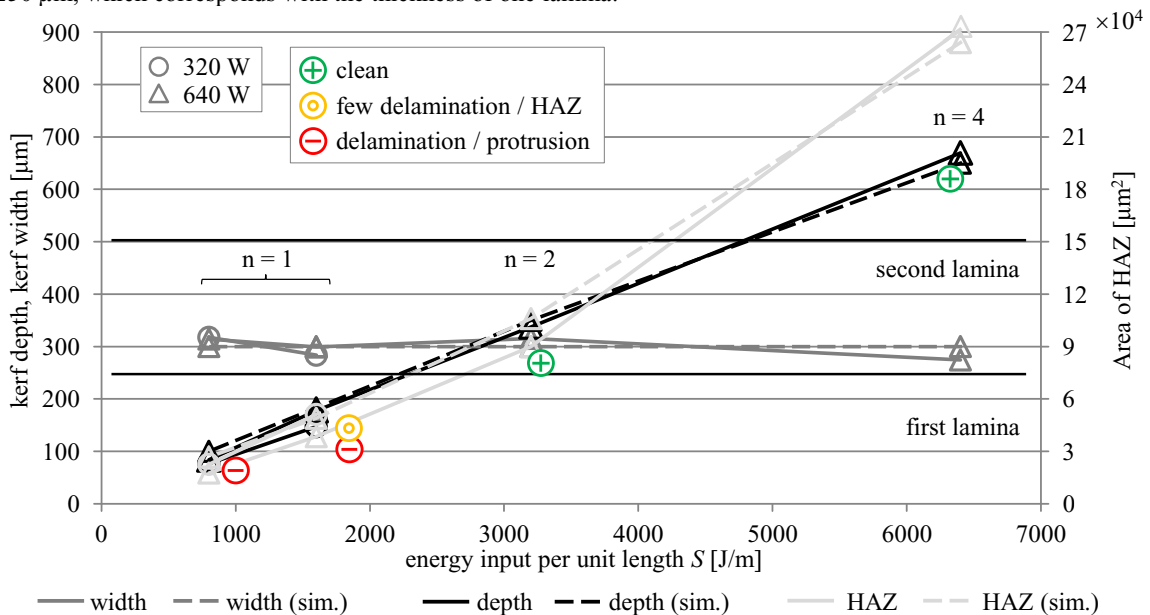

Fig. 6. Influence of kerf geometry on edge quality

The experimental milling result is in accordance with the FEA, which predicts no surface damage for a scored depth of 300 µm (compare Fig. 2b). In addition, the modeled kerf depth, width and HAZ determined based on the simulated cross sections are shown in Fig. 6. They show a good quantitative agreement with the experiment.

5. Conclusions

A novel edge trimming process for FRP, consisting of a laser pre-scoring and a milling step, has been introduced. The process aims at preventing delamination and fiber protrusion at the top lamina. The process and its principles have been examined theoretically and verified through experiments.

- A model for the mechanism of delamination prevention at the top layer through pre-scoring has been presented. Two effects are involved: the interruption of the propagation of delamination at the kerf and the prevention of initial delamination based on a better support of the relevant layers against the cutting force. A finite element analysis of the cutting area is used to demonstrate the impact of the kerf on top layer damage.
- Simulation can be used to predict the kerf geometry and the HAZ resulting from the laser pre-scoring. This is shown using a finite difference and finite volume simulation incorporating heat transfer by conduction as well as forced convection from gaseous process emission to the kerf surface. After calibration, a good agreement between simulation and experimental results is found.
- Cross sections of laser pre-scored kerfs show that the HAZ is considerably reduced compared to laser-only cutting. Moreover, the position of the HAZ is favorably located at a small area around the upper kerf edge. The kerf depth as well as the size of the HAZ increase with the energy per unit length applied.
- Experimental results show that laser pre-scoring can effectively prevent top layer delamination during contour milling. For this purpose, a sufficient kerf depth has to be achieved. In the current experiments, the minimum depth was found to be around 250 µm, which corresponds to the thickness of one lamina. As a small kerf depth is sufficient to achieve delamination prevention, the HAZ as well as the required laser power can be kept small.

References

[1] Hintze, W.; Hartmann, D.: Modeling of delamination during milling of unidirectional CFRP. Proc. CIRP 8 (2013), 444–449
[2] Hintze, W.; Hartmann, D.; Schütte, C.: Occurrence and propagation of delamination during the machining of carbon fiber reinforced plastics (CFRPs) – An experimental study. Compos. Sci. Technol. 71 (15) (2011), 1719–1726.
[3] Karpat, Y.; Bahtiyar, O.; Deger, B.: Mechanistic force modeling for milling of unidirectional carbon fiber reinforced polymer laminates. Int. J. Mach. Tools Manuf. 56 (2012), 79–93
[4] Lai, W.-H.: Modeling of Cutting Forces in End Milling Operations. Tam. J. Sci. Eng. 3 (1) (2000), 15–22
[5] Kalla, D.; Sheikh-Ahmad, J.; Twomey, J.: Prediction of cutting forces in helical end milling fiber reinforced polymers. Int. J. Mach. Tools Manuf. 50 (10) (2010), 882–891
[6] Deutschle, H. M.: 3D Failure Analysis of UD Fiber Reinforced Composites. PhD thesis, University of Stuttgart, 2010
[7] Teti, R.: Machining of composite materials. CIRP Ann. Manuf. Technol. 51 (2) (2002), 611–634
[8] Sheikh-Ahmad, J.: Machining of Polymer Composites. Springer, Boston and MA, 2009
[9] Herzog, D.; Canisius, M.; Schmidt-Lehr, M.; Rörig, B.; Schlude, N.; Hammer, T.; Emmelmann, C.: Cutting Process Suitable for High Volume Production. Kunststoffe International 6 (2014), 28–31
[10] Canisius, M.; Oberlander, M.; Herzog, D.; Schmidt-Lehr, M.; Ploog, P.; Albert, F.; Emmelmann, C.: Correlation between Temperature Field and Heat Affected Zone during Laser Cutting of CFRP. Lasers in Manufacturing Conference, 21.-25. Jun. 2015, Munich
[11] Herzog, D., Canisius, M., Schmidt-Lehr, M., Hergoss, P., Daniel, C., Hallmann, S., Emmelmann, C., Scherner, M.V.: Investigations on the 3D laser cutting of CFRP using a nanosecond pulse fibre laser. Appl. Poly. Compos. 2 (4) (2014)
[12] Schmidt-Lehr, M.; Oberlander, M.; Herzog, D., Canisius, M.; Radek, M.; Emmelmann, C.: Investigations on the process strategy of laser remote cutting of carbon reinforced plastics with a thickness of more than 3 mm. ICCM20, 19.-25. Jul. 2015, Copenhagen
[13] Liebelt, S.: Analyse und Simulation des Laserstrahlschneidens von Faserverbundkunststoffen, Fraunhofer IPK, Berlin, 1998
[14] Hocheng, H.; Tsai, H.-Y.: Advanced analysis of nontraditional machining. New York, Springer, 2013
[15] Reddy, J.N.: An Introduction to the Finite Element Method. Boston, McGraw-Hill, 2006
[16] Herzog, D., Jaeschke, P., Meier, O., Haferkamp, H.: Investigations on the thermal effect caused by laser cutting with respect to static strength of CFRP. Int. J. Mach. Tools Manuf. 48 (2008), 1464–1473
[17] Hintze, W., Cordes, M., Koerkel, G.: Influence of weave structure on delamination when milling CFRP. J. Mater. Process. Technol. 216 (2015), 199–205

16th Machining Innovations Conference for Aerospace Industry - MIC 2016

Online tool wear measurement for hobbing of highly loaded gears in Geared Turbo Fans

[a]Fritz Klocke, [a]Benjamin Döbbeler, [a]Sven Goetz*, [a]Julian Staudt

[a]WZL der RWTH Aachen, Steinbachstr. 19, D-52074 Aachen

* Corresponding author. Tel.: +49-241-8027466; fax: +49-241-80-22293. *E-mail address:* S.Goetz@wzl.rwth-aachen.de

Abstract

Continuous increase in flight passengers alongside with a high demand for fuel efficiency has led to the development of Geared Turbo Fans (GTF). Being a safety-critical part, the gearbox faces strong safety requirements that also account for sophisticated manufacturing processes and monitoring systems. One major issue is tool wear and the threat of tool breakage during the hobbing process. Due to the high costs of both the raw material and the tool, wear induced tool breakage is a major cost driver. Common practice today is to use each tool for a designated time, but in-situ online wear assessment would result in a major reduction of costs. Tool wear of hobs is not spread equally across all cutting edges; hence the assignment of tool wear to each blade would enable a monitoring system to analyze the individual tool life and predict its operational capability. This research paper discusses the general feasibility of a blade-oriented monitoring system for gear hobbing processes. A correlation between tool wear and effective power is found and analyzed. It can be shown that the respective position of the tool wear changes the effective power signal significantly. These findings enable further research on an online, model based and position-oriented tool wear monitoring system.

1. Introduction

1.1. Challenges in Geared Turbo Fans

The drive for economic aero engines has eventually led to the development of Geared Turbofans (GTF), where a gearbox separates the turbo fan from the low-pressure shaft. These gears are subject to very high loads and also very

strict safety requirements. Due to that, hard to machine materials and special alloys are used that require machining with low process parameters (e.g. cutting speed, feed rate). At the same time, tool wear and forces are considerably high, so that the danger of a tool breakage during a machining process is paramount. [1]

Gear hobbing is one of the major gear manufacturing methods, as it has the highest efficiency with outstanding accuracy and quality. However, its kinematics and wear mechanisms are highly challenging. It is therefore difficult to predict the tool wear. Especially when producing large gears, the decision whether the current tool is capable or not of machining one more gear without reaching a critical level of wear is often very difficult. [2]

An online assessment of the hobbing tool can reduce this problem by giving the possibility to decide upon the tool status on a more objective basis and to prevent sudden tool failure during the machining.

1.2. State of the art

Process monitoring can be differentiated between online and offline monitoring systems. [3] Due to a lack of reliable online tool wear monitoring systems, the offline methods are still widely applied. These methods assess the tool wear by optical or visual methods and impose an interruption of the production process. [4] While this operation is often performed by the machine operator, new approaches use image processing methods to automatically assess the tool wear status of a hobbing tool. [5]

However, recent research focused on developing online methods for tool wear monitoring, and some systems are already commercially available. These systems usually rely on indirect measurement, such as cutting forces, vibration, acoustic emission, spindle motor and feed currents. [4] These systems face the challenges that occur from changing cutting conditions. Fussel et al. developed a system that uses cutting forces and a force prediction model and is independent of the cutting conditions. [6] Due to the high complexity of a hobbing process, the combination of several sensor signals within one larger model can increase the accuracy of the system. That is shown in the work of Salgado et al. (2013), where a neural network is used to predict tool flank wear during milling using the feed drive motor current and the cutting vibration. [7] In another work, Salgado & Alonso (2007) used a LS-SVM as an alternative to the neural network in a monitoring system for turning using sound and current signals. [8]

The leading commercially available system is the CTM V6 from ARTIS Marposs. [9] It is capable to create a signature of the process using multi-sensors signals (torque, spindle vibration, power consumption, AE signals, etc.) and then use it to verify the actual process state. However, this system requires a high batch size for teaching and is not able to detect sudden process changes or a minor tool breakage that only affects one blade. Hence, the development of a system that is capable of detecting local wear on a hob or local tool edge breakage would enable a safer and more economical production of highly-loaded gears for GTF.

1.3. Research aim and approach

As stated above, in order to develop a position-oriented tool monitoring system for hobbing, some basic understanding between the tool wear and the measurement signals is paramount. It has been shown that online wear measurement currently is either based on expensive sensors (e.g. piezo electrical force sensors) or available for simple cutting processes, such as turning. However, simulation-based approaches have proven to be successful for complex cutting processes, and forces can be estimated by the use of effective power from the main spindle. [10] The research aim of this paper is hence to analyze the effect of tool wear on the effective power signal, and how the position of the wear affects this signal. To do so, fly cutter hobbing experiments were conducted and both the effective power as well as the tool wear was measured. This was done for three different alloys that are likely to be used for highly stressed GTF gears.

2. Experiments and results

2.1. Description of experimental setup

The experiments were carried out on a Liebherr LC 100 machine using the fly cutter hobbing process. This is a commonly used process to assess tool wear and other tool influences in a hobbing process, as it projects the entire

process on one single blade. The process as well as the parameters used is shown in Fig. 1 (left). The fly cutter passes the workpiece once for each generating position, then shifts back and cuts the next gap.
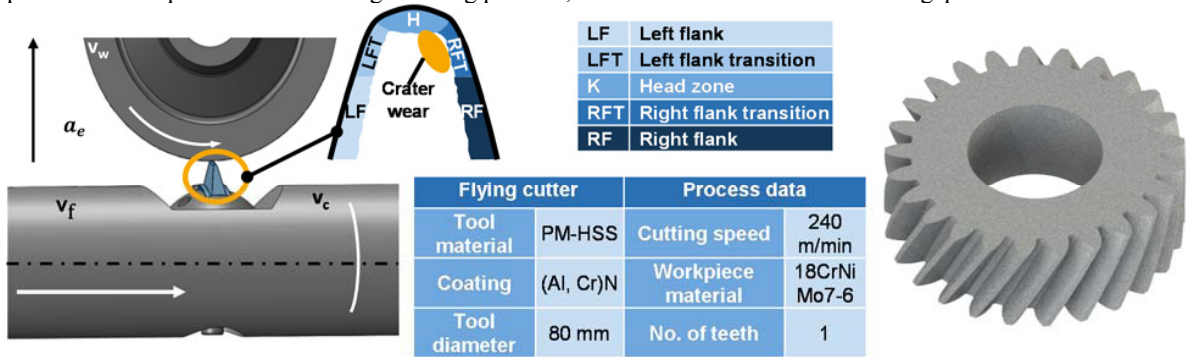

Figure 1: Experiment setup (left) and CAD image of the gear (right)

Three different materials were used for the experiments, out of which geometrically equal gears were produced until the tool life end was reached. The materials used were 18CrNiMo7-6 in different heat treatments (1x forged, 2x quenched and tempered). Fig. 1 (right) shows the CAD image of the gear. The tool wear was measured and assigned to the according area of the blade, as shown in Fig. 1 (left). The entire blade flank was divided into 5 segments to get more precise information on where the wear occurred. The process itself was monitored by measuring the effective power of the main spindle with a frequency of 20 kHz.

2.2. Experimental results

The active power curve was taken throughout the entire process. Fig. 2 (left) shows a peak for each generating position, where the maximum of these peaks first gradually increases, then reaches a steady area and steadily decreases towards the end of each measurement. The blue detail on the left hand side in Fig. 2 shows the power signal of one single revolution. The sampling rate was high enough to measure the detailed course of the signal with high resolution. The right hand side of Fig. 2 shows the respective maxima of these revolutions for one of the peaks (i.e., one generating position). The blue line shows it for a new tool, while the yellow one shows it for the same position, but with a now worn tool. The green line shows the ratio of these curves. It can be observed that this line is a close approximation to a parallel to the x-axis in the area between t = 0 s and t = 60 s. This means, regardless of the level of effective power, tool wear leads to a constant increase of power.
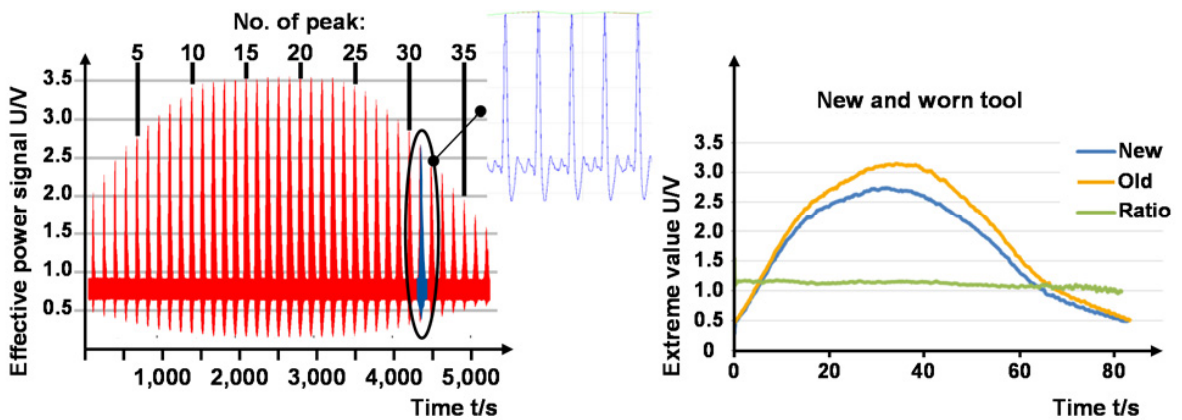

Figure 2: Effective power signal (left) and comparison of the signal from two different tool states (right)

Furthermore, the tool wear was measured. During the experiments it became clear that crater wear would be the determining factor for the tool life time, as the flank wear did not develop as heavily as the crater wear did. It was therefore decided to use crater wear as the determining factor for the end of tool life. This was set at 100 µm of crater wear. Fig. 3 shows the respective amounts of wear for the three materials used for each last gear produced. It can be seen that while material I only slightly exceeded the threshold, material III lead to a wear of more than 300 µm in its third and last gear. However, flank wear is at an equal level compared to the last gears of the other two materials.
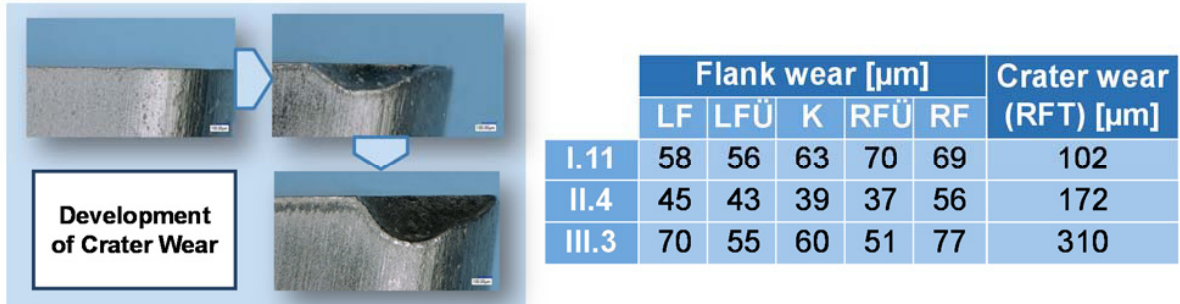

| | Flank wear [µm] | | | | | Crater wear |
	LF	LFÜ	K	RFÜ	RF	(RFT) [µm]
I.11	58	56	63	70	69	102
II.4	45	43	39	37	56	172
III.3	70	55	60	51	77	310

Figure 3: Development of the tool wear for each material

3. Data analysis

3.1. Analysis of active power signal

The data was measured and, to decrease the effect of noise, smoothed with a factor of 12 (Mean value of 12 measurement points). This caused a slight shift in the time of each index. This shift was adjusted by altering the time index of the measurement data with the help of MATLAB. The new signals could then be compared to each other by division. Fig. 4 shows the data for four different gears in the same time interval (bold line) as well as the ratio between the respective line and the first gear (dotted line). It is clearly visible that the signal as well as the ratio increase with the number of gears made by one tool.
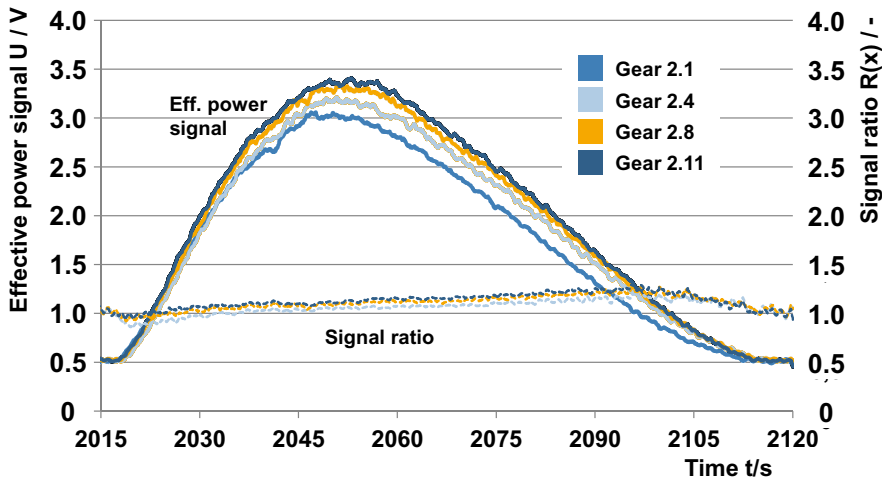

Figure 4: Comparison between the effective power signal of different gears

Furthermore, the ratio not only increases with the number of gears machined, but also with time within one gear. That observation could be made throughout the entire set of measurements. The reason is that the maximum of the signal from gears lately produced is shifted towards later times, thus creating an inclination of the otherwise straight ratio line (compare to Fig. 2). The cause of this will be discussed later in section 3.2.
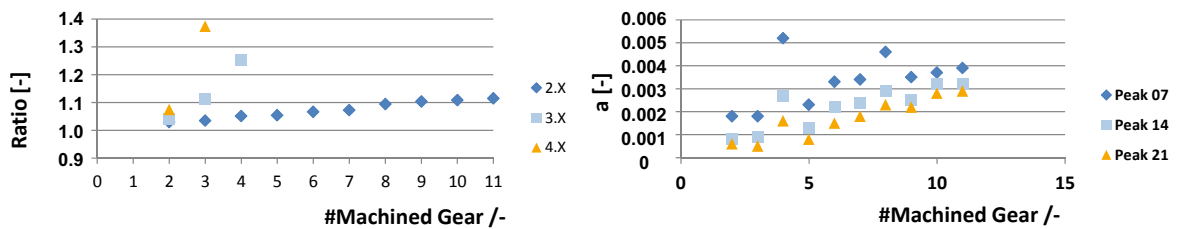
Figure 5: Ratio of the maximum value for peak 14 (left) and Steepness of power ratio curve for experimental series I.x (right)

When looking at all maxima of the same peak (peak 14) and calculate the respective ratios, two things get clear. Firstly, the ratio increases roughly linearly with the number of the gear, although for the material III, there were only 3 gears and thus 2 ratios. Secondly, with a decrease of the easiness to machine of the material, the slope of this inclination increases. This proofs the trivial fact that harder to machine materials cause a higher tool wear. Fig. 5 (left) shows the ratios of the maximum values for peak 14.

In the fly cutter hobbing process, each process step represents one generating position. Therefore, the chip formation differs in each generating position, which results in different wear for each blade. Fig. 5 (right) shows how different peaks (e.g., different generating position) result in a change in the steepness a of the ratio curve, representing the fact that an unequal distribution of the wear changes the effective power development differently. This makes it promising to use the steepness of the ratio curve to determine the exact position of the wear on each blade.

3.2. Analysis of tool wear status

As mentioned above, the major tool wear criterion was crater wear, which occurred in the RFÜ section of the blade. For the material I series, this is also the section where the highest flank wear occurred, which would mean that this section was subject to the highest load. Fig. 6 shows the RFÜ section of the material I series. In the left top section of Fig. 6, the graph shows how the maximum cutting length develops over the unrolled cutting edge. The red circle shows the maximum of that curve, which is in the RFÜ section. It can therefore be concluded that for the material I, the wear reaches its maximum in the area with the highest cutting length.

Fig. 5 (right) shows the inclination of the ratio curve of the power signal. As stated in the previous section, the reason for the positive inclination is that the section with high tool wear (i.e. RFÜ) cuts at a time period of the process which is after the middle, where the maximum of the power curve usually occurs. Since higher tool wear leads to higher power consumption (see section 2), this effect overshadows the effect of the decline of the usual power signal, so that it is still increasing for several seconds, instead of dropping. This leads to the inclination. It is yet to be researched on how exactly the inclination correlates with the position of the crater wear.
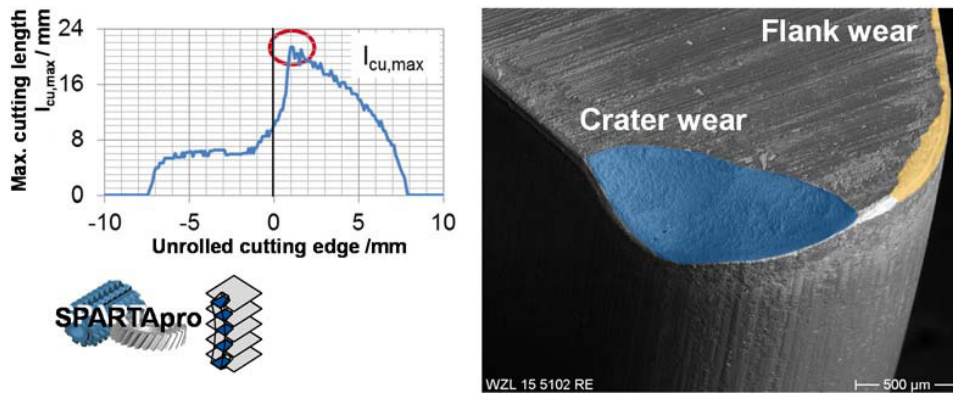
Figure 6: Correlation between maximum cutting length and tool wear position

However, when investigating series II and III, the crater wear is still at the RFÜ section, but the maximum flank wear is at different sections. Since the inclinations of the power signal are similar to series I.x, and the crater wear at RFÜ is still determining the end of the tool life in these series, it is yet to be investigated how flank wear influences the power signal.

4. Conclusion

It was shown that the effective power signal increases with an increase of tool wear, which is an expected observation. However, it could also be noticed that regardless of the value of the power signal, its increase in comparison to a signal from a new tool is relatively constant. This leads to the assumption that the power ratio, gathered at any point of the signal, can be used to assess the tool wear status. Fig. 7 shows the ratio at the respective maximum point of the power signal for all three series and several different peaks.
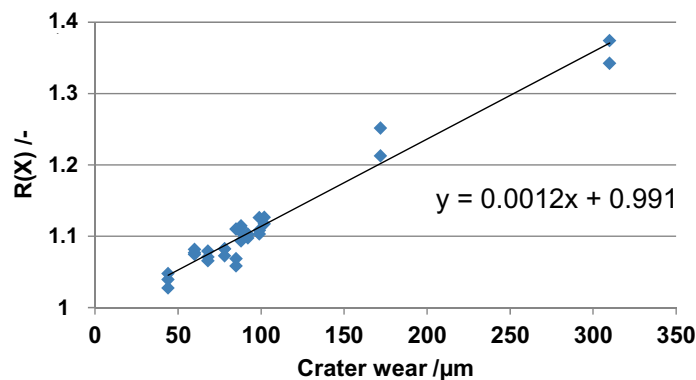

Figure 7: Effective power ratio R(x) over crater wear for selected gears

It can be seen that, regardless of the level of crater wear, the ratio follows (with the exception of few data sets) a straight line, where 100 µm of crater wear are equivalent to 12% increase of the power signal. Since 100 µm was set as the limit for the tool life, only few points could be gathered beyond that point. However, even the very high crater wear of approximately 300 µm lies within close range of that line. It may therefore be assumed that crater wear leads to a linear increase in the effective power signal of a fly hobbing process. It is, however, yet to be analyzed how these finding can be transferred to the real hobbing process.

	R(X)			Coef *a*		
	Peak 07	Peak 14	Peak 21	Peak 07	Peak 14	Peak 21
coef *a*	0,580	0,868	0,959	-	-	-
Crater wear	0,790	0,88116281	0,843	0,506	0,673	0,637
#Gear	0,979	0,992	0,979	0,502	0,848	0,943

Figure 8: Coefficients of correlation for all gears

Fig. 8 shows the coefficients of correlation for several, selected peaks between the ratio R(x) and the inclination coef *a* of the ratio curve, the crater wear and the number of the gear (all left side of Fig. 8) as well as the coefficient of correlation between coef *a* and the crater wear and the number of the gear (right hand side of the same figure). As Fig. 8 suggests, the ratio R(x) correlates rater strongly with the crater wear, and even stronger with the number of the gear. This is one more proof of the feasibility to use the effective power signal for an online tool monitoring system in the hobbing process.

One other thing that can be derived from the data in Fig. 8 is the steepness of the power curve, coef *a*. As can be seen from Fig. 2, peak 7 is at the beginning of the process, while peak 14 is in the middle section and peak 21 in the declining section of the process signal. Therefore, the chip formation is different at each of the peaks. This leads to the assumption that the coefficient coef *a* bears some information on the position of the wear on the blade, as suggested in chapter 3.1. A positive coef *a* would then mean the wear is greater towards RF, a negative would mean it is located rather towards LF. A flat curve, i.e. a very small coef *a*, would mean it is located near the tool tip.

5. Outlook and further investigation

The findings presented in this paper show that the effective power signal bears the potential to give online information not only about the entire hob, but also about each individual blade. It has been shown that the (crater) wear of a single blade correlates strongly with the effective power signal, and there is evidence that the shape of the power signal gives much deeper information, especially with respect to the exact position of the tool wear on the blade. However, these findings were made with a fly cutter hobbing process. It is hence to be investigated how these results can be transferred to the real hobbing process.
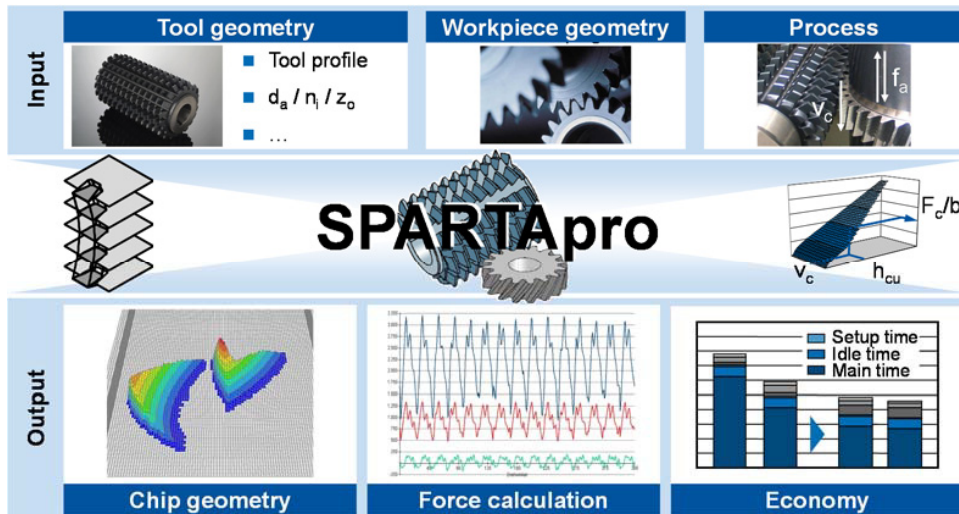

Figure 9: Basic concept of SPARTApro

One possible approach is the combination of the effective power signal with simulation data. As stated in section 1.2, currently available tools use internal power data with low resolution and small sampling rate. These are not able to measure the effect of wear on each single cutting blade. Measuring with external sensors that use a sample rate of up to 20 kHz enables the acquisition of enough information to evaluate the status of each single blade. A simulation of the cutting process with respect to the individual blade would make it possible to determine the excess power and thus the influence of the tool wear on the power signal. SPARTApro is a simulation tool developed at the gear department of WZL and enables such a simulation. [10] Fig. 9 shows the basic concept of SPARTApro. This makes it promising to use the steepness of the ratio curve to determine the exact position of the wear on each blade.

The combination of measurement data and the simulated values bears a large potential for a position-oriented monitoring system for the hobbing process. This information should be enhanced by other sensor signals, such as highly-frequent acoustic emission (AE) in a range of 50 kHz to 1 MHz. It was already shown that tool break results in sharp outburst through the entire spectrum of the AE signal, c.f. Fig. 10. The research goal in this area is to find how exactly these bursts behave for broken blades of a hobbing tool, and if it is also possible to see edge breaks in the signal.
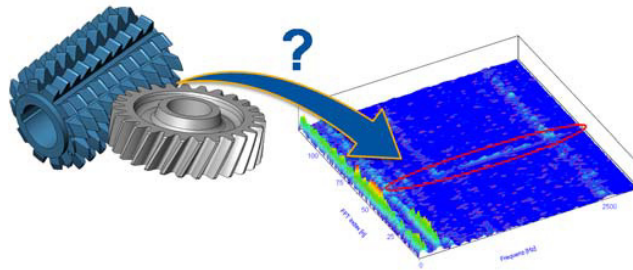

Figure 10: Effect of tool break on AE signal for a face milling tool (red circle)

Acknowledgements

References

[1] Bloomberg Business, *"The little gear that could reshape the jet engine",* Bloomberg Business Week, 15th October 2015
[2] Bouzakis *et al.*, *"Gear Hobbing Cutting Process Simulation and Tool Wear Prediction Models"*, Transactions of ASME, Vol. 124, pp. 42-51, 2002
[3] Klocke*, "Manufacturing processes 1" pp. 386-417*, Springer Verlag, 2011, ISBN 978-3-540-23458-6
[4] Teti et al., *"Advanced monitoring of machining operations",* CIRP Annals - Manufacturing Technology 59 (2010) 717–739, 2010
[5] Claudin, Rech, *"Development of a new rapid characterization method of hob's wear resistance in gear manufacturing"*, Journal of Materials Processing Technology 209, 2009
[6] Fussel *et al., "Real-time tool wear monitoring in milling using a cutting condition independent method"*, International Journal of Machine Tools & Manufacture 89 (2015) 1–13
[7] Salgado et al., *"Tool wear estimation for different workpiece materials using the same monitoring system"*, Procedia Engineering 63 (2013) 608 – 615
[8] Salgado, Alonso, *"An approach based on current and sound signals for in-process tool wear monitoring"*, International Journal of Machine Tools & Manufacture 47 (2007) 2140–2152
[9] Artis sales Online-document (http://www.artis.de/de/files/2011/09/ARTIS_Liebherr_CTM_Waelzfraesen_de.pdf)
[10] Rudolf, "*Adaptierbare Parametrierung von Diagnosesystemen durch Verwendung digitaler Antriebssignale in der Prozessüberwachung"*, Ergebnisse aus der Produktionstechnik 18/2014, Hrsg.: Brecher, C.; Klocke, F.; Schmitt, R.; Schuh, G., Apprumus Verlag Aachen 2014, ISBN 978-3-86359-208-0
[11] Brecher *et al., "Design of gear hobbing processes using simulation and empirical data"*, 9th CIRP Conference on Intelligent Computation in manufacturing Engineering - CIRP ICME '14, Procedia CIRP 33 (2015) 484 – 489

16th Machining Innovations Conference for Aerospace Industry - MIC 2016

Simulation based Planning of Machining Processes with Industrial Robots

J. Brüning[a], *, B. Denkena[a], M.A. Dittrich[a], H.-S. Park[b]

[a]*Institute of Production Engineering and Machine Tools, Leibniz Universität Hannover, An der Universität 2, D-30823 Garbsen, Germany*
[b]*Laboratory for Production Engineering, University of Ulsan, Daehak-ro 93, Nam-gu, Ulsan 680-749, South-Korea*

Abstract

Today, especially machining of large, integral constructed structural parts requires expensive machining centers. In contrast, modern industrial robots are characterized by flexible applications, large working spaces and low capital investment. Therefore, they provide high economical potential for machining applications in aerospace industry. However, their constructive characteristics like low stiffness and high sensitivity to vibrations lead to disadvantages compared with conventional machining centers. Due to this, extruded profiles were used as near to shape pre-products to reduce material removal rates within a new approach. Additionally, several methods for offline and online optimization of robot machining processes were developed and integrated in a new process chain for manufacturing of structural fuselage parts. Thereby, the conventional CAD-CAM process planning chain was extended with simulation based analyzation and optimization methods and a load-depending trajectory planning. The methods for offline process optimization within this novel process chain are presented in this paper.

1. Introduction

Modern aircrafts are designed in order to maximize energy efficiency by low weight. Therefore, the structural components exhibit a minimal remaining material thickness as low as 1 to 2 mm and maximum rigidity. These complex shaped parts are up to 14 m long and typically manufactured from rolled aluminum plates. Today, such parts are

* Corresponding author. Tel.: 49 511-762 18320; fax: +49-511-762-5115.
  E-mail address: bruening@ifw.uni-hannover.de

machined on large machine centers with gantry shaped or hybrid - gantry in combination with a parallel kinematic head - design. The use of these machines is linked to high investments due to the large working space and the high requirements on stability. Regarding flexible applications and large working spaces, modern industrial robots might be an alternative. With low capital investment, robots provide high economical potential for machining applications. However, several effects, like gear backlash or chatter, have to be considered during process planning and machining due to characteristic disadvantages of industrial robots. Exemplary, fig. 1 shows the machined (a) and measured (b) surface with gear backlash induced shape errors.
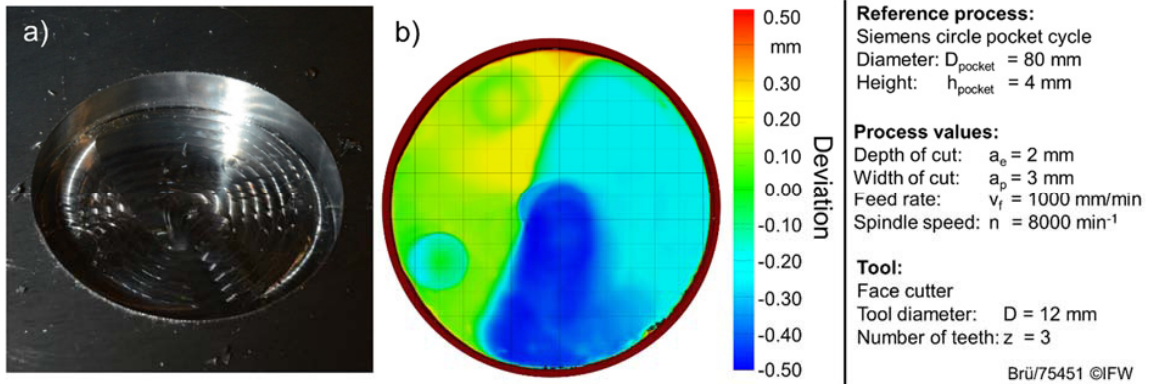

Fig. 1. Characteristic shape errors due to gear backlashes: a) machined surface, b) measured surface.

Challenging processes, like robot machining, requires consideration of technological interactions during process planning. Rehling developed a technological process simulation for the prediction of surface topologies due to process machine interactions like chatter [1]. Therefore the dexel method [2] was used for a time and path discrete analyzation of the cutting conditions. In the field of offline optimization of robot based machining processes, several approaches were presented. Abele et al. investigated the performance of industrial robots for machining applications by experiments and a stiffness model [3]. Bauer et al. analyzed the process machine interactions of robot structure and milling processes and optimized processes by using path manipulation [4]. Lehmann et al. used a similar approach for offline compensation based on calculated tool path deviations [5]. Cen et al. developed an online compensation method based on force sensing and an inverse force model for deviation detection of cutting conditions [6]. A major disadvantage of error based tool adaption is the lack of practical relevance for aerospace applications. Due to legal restrictions, machining processes have to be planned on the desired contour and certificated. In most cases, a later adaption of certificated processes is inadmissible. In addition, full integrated robot modules in the CAD-CAM process chain for aerospace applications are still missing.

Within the research project INNOFLEX novel AlCuLi-alloys and near-net-shape extruded profiles for integral structural parts were analyzed. Main advantages of near-net-shape profiles are the reduction of cutting volume and cutting forces compared to volume precision machining. As a result, the external load of robots is substantially reduced during machining. In combination with a simulation based planning, this can be the starting point to enable an industrial robot for machining applications in aerospace industry.

2. Approach

Aiming for increasing performance of robot based machining processes, the conventional CAD-CAM process planning chain was extended with simulation based analyzation and optimization methods (fig. 2): The developed planning system contains a technological process simulation for a discrete analyzation of the cutting conditions. On this basis, semi-empirical models are utilized for the calculation of process forces [7, 8]. The technological process simulation system is used to characterize and analyze the progress of the initially planned tool paths. Thereby, critical process states, for example peaks of process forces, rapid changes of cutting conditions or axial feed, are identified by knowledge based multi-criteria process analyzation. Critical process states are visualized and avoided by automated

optimization routines like feed rate adaption or cut segmentation. In the next step the process simulation is coupled with a deflection model of the robot [9] and a model of gear backlashes to consider the interaction of process and manufacturing system. Based on the simulation, the production results are predicted, evaluated and optimized by tool path adaption or the specification of adapted robot postures.
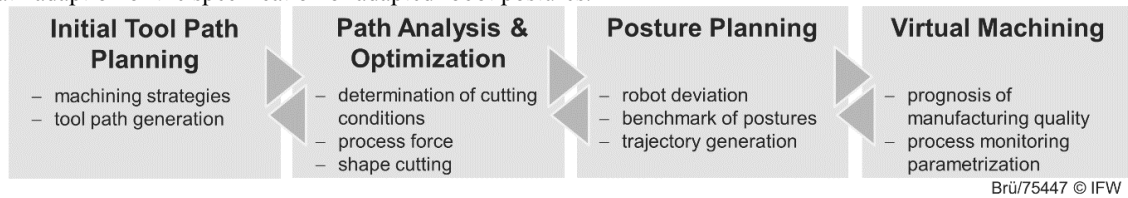

Fig. 2. Simulation based process planning for robot machining.

3. Simulation based tool path analysis and optimization

The initial planed tool path has an evident influence on the achievable manufacturing result. Fig. 3 shows four different surface topologies considering the gear backlash. Changing load direction of strategies zig-zag, helical and trochoidal milling (fig. 3b to d) result in inhomogeneous surfaces. As opposed to this, the homogeneous load conditions of zig strategy lead to smooth surfaces (fig. 3a).
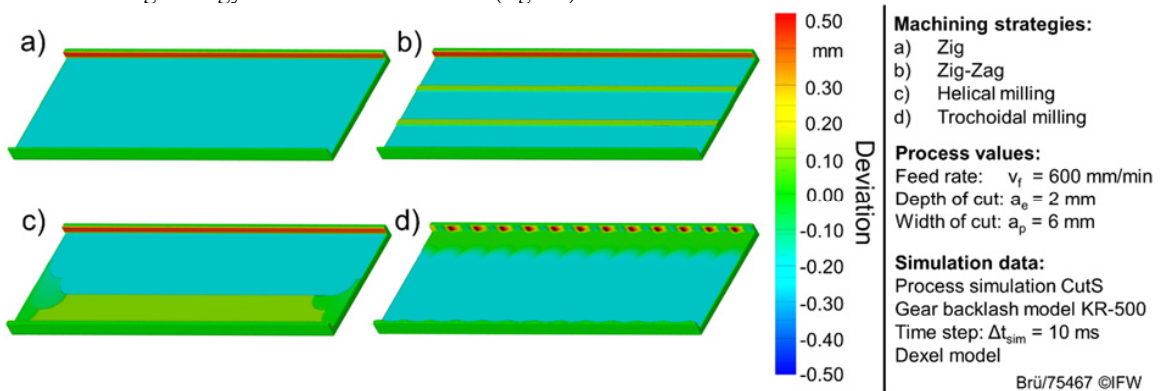

Fig. 3. Influence of machining strategies on surface topology due to gear backlash.

In addition to this, the analysis of the toolpath has the goal to detect and to avoid resulting manufacturing errors in an early process planning step. Due to this, a technological NC simulation developed by IFW named CutS [10] is used to evaluate the initially planned toolpaths. An extension of CutS aggregates continuously position-dependent data during the whole process simulation. The CAM generated tool paths are loaded into the controller model via the neutral formats CL-DATA (DIN 66215) or Standard NC Code (DIN 66025). An appropriate interpreter transforms the motion commands in movements of the tool relative to the work piece. Based on the dexel approach the cutting conditions between tool and workpiece are determined at each time step of the simulation. The knowledge about the current cutting conditions is used to derive geometrical and technological process conditions.

An essential part of the evaluation of machining processes is the prognosis of process forces, due to their main effect on the manufacturing result. The applied process forces model bases on the semi-empirical approach of Weilenmann [7]. This approach allows an efficient calculation of forces based on cutting conditions and a parametric description of the tool shape. Cutting edges and tool rotation are disregarded in the process simulation to decrease calculation time. For an approximate determination of the process force, coefficients are available in large numbers in literature [11]. In addition, coefficients can be specifically determined in experiments. Fig. 4 shows a comparison

of the simulated and the real course of spindle torque for a single pocket operation in an exemplary application. Thereby, a common cutting force coefficient k_c = 780 N/mm² was used for machining aluminum alloy.
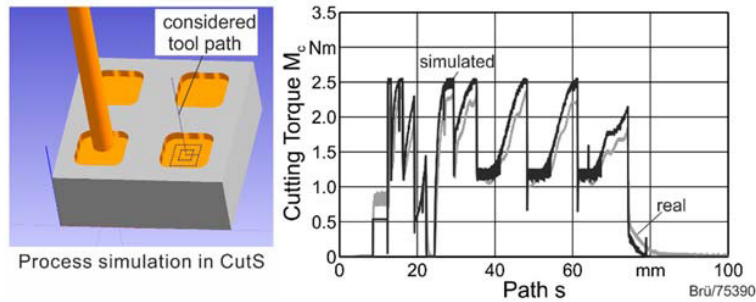

Fig. 4. Simulation of process simulation.

After the simulation, the process is evaluated based on the aggregated data. The different analysis routines use technological knowledge to evaluate the simulated process conditions. The evaluation is based on experimentally determined criteria, which were deposited in the form of mathematical rules and Boolean algebra in different analysis modules. The developed prototype includes an analysis regarding the occurring process forces, process stability, tool immersion behavior and possible structural changes. The basic operation of this analysis modules is exemplary visualized in fig. 5 by reference to a routine to avoid thermally induced structural changes, the so-called soft spots. An important advantage of this approach is that no extensive simulations of physical or metallurgical interactions are necessary. Instead, existing manufacturing knowledge can be used to parametrize rule based analysis functions. The realized routine for avoiding soft spots is based on knowledge of the project partner Premium Aerotec and experimental investigations showed in [12].
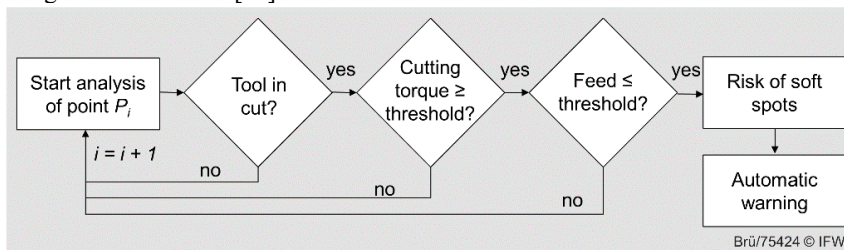

Fig. 5. Offline process analysis.

In addition to the workpiece related analysis of the toolpath, the behavior of the deployed manufacturing system is verified in further toolpath analyses. For example, the analysis routine detects process forces above a given threshold, which results in tool deviations which cannot be balanced by an online compensation [9] within the specified tolerances. In this case, a re-planning or adaption of toolpaths is necessary. The developed optimization routines base on a feed rate adaption or a segmentation of the affected cutting operation. Their use vary depending on the particular requirements. The feed rate adaption is used in the case of a small or local restricted transgressions of the threshold. The segmentation of cutting operations is used in cases in which a feed rate reduction would lead to an inefficient machining compared to operations with a reduced depth of cut a_p.

As a result of changing process conditions, stability behavior of the process can be worsened. These cases are identified by an automated analysis of the process stability on tool and machine specific stability cards (as described in [12]). In case of unaccomplished stability criteria, the user can adjust the affected cutting operation by an automated selection of valid cutting speed.

4. Automated load-optimized prepositioning

Due to the posture and load dependent misalignment of the robot, the positioning of the robot relative to the workpiece has a significant influence on the manufacturing result. Moreover, because of the complex system of equitation of robot kinematics, different valid postures can be used to achieve a path point. Each of these postures has different positioning errors under load. This is important for two aspects: On the one hand this interrelationship allows a load-optimized prepositioning. On the other hand a workload optimized trajectory influences the achievable manufacturing results.

Based on this, a method for the automated pre-positioning of workpiece and robot was developed. The built-up Broetje Automation manufacturing cell with an industrial robot Kuka KR-500 L340-2 uses an additional translational axis for guiding the robot. In addition, the cell has a flexible clamping system provided by J. Schmalz GmbH. This can vary the clamping position of the workpiece by using translational movable, modular vacuum clamps. Due to this, the manufacturing cell has two additional degrees of freedom. Semi-empiric determined accuracy maps describe the robot specific stiffness behavior for different load cases. By using the process data of the initial tool path characterization (compare chapter 3), the expected work load is known for every path point. The positioning of the robot relative to the workpiece is possible within the plane defined by the translational axis and the axes of the clamping system. The combination of accuracy maps and process data allows an automated selection of a process-specific, optimal clamping position of the workpiece. The described approach is schematically illustrated in fig. 6.
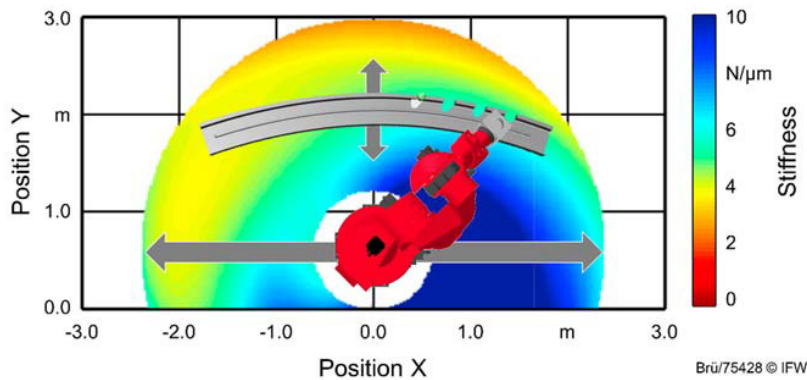

Fig. 6. Using accuracy maps for work piece and robot positioning.

5. Virtual machining

Objectives of the virtual machining are the determination of suitable robot postures, the forecast of the achievable production quality and the teachless parameterization of a process monitoring system. To use the robot models in different steps of planning, a modular approach was developed. This ensures a standardized cooperation of the models in the various planning modules.

5.1. Prediction of workload dependent positioning errors

The basic model for the deviation behavior of the robot is based on a Cartesian stiffness model. This is parameterized locally within the workspace by empirically determined stiffness values. For the simulation of occurring interactions between process forces, robot misalignment and the resulting tool displacement, the Cartesian stiffness model was coupled with the process model. In the first step of each time step, the cutting conditions are calculated for test purposes using the tool displacement of the last time step. These cutting conditions are used for an initial process force calculation. Afterwards, these forces are used within the stiffness model to forecast the resulting tool displacement. Subsequently, the difference between the assumed and the recently determined displacement are

compared. In case of a mismatch of both displacement values, the cutting cycle is repeated with an adapted start value of the tool displacement. In the case of a difference smaller than a given threshold, the assumed displacement is used for the final modification of workpiece model in the current time step. For the consideration of robot posture depending influences like work load depending misalignments in the rotational axis of the robot, this basic method was enhanced by a robot misalignment model described in [9].

5.2. Prediction of gear backlash dependent positioning errors

Changing directions of rotation lead to alternating stresses in the gears of robot axes. These so called gear backlashes lead to incorrect positions of the involved axes and to positioning errors of the end effector. Due to changing strain conditions in the gears, the gear backlash is subject to a hysteresis effect. As shown in fig. 1, especially cutting operations with a large number of changes of rotation directions are affected by gear backlash. Aiming to characterize the gear backlash in the single robot axes, a numerically method for backlash identification was developed on the basis of experimentally determined data of laser trackers and recorded control data. The target positions of the tool center point (TCP) were determined by discrete time steps from the axis data of the control and forward kinematics of the robot. These target positions were compared with the measured tool path data of the laser tracker to calculate the deviation of the TCP. Subsequently, the corresponding axis values for the faulty TCP position were determined based on an inverse kinematics. These axis values were compared with the recorded target axis values to determine the misalignments in every single robot axis. The misalignment corresponds to the gear backlash. Fig. 7 exemplarily shows the extracted hysteresis effect for axis A5 of the used robot.
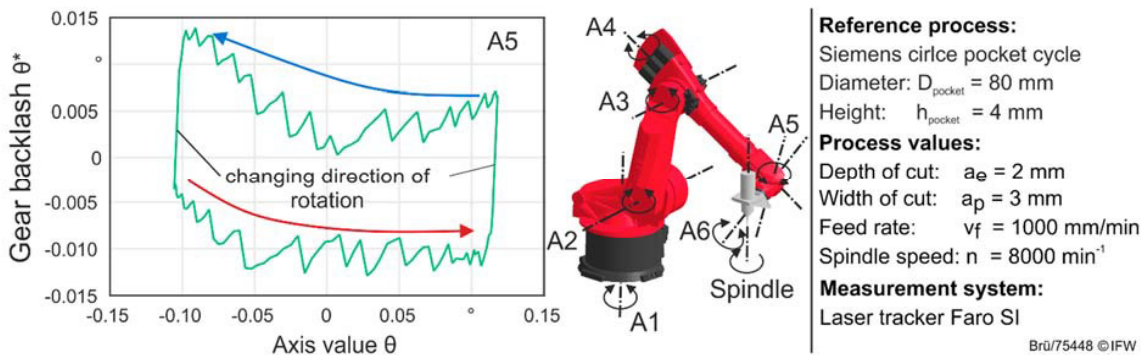

Fig. 7. Backlash in gear axis A5.

The gear backlash values of axes A1 to A6 are shown in tab. 1.

Table 1. Backlash characteristics of axes A1 to A6.

Axis	A1	A2	A3	A4	A5	A6
Lower limit	-0.012°	-0.004°	0.016°	-0.015°	-0.015°	-0.002°
Upper limit	0.006°	0.017°	-0.005°	0.007°	0.014°	0.004°

The determined backlash characteristics were used to parameterize a backlash model in process simulation. The backlash of each axis is assumed as the value of respective error axis additionally to the robot kinematics. The error axes have the same orientation as the respective robot axis. During the process simulation, the respective value of the gear backlash is determined at each time step depending on the current rotational motion and the accordingly error axis value. A comparison of experimentally determined and virtually determined component surface is shown in fig. 8.
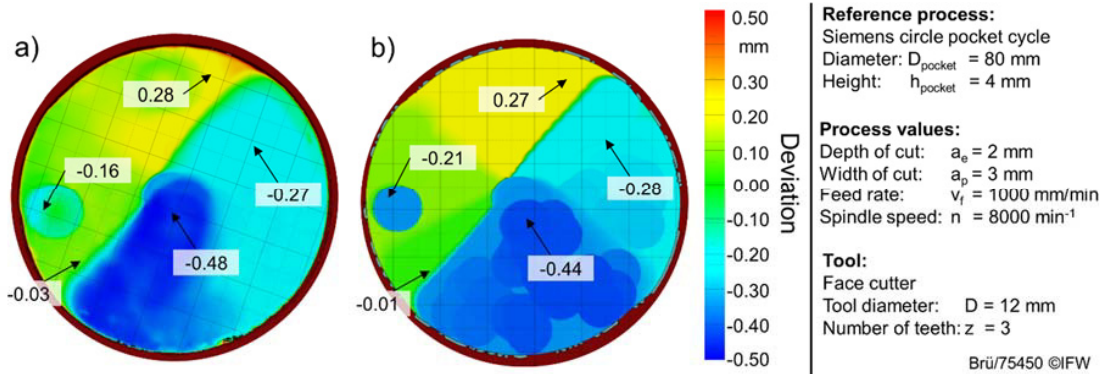
Fig. 8. Comparison of (a) real and (b) virtual machined pocket.

5.3. Automated process assessment

The described models for process machine interactions are used for an automated assessment of the planned machining processes. The main assessment criterion is the compliance of form and position tolerances. Therefore, the virtual machined workpiece model is compared with an integrated model of the target shape including valid tolerances. In the case of a violation of the given restrictions, the programmer is warned automatically by the planning system. The warning includes a detailed description of the process conditions during the affected cutting operation. In the case of a pass of the given restrictions, the aggregated information about the planed process are stored for later use in the case of occurring failures during ramp up.

5.4. Teachless parametrization of process monitoring system

Within the extended CAD-CAM process chain for robot machining, the approach of teachless parametrization of process monitoring systems [13] is used to shorten and optimize ramp up processes. Therefore, obtained process information from the path planning is utilized for configuring the process monitoring system without any teaching processes. As described in chapter 3, information about the process like cutting torque, process forces or cutting conditions is determined by a technological NC simulation. These information was augmented in all steps of the planning process chain. For the determination of process limits, the course of the predicted cutting torque is automated normalized and split into sixteen levels. All neighbored path point with the same level are summarized to one process segment.
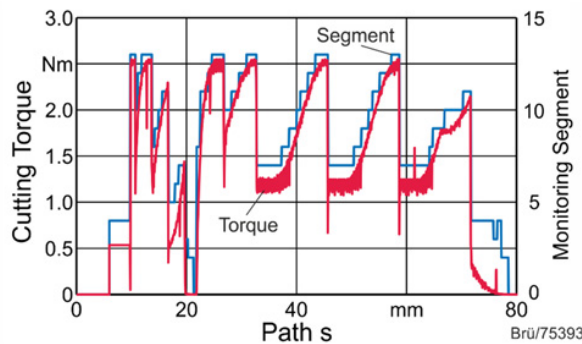

Fig. 9. Process segmentation for parametrization of process monitoring system.

As shown in fig. 9, these segments serve as a qualitative description of the process course for the teachless parameterization of monitoring limits in the process monitoring system. The cutting torque is used because of its adequate correlation with the monitored spindle torque. During monitoring, the expected spindle torque and the derived limits are calculated on the basis of the segments and the measured spindle torque. For the parametrization of the used process monitoring system Artis Genior Modular OA, the segments are exported via a defined XML format. The teachless parametrization enables the process monitoring system to detect variances from the predicted process. Variances can be issued for example by excessively tool wear or a broken tool. Thereby the monitoring system is able to stop the process and avoid further damages of the machined part or the manufacturing system.

6. Conclusion and outlook

This paper presented an approach for an enhanced CAD-CAM process chain for robot machining processes based on several simulation models. On the one hand, the simulation results are used in the different steps of process planning to detect and avoid occurring errors as early as possible. On the other hand, the simulation results are aggregated for an efficient reuse in following planning steps. In the final step, the aggregated process information are used for the teachless parametrization of a process monitoring system.

This example shows the necessity for an augmentation of the process planning with technological knowledge about the process, the manufacturing system behavior and their interactions. Simultaneously, the opportunities of a classical offline process planning are restricted concerning current state information like tool wear, clamping situation and thermal behavior. In the case of robot machining, effects like gear backlash can be predicted and compensated offline. Nevertheless this is connected to a resulting loss of the boundlessness regarding the versatility of the process. Therefore, the borders between process planning systems and manufacturing systems have to be dissipated in the future.

References

[1] S., Rehling: Technologische Erweiterung der Simulation von NC-Fertigungsprozessen, Dr.-Ing. Dissertation, Leibniz Universität Hannover, 2009
[2] T. van Hook: Real-Time Shaded NC Milling Display, Proceedings of the 13th annual conference on Computer graphics and interactive technique, 22 (1986), p. 15-20
[3] E. Abele, M. Weigold, S. Rothenbücher: Modeling and Identification of an Industrial Robot for Machining Applications, Annals of the CIRP, Vol. 56 (2007), p. 387-390
[4] J. Bauer, M. Friedmann, T. Hemker, M. Pischan, C. Reinl, E. Abele, O. von Stryk: Process Machine Interactions Analysis of Industrial Robot Structure and Milling Process Interaction for Path Manipulation in: B. Denkena, F. Hollmann (Eds.), Process Machine Interactions: Prediction and Manipulation of Interactions between Manufacturing Processes and Machine Tool Structures, Springer Berlin Heidelberg, 2013, p. 245-263
[5] C. Lehmann, M. Halbauer, D. Euhus, D. Overbeck: Milling with industrial robots: Strategies to reduce and compensate process force induced accuracy influences, 17th IEEE International Conference on Emerging Technologies and Factory Automation, 2013
[6] L. Cen, S. N. Melkote, J. Castle, H. Appelman: Wireless Force Sensing and Model Based Approach for Enhancement of Machining Accuracy in Robotic Milling IEEE/ASME Transactions on Mechatronics, 21(2016), p. 2227-2235
[7] R. Weilenmann: Beitrag zur Berechnung des Leistungsbedarfs beim Fräsen, Werkstatt und Betrieb, 90(1957), p. 296-298
[8] Altintas, Y:. Manufacturing Automation: Metal Cutting Mechanics, Machine Tool Vibration and CNC Design, Cambridge University Press, 2000
[9] B. Denkena, T. Lepper: Enabling an Industrial Robot for Metal Cutting Operations, 15th Machining Innovations Conference for Aerospace Industry, Procedia CIRP, 35(2015), p. 79-84
[10] B. Denkena, V. Böß: Technological NC Simulation for Grinding and Cutting Processes Using CutS, in P. J. Arrazola: Proceedings of the 12th CIRP Conference on Modelling of Machining Operations, Vol. II, 2009, p. 563-566
[11] W. Degner, H. Lutze, E. Smejkal: Spanende Formung: Theorie, Berechnung, Richtwerte. Hanser, 2009
[12] B. Denkena, J. Brüning, D. Niederwestberg, R. Grabowski: Influence of Machining Parameters on Heat Generation during Milling of Aluminum Alloys, 7th HPC 2016 – CIRP Conference on High Performance Cutting, Procedia CIRP, 46(2016), p. 39-42
[13] B. Denkena, R. Fischer, M. Köller, C. Schmitz, D. Euhus, V. Sellmeier, S. Wolniczak, H. Hilbers: Anlernfreie Prozessüberwachung für die Einzelteilfertigung, Unter Span, Machining Innovations Network 01/2013, p. 14-15

16th Machining Innovations Conference for Aerospace Industry - MIC 2016

Assessing the accuracy of five axis machines by comparing machine measurement data with test work piece deviations

G.H.J. Florussen*, H.A.M. Spaan, T.M. Spaan-Burke

IBS Precision Engineering, Esp201, Eindhoven 5633AD, the Netherlands

Abstract

In aerospace industry the application of five axis machines is increasing and becoming common practice. The determination of the accuracy of such five axis machine however is often difficult or problematic. A significant increase is seen in the certification efforts involved for this industry sector.

To assess the accuracy of a five axis machine within one minute a dedicated Rotary Inspector system has been developed by IBS Precision Engineering. With this measurement system a 3D measuring head is used in combination with a masterball while the machine executes a certain cycle using multiple machine axes simultaneously. Typical tests are specified in ISO10791-6 (e.g. AK1, BK4, CK4) and these are used in this paper to determine the machine's accuracy first, representing normal (milling) machine use. Usually test work pieces are made on a machine and its geometrical deviations are checked on a CMM for certification. The relation between these geometrical test work piece deviations and the measured ISO machine error parameters of the rotary axes is addressed in this paper. In this way the need of milling (many) test work pieces can be reduced significantly for certification purposes.

Keywords: Precision machining; process monitoring

Nomenclature			
YOA	location error of A-axis in Y direction	BOA	squareness error A-axis around Y-axis
ZOA	location error of A-axis in Z direction	COB	squareness error B-axis around Z-axis

* Corresponding author. Tel.: +31 402901270; fax: +31 40 2901279.
 E-mail address: Florussen@ibspe.com

1. Introduction

An innovative measuring method named "Rotary Inspector" (RI) is presented in this paper to assess the accuracy of a five axis machine within one minute. This method uses kinematic tests for which multiple machine axes move simultaneously [1] like in machining complex work pieces as common in aerospace industry.

Test work pieces are generally used to verify the accuracy of machine tools [2-5]. Although this is a well-accepted method, it is expensive due to related costs. A CMM is required to measure the test work piece and the machine down time is regarded as a problem. A considerable certification effort is involved to determine whether a machine tool is within specifications.

The accuracy of a five axis machine tool is currently assessed by using several methods. First the linear axes are calibrated using a laser interferometer and electronic levels. After that the rotary axes are measured by applying a (touch-trigger) probing system as common for CMMs on a machine tool. A master ball is mounted on the machine's table and set to three discrete angles for measurement i.e. C=0°, 120° and 240°. For each rotary axis position the probing system requires five spatial points (i.e. four on equator, one on top) on the master ball to obtain the X, Y and Z coordinates of the master ball center in the machine's volume. A disadvantage of this method is that it only uses three points for each rotary axis; it does not inherent any redundancy. Controller manufacturers offer routines to optimize the machine's parameters based on such a measurement (i.e. Cycle996 for Siemens controllers [6]). The measurement uncertainty of the probing system, the probe synchronization delay errors with the machine's encoder scales and the measuring time are other drawbacks of this method.

The introduction of the R-test [7,8], combining three sensors in an orthogonal nest to determine the center position of a ball in X,Y and Z, instantly enable dynamic measurement of a rotary axis. The typical sampling is 1 kHz, resulting in redundant data: a full circle is measured instead of three points only. Least squares fitting routines are used to estimate the center point from measurement data resulting in the location errors of the rotary axis.
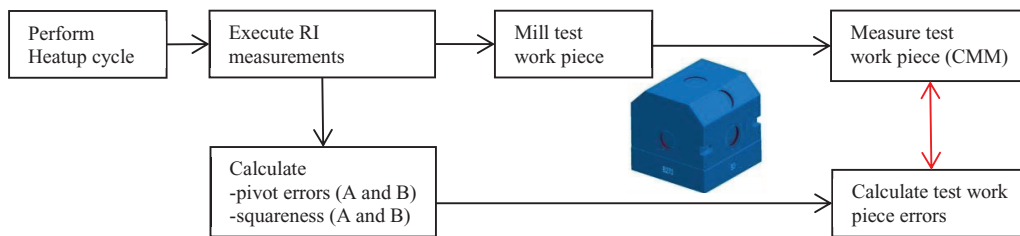

Fig. 1. Flow diagram to compare both methods to assess the accuracy of a five axis machine tool.

The research described in this paper is schematically depicted in Fig. 1. The basic idea is to use measurement data to assess a machine's accuracy first. The Rotary Inspector method is applied to describe the geometrical deviations of a test work piece in this paper. Test work pieces should be milled only when RI measurements indicate that the machine's accuracy is sufficient to prevent making scrap.

First a heat up cycle is executed on a five axis milling machine, see Fig. 1, 2. The spindle rotates 8000 RPM for 20 minutes as done in common use of this specific machine.

After that the 3D measuring head is inserted in the spindle and the kinematic tests specified in ISO 10791-6 [1] are executed in a sequence. As this machine has two rotary axes on the table side (e.g. swivel table or trunnion table machine), the tests BK1, BK2 and BK4 apply. Measurement data obtained is used to calculate these error parameters of a rotary axis [3,7-10]:

- Location errors of the pivot line of a rotary axis
- Squareness errors of the pivot line of a rotary axis

A test work piece has been designed and the impact of the pivot line errors (location and squareness) of both rotary axes is calculated. Finally the experimentally obtained results are compared to validate the Rotary Inspector method as indicated by the red arrow in Fig. 1.

In Chapter 2 the Rotary Inspector method is explained. The designed test work piece is described in Chapter 3. Results are discussed in Chapter 4 followed by the conclusions in Chapter 5.

2. Rotary Inspector

To determine the accuracy of a five axis machine within one minute, the Rotary Inspector has been developed. With this measurement system a 3D measuring head, equipped with three non-contact inductive sensors, is used in combination with a precision master ball [7-10]. The measuring head is mounted in the spindle and the master ball is mounted on the machine's table using an Erowa clamping system to enable a fast and reproducible setup, see Fig. 2.
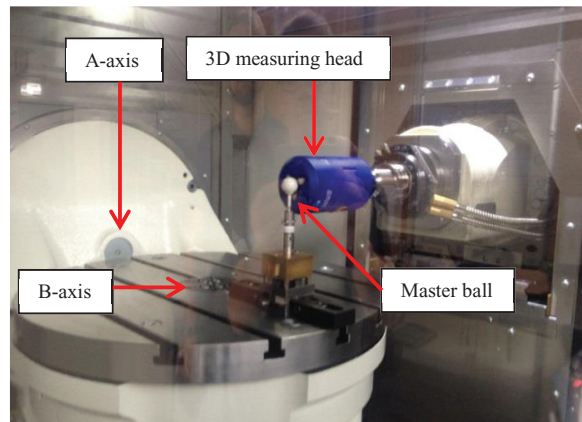

Fig. 2. Rotary Inspector measurement setup on a five axis milling machine.

The measurement uncertainty of this measurement system is less than 1 μm (2σ). Several multi-axis measurement tests are defined in ISO10791-6 and these tests are used to assess the machine's accuracy.

2.1. ISO10791-6 kinematic tests

In ISO 10791-6 five axis machines are divided in three classes: swivel head machines (i.e. Annex A), swivel table machines (i.e. Annex B) and mixed type machines (i.e. Annex C). In this paper a trunnion table machine is used and these three kinematic tests apply:

- BK1 test (three axes)
- BK2 test (three axes)
- BK4 test (five axes)

For the BK1 test the A-axis is commanded to rotate 180° degrees CW and CCW while the Y- and Z-axis follow. This test is visualized in Fig 3.

The relative displacement of the master ball is recorded in time during this cycle, see Fig. 4. The spikes present in are caused by start-stop motions of the linear axes.

The same measurement data is then plotted in the YZ-plane and a (red) circle is fitted using the least squares method, see Fig. 4B). The center point of this fitted circle represents the location errors of the A-axis, YOA and ZOA.

The squareness error BOA is determined in the XZ-plane (not shown) and COA is determined in the XY-plane (not shown). For such squareness error the displacement "out-of-plane" (dx for an A-axis) is evaluated over the radius of measurement.

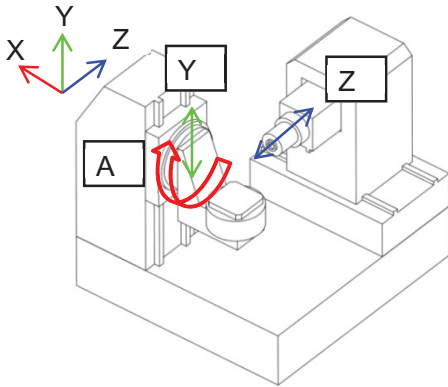The estimated error parameters of the A-axis are shown in Table 1.
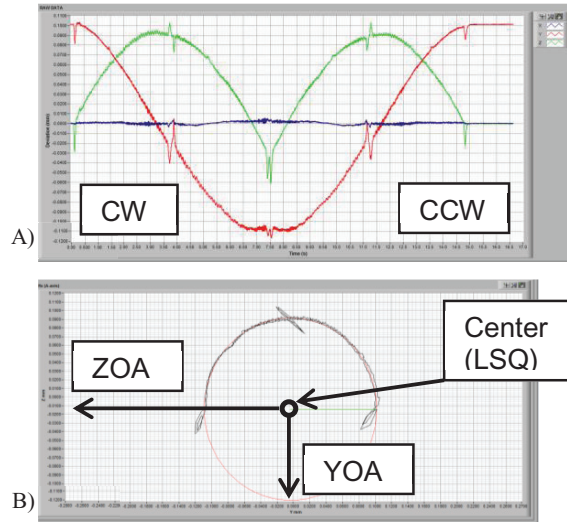
Fig. 3. schematic representation of BK1 test.

Fig. 4. A) Example of measured displacement in X (blue), Y (red), Z (green) for a BK1 measurement; B) Example of BK1 measurement, the measurement data (black) is shown in the YZ-plane with the best fit circle (red).

Table 1. Calculated error parameters from BK1 test.

BK1 test results	Value
YOA	0.0036 mm
ZOA	0.0096 mm
BOA	0.0000°
COA	-0.0009°

For the BK2 kinematic test the same is done for the B-axis. The B-axis is commanded to rotate 360° degrees CW and CCW while the machine's X- and Z-axis follow, see Fig. 5. The ISO error parameters of the B-axis are displayed in Table 2.
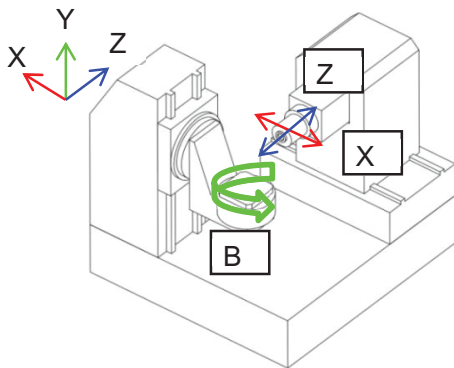

Table 2. Calculated error parameters from BK2 test.

BK2 test results	Value
XOB	-0.0178 mm
ZOB	0.0126 mm
AOB	-0.0012°
COB	0.0008°

Fig 5. schematic representation of BK2 test.

Finally the five axis test BK4 is executed. The B-axis rotates twice the speed of the A-axis while the X, Y and Z axes follow. This test is not used to estimate ISO error parameters but is used to determine the overall accuracy of a machine tool in five axis mode. The results of this five axis test however are beyond the scope of this paper and subject of further research.

3. Test work piece

A test work piece has been designed that is sensitive for the error parameters of a rotary axis and that can be machined within five minutes. It consists of a block having centered rings in each plane, see Fig. 6. Due to non-zero error components rings on opposing sides are displaced relatively. The center point of this block coincides with the center of the master ball within 25 mm; both are mounted on the same position on the machine's table, being 127 mm in Z-direction from the table center, see Fig. 2.

In Fig. 6 a drawing of this test work piece is shown. Each plane contains a ring with a diameter of 30 mm and the depth equals 10 mm. This test work piece is milled in five axis simultaneous mode (TRAORI for Siemens controllers). In Table 3 the rotary axis positions are assigned for each ring.

The errors of the A-axis are reflected in ring1, 5, 6, 7 and 8. The B-axis errors are reflected in ring1, 2 and 4.
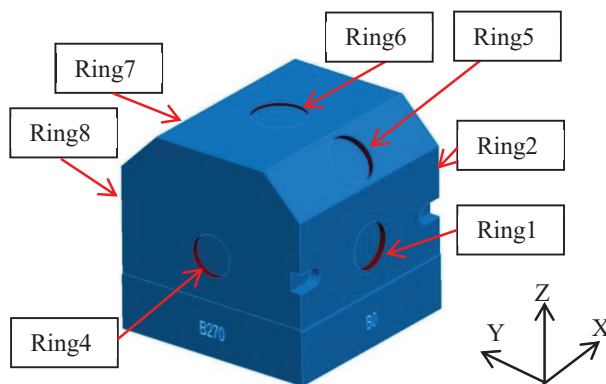

Fig. 6. drawing of test work piece.

Table 3. Rotary axis positions for each ring of the test work piece.

Test work piece	Rotary axis positions
Ring1	A=0°, B=0°
Ring2	A=0°, B=90°
Ring4	A=0°, B=270°
Ring5	A=-45°, B=0°
Ring6	A=-90°, B=0°
Ring7	A=-135°, B=0°
Ring8	A=-180°, B=0°

3.1. Milling strategy

This aluminium test work piece is machined under finishing conditions to limit tool deflection and heat generation as much as possible. Cooling liquid is applied and the rings are milled using circular milling.

Stable cutting is obtained using an Iscar ECA cutter that has the same length as the measuring head, 216 mm, see Table 4. The total machining time is three minutes.

Table 4. Cutting parameters for machining test work piece.

Iscar ECA cutter	
Diameter and length	12 mm and 216 mm
Number of teeth	3
Helix angle	40°
Cutting speed	603.8 mm/min
Depth of cut	2.5 mm
Spindle speed	16000 RPM

3.2. Analysis

A geometrical relation exists between the error parameters of a rotary axis and the relative displacement between opposing rings of the test work piece. This is illustrated with an example first. Parameter YOA displaces the A-axis with respect to the YZ-axes vertically in this case, see Fig. 7.
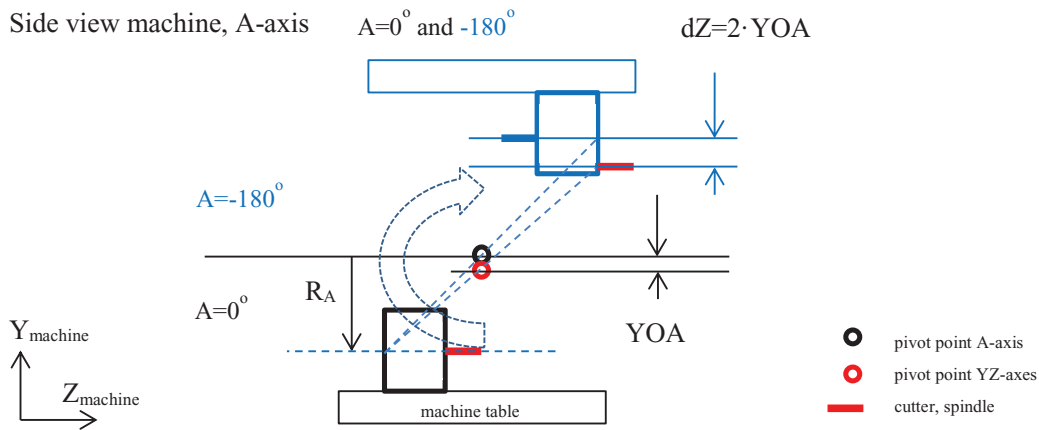

Fig. 7. Impact of error parameter YOA on the ring positions in the front and back plane of the test work piece.

The black ring is present in the front plane of the test work piece and the blue ring in the plane on the back side, made with A=-180°, see Fig. 8.

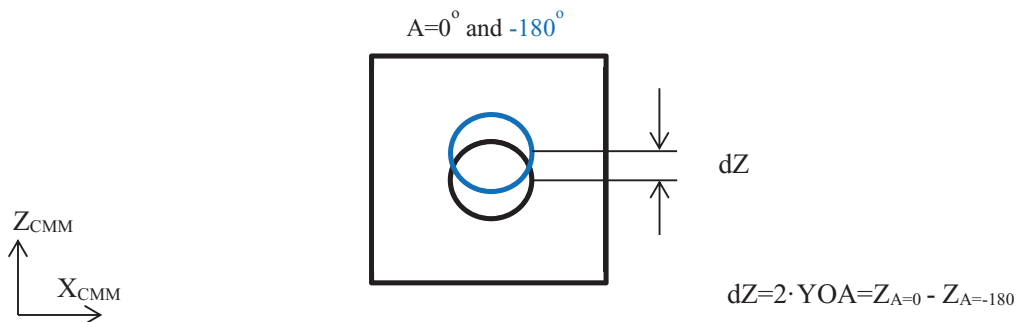Fig. 8. Vertical shift between rings due to YOA.

Because of this, Ring1 (machined at A=0°, B=0°) is shifted vertically relative to Ring8 (machined at A=-180°, B=0°). The vertical shift between Ring1 and Ring8 then equals 2•YOA. A similar analysis can be made for a horizontal shift between opposing rings.

Squareness error COB is derived in a similar way by comparing Ring2 (A=0°, B=90°) and Ring4 (A=0°, B=270°), the side planes of the test work piece. The vertical shift between these rings equals 2•RB•tan(COB) where RB stands for the radius of the master ball trajectory using the B-axis, being 127 mm. Radius RA is depicted in Fig. 7 and equals 237 mm for this setup.

Extending this analysis with ring depths enables to derive a geometrical relation between all eight measured error parameters of both rotary axes and the deviations in ring positions of the test work piece, see Table 5.

The measured ISO parameters of the RI measurements are used to describe the shift between opposing rings using these relations. This is later compared to measured ring shifts using a CMM.

Table 5. CMM results with relative ring positions of test work piece.

Relative shift between rings	Link to ISO error parameter	Ring pair	CMM
A-axis			
dZ	$2 \cdot YOA$	1 and 8	$Z_{ring1} - Z_{ring8}$
dY	$2 \cdot ZOA$	1 and 8	Length error ring1-8
dX	$R_A \cdot \tan(BOA)$	1,6 and 8	$X_{ring6} - (X_{ring1} + X_{ring8})/2$
dX	$2 \cdot R_A \cdot \tan(COA)$	1 and 8	$X_{ring1} - X_{ring8}$
B-axis			
dY	$2 \cdot XOB$	2 and 4	$Y_{ring2} - Y_{ring4}$
dX	$2 \cdot ZOB$	2 and 4	Length error ring2-4
dZ	$R_B \cdot \tan(AOB)$	1,2 and 4	$Z_{ring1} - (Z_{ring2} + Z_{ring4})/2$
dZ	$2 \cdot R_B \cdot \tan(COB)$	2 and 4	$Z_{ring2} - Z_{ring4}$

4. Results

In this chapter the results of both methods are presented and compared. First the CMM measurement data is shown, followed by the results obtained with the RI method.

4.1. CMM data

After at least one night of acclimatization the test work piece is measured on a CMM. The measured ring position is compared to its nominal position and the results are present in Table 6.

Next to these ring positions, the distance between Ring1 – Ring8 minus their nominal distance is measured to verify error parameter ZOA. The distance between Ring2 – Ring4 reflects error parameter ZOB and is listed at the bottom of Table 6.

Table 6. CMM results with relative ring positions of test work piece.

CMM data	X [mm]	Y [mm]	Z [mm]
Ring 1	0.000	-	0.001
Ring 2	-	-0.015	0.002
Ring 4	-	0.016	0.001
Ring 5	0.003	-	-
Ring 6	0.001	0.013	-
Ring 7	0.002	-	-
Ring 8	0.003	-	0.023
Length error Ring 1-8	-	0.026	-
Length error Ring 2-4	0.019	-	-

4.2. Rotary inspector data

In Table 7 the displacement between rings is calculated based on the measured error parameters of the A- and B-axis. This is listed in the second column. The third column contains the same ring shift as measured by the CMM, see Table 7.

The difference between calculated and measured ring shifts is typically smaller than 10 µm, ignoring the outlier at YOA. The machine's thermal behavior is suspected to be responsible for this effect but this requires further research.

Table 7. Test work piece deviations for both methods.

ISO error parameter	Calculated ring shift, RI	Measured ring shift, CMM	Difference
YOA	0.0072 mm	0.022 mm	14.8 µm
ZOA	0.0192 mm	0.026 mm	6.8 µm
BOA	0.0000 mm	-0.001 mm	-1.0 µm
COA	-0.0074 mm	-0.003 mm	4.4 µm
XOB	-0.0356 mm	-0.031 mm	4.6 µm
ZOB	0.0252 mm	0.019 mm	-6.2 µm
AOB	-0.0027 mm	-0.002 mm	0.7 µm
COB	0.0035 mm	0.001 mm	-2.5 µm

Possible sources of deviations in this comparison are the following assumptions applied:

- Perfect milling or cutting process.
- Ignoring errors in the measurement of the test work piece (i.e. ring roundness errors up to 10 µm have been detected in this analysis, most are typically 3 µm or smaller).
- Only the pivot line location and squareness errors of the rotary axes are considered here, all other machine errors have been neglected. As the machine used in this research is new this assumption appears valid
- Thermal behavior of the machine tool. Calculated error parameters can vary 5 to 10 µm when comparing successive RI measurements performed under different conditions i.e. cold versus warm.

Further research focusses on the improvement of the match between the RI method and the test work piece method. Also possibilities concerning the five axis test BK4 will be investigated further to assess the machine's accuracy even faster. This will also be applied to swivel head machines and mixed type machines to cover the entire range of five axis machine tools used in aerospace industry.

5. Conclusions

An innovative measuring method named Rotary Inspector has been presented to assess the accuracy of a five axis machine tool within a minute. Simple test work pieces are used to verify this method and the deviations in ring positions of a test work piece can be described with deviations smaller than 10 µm typically, with a single outlier. The thermal behavior of the machine appears to be significant in this comparison and requires further research.

Acknowledgements

References
[1] ISO 10791-6, Accuracy of speeds and interpolations, ISO, Geneva, 2014.
[2] ISO 10791-7, Accuracy of finished test pieces, ISO, Geneva, 2014.
[3] S. Ibaraki, W. Knapp, Indirect Measurement of Volumetric Accuracy for Three-Axis and five-Axis Machine Tools: A Review, Int. J. of Automation Technology Vol6 No2, p110-124, 2012.
[4] M. Gebhardt, W. Knapp, K. Wegener, 5-Axis Test-Piece – Influence of Machining Position, Proceedings of MTTRF 2012 Annual Meeting.
[5] S. Ibaraki, et al., Machining tests to identify kinematic errors on five-axis machine tools, Precision Engineering, Vol34, Issue 3, July 2010.
[6] Sinumerik 5-axis machining manual, section 2.9, Siemens, Edition 5/2009.
[7] S. Weikert, W. Knapp, R-test, a new device for accuracy measurements on five axis machine tools, Annals of CIRP, 53/1:429-432, 2004.
[8] B. Bringmann, W. Knapp, Model-based 'Chase the ball' Calibration of 5-axes Machining Center, Annals of CIRP vol. 55/1/2006.
[9] G.H.J. Florussen, H.A.M. Spaan, Static R-test: allocating the centreline of rotary axes of machine tools, Lamdamap conference VIII, p196-202, Cardiff, UK, 2007.
[10] H.A.M. Spaan, G.H.J. Florussen, Determining the 5-axes machine tool contouring performance with dynamic R-test measurements, p377-381, Proceedings of 12th Euspen conference, Stockholm, Sweden, 2012.

Multi-point Clamping with Automatic Collision Avoidance for Aircraft Structural Parts Machining

Haibo Liu, Liang Zhao, Te Li*, Bo Hou, Yongqing Wang, Yue Ma, Zhenyuan Jia

aDalian University of Technology, Linggong Road No.2, Dalian and 116024, China

Abstract

In order to solve the problem of machining motion collision between cutter and fixtures, a multi-point clamping system with automatic collision avoidance is proposed for aircraft structural parts. The system is developed in consideration of part localization and modular clamping functions, and independent of CNC machine tools for the convenience of application. And then, a model-based collision detecting algorithm is designed, which can be implemented by comparing the cutter's actual position extracted by ultrasonic sensors, and the calibrated positions of clamping points. Finally, a modular fixture system with automatic collision avoidance was manufactured and tested. From machining experiments, it indicates that the proposed fixture system can be highly efficient and very flexible to meet the aircraft structural parts machining requirements.

Keywords: Multi-point clamping; Automatic collision avoidance; Fixturing; Structural parts; Aircraft;

1. Introduction

With the rapid development of the aircraft manufacturing industry, the relevant machining equipment and approaches have already been the hot fields for the aircraft structural parts[1-3]. The beam frame part is one of the typical parts with the characteristics of structural complexity, low rigidity (thin-walled), high material removal rate and so on. These characteristics bring great challenges to machining. Generally, the machining process becomes more centralized and is desired to be completed within once clamping. Multi-point clamping is an efficient and practical approach to ensure the static and/or dynamic stability for these parts machining. However, it is always inevitable that

_____

* Corresponding author. Tel.: +86-15804064808; fax: +86-0411-84708420.
 E-mail address: dlut_lite@126.com

some clamping points are very close to the machined features, such as slots, ribs, holes and so on. In such a situation, the tool path and posture planning may be disabled to solve the machining motion collision between cutter and clamping points. Actually, traditional multi-point fixture systems are usually manual and inefficient with repeated localization and clamping. Thus, it is a knotty problem for the aviation manufacturing industry.

One common collision avoidance way is that extra boss is reserved on the rough parts for clamping. However this way wastes many raw materials and increases the cost. In recent decades, many flexible fixture systems have been developed and applied to the aircraft structural parts machining[4, 5]. CNA Manufacturing Systems incorporated developed the POGO flexible tooling system that is a turnkey, automated, universal holding fixture used to rigidly hold contoured panels made of metal and/or composites for a variety of manufacturing operations[6]. The POGO system is typically integrated with a CNC machine tool or robot, creating a completely integrated, flexible manufacturing cell. M. Torres company developed the TORRESTOOL that is a flexible universal holding fixture specially designed to support in space aircraft structural components, while they are machined or laser cut[7]. The TORRESTOOL is a modular concept consisting on a number of carriages that move on the X-axis direction, with a number of supports per carriage, which move on the Y and on the Z axes.

In this research, as an alternative practical approach, a multi-point clamping and modular fixture system with automatic collision avoidance is developed. The proposed system can make the cutter move continuously by the ability of automatic collision avoidance, and improve the machining efficiency. The early-warning strategy by the ultrasonic sensors and the detailed collision avoidance method based on the artificial potential field model are proposed. Finally, the validity is tested in the machining experiments.

2. System design

2.1. Structure overview

In consideration of the features of beams frame parts and the flexibility of the process equipment system, some design rules should be observed as listed below,
- **Localization flexibility:** the system can adapt to complex parts with different specifications of structure and size.
- **Modularization:** the number and clamping positions of fixtures can be adjusted in different machining situations.
- **Fixture flexibility:** the force and position of the clamping point can both be changed based on the parts rigidity properties and the cutter planning.

As shown in Fig. 1, the clamping system is designed for the high-efficiency machining of the beams frame parts. It is mainly composed of the bottom board, fixtures, ultrasonic sensors, and tool setting gauge. The bottom board is fixed on the workbench of the CNC machine tool. The fixtures are positioned and fixed on the planned clamping points. Then the parts are put in the exact position and pressed firmly by the fixtures. The ultrasonic sensors are applied to on-line monitoring and position feedback of the cutter. The modular design of the fixture improves the machining flexibility and efficiency.

2.2. Fixture mechanism

The independent modular fixture system is more flexible than the specialized process equipment system. As shown in Fig. 1, the fixture module mainly includes the clamping rod, pressure head, air cylinder, and fixed plate. The clamping rod with two degrees of freedom can move up and down in the direction of *Z*-axis and rotate around the *Z*-axis. Thus, it has the ability of clamping the parts in different heights and avoiding collision. Furthermore, the clamping force with the maximum 7kN on the parts can be adjustable. The optimal clamping force is selected based on the FEA static analysis, which can make sure the local parts deformation in an acceptable range.

2.3. Localization

Six-point location principle is adopted for the parts localization to make sure the structural parts in the correct machining position and orientation. As shown in Fig. 1, the bottom board is fixed on the workbench by six pressing plates. Then the bottom plane of the parts is selected as the localization datum plane. The parts is placed on the support

plates to restrict the translational freedom in *Z*-axis, the rotational freedoms around *X*-axis and *Y*-axis. 2 mm deep groove is milled on the surface of the support plate. Then the translational freedom in *Y*-axis and the rotational freedom around *Z*-axis are restricted. The last translational freedom in *X*-axis is restricted by the pin and the hole. Through the above-mentioned approach, the parts can be localized stably.
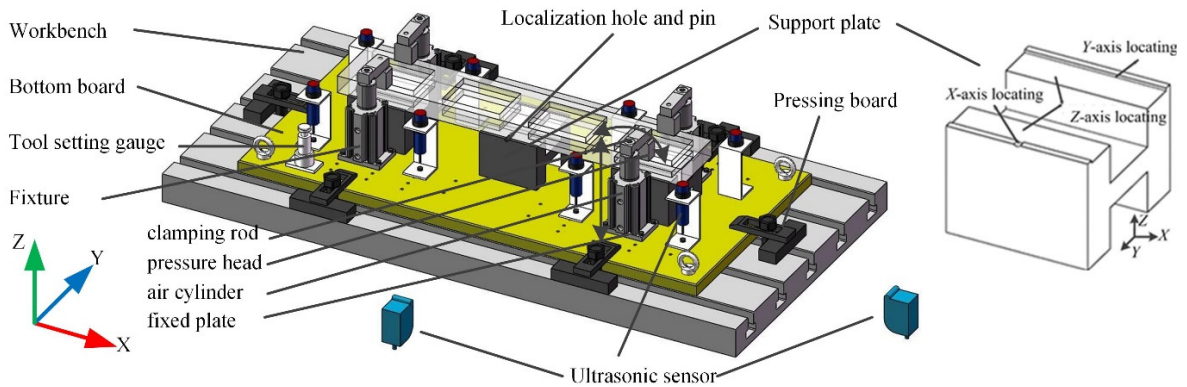

Fig. 1. Fixture configuration for the beam frame part

3. Automatic collision avoidance method based on artificial potential field model

In order to realize the automatic collision avoidance and ensure machining precision and safety, the modular fixtures are controlled in several steps as shown in Fig. 2. In sum, the CNC machine tool works continuously and the relevant collision avoidance detection and control are started once the early-warning occurs.
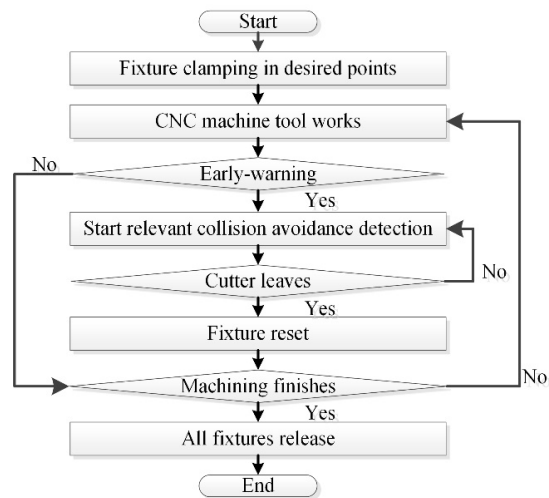

Fig. 2. Control flow chart of automatic collision avoidance method

3.1. Early-warning

As shown in Fig. 1, eight ultrasonic sensors on the bottom board can detect the cutter's position in *Z*-axis and trigger early-warning. The sensors must be installed at some suitable positions in case that the potential collision

cannot be detected in time. The detection of the cutter's position in Z-axis is realized by monitoring the height of the spindle. As shown in Fig. 3(a), the sensor installing distance d should satisfy the relation below,

$$d \leq \sqrt{R^2 - \left(R_f + l_a + R_c\right)^2} \tag{1}$$

where R, R_f, R_c and l_a denote the spindle radius, the diagonal length of the clamping rod, the cutter's radius, and the horizontal safe distance, respectively. l_a is obtained from product of the maximum feed speed of the cutter and the maximum switching time of the fixture.
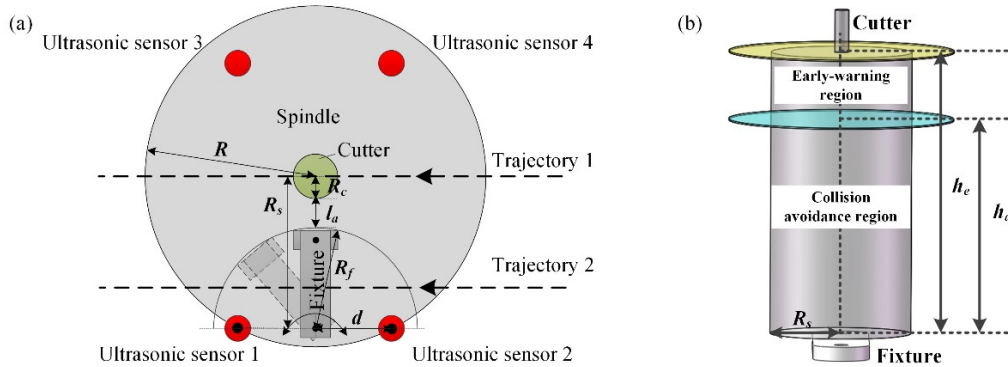

Fig. 3. Early-warning by ultrasonic sensors

When the cutter is moved enough closely to the fixtures in different trajectories and the height of the spindle is lower than the early-warning height h_e, different ultrasonic sensors may be triggered. As shown in Fig. 3(a), when the cutter moves along Trajectory 1, Ultrasonic sensor 2 and 4 will be triggered. When the cutter moves along Trajectory 2 that is close to parts edge, only Ultrasonic sensor 2 can be triggered. Once any ultrasonic sensor is triggered, the relevant fixtures will start the collision avoidance detection.

3.2. Automatic collision avoidance

Every fixture can be controlled independently to avoid the cutter. However, early-warning does not mean that the collision between the fixture and the cutter happens consequentially. In some cases, the cutter may just pass by the region but early-warning by the ultrasonic sensor is triggered. Therefore, a method based on artificial potential field model[8] is proposed in order to judge if the fixture starts to avoid, how the fixture avoids, and when the fixture resets.

As shown in Fig. 4(a), the fixture system is fixed onto the center of the workbench. When the cutter's position $\boldsymbol{O}_c$ is (0,0) in the tool machine coordinate system, the initial distances in the directions of X-axis and Y-axis detected by the sensors are d_{x0} and d_{y0}. So $\boldsymbol{O}_c$ in the coordinate system of O-XYZ can be expressed as,

$$\boldsymbol{O}_c = \left(x_c, y_c, z_c\right)^T = \left(d_x - d_{x0}, d_y - d_{y0}, d_z\right)^T \tag{2}$$

where d_x, d_y, and d_z are the detection distances by ultrasonic sensors in the directions of X-axis, Y-axis, and Z-axis, respectively.

After clamping points C_i (i=1,2,$\cdots$,n) are selected, the coordinates $\boldsymbol{C}_i$=$(x_i, y_i, z_i)^T$ (i=1,2,$\cdots$,n) are certain in O-XYZ. The end point and rotational axis of the fixture i are denoted as $\boldsymbol{O}_{fi}(x_{fi}, y_{fi}, z_{fi})^T$ and $\boldsymbol{O}'_{fi}(x'_{fi}, y'_{fi}, z'_{fi})^T$ (i=1,2,$\cdots$,n). The vector $\boldsymbol{a}_i$ is $(x_{ai}, y_{ai}, z_{ai})^T$.

The collision avoidance detection is implemented in two steps. The detection in the direction of Z-axis is firstly applied to judging if the cutter would indeed work closely to the clamping point. If $z_c < h_a$ is true, it declares that the

cutter will be in the collision avoidance region and the detection in the horizontal plane should be started immediately. The horizontal detection should solve three problems as follows,

- If it is necessary for the fixture to avoid,
- The rotational direction of avoiding,
- When the fixture resets.

In order to solve these problems, the avoidance method is proposed based on artificial potential field. In the system, the clamping point, the cutter, and the fixture are regarded as the target point, the barrier, and the controlled object, respectively. Generally, the artificial potential field contains two aspects: the gravitational function and the repulsive function. However, only the repulsive function $\boldsymbol{F}_{re}(\boldsymbol{O}_{fi})$ is considered here and it can be obtained by,

$$\boldsymbol{F}_{re}\left(\boldsymbol{O}_{fi}\right)=\left(F_x,F_y\right)^T=\begin{cases}0 & \left\|\boldsymbol{O}'_{fi}-\boldsymbol{O}_c\right\|\ge R_s \\[2mm] \eta\left(\dfrac{1}{\left\|\boldsymbol{O}'_{fi}-\boldsymbol{O}_c\right\|}-\dfrac{1}{R_s}\right)\dfrac{\boldsymbol{O}_{fi}-\boldsymbol{O}_c}{\left\|\boldsymbol{O}_{fi}-\boldsymbol{O}_c\right\|} & 0\le\left\|\boldsymbol{O}'_{fi}-\boldsymbol{O}_c\right\|<R_s\end{cases} \tag{3}$$

where $\boldsymbol{F}_{re}(\boldsymbol{O}_{fi})$, η, and R_s denote the repulsive force, the repulsive constant and the safe radius as shown in Fig. 4(b), respectively.

Based on $\boldsymbol{F}_{re}(\boldsymbol{O}_{fi})$, the rotational speed θ of the fixture is controlled as,

$$\theta=\begin{cases}0 & \left|\boldsymbol{F}_{re}\left(\boldsymbol{O}_{fi}\right)\right|=0 \\[2mm] \pi/2 & \left(\left|\boldsymbol{F}_{re}\left(\boldsymbol{O}_{fi}\right)\right|\ne0\right)\cap\left(F_x\cdot y_{ai}-F_y\cdot x_{ai}\ge0\right) \\[2mm] -\pi/2 & \left(\left|\boldsymbol{F}_{re}\left(\boldsymbol{O}_{fi}\right)\right|\ne0\right)\cap\left(F_x\cdot y_{ai}-F_y\cdot x_{ai}<0\right)\end{cases} \tag{4}$$

where ω_m is the maximum rotational speed.

The algorithm and the control system are implemented on the industrial computer that is completely independent of the CNC system. Based on Eq. (4), once the cutter steps into the safety area as shown in Fig. 4(b), the fixture will be turned to the opposite side. After the cutter leaves, the fixture will reset and press onto the parts again.
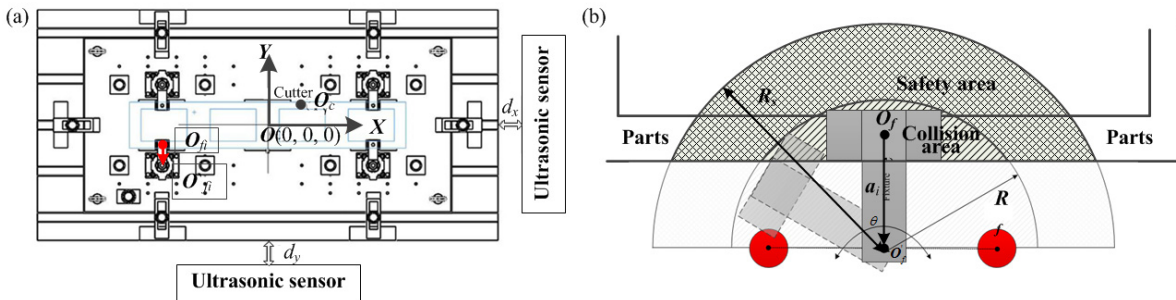

Fig. 4 Avoidance model

4. Experiment verification

In order to verify the validity of the proposed fixture system, an aluminum alloy structural frame with the size of 560mm×110mm×16mm is tested, on which the grids for weight reduction should be machined. Based on the FEA analysis results, four fixtures are selected to fix the parts and the clamping force of each fixture is 370N. The diameter of milling cutter is 10mm. The spindle speed is 2000rpm. As shown in Fig. 5(a), the four fixtures are controlled

simultaneously to press onto the frame parts. As shown in Fig. 5(b), the cutter moves closely to the fixture from the right side. The clamping rod of the fixture rotates left immediately and succeeds to avoid the cutter. After the cutter leaves away, the clamping rod resets quickly as shown in Fig. 5(c). When the machining is finished, all the four fixtures raises up simultaneously. Fig. 5(d) shows the machined parts.

The experiment results prove that the proposed fixture system with automatic collision avoidance can realize the avoiding of the cutter and the continuous work of the CNC machine tool. The machining efficiency increases by at least 30%.
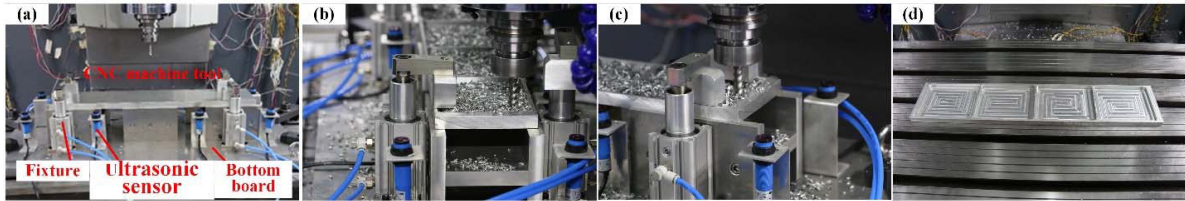

Fig. 5 Machining experiments

5. Conclusion

In this paper, a modular fixture system with automatic collision avoidance is proposed for the high-efficiency machining of the beams aircraft frame parts. The automatic collision avoidance control method is proposed based on the artificial potential field. The experiment results indicate that the proposed fixture system can be applied to the high-efficiency machining of beams frame parts, and realize the continuous work of the CNC machine tool by avoiding the cutter movement collision actively.

Acknowledgements

References

[1] S. Pantelakis, K. I. Tserpes. Adhesive Bonding of Composite Aircraft Structures: Challenges and recent developments. Science China-Physics Mechanics & Astronomy, 2014, 57 (1): 2–11.

[2] I. Alexander, G. Vladimir, P. Petr, et al. Machining of Thin-walled Parts Produced by Additive Manufacturing Technologies. Procedia CIRP, 2016, 41: 1023-1026.

[3] S. Tyagi, N. Shukla, S. Kulkarni. Optimal Design of Fixture Layout in a Multi-station Assembly Using Highly Optimized Tolerance Inspired Heuristic [J]. Applied Mathematical Modelling, 2016, 40 (11-12): 6134-6147.

[4] H. Wang, Y. Rong, H. Li, et al. Computer Aided Fixture Design: Recent Research and Trends. Computer-Aided Design, 2010, 42 (12): 1085-1094.

[5] K. Shen, Y. C. Wang. Computer-controlled Flexible Fixture Based on Multi-point Technology. World Scientific Publ Co Pte Ltd, Wuhan, CHINA, 2015, 199-206.

[6] http://www.cnaflextool.com/cnaflextool/default.htm.

[7] http://www.mtorres.es/en/aeronautics/products/carbon-fiber/torrestool.

[8] S. Hoshino, K. Maki. Safe and Efficient Motion Planning of Multiple Mobile Robots Based on Artificial Potential for Human Behavior and Robot Congestion. Advanced Robotics, 2015, 29 (17): 1095–1109.

16th Machining Innovations Conference for Aerospace Industry - MIC 2016

Improving the sensory capabilities of an electromagnetic guided rotary table for the use in machine tools

Berend Denkena, Tilmann Brühne*

Institut for Production Engineering and Machine Tools, Leibniz Universität Hannover, An der Universität 2, D-30823 Garbsen, Germany

Abstract

Difficult-to-machine materials are still challenging the production industry. Examples are highly complex components of aircraft engines. Alongside innovative processes, also improved machine tool components are helping to comply with the demands of this task.

This paper presents a swivel rotary table with an active magnetic bearing (AMB). Opportunities in machining through employing a workpiece-sided AMB are presented. The inherent capabilities to work as a sensor and actor as well as its stiffness and damping depend on the precise knowledge of the magnets characteristics. Therefore, a methodology to automatically identify the characteristic curve is presented.

Keywords: active magnetic bearing; AMB; swivel rotary table; machine tool

1. Introduction

Active magnetic bearings (AMB) are a growing technology for coping with high demands in industrial challenges. Due to the fact that magnetic bearings neither have any mechanical friction nor need lubrication, they can be used in high speed and hazardous environments. There are no risks of inflammation. Furthermore, damping and stiffness can be adjusted to the needs. An impressive example for the use of this technology are modern gas turbines made by the company Siemens [1]. Rotors of multiple tones are magnetically guided in 5 degrees of freedom (DOF) during their use. The safe properties reduce the risk of inflaming the gas and raise the turbines efficiency.

* Corresponding author. Tel.: +49 (0)511 762 18067; fax: +49 (0)511 762 5115.
 *E-mail address:* bruehne@ifw.uni-hannover.de

Moreover, AMBs can be used in a variety of applications such as the well-known magnetically levitating train "Transrapid" or in production environments e.g. machine tools. Examples for linear magnetic guides in machine tools are the machine prototypes "Schnelle Maschine" and "Neximo" ([2], [3]). Both guides are implemented in the z-axis. A stand-alone rotary table is presented in [4] and a swivel rotary table for machine tools is presented in [5]. The last mentioned prototype of a swivel rotary table is further presented in this paper.

Nomenclature

δ_A	levitating rotor displacement at the magnets (vector)
δs	measured rotor displacement at the sensors (vector)
F_A	magnet force vector
J_A	Jacobian matrix to transform the generalized pose to δ_A
Js	Jacobian matrix to transform the generalized pose to δs
M	mass matrix of levitating rotor
q	generalized pose
Q	generalized forces

2. The magnetic guided swivel rotary table

To machine complex parts with high demands on form and accuracy 5-axis machine tools are used. Beside the three standard linear axis (x, y and z) a rotary motion for turning and a swivel motion for tilting are used. These two motions are implemented into swivel rotary tables. Common swivel rotary tables rely on YRT roller bearings. By interchanging them with an AMB the performance and usability can be extended. Especially, higher rotating speeds and adjustable damping and stiffness are beneficial. Complex vibration prone machining parts, for example aircraft components, can achieve a higher precision due to the controlled damping. In [6] the shifting stability lobes due to the changing eigenfrequency are shown for a milling process while re-contouring a blisk.
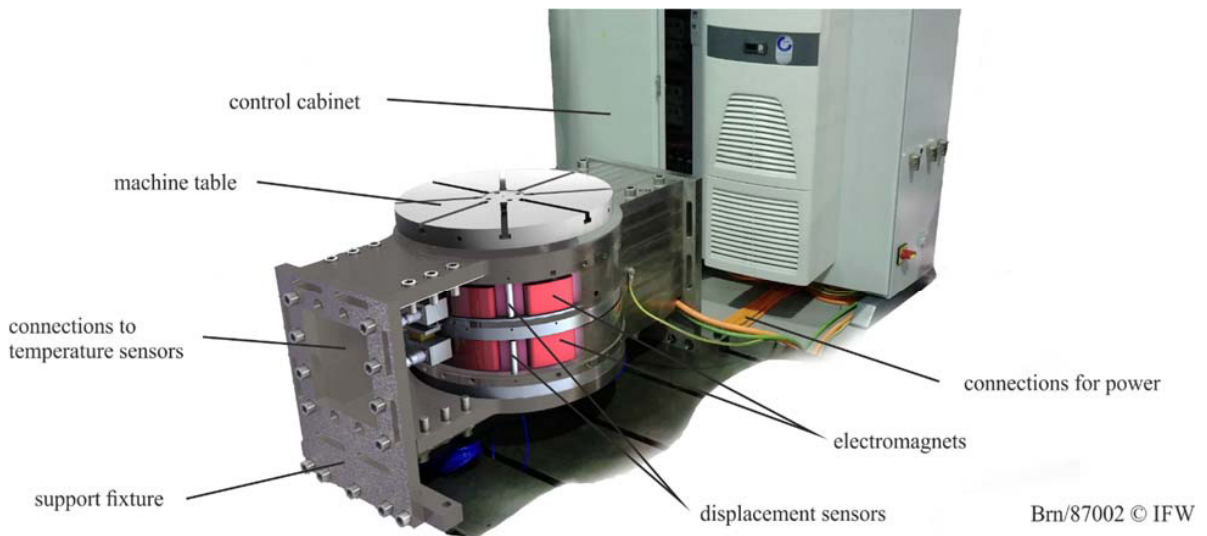
Fig. 1. Picture of the magnetic guided swivel rotary table with CAD overlay.

To design a magnetically guided swivel rotary table a methodology was given in [5]. In Figure 1 a picture with overlaid CAD of the assembled prototype can be seen. The overall proportions are according to a standard machine table with a diameter of 500 mm. The conceived mounting to the swivel motors is on the left and right side of the prototype. Therefore, all connections for sensors and power are lead to the sides. A support fixture is attached to analyze the AMB characteristics outside of the machine tool. In the background of Figure 1 the control cabinet containing the standard Siemens drive technology and sensor evaluation units is shown. Eddy current sensor are used to measure the levitating object's displacement.

Similar to AMBs in gas turbines, 5 DOF have to be controlled. This task is performed by four radial electromagnets and eight axial electromagnets. Maxwell's pulling force formula can be used to roughly calculate the force of an individual magnet. In summary, the electromagnet force F_{Em} is proportional to the square of the electric current i and the distance δ_A to the attracted object.

$$F_{Em} \sim \frac{i^2}{\delta_A^2}$$

(1)

By pairing two opposing magnets it is possible to circumvent the nonlinear characteristic. For this purpose, both magnets receive a bias current I_0 besides a control current I_C which is added to the upper and subtracted from the lower magnet, as seen in Figure 2. Therefore, all 12 magnets are designed to work in pairs and thus each magnet has a counterpart on the opposing side with reversed force direction. Each pair combines the two nonlinear current to force characteristics to one linearized characteristic.
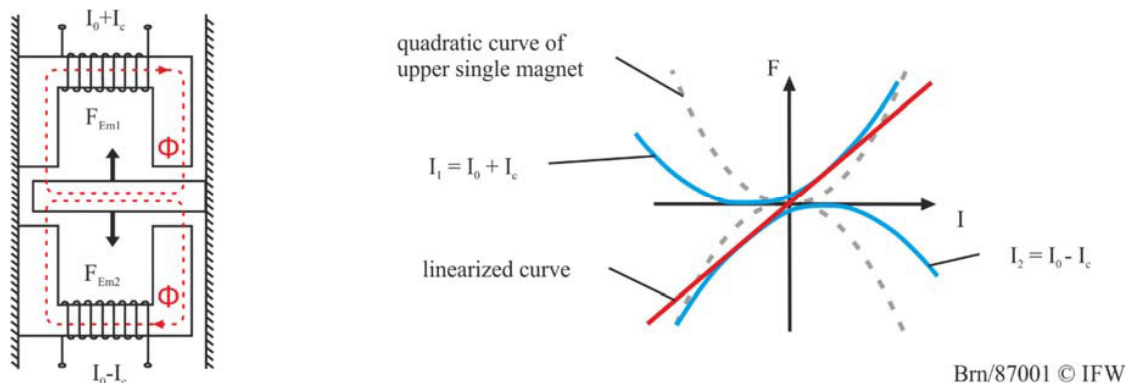

Fig. 2. Opposing magnets and the resulting linearization.

It is possible to reduce the number of needed inverters by half by using standard 3-phase Siemens inverter technology. Details can be seen in [7]. Figure 3 shows the magnet arrangement as well as the levitating (and rotating) disk of the rotor which is connected to the shaft in the center. On top of the shaft the machine table is mounted (not displayed; see Figure 1). The radial magnets are designed as an E-core with a bended magnet surface. In contrast, the axial magnets are designed as a double E-core with two coils and an even magnet surface. A direct drive is attached below the disk to enable rotation (not displayed).

3. Identification of the characteristic magnet curve

For stable levitation in AMBs a closed loop controller is needed. Basic closed loop controllers are for example "PID" or "state space" controllers. Both controllers are linear controllers and therefore need a linearized controlled system at a defined operating point. Hence, the precise knowledge of the magnets nonlinear current-distance-force characteristic curve is key to the performance. The controller can be enhanced by adding a state observer which

estimates non measurable variables. Hereby, the control accuracy often can be improved and the additional information can be further used. One example is the force observer. It can be utilized for additional functions to obtain cutting forces, calculate the tool deflection, measure the decreasing workpiece weight and its eccentricity or the metal removal rate.
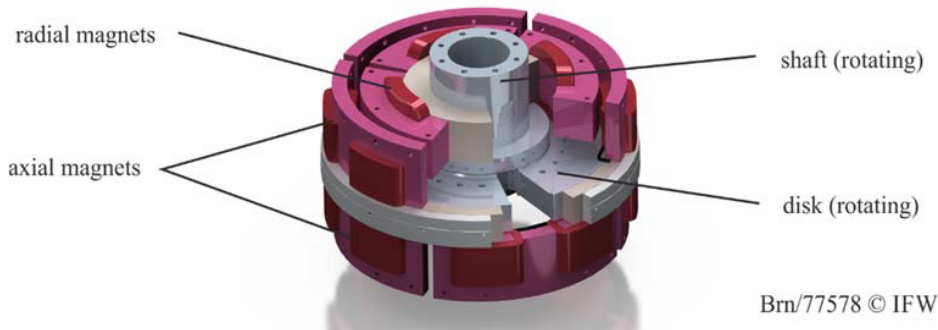

Fig. 3. The magnet arrangement of the swivel rotary table.

A stored current-distance-force characteristic curve is used by the observer to calculate the magnet forces. Obviously, the accuracy of the functions depends on the accuracy of the curve! This curve can be roughly estimated by using equivalent magnetic networks or FEM. Further precision can be gained by measuring the "true" characteristic within a test stand. Although the characteristic may be measured, after mounting the magnet during assembly the precise distance to the levitating object is unknown. This is due to mounting and machining tolerances within the whole assembly.

Thus, a more precise characteristic curve has to be identified after assembly for each magnet pair separately. To circumvent a mechanical test-stand with a force sensor, an automatic identification using an accelerometer is presented in the following.

3.1. Position signal used for identification

The identification algorithm is applied while levitation. Hence, a stable closed loop controller as well as an acceleration sensor are needed. Using a sinusoidal position setpoint instead of a steady position an acceleration proportional to the magnet force can be measured. A variation of the sinus frequency enables different acceleration measurements at the same position. The three dimensional characteristic curve of the magnet (force-current-position) can be gained by repetition at different positions.
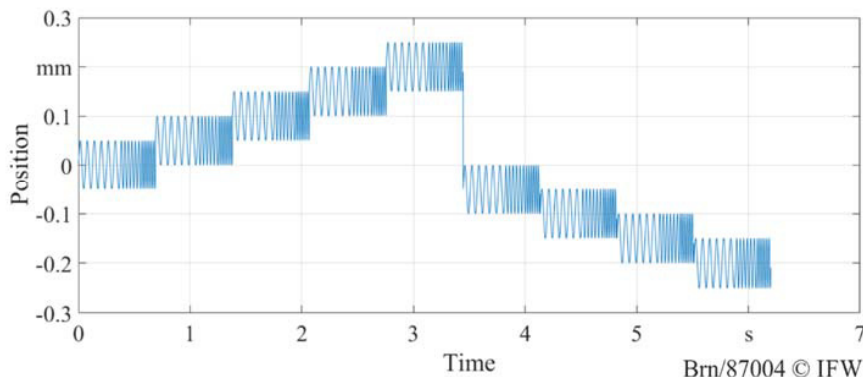

Fig. 4. Sinusoidal position signal used for identification.

The following assumptions are taken as a basis:

- Low sinus frequencies lead to a near stationary characteristic curve
- The position changes are to slow to cause controller instability
- Measured signals can be separated from disturbances using a low pass filter

In the subsequent example the total distance between magnet and levitating rotor is 1 mm. The usable air gap for positioning is reduced to ± 0,3 mm by the safety bearings to prevent damage to the magnets by an emergency stop. Another 50 μm are used as a minimum positioning distance to the safety bearings to avoid contact and controller instability. Figure 4 shows the position signal for an identification applying three frequencies (100 Hz, 200 Hz, 300 Hz) at nine different positions. The radial x-axis was identified.

3.2. Reconstructing the characteristic curve

In Figure 4 above the position signal is shown for one translational motion. The signal has to be repeated for each translational direction of motion. The Jacobian matrix **Js** is used to relate the generalized pose **q** to the displacement sensors **δs**.

$$\delta_s = J_s\, q \tag{2}$$

To obtain the generalized pose from the sensors measurement the Moore-Penrose-Pseudoinverse is applied.

$$q = J_s^+\, \delta_s \tag{3}$$

The generalized pose **q** is related to the rotor displacement at the magnet by the matrix **J$_A$**.

$$\delta_A = J_A\, q \tag{4}$$

If the levitating rotor is regarded as a rigid body and generalized coordinates are used, the equation of motion assembles as:

$$Q = M\, \ddot{q} + M\, g \tag{5}$$

Where **Q** are the generalized forces, **M** is the mass matrix, **q** is the pose and **g** is the gravitational vector. The stiffness matrix and the damping matrix become zero because the rotor acts as a single mass. Additionally, disturbance forces due to permanent magnets of the direct drive have not been regarded.

Two magnets are combined as one actor. Therefore, the combined force **F$_A$** can be determined by

$$F_A = J_A^{T+}(M\, \ddot{q} + M\, g) \tag{6}$$

The magnets current can be read from the inverter. The second derivative of **q** is measured by the acceleration sensor. Hereby, the three axes of the magnet's characteristic curve are determined. Obviously, the levitating mass has to be known in advance. This is achieved either by measuring the mass matrix or reading it directly from CAD. The latter is the easiest way but implies correct assigned materials and a precise fabrication.

Figure 5 shows the obtained data points in black using the above identification signal.
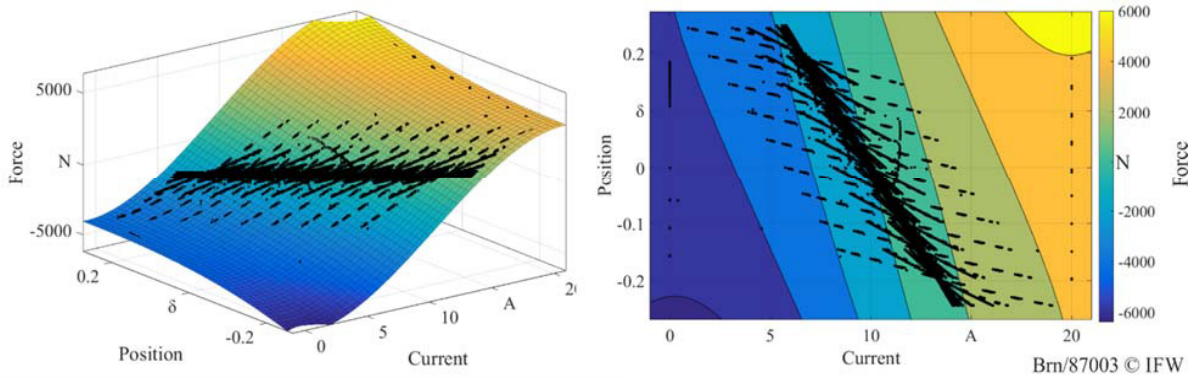
Fig. 5. (a) Obtained data points (black) on fitted characteristic curve; (b) Top view.

It can be seen that the majority of data points accumulate around 10 A. This is plausible considering it is the mean operating current I_0 for stable levitation. By fitting for example a third degree polynomial the characteristic curve is reconstructed (Figure 5). The shown data is determined by a closed loop controlled Matlab/Simulink model of the AMB. In a following study the effects of sensor noise on the data accuracy are examined using the prototype.

4. Summary

Complex machining parts demand innovative machine tools. Electromagnetic guides can enhance the machine tool performance by adaptive damping and stiffness. Further benefits are the friction and lubricant free levitation as well as the inherent capabilities to work as sensor and actor. A prototypical electromagnetic guided swivel rotary table is presented. Details regarding the overall set-up and the magnet arrangement are shown. To achieve precise force measurements using the prototype, the magnet's characteristic curve considering mounting tolerances has to be known. Hence, a method to identify the characteristic curve is presented. It utilizes an acceleration sensor as well as sinusoidal oscillations at different levitation positions. Finally, the identified curve is shown.

References

[1] Siemens AG, SIMOTICS Active Magnetic Bearing Technology, http://www.siemens.com/global/en/home/products/drives/motors/high-voltage-motors/simotics-active-magnetic-bearing-technology.html, 06/2016

[2] B. Denkena, F. Kallage, M. Ruskowski, K. Popp, H.K. Tönshoff, Machine Tool with Active Magnetic Guides, Annals of the CIRP, (53/1) 333-336, 2004.

[3] O. Guemmer, Produktivitäts- und Genauigkeitssteigerung von Fräsmaschinen durch ruckentkoppelte Vorschubantriebe und magnetische Führungseinheiten, Dr.-Ing. Dissertation, Universität Hannover, 2014.

[4] O. Petzold, Modellbildung und Untersuchung eines magnetisch gelagerten Rundtisches, Dr.-Ing. Dissertation, Universität Magdeburg, 2006.

[5] B. Denkena, D. Dahlmann, F. Flöter, T. Brühne, Conceptual design for electromagnetic guided rotary table in machine tools, 5th Machining Innovations Conference (MIC 2014), Procedia CIRP 24 (2014) 80 – 85, 2014.

[6] F. Flöter, L. Pohle, B. Denkena, L. Panning-von Scheidt, J. Wallaschek, Mistuning of blisks during milling processes, Deutscher Luft- und Raumfahrtkongress 2015, Rostock, 2015.

[7] J. Denk, D. Stoiber, H.G. Köpken, H. Walter, Industrialization of AMB systems with standard drive technology, IEEE transactions on industry applications, vol. 49, no. 2, march/april, 2013.

16th Machining Innovations Conference for Aerospace Industry - MIC 2016

Automated dressing of graphite electrodes for electrical discharge machining (EDM) of seal slots in turbine components

Eckart Uhlmann[a,b]; David C. Domingos[a,]*

[a]Fraunhofer Institute for Production Systems and Design Technology IPK, Pascalstrasse 8-9, 10587 Berlin, Germany
[b]Institute for Machine Tools and Factory Management IWF, Technische Universität Berlin, Pascalstrasse 8-9, 10587 Berlin, Germany

Abstract

The die-sinking EDM is applied in the aerospace industry for the machining of seal slots in blades and in structural components made of nickel-base alloys, normally applying graphite electrodes. The objective of this work was the development of a technology to dress the graphite electrodes inside the EDM machine tool, with the aim of rebuilding the original shape of the worn electrodes between EDM cycles. The milestones consisted on (I) understanding the wear behavior of the electrodes while machining the slots, (II) the development of the dressing technology applying the DoE-method and determination of statistically high influencing parameters, and finally (III) the integration of the dressing technology into the process chain.

1. Introduction

The high demands on next generation aero engines, with challenging targets for CO_2, NOx and noise emissions according to CLAIRE (technology program *Clean Air Engine* from MTU Aero Engines, Germany), push new technological developments such as the application of new materials and new manufacturing technologies as well as the development of automated process chains [1, 2]. The fabrication of seal slots in blades and further components in the aerospace industry is usually carried out by die-sinking EDM. Latest developments to improve this

---

* Corresponding author. Tel.: +49 (0) 30 39006-413; fax: +49 (0) 30 3911037.
  E-mail address: david.carlos.domingos@ipk.fraunhofer.de

manufacturing step focused on reducing the machining times and relative wear of electrodes through process optimization as well as on the development of the vibration-assisted EDM-technology [3, 4, 5, 6]. The current work focuses on the automation of the EDM of seal slots, by means of dressing the tool electrodes inside the machine tool, thereby eliminating a further manipulation of the electrodes by the machine operator.

2. Machine tool and materials

The machine tool GENIUS 1000 from company Zimmer&Kreim and the dielectric fluid IME-MH from company Oelheld were applied for conducting the experimental investigations on die-sinking EDM of seal slots and on dressing of the worn graphite electrodes.

Two distinct graphite electrode materials were applied in the EDM of the seal slots in turbine components: ultrafine graphite EDM-3 from company Poco Graphite Inc., USA, and ultrafine graphite HK-6 from company Tokai Carbon Co. Ltd., Japan. Both materials find application in the aerospace industry, are isotropic and ultrafine graphite (1 µm – 5 µm) according to their primary particle sizes prior to the forming, coking and graphitization processes. The main physical properties of both graphite types are presented in Table 1.

Table 1. Physical properties of the graphite electrodes [7, 8].

Physical Properties	EDM-3	HK-6
Density ρ [g cm^{-3}]	1.81	1.86
Average particle size [µm]	< 5	3
Specific electrical conductivity σ_0 (273,15 K) [m S mm^{-2}]	0.064	0.083
Specific electrical resistance ρ [µ Ω m]	15.6	12
Hardness [Shore A]	73	68

The nickel-base casting alloy MAR-M247 was chosen as workpiece material for the experiments, as this is considered a very important Ni-base material for the turbomachinery industry [6], finding many applications there. The alloy went through a hot-isostatic-pressing (HIP) process followed by a heat treatment [9], possess a density $\rho = 8.54$ g/cm3, a hardness given in Rockwell C ranging between $30 < HRC < 40$, and a melting point between $T_m = 1,315$ °C and $T_m = 1,340$ °C [10]. The SEM-images in Fig. 1 present the conventional casting polycrystalline microstructure and the concentration of the carbides at the grain boundaries, resulted from the HIP process. Further carbides are also solidified within the γ-matrix. The γ-matrix is brighter and possess a net-like mesh form, while the dark γ'-phase is placed inside this matrix. The most available elements of the alloy can be identified at the EDX-analysis of the overall sample, which are Ni, Co, Cr, W and Al.
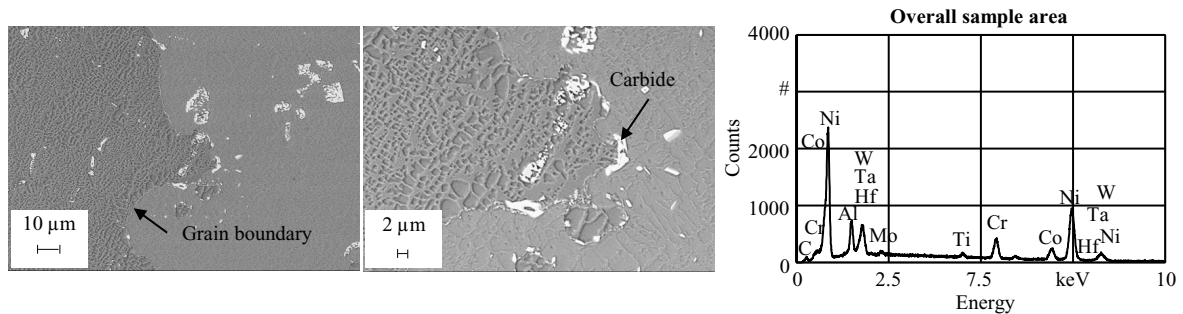

Fig. 1. Metallographic and energy dispersive X-ray (EDX) analyses of the applied nickel-base casting alloy MAR-M247.

A total of four materials were selected and applied as dressing plates in the experiments, being two metallic and two graphite materials. The materials applied as dressing plates were the following: ultrafine graphite EDM-3, copper infiltrated graphite EDM-C3 (Poco), fine grained cemented carbide CF-H40S (Ceratizit) and ordinary brass CuZn36. The main physical properties of these materials are presented in Table 2, considering their application as electrodes at EDM.

Table 2. Physical properties of the applied dressing plates [9].

Physical Properties	EDM-C3	CuZn36	CH-H40S
Average particle size [μm]	< 5	15 - 30	0.8 - 2.5
Specific electrical conductivity σ_0 (273.15 K) [m S mm^{-2}]	0.3125	15.15	18.87
Thermal conductivity λ (273.15 K) [W m-1 K-1]	> 110	120	90
Melting point / Sublimation point* [K]	3350*	920	2860

3. Development of the dressing technology

3.1. Description of the dressing process

Commonly, in the die-sinking EDM, the tool electrodes are fixed to the mandrel of the machine tool, while the workpieces to be processed are clamped on the machine table. The material removal rate V_W thus describes the volume of material removed from the workpiece per time unit, the workpiece being in the present study the MAR-M247 plates. The electrode wear rate V_E describes the volume of material removed from the tool electrode per time unit, meaning the volume removed from the applied graphite electrodes fixed on the mandrel. By the end of the EDM process, the cavities in the MAR-M247 workpieces are produced and the electrodes present a tool wear, which can be measured especially on the corners and frontally. The EDM process (right) and the wear pattern of the tool electrodes (left) are presented in Fig. 2.
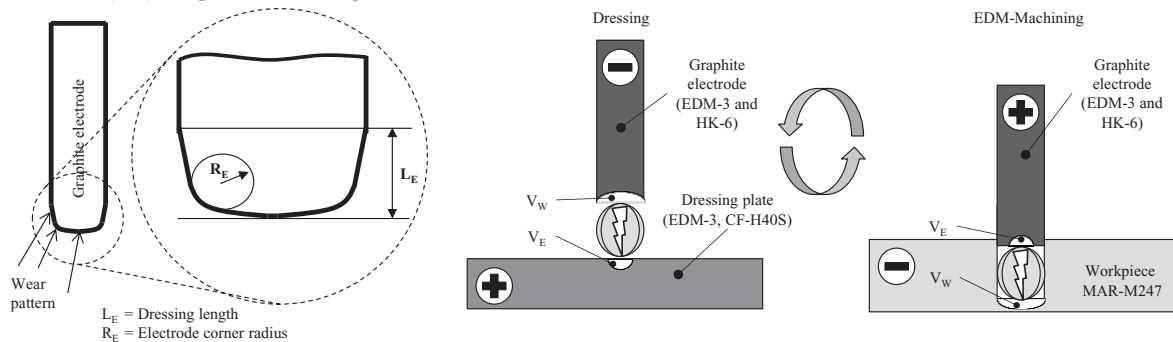

Fig. 2. Schematic representation of the wear of graphite electrodes and of the EDM and dressing processes.

During the deployment of the dressing technology the described set-up becomes the opposite, because the process now focuses on removing material from the former tool electrodes, which are fixed to the mandrel of the machine. The former graphite electrodes become thus the workpieces to be machined. On the other hand, the dressing plates fixed to the machine table constitute the tool electrodes during the dressing process. By performing this development, the polarity of the machine mandrel has to become negative. Although the definitions for material removal rate V_W and tool wear rate V_E continue unmodified with this set-up, the V_W now refers to the volume of material removed from the former electrodes fixed on the mandrel, while V_E refers to the volume of material removed from the dressing plates (Fig. 2).

3.2. Wear pattern development of graphite electrodes and technological boundary conditions

The development of the dressing technology based on the definition of the boundary conditions regarding the wear pattern development of graphite electrodes after subsequently EDM cycles. The die-sinking EDM of the seal slots was conducted applying a previous developed technology, and the main EDM parameters are presented in Fig. 3. The diagram shows that the corner radius of electrode R_E continuously increased by increasing the number of EDM cycles, especially due to the fact that the electrical discharges spark in the region with the highest electric field enhancement, e.g. electrode corner radiuses. This wear behavior helped to determine the minimal dressing length

$L_{E,min}$ necessary to rebuild the original shape of the electrodes, which should be at least as long as the electrode radius R_E after one machining cycle. Therefore the value $L_{e,min} = 600$ µm was set as boundary condition. In order to avoid waste of graphite electrodes, the maximum frontal dressing length of the electrodes was set $L_{E,max} = 800$ µm. The dressing time t should be as short as possible (t < 4 min), with the aim of implementing the technology in a production chain. The error bars in all figures of this paper refer to the standard deviation of the measurements.
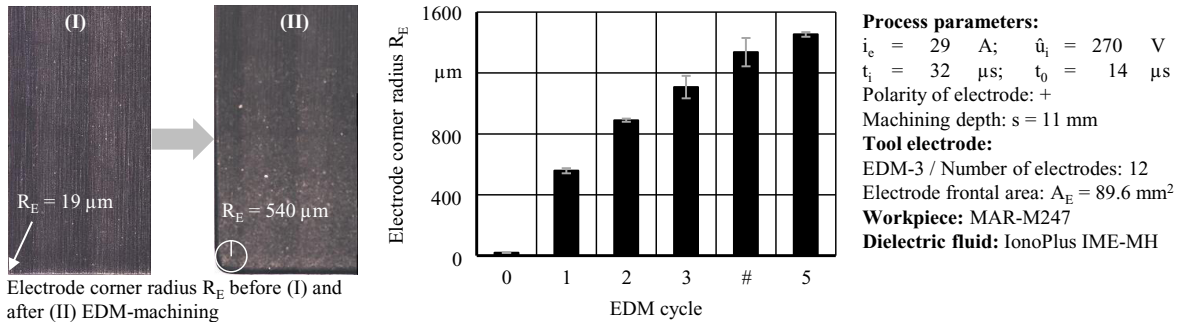

Electrode corner radius R_E before (I) and after (II) EDM-machining

Process parameters:
i_e = 29 A; $\hat{u}_i$ = 270 V
t_i = 32 µs; t_0 = 14 µs
Polarity of electrode: +
Machining depth: s = 11 mm
Tool electrode:
EDM-3 / Number of electrodes: 12
Electrode frontal area: $A_E = 89.6$ mm²
Workpiece: MAR-M247
Dielectric fluid: IonoPlus IME-MH

Fig. 3. Development of the corner radius of electrodes R_E after subsequently EDM cycles.

3.3. Analysis of distinct dressing plate materials

The first analysis comprised the comparison of the four distinct materials applied as dressing plates, by means of understanding the influence of dressing process parameters and of the materials on the dressing process. Four dressing process parameters were varied in the experiments for each dressing plate material, and the levels for the process parameters are presented in Table 3, together with the best results achieved for each material. The dressing parameters applied to achieve the mentioned best results are signed bold. Brass CuZn36 did not reach the set $L_{e,min} = 600$ µm due to the high wear of this dressing plate, which can be led back to the low melting point of brass. The cemented carbide CF-H40S presented good results for the dressing technology and one parameter set tested was able to fulfill all requirements on process outputs, with dressing length $L_E > 600$ µm, material removal rate $V_W = 15.8$ mm³/min and short machining time t = 3.5 min. The low wear of the dressing plate made of cemented carbide, which is confirmed by the high frontal dressing length L_E achieved on the electrodes, is a result of a combination of low specific electrical resistivity of the bonding material cobalt and the high sublimation point of tungsten carbide [11]. Both the discharge current i_e and the erosion time between flushing intervals t_{ero} possess a high significant influence on at least two process outputs, enabling the further optimization of the dressing process; the influence of the pulse duration t_i and pulse interval time t_0 on process outputs was statistically indifferent. These results described here deal with the development of the dressing technology applying CF-H40S as dressing plate.

Table 3. Levels for the dressing process parameters and best results.

Dressing plate material	t_i [µs]		t_0 [µs]		i_e [A]		t_{ero} [s]		t [min]	V_W [mm³/min]	L_E [µm]
	+	-	+	-	+	-	+	-			
EDM-3	**75**	56	**56**	42	14.8	**8.3**	**2**	0.5	**4.9**	**13.3**	722
EDM-C3	**100**	75	56	**42**	14.8	**10.8**	**2**	0.5	**3.5**	**15.3**	604
CuZn36	320	**240**	240	**180**	**8.3**	4.0	**2**	0.5	**3.0**	**11.4**	371
CF-H40S	**320**	240	**240**	180	**14.8**	10.8	**2**	0.5	**3.5**	**15.8**	614

3.4. Technology optimization with full-factorial experimental design

A full-factorial analysis of the influence of the discharge current i_e and erosion time between flushing intervals t_{ero} on process outputs applying cemented carbide as dressing plate are presented in Fig. 4. The material removal rate V_W, frontal dressing length L_E and electrode wear rate V_E are displayed in the figure. The raise of the discharge current i_e guides towards an increase of the material removal rate V_W, decrease of the frontal dressing length L_E and

increase of the electrode wear rate V_E, as a result of higher discharge energy available [11]. The steep increase of the electrode wear rate V_E with increasing discharge current i_e leads to the reduction of the frontal dressing length of the graphite electrode. The best results with CF-H40S towards the fulfillment of the defined boundary conditions were achieved with a discharge current i_e = 10.8 A and erosion time between flushing intervals t_{ero} = 4.0 s. This technology led to a material removal rate V_W = 14.92 mm³/min, a frontal dressing length L_E = 594 µm and a machining time t = 3.57 min. The difference between the results achieved at 3.3 and 3.4 is due to the fact that the electrodes applied during the experimentation at 3.3 were worn electrodes ($R_E > 600$ µm), while nearly sharp electrodes ($R_E < 600$ µm) were applied at 3.4.
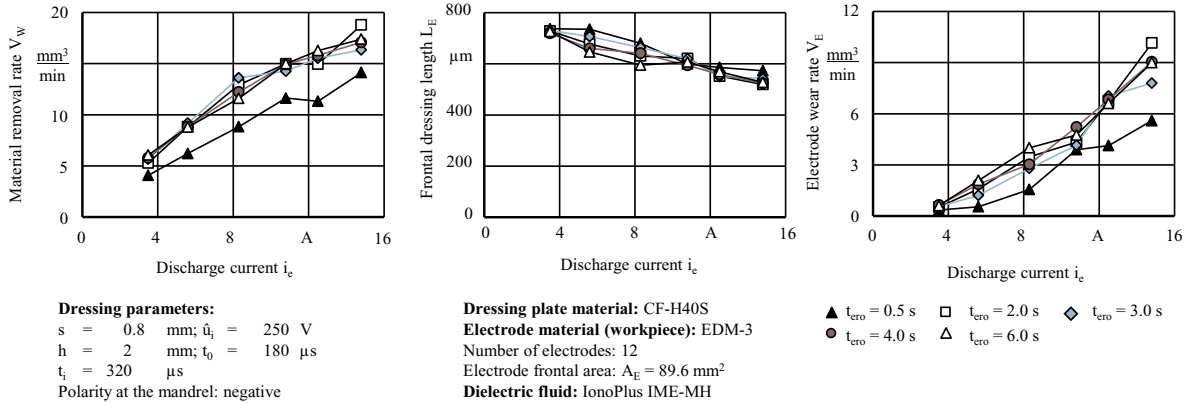

Dressing parameters:
s = 0.8 mm; û$_i$ = 250 V
h = 2 mm; t$_0$ = 180 µs
t$_i$ = 320 µs
Polarity at the mandrel: negative

Dressing plate material: CF-H40S
Electrode material (workpiece): EDM-3
Number of electrodes: 12
Electrode frontal area: A_E = 89.6 mm²
Dielectric fluid: IonoPlus IME-MH

▲ t_{ero} = 0.5 s   □ t_{ero} = 2.0 s   ◇ t_{ero} = 3.0 s
● t_{ero} = 4.0 s   △ t_{ero} = 6.0 s

Fig. 4. Influence of discharge current i_e and erosion time between flushing intervals t_{ero} on the dressing results.

3.5. Influence of electrode material on the dressing process

The dressing technologies developed so far considered only the application of electrode materials made of graphite EDM-3. At this stage, this technology was extended for dressing graphite electrodes made of the material HK-6, which was also used as electrode material for producing the high aspect ratio cavities in MAR-M247. The machining depths studied were s = 0.8 mm, s = 0.9 mm and s = 1.0 mm and the results are presented in Fig. 5. The machining time t and the frontal dressing length L_E increase linearly with the rising machining depths s, both for graphite electrodes made of EDM-3 and HK-6, showing the stability of the dressing process while machining with relative small machining depths s. The material removal rate V_W increases slightly for the graphite electrodes type EDM-3, remaining almost constant for electrodes made of graphite HK-6.

Dressing plate material:
CF-H40S
Dielectric fluid:
IonoPlus IME-MH

Electrode material (workpiece):
EDM-3 and HK-6
Number of electrodes: 12
Electrode frontal area: A_E = 89.6 mm²

Dressing parameters:
û$_i$ = 250 V; h = 2 mm
t$_o$ = 180 µs; t$_i$ = 320 µs
i$_e$ = 10.8 A; t$_{ero}$ = 4 s
Polarity at the mandrel: negative

Frontal dressing length ΔL   Machining time t   Mat. removal rate V_W Elec. wear rate V_E
▲ HK-6   HK-6 ■   ▲ HK-6   HK-6 ■
△ EDM3   EDM3 □   △ EDM3   EDM3 □   ▲ HK-6   △ EDM-3
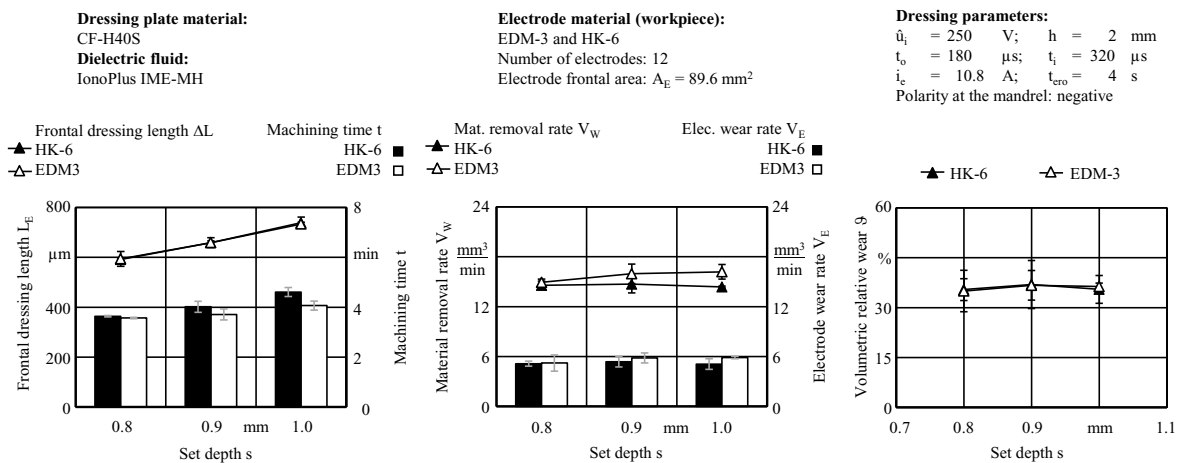

Fig. 5. Influence of workpiece material on the dressing results applying graphite cemented carbide CF-H40S as dressing plate.

The material removal rate V_W is higher and the machining time t is shorter while dressing the graphite electrodes made of EDM-3 in comparison to HK-6. This relies on the difference of grain size between both materials and on the material removal mechanisms during the EDM applying graphite electrodes. The volumetric relative wear ϑ for EDM-3 and HK-6 remains almost constant with increasing machining depth s, with very similar values for both materials. This is a result of a constant material removal rate V_W and a constant electrode wear rate V_E while dressing HK-6, while both values slightly increase while dressing the graphite EDM-3. A machining depth s = 0.9 mm was chosen for both electrode materials EDM-3 and HK-6 during the integration of the dressing technology into an automated production cycle applying a dressing plate made of cemented carbide CF-H40S. The dressing technology enabled the fulfillment of all requirements while applying the tool electrodes EDM-3, with a material removal rate V_W = 15.95 mm^3/min, a frontal dressing length L_E = 658.9 µm and a machining time t = 3.71 min. For the graphite electrodes made of the material HK-6, a material removal rate V_W = 14.7 mm^3/min, a machining time t = 4.02 min and a frontal dressing length L_E = 658.3 µm were achieved.

4. Integration of the dressing technology into the process chain

The implementation of the dressing technology with the dressing plate fixed to the machine tool was carried out with dressing plate material cemented carbide CF-H40S, and for the two distinct graphite electrode materials tested, namely EDM-3 and HK-6. Fig. 6 shows the experimental set-up for the integration of the dressing technology into the process chain. A total of 12 graphite electrodes, totalizing an electrode frontal area of A_E = 89.6 mm^2, are dressed simultaneously and are subsequently applied for producing 12 seal slots in the workpiece made of nickel-base casting alloy MAR-M247. The schematic representation of both dressing and EDM presented in Fig. 2 also helps understanding the experimental procedure applied.
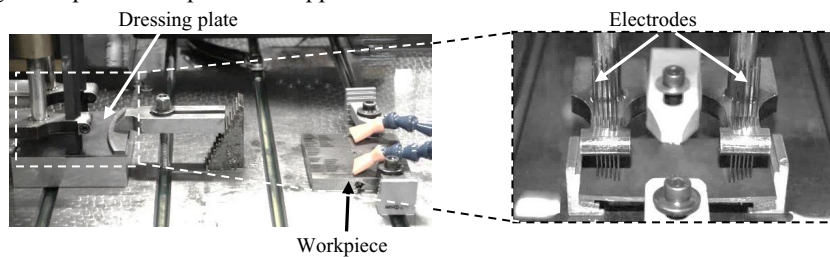

Fig. 6. Experimental set-up for the integration of the dressing technology into the process chain.

The seal slots are produced in the workpiece by means of the EDM and the tool electrodes present a worn profile after this step. Afterwards, the dressing process starts on the dressing plate and, subsequently, the tool electrodes present a renewed profile. The EDM process starts over again and this automated production cycle is repeated continuously for the machining of the slots in MAR-M247. The analysis of results comprised the measurement of the radius of electrodes after machining and dressing, of the radiuses inside the cavities, of the surface roughness of cavities, and finally a metallographic analysis of the sub-surface applying the SEM. Fig. 7 presents the process results both for EDM (top) of slots as well as for dressing of tool electrodes (bottom). The material removal rate V_W during the EDM of seal slots is higher for the graphite electrodes HK-6 than for the electrodes EDM-3, with $V_{W(HK-6)}$ = 49.4 mm^3/min and $V_{W(EDM-3)}$ = 32.6 mm^3/min, respectively. This is a result of the lower specific electrical resistance ρ of HK-6, combined with the smaller primary grain size of this graphite, resulting in better process behavior and less buildup of remelted material on the electrode. The volumetric relative wear ϑ is higher for EDM-3 than for HK-6 electrodes, due to the bigger primary grain size of the graphite EDM-3 and the known wear mechanism of graphite electrodes [12] during EDM. As the material removal mechanism of graphite during EDM consists on the sublimation of the bonding material that was graphitized during the graphitization, thereby breaking off the whole primary grains of the bond, the higher grain size of EDM-3 electrode leads to higher volumetric relative wear ϑ. Regarding the dressing technology, the frontal dressing length L_E achieved for all electrode materials tested are in accordance with the boundary conditions for the dressing technology, with 600 µm < L_E < 800 µm. The material removal rate V_W during the dressing process is higher while dressing the

EDM-3 electrodes due to the higher grain size of this material and again due to the material removal mechanism of graphite during EDM previously explained.

Fig. 7. Process results for the EDM of seal slots and dressing of distinct tool electrodes applying dressing plate material CF-H40S.

The following analysis focused on the measurement of the corner radius of electrodes R_E and on the corner radius of produced cavities R_C with increasing number of dressing cycles. The Fig. 8 (left) clearly shows the difference of the corner radius of electrodes R_E after the EDM of successive set of cavities in alloy MAR-M247, with and without the application of the dressing technology. The electrode corner radius R_E increases uninterruptedly with increasing number of cycles, if these electrodes are not dressed between the EDM cycles, while the radiuses of tool electrodes R_E that went through the dressing maintained almost constant values with increasing number of EDM cycles.
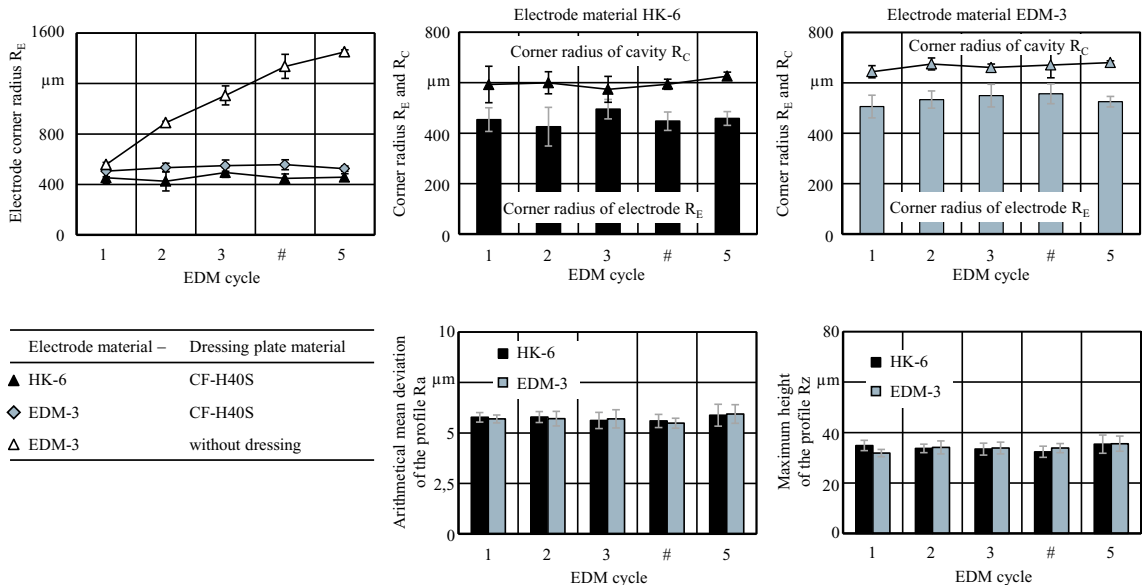

Fig. 8. Corner radius of electrodes R_E, corner radius of cavities R_C and surface roughness of seal slots Ra and Rz.

The two remaining upper diagrams show the corner radius of electrode R_E and of cavity R_C both for HK-6 and EDM-3 with increasing number of EDM cycles. It is clear that both R_E and R_C remain almost constant with increasing number of cycles, being the radius of cavities R_C a function of the radius of electrodes R_E and of the machining gap. R_C is also always below the required tolerance $R_C < 1$ mm. The corner radiuses of produced cavities R_C applying the electrodes EDM-3 are higher than the radiuses applying the HK-6 electrodes, as a consequence of higher volumetric relative wear of EDM-3 during EDM. These results also confirm that the electrode materials that exhibit less relative wear during the die-sinking EDM process enable the production of more precise cavities in the workpieces. The values for the arithmetical mean deviation of the profile Ra and the maximum height of the profile Rz remain constant during all five EDM cycles and the values are very similar for both electrode materials, meaning that the dressing process has no influence on the surface roughness of produced cavities. The SEM-images, which are not presented here, also showed no influence of the dressing technology on the surface integrity of parts.

5. Conclusions

The development of the dressing technology was carried out in this work, with the analysis of four distinct dressing plate materials. The results presented focused on the application of fine grained cemented carbide CF-H40S as dressing plate. The statistical analysis showed that the parameters erosion time between flushing intervals t_{ero} and discharge current i_e possessed a high significant influence on at least one process output, being thus applied in the full-factorial optimization. The full-factorial analysis enabled the choice of the optimized electrical parameters prior to the integration of the dressing technology into the process chain. The integrated technology enabled the fulfillment of technological boundary conditions set on the process, including minimal material removal rate $V_{W,min} = 13.44$ mm³/min and frontal dressing length $L_E > 600$ µm. The radii both of tool electrode R_E as well as of the produced cavities R_C remain constant with increasing number of produced cavities, with R_C within the required tolerances set by the OEMs ($R_C < 1$ mm), guaranteeing therefore the form accuracy of seal slots. The dressing technology has nearly no influence on the subsequently EDM process regarding both the surface roughness and the surface integrity of the parts. The dressing technology proved to be an alternative during the production of seal slots in turbine components, and may lead to a fully automation of the EDM of these features. The manipulation by the operator can be reduced or eliminated, reducing the set-up times and finally achieving full process automation.

References

[1] K. Steffens, H. Wilhelm: Next engine generation: Materials, Surface Technology, Manufacturing Processes – What comes after 2000? URL: http://www.mtu.de (access 02/2016).
[2] K. Steffens, A. Schäffler: Advanced Compressor Technology – Key Success Factor for Competitiveness in modern Aero Engines, information on http://www.mtu.de (access 02/2016).
[3] E. Uhlmann, D.C. Domingos (2013): Investigations on Vibration-Assisted EDM-Machining of Seal Slots in High-Temperature Resistant Materials for Turbine Components. Procedia CIRP 6:71-76.
[4] Uhlmann, E.; Domingos, D. C. (2013): Development and Optimization of the Die-Sinking EDM-Technology for Machining the Nickel-Based Alloy MAR-M247for Turbine Components. Procedia CIRP 6:181-186.
[5] E. Uhlmann, D. C. Domingos (2016): Investigations on Vibration-assisted EDM-machining of Seal Slots in High-Temperature Resistant Materials for Turbine Components - Part II. Procedia CIRP 42:334-339.
[6] F. Klocke, A. Klink, D. Veselovac, D. K. Aspinwall, S. L. Soo, M. Schmidt, J. Schilp, G. Levy, J.-P. Kruth (2014): Turbomachinery component manufacture by application of electrochemical, electrophysical and photonic processes. CIRP Annals - Manufacturing Technology 63(2), pp. 703-726.
[7] POCO GRAPHITE INC: Technical Manual. Texas, USA. Corporate Literature. 2014. URL: http://edmtechman.com/about.cfm (access 03/2016).
[8] TOKAI CARBON DEUTSCHLAND GMBH: Funkenerosion Graphit-Marke HK-6. Material data-sheet. 2014.
[9] DONCASTERS PRECISION: Verification certificate for material MARM247, according to DIN EN 10204 3.1. Bochum, 2013.
[10] J. R. Kattus: Aerospace Structural Metals Handbook, code 4218, p.1-8, Purdue Research Foundation, West Lafayette, Indiana, 1999.
[11] F. Klocke: Theoretische Modelle zur Funkenerosion - Grundlagenuntersuchungen an elektrischen Entladungen unter flüssigen Dielektrika. Abschlussbericht zum Forschungsvorhaben Kl 500/23-1. 2002.
[12] A. Karden: Funkenerosive Senkbearbeitung mit leistungssteigernden Elektrodenwerkstoffen und Arbeitsmedien. Bericht aus der Produktionstechnik. Hrsg.: Klocke, F. Aachen: Shaker, 2001.

ELSEVIER

16th Machining Innovations Conference for Aerospace Industry - MIC 2016

Physics-Based Model to Predict Forces and Chip Morphology in the Machining of a Ti-6Al-4V Alloys for Aeronautical Applications

Omar Fergani[a,*], Zoubir Atmani[b], Mohamed Zenasni[b] , Knut Sorby[c]

[a]NTNU- Department of Engineering Design and Materials, Norwegian University of Science and Technology, Trondheim, Norway

[b]ENSAO, Equipe de Mécanique et Calcul Scientifique, Morocco

[c]NTNU- Department of Production and Quality Engineering, Norwegian University of Science and Technology, Norway

Abstract

The understanding of the cutting process for Ti-6Al-4Valloys is a substantial challenge for process planning in the aerospace industry due to their large-scale utilization. The recent advances in physics-based simulation tool show great capabilities to reduce the operating cost while maintaining the desired product properties. This paper presents a new physics-based materials model capable of capturing accurately the plastic deformation behavior of a Ti-6Al-4V alloys. The model uses the so-called mechanical threshold stress (MTS) theory as a basis for the predictions. The model's ability to predict the dimensions of the shear band is evaluated by comparing finite element simulation and experimental results. The results show good predictability for both the cuttings forces and chip morphology. Overall, it is suggested that the model can be used for planning of machining processes in industrial practice.

1. Introduction

The high performance cutting of Titanium alloys specifically Ti-6Al-4V has been investigated extensively by industry and academia. Titanium alloys present high strength, low density, low thermal conductivity and heat capacity. They are considered hard to machine alloys. During the machining, a chip segmentation phenomena is observed. Different problems related to severe tool wear and process instability are associated to the chip segmentation. On the

* Corresponding Author. Tel.: +4792032386 - E-mail address: o.fergani@ntnu.no

other hand, one might think that the chip segmentation is a beneficial aspect because of cutting forces reduction. For many years, researchers presented innovative solutions to achieve stable machining process such as the development of new materials and geometries for the cutting inserts or innovative lubrication solutions, cryogenic cooling as an example. Aerospace industry has adopted high speed machining of Titanium due to the increasing productivity requirements. New issues related to tool wear, high vibration as well as alternated surface properties are observed. For these reasons, the need of a physics based understanding of the chip formation during the machining of Titanium alloys is still a hot topic. Reveling the fundamental understanding of the chip segmentation in the machining of titanium alloys will enable a better understanding and control of the surface integrity. Pioneering work of Shaw et al [1] investigated some aspects of the chip formation. They explained that the segmented chip is a result of a competing thermal softening and work hardening of the material in the primary deformation zone. Later, Shaw et al [2] introduced the concept of Adiabatic Shear Bands (ASBs) are the results of the thermal properties of titanium alloys. Later, Komunduri and Turkovish [3] proposed a step by step analysis based on experimental results obtained through variating the cutting speed in orthogonal configuration. The deformation was recorded under scanning electron microscope (SEM) and video camera at higher speeds. Their main finding is that high strain are mainly confined to the shear bands. It is clear that the understanding of the chip formation process in the machining of Titanium is key to achieve higher productivity and better surfaces. Another mechanism is proposed as dominating the chip segmentation due to ductile fracture. A crack initiation and propagation is observed experimentally. Shaw et al [1], after the proposition of the competing softening/hardening, concluded that a ductile fracture on the free surface of the chip is at the origin of this behavior during the machining. Large number of report confirmed this assumption through simulations and experimental work. In an early work by Nakayama [4] the saw tooth chip formation during the machining of hard steel is interpreted by the fracture initiation on the free surface. The reason behind this is interpreted through the weak value of hydrostatic pressure in these locations. Using a ductile fracture criteria, Obikawa and Usui [5] proposed a finite element model capable of predicting the chip morphology. The model included the effect of stress, strain, strain rate and temperature in the prediction. Gente [6] presented a controlled experimental work to support the fact that the Catastrophic Adiabatic Shear (CAS) is no happening during the machining of Titanium alloys. Instead, the thesis of a fracture is supported.

Based on the recent review and state of the art in the machining of titanium alloys, it is clear that the understanding of the chip formation is not yet elucidated. Different issues related to the formation of adiabatic shear bands and fracture locus in the segmented chip is to be answer. In this study, we propose a physics based model to help answer these questions. The numerical model based on finite element is validated through a comparison of the simulated and experimental cutting forces. The model is also validated through a comparison of the length of the shear band. The state of stress is simulated to better interpret the chip morphology and the fracture locus. Finally, the model is utilized to investigate the obtained chip at different cutting conditions.

2. Materials and experiments

Orthogonal machining of Ti6Al4V is performed on an OKUMA Genos L200E-M machine. The insert and materials properties are presented in Table.1. The insert has a rake angle of 0°. The chamfer is measured to be 6° as shown in the model in Fig.1.

Table 1: Materials and cutting insert properties.

mechanical properties	E(Gpa)	G(Gpa)	ν	ρ(kg/m^3)	T$_m$(K)	Thermal conductivity (W/m k)	specific heat (J/kg.k)

Workpiece (Ti6Al4V)	110	49.02	0.3	4430	1905	16	670
Tungstencarbide	534	*	0.22	11900	*	50	400

Three cutting conditions are performed for the purpose of this study. Machining at different cutting speeds is performed. V_c=15 m/min, V_c=30 m/min and V_c=60 m/min. The feed is fixed to f= 0.12 mm. The cutting forces are measured using a Kistler dynamometer. The obtained chip are characterized using optical microscope in terms of morphology and shear band.

3. Physics modeling

3.1 Finite Element Modeling

A standard implementation of a 2D orthogonal cutting model based on the Lagrangian approach is developed in Abaqus/Explicit software and inspired by the previous work of Atlati et al [7], both to simulate the cutting process using de MTS model and segmentation prediction in the chip by coupled MTS-damage JC. The Lagrangian-FE formulation has been seen as an interesting method to simulate discontinuous chip formation under a steady state condition. It mainly enables the simulation with the need of a separation criteria, such as a critical stress state achieved at a specified distance ahead of the tool tip or a damage evolution parameter for the elements deletion. Each layer of the workpiece mesh is defined with specific behavior. In Part1, MTS with damage, in Part2, MTS without damage. Part3 MTS damage with element delete. Finally, in Part4 MTS without damage is implemented (see Fig. 1). This separation in different section is implemented to reduce the computational time.
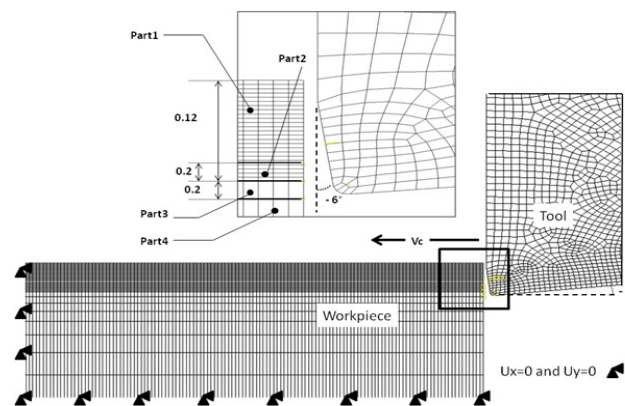

Fig. 1. Description of the finite element model with mesh, tool geometry and boundary conditions

The contact behaviour at the tool–workpiece interface is defined by the relationship between the normal friction stress p and the shear friction stress τ_f. The friction value is selected to be 0.4. The details about the friction coefficient selection Atlati et al [7].

3.2 Mechanical Threshold Flow Stress (MTS)

During the machining process, the complex thermomechanical loading will lead to a complex material deformation and microstructure evolution. The capacity of the model to capture these changes is therefore critical. In this work, we base the flow stress prediction on an approach to predict the variation of dislocation energy at stage III hardening of the materials, here Ti6Al4V. For many years, the Johnson Cook model is used to predict machining forces and deformation. However, the JC model presents clear limitation due to the simplification in terms of microstructure

dynamics. In this study, we propose to integrate a physics based model based on the Mechanical threshold flow. The so called Kocks-Mecking to predict the flow stress of the material during the machining process.

$$\sigma_y = \sigma_a + S_I(\dot{\varepsilon},T)\hat{\sigma}_I + S_S(\dot{\varepsilon},T)\hat{\sigma}_S + S_D(\dot{\varepsilon},T)\hat{\sigma}_D \qquad (1)$$

where σ_a is the athermal stress, $\hat{\sigma}_I$, $\hat{\sigma}_S$, and $\hat{\sigma}_D$, are the threshold stresses that represent respectively dislocation-interstitial, dislocation-solute and dislocation-dislocation interactions. $S_I(\dot{\varepsilon},T)$, $S_S(\dot{\varepsilon},T)$ and $S_D(\dot{\varepsilon},T)$ represent the ratios between the yield stress at a specific strain rate and temperature and the yield stress at 0 K for each dislocation obstacle. The physics interpretation of the four terms represented in Eq (1) are respectively: athermal strength, the strengthening due to dislocation-interstitial interactions, the strengthening due to dislocation-solute interactions, and the dislocation-dislocation. The proposed model constants are reported for the case of Ti6Al4V in Da Silva and Ramesh [8]. The model behaviour under different temperature is simulated and compared to the experimental work of Hammer [9]. Fig.2 shows the comparison results. The model show good capacity in capturing the measured stress-strain behaviour. Other test are performed for higher strains in order to further validate the model. The obtained results suggest that the model is good at capturing the materials behaviour at low and moderate temperature. For the case of 600ºC, the model is not capable of predicting accurately the yield stress. Further investigation for the model capacity at high strain rate is underconsideration.
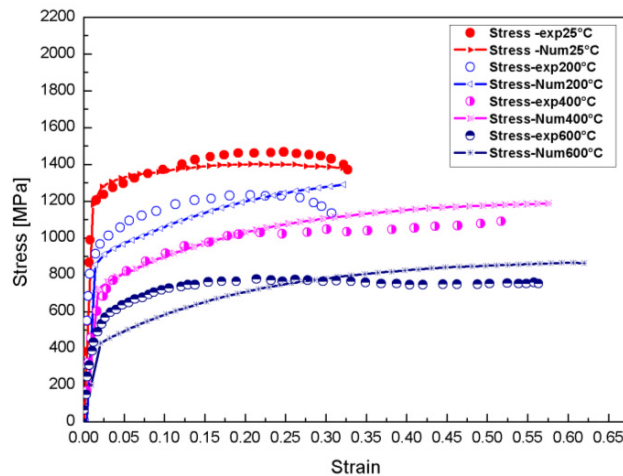

Fig. 2. Flow stress validation under compression for strain rate of 1s⁻¹at different temperatures
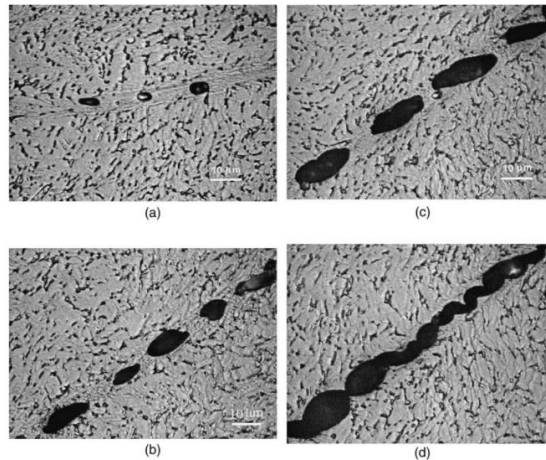
3.3 Damage Model and Stress Triaxiality

During the machining of Titanium alloys and specifically the Ti6Al4V. Fracture happening in the shear band has been observed. It is therefore important to reflect this behaviour in the modelling of the machining approach. The stress triaxiality could play based on the work of Bao [10] an important role in the explanation of the fracture behaviour. Depending on the material, ductility may decrease when stress triaxiality decreases from 1/3 in the case of a pure tension to 0 for pure shear. Garrison and Moody [11] described the step by step ductile fracture as void nucleation, void growth and finally void coalescence. To capture the damage accurately, a JC damage model is proposed in this work. The model capture the initiation and propagation of the damage as described by Fig. 3.

Fig. 3. Damage evolution based on Abaqus [12]

The initialization of damage is described by the following relationship where strain is given by:

$$\bar{\varepsilon}_i = \left[d_1 + d_2 \exp(d_3(P/\bar{\sigma})) \right] \left[1 + d_4 ln\left(\dot{\bar{\varepsilon}}_p \middle/ \dot{\bar{\varepsilon}}_0 \right) \right] \left[1 - d_5 \left((T - T_0)/(T_f - T_0) \right) \right] \quad (4)$$

Where $\bar{\sigma}$ is equivalent von Mises stress, P is the hydrostatic pressure. The $P/\bar{\sigma}$ refers to the stress triaxiality. The variables are the parameters of initiation of damage to the machined material to determine experimentally .The damage is initiated when $\omega_d = 1.0$. The JC damage coefficient used in this study are (d1: -0.09, d2: 0.25, d3: -0.5, d4: 0.014 d5: 3.87) as reported from the previous work of Johnson and Cook [13]. Previous investigation by Xue et al [14] of the fracture in the shear band of the machined chip concluded that the three stages of the fracture are observed. He reported experimental evidences of nucleation, growth and coalescence of fracture in the ASBs. He concluded that these sites are idea fracture locus during the machining of Ti6Al4V as shown in
Fig. **4**.

Fig. 4. Void initiation, growth and coalescence based on the work of Xue et al [14]

4. Results and Discussions

4.1 Model validation using forces and shear band

The predicted and measured forces are compared after calibration. The calibration procedure consisted in using the experimental collected data from V_c= 15m/min and adapted the model to make it capable of predicting accurately the value. This was done through a very small adaptation of the friction coefficient. Then, the experimental data are measured to the average as due to the chip segmentation, some variations are observed. Fig.5 shows the obtained results for the case where V_c= 60m/min. It is clear that the model was capable of capturing the cutting forces in both directions. The prediction model is also capable predicting the variation of cutting forces associated to the chip segmentation phenomena. These in some cases are substantial as variation of 50% can be observed in some cases. This might be associated more to a fracture initiation in the shear band rather than the apparition of the adiabatic shear band. In the next section, physics based interpretation of the fracture initiation described initially in the literature is discussed.
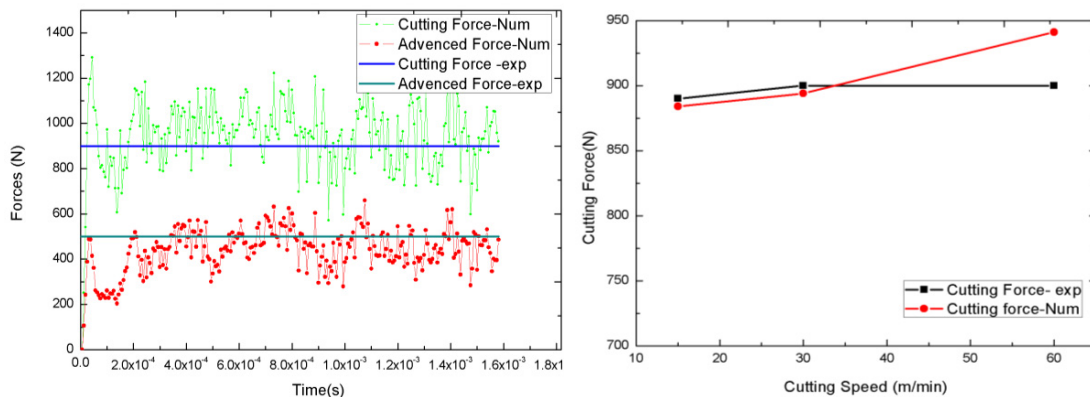
Fig. 5. Comparison between the predicted cutting forces and the average of measured forces using dynamometer

The formation of segmented chip is inherent to the machining of Titanium alloys. The segmented sections of the chip are separated by a shear band. It is reported that the adiabatic shear band (ASB) shape changes following the variation of the cutting parameters. The ASB can be characterized by it width. In this work, microscope image of the shear band is compared to the obtained simulated results. Fig.6 shows the obtained shear band for the case of V_c=60m/min. Severe deformation is observed in the shear band. The simulated shear strain is found to be 5 on average. The shear band was measured to be 12.2 µm, the average simulated results in found to be 12 µm. The accurate results are attributed to the capacity of the materials deformation model to capture the deformation.
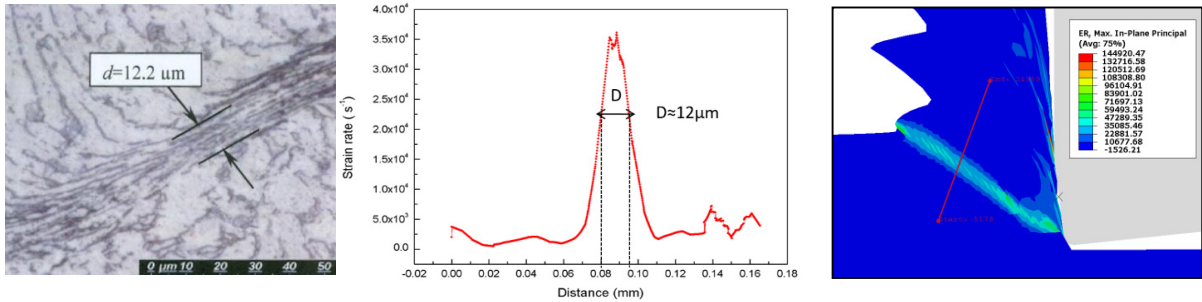
Fig. 6. Comparison between measured shear band in the obtained chip and the predicted using the simulation for the V_c=60 m/min

4.2 State of stress and strain

Fig. **7** (b) shows the typical fracture obtained in a shear band. The initiation of fracture locus on the shear band is important to capture to plan a stable machining process. The state of the stress through stress triaxiality is part of the damage model. We investigate the stress triaxiality in each machined sample. Based on Bao [15]**,** if the value pf stress triaxiality are higher than 1/3, the fracture locus could appear, the shear band become therefore an ideal spot for fractured shear. For the vase of V_c= 60 m/min, the simulation predicted very high strain in the shear band between 4 and 5(Fig.7 (a)). Also, stress triaxiality values are presented in Fig.7 (b). The ideal condition for observing a fracture locus are obtained. Results from the experiments confirm the predicted data. Fracture locus and fracture along the shear band could be clearly seen.

(a)   **(b)**
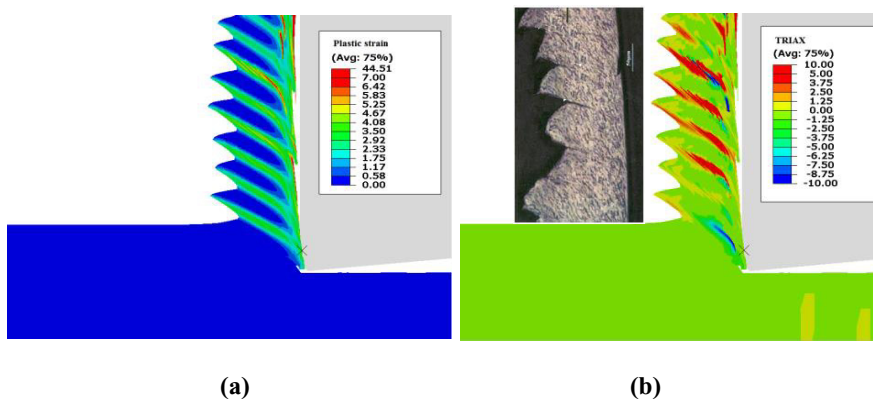
Fig. 7. (a) Plastic strain, (b) Stress triaxiality and associated obtained chip

The fracture mechanism happening in the segmented chip specifically at the ABSs can be explained by the nature of the machining operation. The homogenous shear stress associated to a compressive stress the second half of the shear plan and a tensile on the other create an instable deformation experienced by the materials at the shear band. In addition to the stress triaxiality, Fig. 8. shows the state of hydrostatic stress in the ASB. It appears that the hydrostatic stress are very weak. This association of high stress triaxiality and very weak hydrostatic pressure can be at the origin of the fracture locus in the ASB.
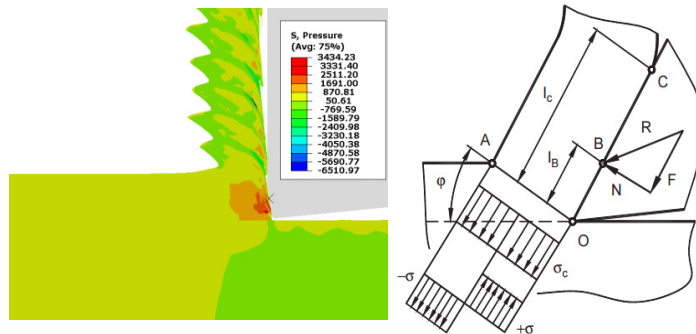
Fig. 8. Predicted hydrostatic pressure in the chip shear bands

The results presented in Fig.9 demonstrate the influence of the cutting speed on the stress triaxiality in the chip. It is evident from the simulation results that the increase of the cutting speed is at the origin of the tension and compression profile inside the chip as clearly shown in the case of Vc=500mm/min. Using low cutting speeds, the chip is under only one type of stress (compression) as it is showed in the case of Vc= 90m/min. This is clear evidence that the stress triaxiality will play a key role in the chip segmentation. It can also be used as a parameters to predict the fracture in the chip.
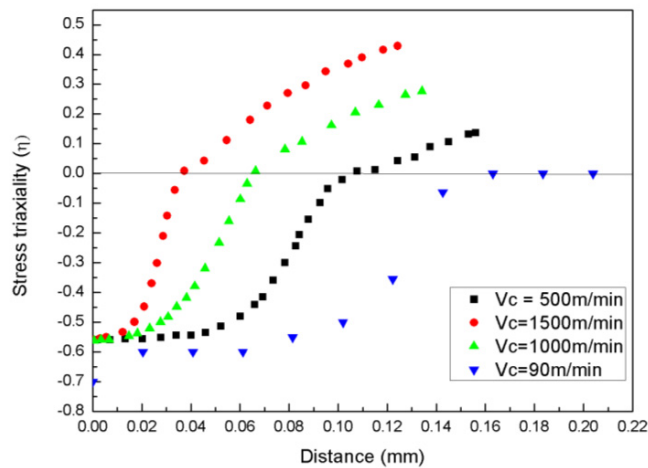
Fig. 9. Predicted hydrostatic pressure in the chip shear bands

4.3 Chip morphology and frequency

The developed model in this study is used to explore the the chip morphology behavior at different cutting speeds. Chip morphology can be defined by the deformed chip thickness H, the orthogonal peak to valley length h and finally, the inclined peak to valley L. Theses parameters are defined in Fig.10. Using the numerical model, the values of H, h and L are evaluated for each cutting speed. Results showed in Fig.10 suggest that the increase of the cutting speed reduces drastically the value of H. However, slight variation of h and L are observed during the increase of the cutting speed.
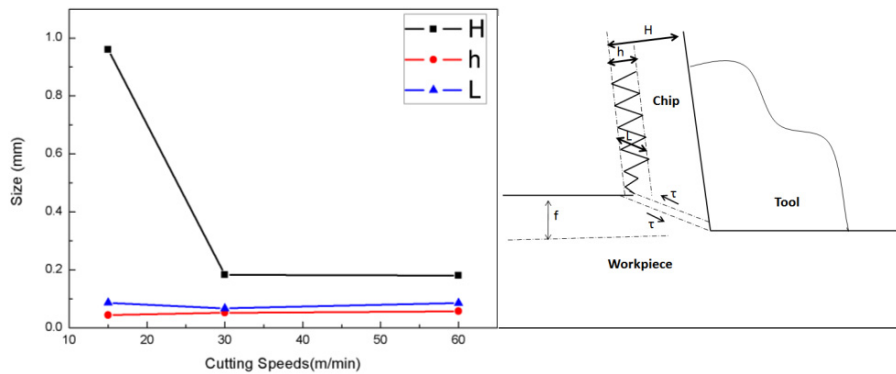
Fig. 10. Predicted parameters defining the chip morphology

5. Conclusion

In this work, a new physical model to capture the material deformation based on microstructure attributes is implemented in a numerical code using FORTRAN subroutine. The model is used to simulate and predict the orthogonal machining of Titanium alloys. The model is validated experimentally using machining experiments. The results of this work can be summarized as follow:

- MTS based flow stress model showed high capacity to predict deformation of Ti6Al4V accurately.
- The materials model enabled the model to capture the chip segmentation accurately. The cutting forces, the chip morphology and the size of the shear band are validated experimentally.
- The severe deformation experienced in the shear band can lead to the formation of fracture locus. This is explained through the analysis of the stress state and triaxiality. It is found also that the increase of the cutting speed induces more fracture locus in the shear bands
- The proposed model showed ability to predict chip morphology for different cutting conditions. The frequency of fracture can also be predicted thanks to the accurate prediction of stress triaxiality.
- Further investigation is in progress for higher speed in order to achieve optimal process planning for high productivity machining.

References

[1] Shaw, M. C., 2005, Metal Cutting Principles, 2nd ed., Oxford University Press, Oxford, UK.
[2] Shaw, M. C., Dirke, S. O., Smith, P. A., Cook, N. H., Loewen, E. G., and Yang. T., 1954, "Machining Titanium," U.S. Air Force, MIT Report.
[3] Komanduri, R., and Von Turkovich, B. F., 1981, "New Observations on the Mechanism of Chip Formation When Machining Titanium Alloys," Wear, 69(2), 179–188.
[4] Nakayama, K., Arai, M., and Kanda, T., 1988, "Machining Characteristics of Hard Materials," CIRP Ann.-Manuf. Technol., 37(1), 89–92.
[5] Obikawa, T., and Usui, E., 1996, "Computational Machining of Titanium Alloy-Finite Element Modeling and a Few Results," ASME J. Manuf. Sci.Eng., 118(2), 208–215.

[6] Gente, A., and Hoffmeister, H. W., 2000, "Chip Formation in Machining Ti6Al4V at Extremely High Cutting Speeds," CIRP Ann., 50, 49–52.

[7] Atlati S, Haddag B, Nouari M, Zenasni M. 2011,"Analysis of a new Segmentation Intensity Ratio ''SIR'' to characterize the chip segmentation process in machining ductile metals". Int. J. Mach. Tools Manuf. 51, 687-700.

[8] Da Silva M.G, Ramesh K .T, 1997, "The rate-dependent deformation and localization of fully dense and porous ti-6Al-4V", Materials Science and Engineering: 232(1-2), 11-22.

[9] Hammer, B.S. Plastic Deformation and Ductile Fracture of Ti-6Al-4V under various loading conditions, Ph.D. Thesis, The Ohio State University, 2012

[10] Bao, Y. B., 2005, "Dependence of Ductile Crack Formation in Tensile Tests on Stress Triaxiality, Stress and Strain Ratios," Eng. Fract. Mech., 72 (4), 505–522.

[11] Garrison, W. M., and Moody, N. R., 1987, "Ductile Fracture," J. Phys. Chem.Solids, 48(11), 1035–1074.

[12] ABAQUS/EXPLICIT Analysis User Manual, Version 6.11.

[13] Johnson, G. R., and Cook, W. H., 1985, "Fracture Characteristics of Three Metals Subjected to Various Strains, Strain Rates, Temperatures and Pressures," Eng. Fract. Mech., 21(1), 31–48.

[14] Xue, Q., Meyers, M. A., and Nesterenko, V. F., 2002, "Self-Organization of Shear Bands in Titanium and Ti-6Al-4V alloy," Acta Mater., 50 (3), 575–596.

[15] Bao, Y. B., and Wierzbicki, T., 2004, "A Comparative Study on Various Ductile Crack Formation Criteria," ASME J. Eng. Mater. Technol., 126 (3), 314–324.

[16] Bing Wang, Zhanqiang Liu, 2016, "Evaluation on fracture locus of serrated chip generation with stress triaxiality in high speed machining of Ti6Al4V", Materials and Design (98), 68–78.

16th Machining Innovations Conference for Aerospace Industry - MIC 2016

Effect of α and β phase volume fraction on machining characteristics of titanium alloy Ti6Al4V

Sandip Patil* , Swapnil Kekade, Kamlesh Phapale, Shital Jadhav, Amit Powar, Ashish Supare ,Dr. Rajkumar Singh

Kalyani Centre of Technology and Innovation, Bharat Forge Ltd. Pune 411036, India

Abstract

Microstructure of titanium alloys has great influence on the manufacturing processes. In the current investigation the effect of change in volume fraction of alpha and transformed beta phase in the bimodal titanium alloy Ti6Al4V was discussed in relation with the mechanical and machining performance. The quenching process in STA (solution treatment and annealing) heat treatment was delayed by 30, 50 and 70 sec to get different microstructural morphology in each heat treated specimen. Face turning experiments with dry and high pressure coolant environment were performed on the solution treated samples. A detailed chip mechanism and microstructural analysis was performed to investigate the role of quench delay and subsequent change in phase volume fraction on thermal softening and frictional phenomenon in machining. The specimen treated with quench delay of 50 sec exhibited poor machinability because of thermal and frictional shock generated at the cutting zone.

1. Introduction

Titanium alloys such as Ti6Al4V are extensively used in the aerospace industry for structural as well as engine components such as fan blades, disks, shafts, etc. due to their superior properties such as excellent strength-to-weight ratio, strong corrosion resistance and ability to retain high strength at elevated temperatures. However, titanium still possesses some undesirable properties in particular, low thermal conductivity, high strength, high hardness, high chemical reactivity, etc. which results into more friction and cutting heat leading to poor machinability[1-5]. Titanium alloy Ti6Al4V is the most popular alloy among the titanium alloys; it contains alpha and beta phases in the percentage volume fraction with reference to the heat treatment followed. This volume fraction further determines the deformation behavior and mechanical properties of this alloy under both quasi-static and dynamic loading conditions [2]. Both α and β phases are relatively soft but α – β interface is an effective stoppage to dislocation and crack propagation [2, 4]. It has been reported by various researchers that the machinability of titanium alloys is strongly affected by the heat

treatment process and subsequent microstructure produced [2, 5-7, 9]. A detailed research was found on mechanical and machining aspects of globular, bimodal and fully-lamellar microstructures of titanium alloy Ti6Al4V [6-7]. Titanium alloys with coarse grain microstructure such as beta annealed input condition leads to high shear stresses and correspondingly higher cutting forces and are more difficult to cut than the finer grain structure [2, 5]. It was also reported that main cutting force during machining of titanium alloy Ti6Al4V with globular phase morphology is lower than that of bi-modal and fully lamellar phase morphologies at cutting speed lower than 100m/min [2, 5-7]. The Widmanstätten microstructure showed more inhomogeneous deformation with presence of large lamellae even at the lowest feed rate [2, 9]. However, the effect of change in volume fraction of alpha and beta phase of heat treated titanium alloy Ti6Al4V on the machinability aspect has not been investigated. Therefore, the objective of current research is to investigate the effect of change in phase fraction on mechanical and machining behavior for titanium alloy Ti6Al4V. For this purpose, samples of Ti6Al4V were subjected to solution treatment and annealing (STA) process with introducing various quench delays. These quench delays used resembles the actual transfer time used in aerospace industries to transfer the heated parts from heating furnace to quench tank. The machinability aspect was investigated using face turning experiments in terms of frictional and thermal softening phenomenon using detailed parameters of chip mechanism and chip microstructure.

Nomenclature

QD	Quench delay
WQ	water quench
HP	High pressure
BUE	built-up-edge
STA	solution treatment and annealing
Ɣ	shear strain in shear band
AMS	Aerospace Material Specification

---

2. Experimental details

2.1. Heat treatment

The raw input for titanium alloy Ti6Al4V with chemical composition as per AMS 4928 was procured in the form of round specimen (Ø70 mm) in annealed condition. The beta transition temperature for the material was assumed to be 995^0C. As shown in Fig.1, the as-received micro sample (transverse direction) shows equiaxed grains of α-phase with β-phase. The β-phase settles along the grain boundaries of equiaxed α-phase. Annealing relieves residual stresses in the material and influence grain recrystallization and growth [4].
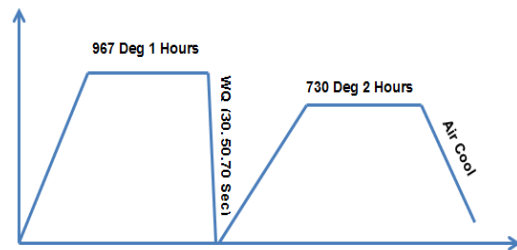

Fig.1 As received microstructure of titanium alloy Ti6Al4V in annealed condition   Fig. 2. Heat treatment (solution treatment and annealing)

   As shown in Fig.2, the samples were solution treated at 967°C and hold for 1 hour. A Batch of three samples each subjected to water quenching with quench delays of 30, 50 and 70 sec respectively. These samples were further annealed at 730 °C for 2 hours and then cooled in air. A box type laboratory scale muffle furnace of make Therelek

was used for the heat treatment process. The uniformity achieved inside the furnace was +/- 3 °C. It was a temperature controlled furnace heated by electric coils and could achieve a maximum of 1200 °C and having facility of varying the heating rate up to max.12 °C /min. A small sample was sliced from each heat treated specimen for optical analysis. The sample was initially hot mounted using Citopress-10 mounting device with Poly-Fast resin. The mounted sample was polished using an automatic polishing device Tegramin-30. The mounted and polished sample was etched using Kroll's reagent for the period of 10 seconds. The etched sample was analyzed using optical microscope of make Zeiss with Axio-Imager Z.2m. The micrographs were further analyzed for phase distributions using the software Axio-Vision. Vickers hardness tests were performed using Clemex make microhardness tester on the heat treated samples using 500 g load. Tensile tests were performed at constant crosshead speed with an initial strain rate of 0.005 min-1. Fig. 3 a-c shows the optical micrographs of quench delayed samples and Fig. 4d-f shows corresponding investigation of volume fraction of alpha and transformed beta phase. From microstructures shown below, it is seen that quench delays provides remarkable effect on the phase composition in titanium alloy Ti6Al4V.

As shown in Fig. 3, solution treatment and annealing (STA) heat treatment resulted into bimodal distribution of interconnected equiaxed primary α grains (bright) and lamellar α+ β colonies (transformed β) (dark) [2,4-5]. A careful investigation of volume fraction of phases was carried out from these micrographs by using an image analyzer tool and the results are shown in Fig. 4 and Table I. An increase in quench delay from 30 sec to 70 sec, resulted into higher volume fraction of primary alpha (red) and reduced percentage of transformed beta (green).
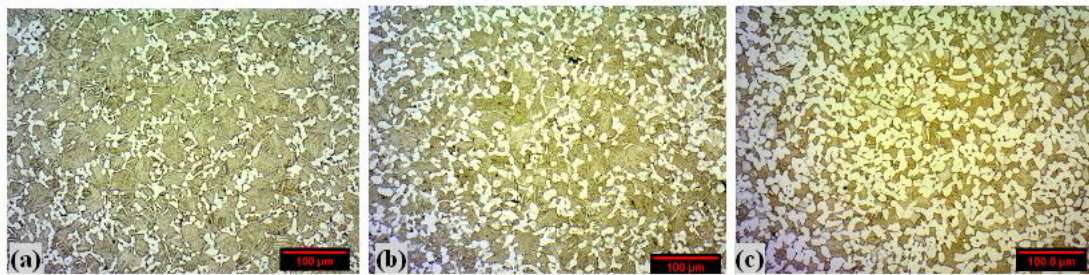
Fig. 3 Optical micrographs of heat treated (solution treated and annealed) titanium alloy Ti6Al4V with quench delay of (a) 30 sec (b) 50 sec (c) 70 sec (100 X)
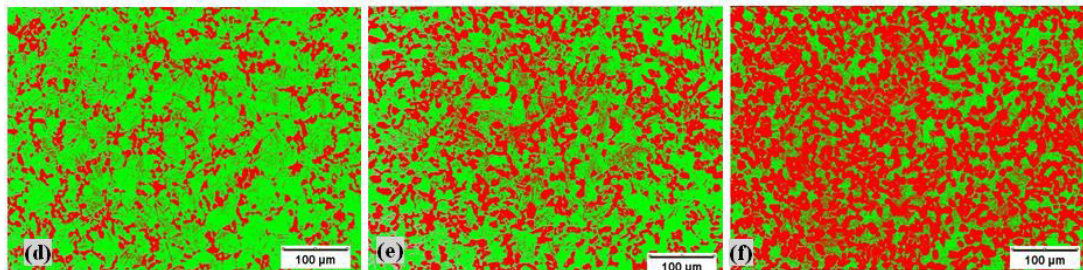
Fig.4 Phase mapping of solution treated and annealed titanium alloy Ti6Al4V with quench delay of (d) 30 sec (e) 50 sec (f) 70 sec (100X).

Table 1 Phase analysis and mechanical properties

Quench delay (sec)	Primary α (%)	Transformed β (%)	UTS (MPa)	YS (MPa)	Hardness (HRc)
30	30	70	1073	1034	37.2
50	49	51	1006	998	35.6
70	67	33	993	950	32.5

The effect of increase in volume fraction of alpha on the mechanical properties was clearly visible as shown in Table 1 where a gradual diminution in strength and hardness was recorded with the increase in quench delay from 30 sec to 70 sec.   Direct quenching in water from 967 °C resulted into formation of a martensitic structure. This martensite structure is of hexagonal α' type with acicular morphology in different orientations. The α'-martensite further transforms during tempering heat treatment and decomposes to equilibrium α and β. This transformation to α is in the form of fine precipitate that is nucleated heterogeneously at martensite plate boundaries or at internal structures such as twins [4]. An increase in the quench delay before quenching offered an extra time to precipitate equilibrium α instead of α'-martensite which further resulted into percentage increase for alpha phase and percentage decrease for transformed beta phase in the bimodal microstructure of titanium alloy Ti6Al4V.

2.2. Machining

Titanium alloy Ti6Al4V quench delayed samples of 30 sec, 50 sec and 70 sec were used as an input for face turning operation performed using DMG Turn Mill center – CTX beta 1250 TC as shown in Figure 5. All the turning experiments were performed at room temperature using dry cooling environment as well as using high pressure coolant of 50 bar. Total 6 sets of experiments were performed with first 3 nos. of experiments QD 30 – DRY, QD 50-DRY and QD 70- DRY using dry cutting environment followed with remaining 3 nos. of experiments QD 30 – HP coolant, QD 50-HP coolant and QD 70- HP coolant with high pressure coolant application. A constant cutting speed of 90 min/min, feed rate of 0.3 mm/rev and depth of cut of 1 mm was used for all the experimentations.

Fig. 5 Face turning set up

Fig. 6 On machine high pressure coolant set up for rake face of the tool

Face turning operation was performed using carbide insert CNMG 120408-NFT WSM20- Walter make. As shown in Fig. 6, for high pressure coolant assisted experiments, a constant coolant pressure of 50 bar was directed at the chip tool interface near the rake face of the tool. Cutting chips collected after each cutting trial were polished and etched for detailed optical and scanning electron microscopy to reveal the chip mechanism and chip microstructure during machining.

3. Results and Discussion

3.1. Effect on chip thickness and shear angle

In this quantitative analysis of chip mechanism, as shown in Fig.7a-c, chip thickness, shear angle, shear band spacing, shear strain in shear band, shear displacement in shear band, etc. were discussed and their significance was correlated with the machinability of different alpha and beta phase volume fraction in titanium alloy Ti6Al4V. The generation of thicker, uneven chips is not favorable for high quality machining as these chips affects the tool cutting area, resulting in non – uniform friction and generating high cutting temperature, high cutting forces and rapid tool wear, etc. [10-11]. Higher shear angle represents less deformation along the shear plane which contributes to less cutting forces. More amount of shear deformation along the shear plane resulting from normal stresses will represent

more crack formation at the shear zone. An increased spacing between shear bands will represent less amount of cutting temperature and subsequently less shear band formation. The value of shear strain in the shear band is essential to understand the extent of shear localization [9-11].
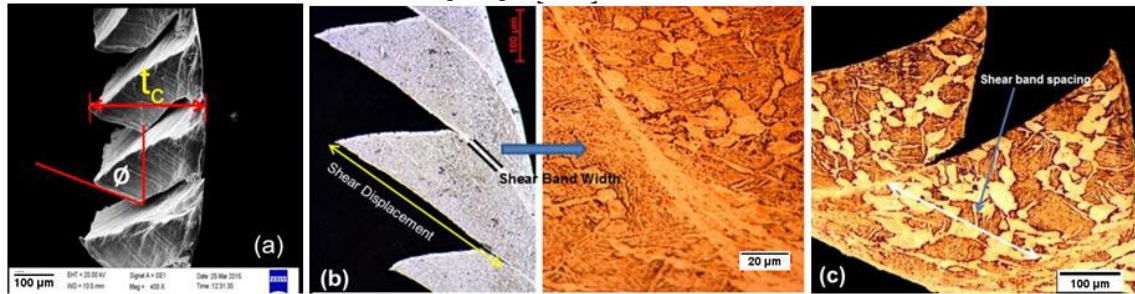

Fig.7 (a-c) Chip mechanism

As shown in Fig. 8, the effect of change in quench delay and the subsequent phase composition was clearly seen on the chip thickness. The impact of change in phase composition was more critical during dry machining. The adhesion of titanium may have resulted to an increased friction between chip and the tool rake face which ultimately produced thicker chip [3]. With the use of high pressure coolant machining approach, the adhesion and subsequent formation of BUE on the tool surface was reduced. This was mainly because of reduction in contact time between tool and chip [3]. However, with both the machining approach an increase in quench delay from QD 30 to QD 70 resulted in higher chip thickness. In particular, compared to quench delayed samples with QD30 and QD 70, the specimen with QD 50 showed highest chip thickness. This shows that as explained in Table 1, phase composition of 51% transformed beta and 49% primary alpha has resulted into more amount of friction at the interface. This may be because of the frictional shock created during machining of ductile primary alpha phase with the higher strength transformed beta phase.
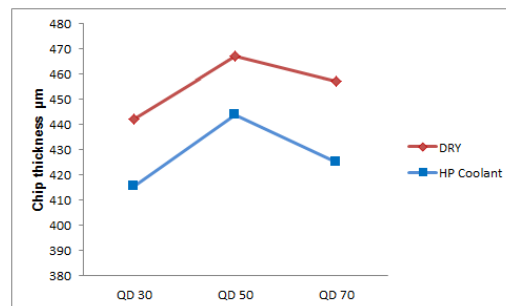
Fig.8 Effect of phase change on chip thickness

The shear plane angle increases with reduction in friction at the tool-chip interface [2]. As shown in Fig. 9 and Fig. 10a-b, with the increase in alpha percentage against the transformed beta in the bimodal microstructure of titanium alloy Ti6Al4V, the shear angle was found to be drastically reduced for QD 50 with alpha 49% and transformed beta 51%. This shows that during machining of QD 50, the cutting tool may have experienced alternate work hardening and thermal softening characteristics of alpha and transformed beta counteracting on each other resulting to BUE and excessive grain deformations which further contributed to an increased cutting force.   However, with the use of high pressure coolant machining approach the intensity of frictional cutting was relived to some extent, this may be because of adequate lubrication provided at the cutting interface.
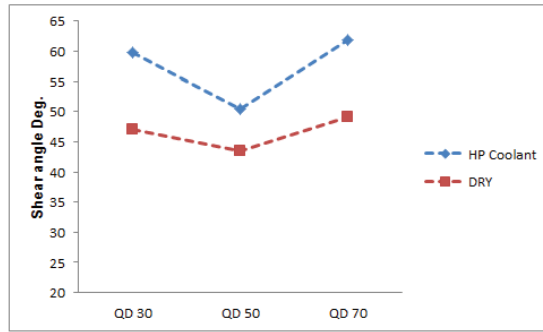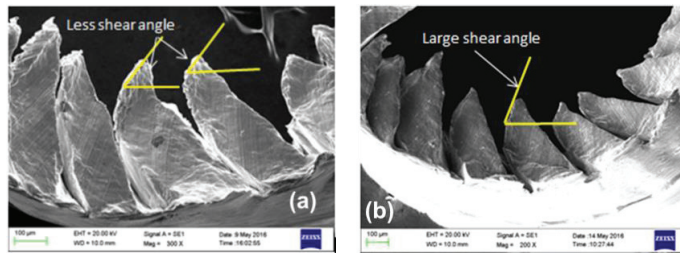
Fig.9 Effect of phase change on shear angle

Fig.10 a-b Shear angle measured during DRY and HP coolant experiments (QD 50)

3.2. Effect on shear deformation

As shown in Fig. 11, Fig. 12, Fig. 13, and Fig.14a-f, alternate dual phases with high strength of transformed beta and ductile primary alpha affects the shear deformation process in machining. As explained in Fig. 11 and Fig. 12, for QD 50 with the lesser amount of difference between volume fraction of transformed beta and primary alpha, none of the phase acts as a dominant phase fraction in titanium alloy Ti6Al4V. During machining process this will promote excess friction and thermal softening behavior resulting to an increased shear band formation with great amount strain in the shear band but reduced crack formations at the shear plane. The shear strain in the shear band was measured by [11]:

$$\Upsilon = \text{shear displacement / shear band width}$$
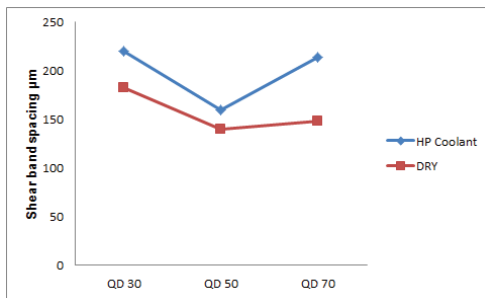
Fig. 11 Shear band spacing
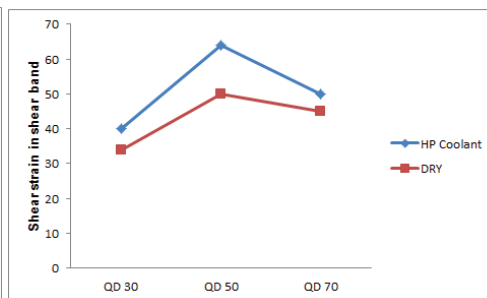
Fig.12 Shear strain at the shear plane

As shown in Fig. 13 and Fig.14b-d-f, during dry machining, an increase in the primary alpha content reduces the crack formations at shear zone of the chip. As shown in Fig. 14d, for QD 50 - DRY, the absence of crack formations shows that the higher amount friction between tool and chip resulted to an excessive plastic deformation. This can be revealed from the gradual increase in shear strain measured in shear band for QD 50 – DRY. However, this excess shear strain measured at the shear band has not contributed to crack formations but delayed cracking [5]. The formation of very thin and multiple or twins shear bands for the chips of QD 50-DRY can also explain the thermal softening phenomenon during dry machining [5, 10-11]. However, as shown in Fig. 14 a-c-e, high pressure coolant machining has resulted in increased crack formations along the shear plane.

	QD 30	QD 50	QD 70
HP Coolant	283.3986667	131.1935	220
DRY	220	100	186.433
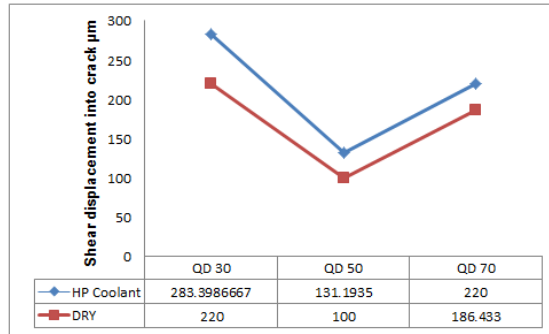
Fig.13 Crack formations at the shear plane
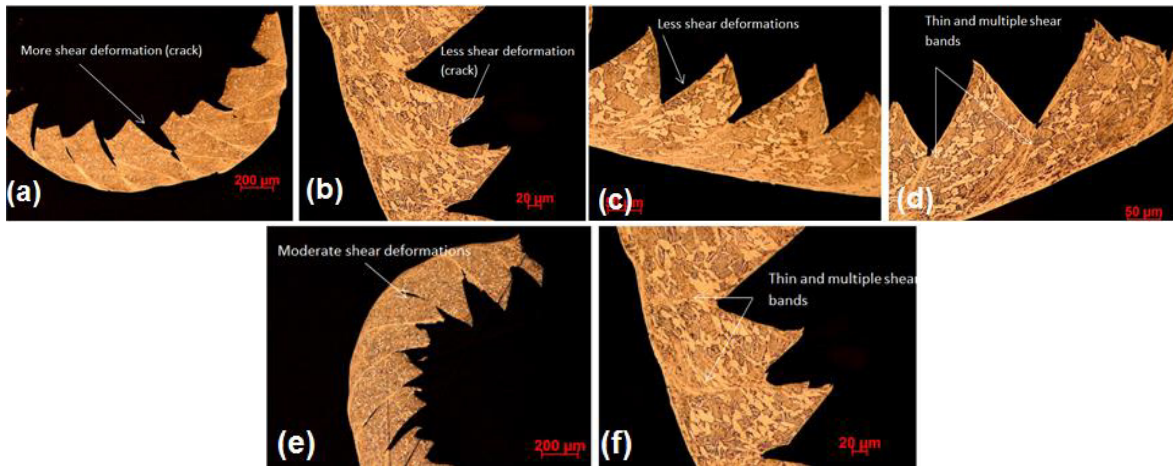
Fig. 14(a-f) Shear deformation during Dry and HP coolant machining

Conclusions

The current investigation showed that the wrong industrial practices of delayed quenching because of the transfer time associated with furnace and quench tank makes significant effect on the volume fraction alpha and beta percentage during solution treatment and annealing of titanium alloy Ti6Al4V. An increase in the quench delay promotes the precipitation of alpha rather than the formation of α' martensite. After annealing process, this will contribute to more amount of alpha phase than that of transformed beta. The increase in alpha content with an increase in quench delay from 30 sec to 70 sec leads to reduction in mechanical strength and hardness of solution treated

titanium alloy Ti6Al4V. During machining process, this effect of change in volume fraction was clearly visible on the chip mechanism and microstructural aspect. For QD 50 - DRY, reduction in difference between the volume percentage of alpha and beta phases resulted to an alternate hard and soft cutting which generated thermal and frictional shock at the cutting face leading to higher chip thickness, less shear angle, less crack formation, increased shear band formations, etc. to impair the machinability. Use of high pressure coolant generates adequate lubrication at the cutting interface to reduce the overall effect of phase change on machinability of titanium alloy Ti6Al4V.

Acknowledgements

References

[1] Berend Denkena, Thilo Grove, Patrick Helmecke, The Effect of Microstructure on the Machinability of Ti6Al4V, Ti-2015: The 13th World Conference on Titanium TMS, 2015.

[2] Shoujin Sun, Milan Brandt, John P.T. Mo, Effect of Microstructure on Cutting Force and Chip Formation during Machining of Ti-6Al-4V Alloy, Advanced Materials Research Vols. 690-693 (2013) pp 2437-2441.

[3] Sandip Patil, Swapnil Kekade, Pravin Pawar, Effect of Coolant Pressure on Machinability of Titanium Alloy Ti6Al4V, Applied Mechanics and Materials, Vol. 826(2015), pp 82-87.

[4] F.X. Gil Mur, D. Rodriguez and J.A. Planell, "Influence of tempering temperature and time on the α'-Ti-6A1-4V martensite," Journal of Alloys and Compounds 234, pp. 287-289, 1996.

[5] Sandip Patil, Pravin Pawar, Shital Jadhav, Ashish Supare, Amit Powar, S Kekade, Dr.RKP Singh, Correlation between heat treatment, microstructure and machinability for Ti6Al4V, International Journal of Mechanical And Production Engineering, Volume- 3, Issue-6, June-2015.

[6] S. Cedergren , G. Petti, G. Sjoberg, On the influence of work material microstructure on chip formation, cutting forces and acoustic emission when machining Ti-6Al-4V, Procedia CIRP 12 (2013) 55 – 60.

[7] Navneet Khannaa, Ainhara Garayb, Luis M. Iriarteb, Daniel Solerb, Kuldip S. Sangwana and Pedro J. Arrazolab, "Effect of heat treatment conditions on the machinability of Ti64 and Ti54M alloys", Procedia CIRP 1,477 – 482, 2012.

[8] M. Nouari, H. Makich, Experimental investigation on the effect of the material microstructure on tool wear when machining hard titanium alloys: Ti–6Al–4V and Ti-555, Int. Journal of Refractory Metals and Hard Materials 41 (2013) 259–269.

[9] Mohammed Nouari and Hamid Makich, On the Physics of Machining Titanium Alloys: Interactions between Cutting Parameters, Microstructure and Tool Wear, Metals 2014, 4, 335-358.

[10] Sandip Patil, Shashikant Joshi, Asim Tewari, Suhas Joshi, Modelling and Simulation of Ultrasonic Assisted Machining of Titanium alloy Ti6Al4V, International Journal of Ultrasonic, 54 (2014) 694-705.

[11] Shashikant Joshi, Pravin Pawar, Asim Tewari, and Suhas Joshi, "Effect of β-phase fraction in titanium alloy on chip segmentation in their orthogonal machining", CIRP journal of manufacturing science and technology, vol.7, pp. 191- 201, 2014.

16th Machining Innovations Conference for Aerospace Industry - MIC 2016

Effect of water oil mist spray (WOMS) cooling on drilling of Ti6Al4V alloy using Ester oil based cutting fluid

Sandip Nandgaonkar [a], T V K Gupta[b], Suhas Joshi[c]*

[a] *TAL Manufacturing Solutions Limited, Nagpur, India,* [b] *Department of Mechanical Engg., VNIT Nagpur, India,* [c]*Department of Mechanical Engg. IIT Bombay, India*

Abstract

This paper explains environment friendly water oil mist spray (WOMS) cooling method which is used to obtain lower cutting temperature and higher lubrication at tool chip interface during Ti6Al4V twist drilling process. WOMS is Ester oil based minimum quantity lubrication (MQL) technique but different than neat oil or straight oil based MQL techniques due to combined application of water and oil. Drilling experiments at maximum cutting speed of 50 m/min and 167mm^3/s material removal rate (MRR), using a 8mm diameter TiAlN coated solid carbide twist drill are conducted under dry machining and WOMS cooling environment. The effect of WOMS are mainly discussed with different cutting parameters, twist drill geometry and compared with dry cutting conditions. A comprehensive evaluation on the cooling effects of WOMS was carried out by spray characterization and subsequent drilling tests. This work is focused on the combined study of tool wear evolution, drill geometry, quality of machined holes under WOMS cooling environment. Drilling under WOMS condition observed 66% higher tool life than dry cutting environment. Experimental results indicated that drilling under WOMS cooling had better cooling effects, higher tool life, optimum cutting parameters.

*Keywords:*WOMS cooling; twist drilling; Ti6Al4V; tool geometry; tool life, tool wear

* Sandip Nandgaonkar, Tel.: +91-9075013452.
 E-mail address: sd.nandgaonkar@gmail.com

1. Introduction

Titanium alloy is one of the popularly used materials in aerospace industry in view of its unique properties such as high strength-weight ratio, low density, corrosion resistance, and hot hardness. Apart from these uncommon properties, it has reputation for poor machinability due to its low thermal conductivity, modulus of elasticity and high chemical reactivity [1]. During machining of Ti6Al4V, lot of heat generation takes place and major portion of the heat is transferred to the cutting edge. High tool-work interface temperature and friction are the two major issues in machining this alloy. Low cutting speeds of the order of 30-40 m/min are generally used in machining titanium alloy due to significant reduction in tool life at slight increase in cutting speeds. Cutting tool geometry, tool coatings, cutting fluid are some of the key parameters to improve Ti machining performance. Apart from these difficulties, and due to increased awareness of environment, health and safety (EHS) guidelines, industry has been making efforts to adopt either to eliminate or reduce cutting fluid consumption globally by implementing different initiative methods like green machining, near-dry machining, minimal quantity of lubrication (MQL), Nitrogen cooling, etc.

The primary objective of supplying coolant under high pressure to the cutting zone is to reduce tool-work piece and tool-chip interface temperature which results in increased tool life. The secondary objective is to reduce friction at the tool-work interface. It is found that application of highly pressurized cutting fluid during machining for aerospace material like Ti6Al4V results into longer tool life. Cutting fluid reduces not only temperature and friction but also reduces cutting forces and welding of chips to cutting tool that are commonly found in Ti6Al4V machining [1]. Several researchers worked on the application of cutting fluids in various forms of machining. The cutting fluids could be in the form of liquid, gas, gaseous-fluid or solid. While both the purposes are important for a cutting fluid; for machining a work material with poor thermal conductivity, extraction of localized heat is much more important. Several studies have been conducted as discussed in the following sections. Several strategies have been tested for coolant applications which include identifying most relevant combination of coolant and lubricant. Various coolants used include compressed air, cold water, liquid nitrogen, carbon dioxide snow, etc., and several lubricants like straight oils and neat oils have also been characterized. Recently, the use of combination of above techniques has been undertaken, some typical combinations include high pressure cooling with neat oil, cold water mist jet, nitrogen-oil mist, compressed cold nitrogen gas-oil mist, carbon dioxide-snow, etc. These strategies have been evaluated to identify effect of cutting fluids on cutting forces, chip morphology and tool wear.

Rough turning with flood and high pressure cooling is carried out by diluting a high-lubricity emulsion coolant with 6% water concentration [2]. This improves tool life at 7MPa coolant pressure against conventional machining. Further, a high pressure cooling was carried out with use of neat oil and jet application parameters like coolant pressure, angle of impingement of jet, spot distance and nozzle diameter were analysed to study their effect on tool wear and chip morphology [3]. The observed results present further improvement in tool life which was twice as that of cryogenic cooling. However, typically broken chips were observed at such high jet momentum. Also applying coolant at flank face did not show any improvement in tool wear rate and tool damage. Cryogenic cooling includes use of safe, clean, non-toxic coolants like liquid nitrogen which is one of costliest cooling techniques. Also, it was reported that feed and depth of cut influence more on tool wear and cutting forces in the presence of cryogenic cooling [4,5]. However, such high cooling did not affect the friction coefficient in some cases, while in some cases this coefficient is increased. Recently, mist-based cooling techniques have been identified as the most effective lubrication and cooling strategy, which provide improved cutting fluid properties.

Cold water mist jet covers heat convection of three phases including cold air, droplet and even ice particles. The reports reveal that the spray characteristics like particle size and impingement velocity play an important role in enhancing lubricating and cooling properties of mist jet [6]. The work also reveals that by conducting spray characterization experiments, a significant reduction in cutting temperature was observed. At particular jet velocity, the enhanced heat transfer and lubrication are evident. Cold water mist jet has been identified as an effective eco-friendly cooling method. With identification of mist-based cooling as an important technique, several other combinations were tried including nitrogen-oil mist cooling and compressed cold nitrogen-oil mist based cooling.

N. K. Dhar [7] used vegetable oil as MQL lubricant during turning AISI 9310 alloy steel. His experimental results and observations conclude that the vegetable oil based MQL drastically improves surface finish and reduces tool wear. A detailed study has been carried by them for spray characterization, flow pressure, nozzle diameter, and droplet diameter that reduce tool wear during turning of alloy steel. Rahim and Sasahara [8] evaluated impact of palm oil and ester oil based MQL on drilling of Ti6Al4V using TiAlN coated carbide drills at cutting speed of 60m/min and federate of 0.1mm/rev. Drilling under palm oil based MQL shows lower cutting forces than flood cooling. The palm based MQL have higher viscosity than ester oil, but tool life of the drill under palm oil based MQL, ester oil based MQL and flood cooling was 314 seconds approximately in each case [8]. This shows that the flood condition can be replaced by palm oil or ester oil based MQL, but at the same time it is observed that the condition based on these coolants results into alleviating pollution. At higher cutting speeds, burning at the tool-chip interface takes place. Rodrigo and Walter [9] evaluated the generation of temperature with external MQL, internal MQL while drilling of Ti6Al4V using uncoated and coated carbide drills. The results reveal that internal MQL exhibited the lowest temperature in comparison to external MQL at 30-50m/min cutting speed.

The above literature gives a detail overview of MQL and other near dry cooling and their impact on Ti alloy machining, tool wear mechanisms, tool failure modes and impact of different cooling techniques to reduce tool wear. But no literature is available which says about simultaneous reduction of temperature and friction. In Ti6Al4V machining, small changes in cutting speed results into major change in temperature at tool chip interface due to low thermal conductivity. In such cases, it is difficult to control temperature by controlling friction. To reduce cutting temperature in Titanium machining, new dual cooling approach is introduced with the help of WOMS cooling technique. The present work is an attempt to investigate tool wear during Ti6Al4V drilling under near dry cutting technique like WOMS and validate its results with drilling under dry cutting environment. However, in WOMS cooling, spray characterization plays a vital role due to differences in viscosity of water and Ester oil.

This article highlights the effect of different drill geometry to optimize the performance of Ti6Al4V drilling. Presently, cutting edge preparation is becoming a popular method to improve tool life. Fernando and Rodrigo [10] evaluated effect of cutting edge preparation on the surface integrity after dry drilling of die steel, AISI P20. The authors observed that higher roughness values during drilling with the help of sharpened drill with cutting edge radius. The work concluded with various cutting edge preparations in the form of cutting edge radius influencing the cutting force and tool life improvement. Moises and Milton[11] studied the influence of twist drill main cutting edge preparation in drilling of SAE 4144M hardened and tempered steel with simply sharpened, 40μm rounding and 40μm×0.12 × 15º chamfered HSS twist drill. The work attempted by preparing twist drill cutting edge chamfer and rounding shows 8 times higher tool life than twist drill without edge preparation. Wyen and Wegener [12] had done extensive research on the influence of cutting edge radius from 10μm to 50μm on cutting forces in turning of Ti alloy. The results also reveal that the cutting edge radius is directly proportional to friction coefficient. Denkena and Biermann [13] had done detailed study of cutting edge preparation methods and characterization of cutting edge radius with respect to tool wear, cutting forces during machining of low alloyed steel.

The above literature gives an overview of edge preparation techniques and characterization, but there is a necessity to compare two different edge preparation techniques specifically for Ti6Al4V drilling. This work presented in this paper, shows the influence of rounded and chamfered cutting edges under dry cutting and WOMS cooling on the performance of Ti6Al4V drilling.

## 2. Experimental setup and spray characterization

2.1. Experimental details

The drilling experiments were carried on a vertical CNC machining centre (Harding VMC 600II) with 20kW of power having a maximum rotational speed of 15,000 rpm. The work piece considered is Ti6Al4V plate of size 25×150×18 mm^3 and a 8mm diameter solid carbide twist drill with TiAlN coating is used. The drill considered has different point angle and cutting edge geometry and experiments are conducted under WOMS cooling and dry cutting conditions as mentioned in Table 1. Section 2 gives the WOMS cooling and its spray characterization setup. Figure 1 (a) shows the schematic of the experimental process.

Table 1 Details of Drill Geometry

Drill type	Drill Diameter (mm)	Flute Length (mm)	Overall Length (mm)	Point angle (degree)	Chamfer radius(μm)	chamfer distance (μm) and angle (degree)
I	8	50	100	130°	Radius40μm	-
II	8	50	100	130°	-	Chamfer 20μm x15°
III	8	50	100	140°	Radius40μm	-
IV	8	50	100	140°	-	Chamfer 20μm x15°

In present work, ester oil and water combination is used for mist formation. Selection of oil mist fluid depends on performance of spray cooling in terms of reduction of friction and temperature at tool-chip interface. Pressure flow, viscosity and velocity of spray coolant are the key attributes which impact the friction and temperature. These attributes depend mainly on percentage of oil in WOMS cooling mixture. To mix exact proportion of oil in water oil fluid, a customized fixture is developed. The design of mixing chamber includes high pressure mixing of oil and water inside the chamber. Pressurized air at 0.6MPa enters the chamber causing a violent mixing of two liquids. The chamber contains a capillary at the centre. The pressurized air drives the oil-water composition to enter into the capillary. The capillary is then connected to a nozzle of small diameter. Mixing chamber specifications include filter regulator, flow control valve-air, flow control valve-oil, level gauge, mixing chamber and nozzle with delivery nylon pipe. Figure 1 (b) shows the fabricated mixing chamber with required details.
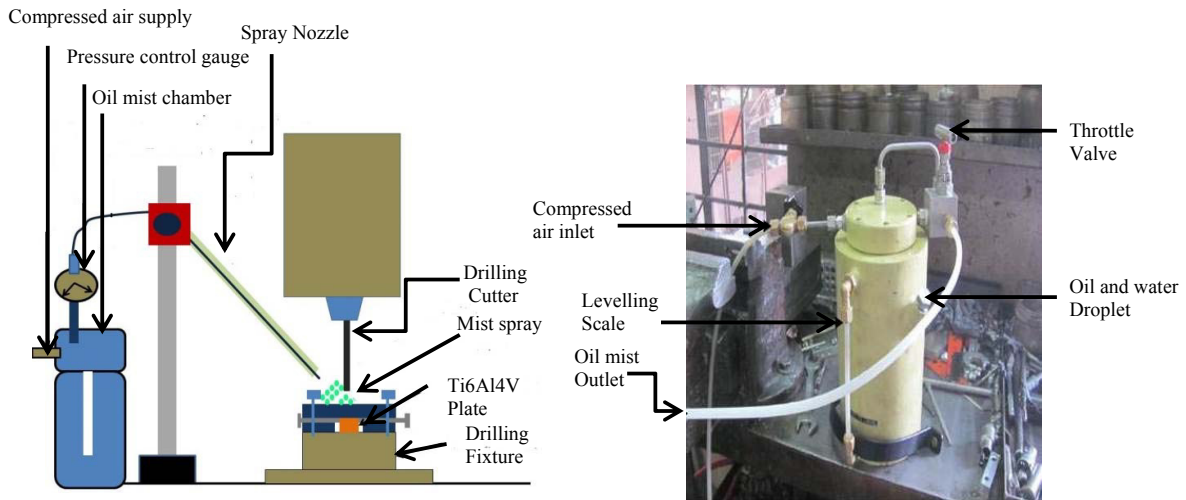
(a) Schematic of drilling with WOMS cooling (b) Fabricated mixing chamber

Fig.1Schematic of WOMS cooling system and actual details water oil mixture chamber

2.2. Droplet size measurement of oil-mist spray

Diameter of impinging droplets determine the behaviour of mist, a large droplet fails to effectively penetrate into interfacial region while a very small droplet becomes inefficient in removing heat. Characterization of droplet diameter is measured by using PDIA (particle droplet image analyzer) instrument. PDIA is basically a simple instrument in which one camera and laser are used to take images of oil mist spray. In current experiments, a laser source placed under spray and a high resolution DSLR camera (12 MP) that is used to capture images of spray. Spray samples include 20% mist and 40% mist precisely sheared and sprayed at 0.6MPa pressure. The spray region is kept in a dark space with only laser source to enhance visibility of droplets. The spray is then passed from an area covered by the laser which undergoes diffraction. This diffraction gives us volume occupied by every droplet

passing through laser and can be used to calculate diameters of droplets. It gives a normal distribution curve of droplet diameter versus number of droplet passing through nozzle. To adjust the angle, height and flow direction of nozzle, a small stand is designed as shown in Fig.2 (a). A high definition digital camera is kept perpendicular to WOMS nozzle and laser beam is adjusted in horizontal direction but parallel to WOMS nozzle and perpendicular to camera. Figure 2 (b) shows schematic of WOMS cooling stand. Images recorded are then processed in image processing toolbox of Matlab software.
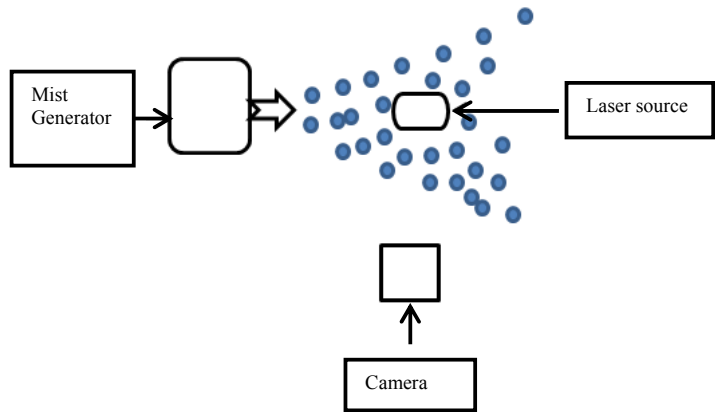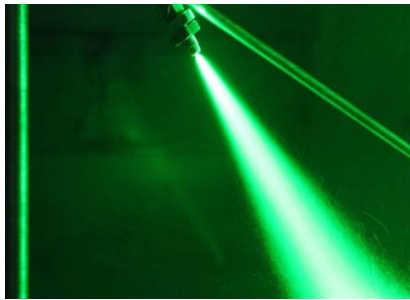
  (a)Laser image of WOMS stand   (b) Schematic of PDIA setup

Fig.2 WOMS cooling stand and PDIA set up for droplet measurement

2.3. Viscosity measurement

A Rheometer is used for measuring the viscosity of different oil mist samples. The MCR301 rheometer is equipped with tool master system for online measurement of viscosity has a maximum torque rotation of 0.2pa-s. A sample is taken into a 5ml beaker and placed under a stirrer. The sample is stirred at a constant shear rate with a frequency of 1500 per seconds. The interfacial liquid between stirrer and beaker undergoes shearing and its viscosity is calculated. The shear stress or resistance of sample against the flow is measured and subsequently shear viscosity is evaluated. A sample shearing time undertaken is 20 minutes and online recordings of shear viscosity values are studied. Viscosity results obtained by rheometer are mentioned in Table 2.

Table 2 PDIA results for droplet diameter for sample I and II

Sr.no.	Oil: water ratio	Diameter of particle of minimum diameter	Diameter of particle with maximum quantity	Viscosity
Sample I	2:3	19.24μm	20μm	0.009 pa-s
Sample II	1:4	28.53μm	25μm	0.015 pa-s

Mist samples are studied within Newtonian range with variation in shear viscosity with shear stresses almost negligible. Shear stresses increase temperature of liquid till the shear viscosity reaches a constant value within the working range. Here temperature dependence of shear viscosity is neglected. Shear viscosity of sample I is lower than sample II due to low oil concentration in the mist.

2.4. Spray Characterization results

On literature review [4, 5, 6, 7], sample I and II were found to be the most suitable oil mist spray combination for the required cooling and lubrication based on viscosity and droplet size. Minimum droplet diameter of sample I is

19.24µm and least viscosity is 0.09pa-s. Viscosity and droplet size results obtained by rheometer and PDIA respectively are mentioned in Table 2 and it shows that viscosity of sample I is lower than sample II. Sample I is selected as a final oil mist combination due to its minimum droplet diameter and lower viscosity.

3. Results and discussions

3.1. Tool life analysis

Table 3 Tool life under different cutting conditions

Exp. No.	Drill type (Point Angle Cutting Edge Geometry)	Tool life under dry cutting conditions		Tool life under oil mist cooling condition in terms of no. of holes		Max. flank wear (mm)		Increase in tool life in percentage
		No. of drilled holes	Drilling distance (mm)	No. of drilled holes	Drilling distance (mm)	Dry drilling	Oil mist cooling	
1	I	6	120	6	120	0.40	0.30	0.00
2	II	6	120	8	160	0.21	0.20	33.33
3	II	6	120	10	200	0.39	0.22	66.67
4	IV	6	120	7	140	0.32	0.30	16.67
5	II	5	100	5	100	0.36	0.28	0.00
6	IV	4	80	6	120	0.39	0.24	50.00
7	I	4	80	5	100	0.42	0.31	25.00
8	III	6	120	8	160	0.28	0.36	33.33
Total		43	860	55	1100			27.90

The work presented in this paper is focused on the evolution of tool wear during drilling of Ti6Al4V alloy. To understand the various wear patterns, experiments were conducted at dry cutting and oil mist cooling conditions as per design of experiments. In the present experimental set, to drill one complete hole 18mm depth, a minimum 20mm deep drilling need to be performed. Therefore, tool life of drilling cutter is measured in terms of number of holes or drilling length in the multiples of 20mm. The tool wear is measured with the help of a tool maker's microscope. Table 3 presents a comparative analysis of the tool life under the specified machining conditions. In the present work, 43 holes are drilled under dry cutting environment and 55 holes are drilled under WOMS cooling conditions. Overall, there is a 27% increase in tool life after completion of 8 experiments under the specified conditions. As per results mentioned in Table 3, there is very less impact of point angle on tool wear and subsequent cutting forces. The results from Table 3, it is clear that that out of 16 primary experiments, drilling with twist drill with cutting edge chamfering shows best cutting performance in the form of highest tool life. Exp. No. 1 shows that twist drilling with cutting edge rounding results into poor tool life. Table 4 and 5 shows that cutting edge rounding increases higher friction after tertiary wear zone during Exp.1.

3.2. Tool wear analysis

The flank wear measurement with tool maker's microscope is carried out after every 10 mm drilling distance until the maximum flank wear criteria is achieved. The details mentioned in Table 4 and Table 5 presents the overall variation of flank wear with cutting time, break in period (primary), steady state wear region (secondary) and failure region (tertiary) of all the drills used during dry drilling and under WOMS cooling conditions. Tool wear region is distinguished into primary, secondary and tertiary region on the basis of cutting time. In all experiments, Exp. 3 and Exp. 7 show the critical results in terms of highest tool life and poor tool life respectively. Apart from similarity in wear patterns it shows considerable variation in wear limit with respect to cutting time. Table 4 and Table 5 represents tool wear details in a phased manner where the drilling is performed at cutting speed of 40m/min and

50m/min respectively. From these tabular details, drilling results of Exp. 2 reveals least flank wear and Exp. 4 shows maximum flank wear in tertiary zone in dry drilling condition at lower cutting speed. Comparison of both experiments shows that during dry drilling, maximum point angle plays key role in minimizing flank wear. The major reason is that higher point results into higher cutting forces which result into less flank wear.

Least flank wear is observed in Exp. 3 as per results in Table 4 and Exp. 4 shows maximum flank wear in tertiary zone in oil mist cooling condition as per Table 4. Comparison of both experiments shows that cutting edge chamfering and cutting edge rounding is dominant factor in minimizing flank wear as tool with cutting edge rounding result into more friction at tool work piece interface.

Table 4 Tool wear zones during dry drilling cooling condition

Exp. No	Cooling condition	Speed (m/min)	Feed rate (mm/rev)	Drill type	Initial Wear (mm)	Intermediate wear (mm)	Final Wear (mm)
1	Dry	40	0.06	I	0.113	0.186	0.217
2	Dry	40	0.06	III	0.113	0.163	0.165
3	Dry	40	0.1	II	0.115	0.125	0.188
4	Dry	40	0.1	IV	0.156	0.16	0.238
5	Dry	50	0.06	II	0.170	0.175	0.217
6	Dry	50	0.06	IV	0.179	0.236	0.382
7	Dry	50	0.1	I	0.180	0.223	0.422
8	Dry	50	0.1	III	0.075	0.163	0.283

The details mentioned in Table 5, represent tool wear vs. cutting time for the Exp. 5-8 respectively in which drilling is performed at higher cutting speed (50m/min). Tabular results of Exp.5 shows least flank wear and Exp. 7, shows the maximum flank wear in tertiary zone in dry drilling condition. Comparison of these two experiments shows that during dry drilling at higher cutting speed, cutting edge rounding and higher feedrate plays key role in increasing flank wear. Higher cutting speed results in increasing temperature at the cutting edge due to its low thermal conductivity of Ti6Al4V. The rise in temperature, and increased contact area are due to cutting edge rounding which results into excessive friction at tool-work piece interface. This friction results into more abrasion and attrition flank wear.

The least flank wear is observed in Exp. 5 and Exp. 6 shows maximum flank wear in tertiary zone in oil mist cooling conditions. The tool wear result of Exp. 5 and Exp. 6 shows that cutting edge rounding is again a dominant factor in increasing flank wear at higher cutting speeds. Apart from cooling effect in WOMS condition, due to high speed cutting, temperature rises rapidly at lower speed. Overall the process results into more abrasion, attrition of the tool wear.

Table 5 Tool wear zones during oil mist cooling condition

Exp. No.	Cooling condition	Speed (m/min)	Feed rate (mm/rev)	Drill type	Initial Wear (mm)	Intermediate wear (mm)	Final Wear (mm)
1	oil mist	40	0.06	I	0.032	0.039	0.141
2	oil mist	40	0.06	III	0.031	0.035	0.160
3	oil mist	40	0.1	II	0.031	0.051	0.110
4	oil mist	40	0.1	IV	0.034	0.041	0.202
5	oil mist	50	0.06	II	0.041	0.051	0.108
6	oil mist	50	0.06	IV	0.062	0.062	0.243
7	oil mist	50	0.1	I	0.062	0.103	0.210
8	oil mist	50	0.1	III	0.040	0.041	0.183

3.3. Analysis of tool failure modes

Tool failure has been analyzed and differentiated into three different stages like primary wear (0-20mm drilling distance), secondary wear (21-50mm drilling distance) and tertiary wear (51-80mm drilling distance or flank wear limit or tool failure). Stereo and optical images gave microscopic analysis of tool wear. During primary wear zone, there is a uniform coating across the flank face of cutting lips and sharpness at the cutting edge. During dry drilling, microscopic inspection shows that chamfering of cutting edge started after 10 mm drilling distance and welding of chips or adhesion of work piece material started after 20 mm drilling distance. Small micro chipping also found on flank face of cutting edge. After primary wear zone or break in period, twist drill shows steady tool wear rate up to certain rate in every experiment. Micro-chipping on flank face or catastrophic failure takes place after the steady state wear zone. It increases the chamfering of cutting edge and adhesion or welding of chips.

| (a) flank wear | (b) corner wear | (c) crater and chipping |
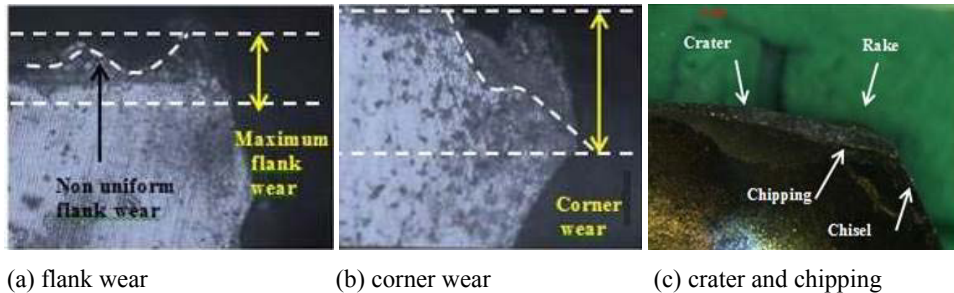
Fig.3 Major wear during dry drilling
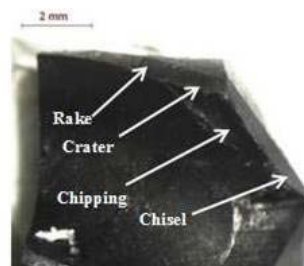
Fig.4 crater and chipping wear during drilling under WOMS cooling condition

Excessive adhesion results into weakening of cutting edge and leading to excessive flank wear and start formation of corner wear. Figure 3(a) and (b) shows excessive flank wear at one edge and corner wear on the other edge during dry drilling. In this case at 50m/min, weakening of cutting edge takes place resulting into breakage of the cutting tool. Apart from tool wear on the cutting edge, burning of chips was observed in both types of experiments under dry and WOMS cooling, but burning observations are very few during under WOMS environment. During dry conditions, extreme friction and high temperature at high cutting speeds results into burning of chips. Under oil mist cooling conditions, moderate friction and the presence of oil mist droplet at tool chip interface results into combustion of chips. Because of above reasons, in dry cutting, rake face wear are observed. Figure 3 (c) and Fig. 4 shows wear on rake face and wear on helix surface near chisel edge after drilling 4 holes in dry condition and after drilling 5 holes under WOMS cooling condition.

3.4. Conclusion and future scope

The WOMS cooling condition gives better results in terms of improvement in flank wear, increased tool life in drilling of Ti6Al4V as compared to dry drilling conditions. Uniform flank wear, micro-chipping, thermal cracking are the dominating tool failure modes for high speed drilling of Ti6Al4V alloy. However, thermal cracking has been observed to be severe under dry cutting conditions. In dry conditions, it is also observed that adhesion, abrasion, attrition and diffusion are dominant wear mechanisms, while in case of oil mist cooling conditions, the major wear mechanisms are adhesion and abrasion. Twist drill with cutting edge chamfering shows better performance in term of tool life.

This work is based on experimental results and mist spray characterization only and there is wide scope to validate above results by modelling and simulation of drilling process with FEM software tools with mathematical modelling techniques available. This work presents tool wear results of drilling under WOMS cooling conditions with ester oil based MQL in comparison with dry drilling, but there is a wide scope to use different oil combinations like palm oil, coconut oil, etc., to reduce friction and maintain minimum optimum temperature at tool-chip interface.

Acknowledgements

References

[1] E.O.Ezugwa, Z.M.Wang, Titanium alloy and their machinability-a review, Journal of Materials Processing Technology, 68 (1997) 262-274.
[2] Sharma V.S., Dogra M., Suri N.M., Cooling techniques for improved productivity in turning, International Journal of Machine Tools & Manufacture, 49 (2009) 435–453.
[3] Nambi Muthukrishnan, Paulo Davim, Influence of Coolant in Machinability of Titanium Alloy, Journal of Surface Engineered Materials and Advanced Technology, 2011, 1, 9-14.
[4] Hong S.Y., Ding Y, Cooling approaches and cutting temperatures in cryogenic machining of Ti-6Al-4V, International Journal of Machine Tools & Manufacture, 41 (2001) 2245–2260.
[5] Birmingham M.J., Kirsch J., Sun S., Palanisamy S., Dargusch M.S., New observations on tool life, cutting forces and chip morphology in cryogenic machining Ti-6Al-4V, Materials Science Forum, Vols. 654-656, 2010, pp. 2531-2534.
[6] Rukosuyev M., Goo C.S., Martin B.G. Jun, Understanding the effects of the system parameters of an ultrasonic cutting fluid application system for micro-machining, Journal of Manufacturing Processes 12 (2010) 92–98.
[7] M.M.A. Khan, M.A.H. Mithu, N.R. Dhar, Effects of minimum quantity lubrication on turning AISI 9310 alloy steel using vegetable oil based cutting fluid, Journal of Materials Processing Technology 209 (2009) 5573–5583,2009.
[8] E.A. Rahim, H.Sasahara, A study of the effect of palm oil as MQL lubricant on high speed drilling of titanium alloys, Tribology International 44 (2011) 309–317.
[9] Rodrigo Panosso Zeilmann, Walter Lindolfo Weingaertner, Analysis of temperature during drilling of Ti6Al4V With minimal quantity of lubricant, Journal of Materials Processing Technology 179 (2006) 124–127.
[10] Moreira Bordina, Rodrigo Panosso Zeilmanna, Effect of the cutting edge preparation on the surface integrity after dry drilling, Procedia CIRP 13 (2014) 103 – 107.
[11] Moises Izaias de Santanaa, Milton Luiz Pollib, The Influence of Twist Drill Main Cutting Edge Preparation in Drilling Process, Materials Research. Sup 2, 18 (2015), 148-153.
[12] C.F. Wyen, K. Wegener, Influence of cutting edge radius on cutting forces in machining titanium, CIRP Annals - Manufacturing Technology, 59 (2010) 93–96.
[13] B.Denkena, D.Biermann, Cutting edge geometries, 2014, CIRP Annals - Manufacturing Technology, 63 (2014) 631–653.

16th Machining Innovations Conference for Aerospace Industry – MIC 2016

Virtual Machining: Capabilities and Challenges of Process Simulations in the Aerospace Industry

P. Wiederkehr[a], T. Siebrecht[a,*]

[a]*Institute of Machining Technology, TU Dortmund University, Baroper Str. 303, 44227 Dortmund, Germany*

* Corresponding author. Tel.: +49-231-755-5819; fax: +49-231-755-5141. *E-mail address:* siebrecht@isf.de

Abstract

Milling processes for the manufacturing of parts for aerospace applications can be influenced by various effects. When machining structural parts with high material removal rates, the stiffness of the machine tool can be a limiting factor because chatter vibrations. Additionally, vibrations of thin-walled structures, e. g., the blades of impellers or turbines, can lead to chatter vibrations and surface location errors. Thermo-mechanical deformations are another cause for violations of given shape tolerances. Geometric physically-based process simulations can be used to analyze milling processes with regard to these effects in order to optimize the process parameters. In this paper, an overview of several applications of a geometric physically-based simulation system for analyzing different effects during milling processes is presented. Depending on the relevant effects, process forces, the dynamic behaviour of the tool-spindle-machine system, vibrations of workpieces and fixture systems, as well as thermo-mechanical deformations are calculated.

Keywords: Milling, Geometric modeling, Surface

1. Introduction

In many industrial sectors and especially the aerospace industry, increasingly complex parts have to be manufactured efficiently, while achieving the required surface qualities and reducing the production costs. Milling processes are used to manufacture various components, e. g., impellers or structural parts [1]. Numerous different problems can arise during these machining operations. During the milling of structural parts, process configurations with high material removal rates can lead to chatter vibrations due to the limited stiffness of the milling tools or components of the machine [2]. When manufacturing parts with thin-walled structures, e. g., impeller or turbine blades, the reduced stiffness of these workpiece can cause similar problems. In addition to the process dynamics, the quality of the produced parts can be reduced because of thermo-mechanical effects.

Due to the high complexity of the various effects possibly influencing the result of a milling process and their interactions, the optimization of the processes is a non-trivial task. In many cases, time-consuming and costly run-in processes are required. Geometric physically-based simulation systems [3] provide a flexible and efficient method for analyzing and optimizing milling processes based on a calculation of the geometric engagement situation between the milling tools and the workpieces. At the Institute of Machining Technology (ISF), a geometric physically-based process simulation software is being developed. In this paper, several different applications of this simulation system for analyzing and optimizing different milling processes in order to solve problems which are relevant for the aerospace industry, e. g., workpiece vibrations [4], are presented. While the details of the applications are described in the referenced literature, this paper should give an overview of the recent possibilities of the simulation system for the aerospace industry.

First of all, an overview of the basic modeling approach of the simulation system is given in Section 2. In Section 3, chatter vibrations resulting, e. g., from the dynamic behavior of the machine tool, are analyzed. For simulating the machining of thin-walled impeller blades, the modeling of workpiece vibrations is described in Section 4. The simulation of workpiece deflections resulting from the usage of advanced fixture systems is presented Section 5. The influence of thermo-mechanical deformations on the process result can be analyzed using a hybrid simulation approach as well, which is shown in Section 6. In Section 7, a short conclusion and an outlook on future extensions of the simulation system is given.
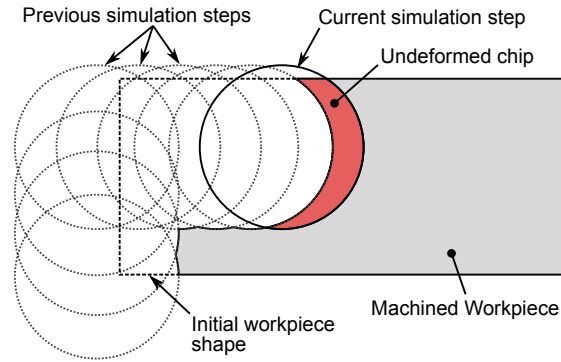
Figure 1: CSG based model of the workpiece shape (cf. [7]).

2. Simulation of machining processes

While several approaches for modeling and simulating machining processes, e. g. analytical approaches [5], exist, a geometric physically-based simulation system provides flexible methods for analyzing milling processes. For this purpose, the milling tools and the workpiece shape have to be modeled. This can be achieved by using the Constructive Solid Geometry (CSG) modeling technique [6] to represent the ideal shape of the rotating tools. In many cases, these shapes comprise simple geometric primitives, e. g., cylinders, spheres, or tori, which are combined using union, difference, and intersection operators. The same modeling technique can be used to represent the shape of the workpieces, which changes during the simulated material removal. This is done by subtracting the CSG model of the rotating milling tools from the initial stock shape, e. g., a simple box or a more complex shape modeled as a triangle mesh, at discrete simulation steps, as shown in Figure 1. Each simulation step corresponds to one feed per tooth. The movement of the tools in relation to the workiece is calculated by interpreting NC programs based on the kinematics of the simulated machine tool. An advantage of this approach is the possibility to optimize the NC programs directly using the simulation results and to run the optimized programs on a real machining center without further conversions.

In order to use the simulation system for more advanced analyses than the calculation of the geometric material removal, additional models, e. g., for the prediction of process forces or the dynamic behavior of the tools, can be integrated. The calculation of process forces is based on a non-linear empirical force model [8] using the undeformed chip thickness h:

$$f_c = bk_c h_0 (\frac{h}{h_0})^{1-m_c}, f_n = bk_n h_0 (\frac{h}{h_0})^{1-m_n}, f_t = bk_t h_0 (\frac{h}{h_0})^{1-m_t},$$

where b is the width of cut, $h_0 = 1$ mm, and k_c, m_c, k_n, m_c, k_t, m_t are the force model coefficients for calculating the cutting forces f_c, f_n, and f_t in cutting, normal, and tangential direction, respectively. f_n is facing away from spindle axis in radial direction and f_t is perpendicular to f_c and f_n. For obtaining the undeformed chip thickness h, the undeformed chip shape has to be analyzed, which corresponds to the intersection between the workpiece and the CSG model of the tool in the current simulation step. The thickness of this intersection can be analyzed by casting and intersecting rays.

The parameter values of the process force model have to be specified for different workpiece materials and milling tools. Therefore, calibration experiments are required to obtain these values. By measuring the process forces during the calibration experiments and comparing them to forces calculated by simulating the same milling process, the parameter values of the force model can be optimized until the measured and simulated process forces match as closely as possible [9]. Usually, simple slot or flank milling operations are sufficient, but it should be ensured that there are no process vibrations.

In combination with this force model, the described CSG-based model of the tools and the workpieces provides a fast and accurate way for calculating process forces. However, a visualization of the resulting workpiece shape and surface location errors, which could be required to optimize the machining operation, is difficult due to the implicit nature of the modeling technique. Therefore, a multi-scale modeling approach is implemented by extending the CSG model with an additional multi-dexel model [10] of the workpiece shape. The multi-dexel model is cut in addition to the CSG model in each simulation step. By explicitly storing local surface location errors at each dexel, an efficient visualization of the workpiece is possible by coloring the endpoints of the dexels accordingly [11]. The calculation of process forces is still based on the CSG model only.

3. Analysis of process stability

In order to optimize milling processes with respect to vibrations, the dynamic behavior of the tool-spindle-machine-system has to be modeled as well. The dynamic compliance of a tool can be described by frequency response functions (FRFs), which can
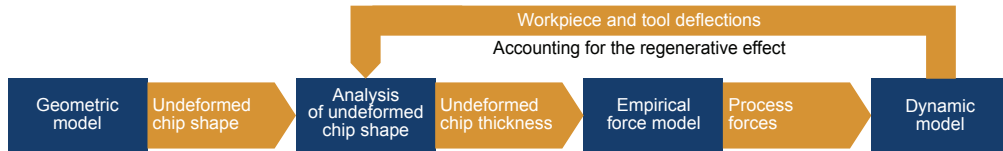
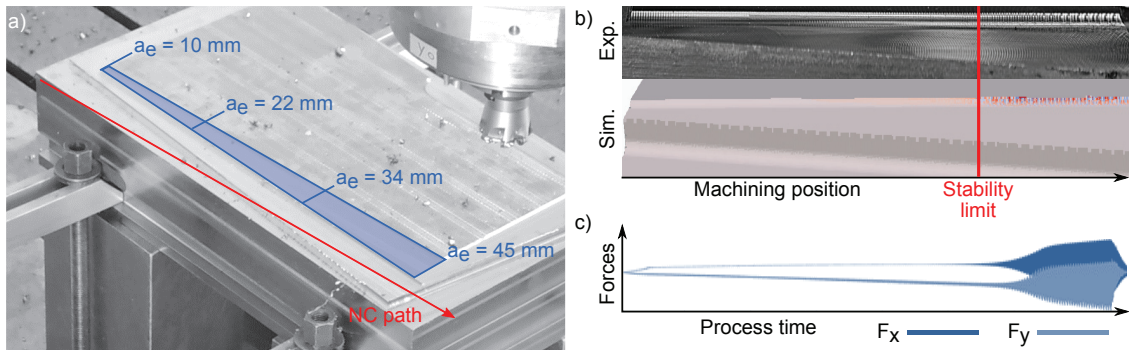Figure 2: Schematic overview of the simulation system (cf. [7]).

Figure 3: Comparison of simulated and experimental surface location errors resulting from machine tool vibrations (cf. [17]).

be measured using impact hammer tests or electro-magnetic shakers [12]. These frequency response functions are represented using uncoupled models of damped harmonic oscillators, which are described by their eigenfrequency, modal mass, and damping coefficient. Each oscillator corresponds to one eigenmode. During the simulation of a milling process, the calculated process forces are used as excitation of the oscillators in each simulation step. The deflection of the tool is calculated as the superposition of the resulting deflections of the oscillator models. In order to account for different dynamic compliances in x-, y- and z-direction, every direction is modeled separately. By taking the deflections of the tool into account when calculating the undeformed chip thicknesses using the CSG model, the regenerative effect is modeled and, thus, chatter vibrations can be predicted. A schematic overview of the steps required for simulating the process dynamics is shown in Figure 2.

The deflections of the tool are simulated as displacements of their respective models. The influence of the tool holder, the spindle, or components of the machine tool itself are not modeled explicitly. However, by measuring the dynamic compliance of the tools in the spindle, the resulting frequency response functions are influenced by all relevant components. When machining large structural parts using comparatively stiff tools, chatter vibrations can be caused by the compliance of the structure of the machine tool. In contrast to the tools, the dynamic behavior changes when the axes of the machine move [13,14]. In order to take this account in the simulation, the FRFs of the tool are measured in different poses, where the kinematic configurations of the machine are different [15].

An examplary milling process showing chatter vibrations caused by the compliance of components of the machine is shown in Figure 3. Using a medium-scale machining center, a workpiece (1.2312 steel) was machined with a toroidal cutter with seven cutting edges, a diameter of $d = 52$ mm, and a corner radius of $c_r = 5$ mm. The spindle speed and feed velocity were $a_p = $ mm, $n = 1225$ min^{-1}, and $v_f = 1715$ mm min^{-1} respectively. The radial depth of cut a_e was increased from 10 mm to 45 mm throughout the process using an upmilling strategy. To parameterize the simulation system, the dynamic compliance of the tool was measured in a different pose at the same positions as used during the milling process. The resulting FRFs, which comprise the dynamic behavior of the tool, the spindle, and the machine, were used to define the oscillator-based model of the system. The parameter values of the oscillators can be found using evolutionary optimization methods for fitting the FRF of the oscillator model to the measured FRF [16]. A comparison of the surface of the machined workpiece and the surface location errors resulting from the process simulation is shown in Figure 3b. Figure 3c shows the simulated process forces. At about two thirds of the process, chatter marks are clearly visible in the experiment and the simulation. At this point of time, the process forces become significantly higher and unstable. Concluding from the agreement of the simulation results with the experiments, the presented simulation system is capable of predicting the stability of milling processes, which can by limited by the dynamic compliance of the machine tool, and resulting surface location errors.

The optimization of machining processes is a major application of the presented simulation system. Figure 4 shows a pocket workpiece with multiple steps, where chatter marks are present in the corners, resulting from an increased engagement angle and higher cutting forces. Corresponding to the visible chatter marks, the process simulation predicts high surface location errors in the corners as well, so the unstable process section could be identified. In order to optimize the process, different process parameter values, e. g., for spindle speed or depth of cut, can be chosen. However, conducting experiments for evaluating different process parameter values is time consuming and expensive. Therefore, simulations can be used to improve the parameter values. In the presented example, the axial depth of cut was decreased from 4.5 mm to 1.125 mm, leading to stable process conditions even in the corners. Applying the optimized parameters to the process, no chatter marks are visible anymore.
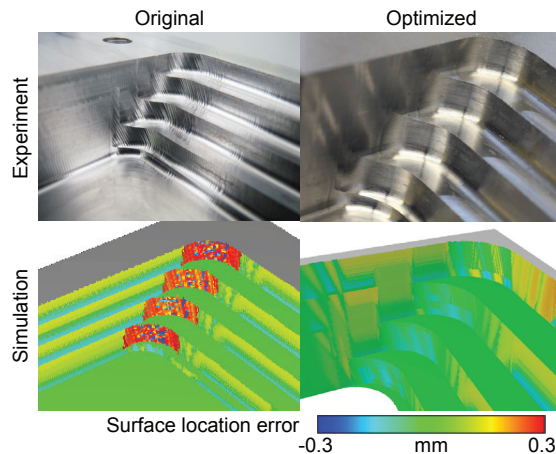
Figure 4: Simulation-based optimization of the milling of a pocket, where chatter marks are present in the corners (cf. [3,18]).

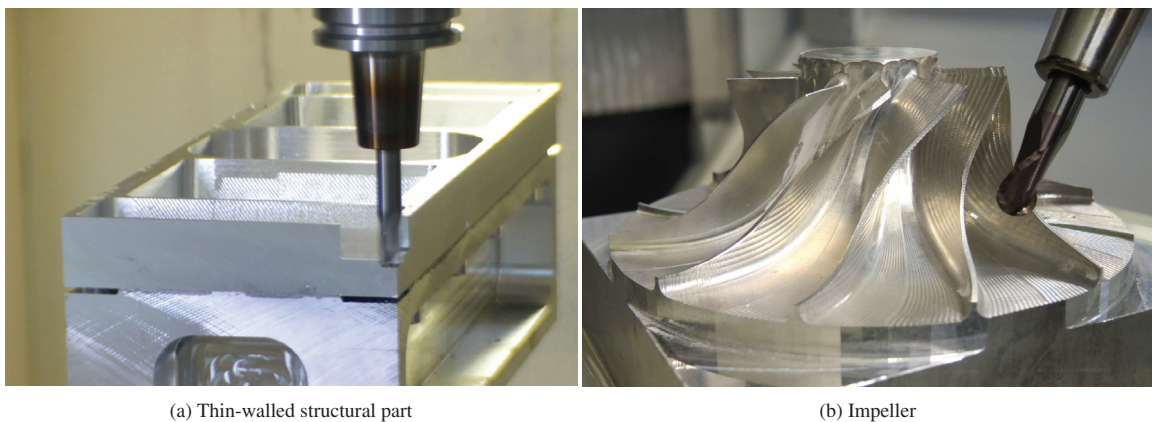(a) Thin-walled structural part   (b) Impeller

Figure 5: Machining thin-walled aerospace parts.

In addition to the pose of the tool and the resulting kinematic configurations, the dynamic behavior of the machine is influenced by other effects, e. g., temperatures, as well. By measuring the FRFs of the tools in the spindle at different temperatures of the machine and modeling these FRFs with independent oscillator models, this influence can be taken into account during milling simulations [19].

4. Simulation of workpiece vibrations

When manufacturing different kinds of weight-optimized parts for the aerospace industry, workpieces with thin-walled structures have to be machined [1]. Figure 5 shows an exemplary structural part and an impeller. Due to the high susceptibility to vibrations of these parts, workpiece deflections can become relevant in addition to the vibrations of the tools or the machine tool. In contrast to the behavior of the tools, the dynamic compliance of the workpieces varies locally according to the mode shapes [1,20]. Therefore, it is not sufficient to measure and model the dynamic compliance at a single location of the workpiece surface [21]. An interpolation of the dynamic behavior between multiple discrete measurement points is possible using triangle meshes [22]. The measurements at these points can be conducted by exciting the workpiece at a fixed location with an impulse hammer while measuring the deflections at multiple different locations with a laser triangulation sensor. Using this information, the frequency response functions at each measurement point as well as any transfer function between the measurement points can be calculated, so the local dynamic behavior can be simulated at each of these points [23]. However, most of the time, the tool center point (TCP) is not located directly at one the measurement points. By connecting the measurement points with a triangle mesh, the three vertices of one of the triangles can be used to interpolate the local dynamic behavior for any tool pose. This triangle is chosen by finding the nearest neighbor to the centroid of the undeformed chip shape on the triangle mesh. The barycentric coordinates of this nearest neighbor can be used as weighting factors for interpolating the deflections at the three vertices of the triangle.
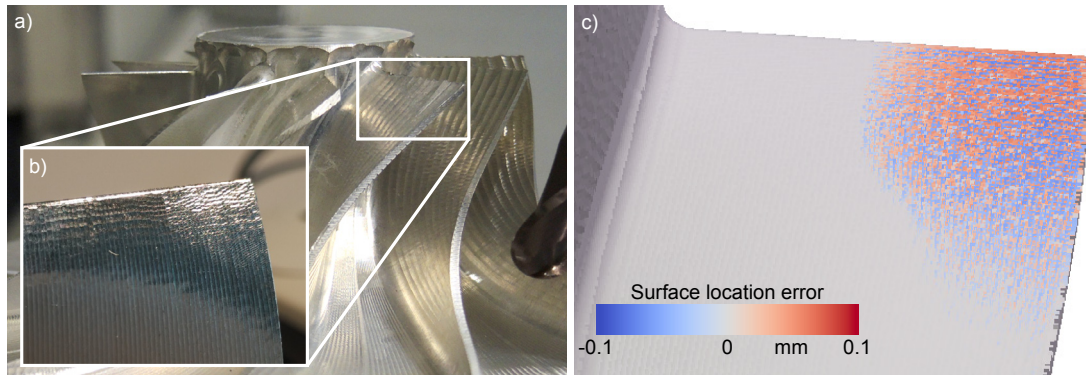
Figure 6: Comparison of chatter marks (b) on the tip of an impeller blade (a) to simulated surface location errors (c).

An application of the described model of workpiece vibrations for optimizing the milling of the impeller shown in Figure 5b is presented in Figure 6. During the finishing operation, the thickness of the blades is rather low already, resulting in chatter marks at the tip (Figure 6b). For this operation, a ball-end cutter with a diameter of $d = 4$ mm and two cutting edges was used with a spindle speed of $n = 22\,000$ min^{-1} and a feed velocity of $v_f = 2200$ mm min^{-1}. The behavior of the workpiece material (aluminium EN AW 7050) was modeled by using the cutting force coefficients $k_c = 611$ N/mm^2, $k_n = 123$ N/mm^2, $k_t = 0$ N/mm^2, $m_c = 0.21$, $m_n = 0.442$, and $m_t = 0$. The dynamic behavior of the blade was measured at nine different positions with impulse hammer tests after conducting the roughing operation. The parameter values of the oscillator-based model of the process dynamics were estimated as approximately 4.0 kHz, 7.7 kHz, 9.4 kHz, and 11.4 kHz. While the eigenfrequency are equal at all measurement points, the masses and damping coefficients vary according to the mode shapes The surface location errors were calculated using the simulation system and the result is shown in Figure 6c. In the simulation result, chatter marks with a surface location error of approximately 0.06 mm are clearly visible at the tip of the blade as well. Regarding the location and size of the chatter marks, a high correspondence with the experimental results can be observed, so the simulation system was applicable for this case, using the described method for interpolating the dynamic workpiece behavior.

5. Clamping of thin-walled workpieces

The described method for modeling vibrations of workpieces as presented in Section 4 can also be used to simulate the influence of clamping devices on the machining process. As with thin-walled workpieces, the dynamic compliance of the clamping devices varies at different positions according to the mode shapes. Additionally, the mass of the clamped workpiece is reduced due to machining, so the behavior of the fixture can be expected to change as well. To take this into account, the same interpolation approach which was already presented for modeling workpiece vibrations, can be used in the simulation. It was shown in Section 3 that information about the behavior of individual components of the machine tool is not required for modeling their influence on the milling process if the dynamic compliance of the milling tool was measured in the machine. This simplification can be applied to workpieces in complex clamping devices as well because only the deflections of the workpiece at the engagement position are influencing the process forces and, thus, the chatter vibrations.

Figure 7 shows an advanced clamping device for reducing workpiece distortions after the machining of medium-scale structural parts for the aerospace industry, which was designed by the Institute of Manufacturing Technology and Quality Management (IFQ) in Magdeburg [24]. If these kind of workpieces are clamped directly to the machine table, internal stresses in the material resulting from the production process are released during the machining process. By holding the workpiece in place while milling, deformations are restricted and a relaxation is prevented. However, as soon as the finished part is removed, significant distortions, e. g., bending along the longest side, can occur. The presented clamping system comprises floating, hydraulically actuated clamps which can be released to allow the workpiece to move freely in one direction. In order to reduce the final distortions of the workpiece, the machining is paused after removing a small amount of material. Then the floating degree of freedom of the hydraulic clamps is released, allowing the workpiece to relax. In the relaxed state, the clamps are fixed again and the milling process is continued. Using this approach, only the distortions occurring after the last reclamping step should be present when releasing the part from the fixture.

While there are some positive side effects when using the presented fixture, e. g., reduced setup times and the ability to machine both sides of the part without a second clamping, the application of the hydraulic clamps can be expected to result in a higher susceptibility to workpiece vibrations in comparison to a classical setup. Using process simulations, the influence of these fixture systems can already be taken into account during the design of the device. Classically, Finite Element simulations are used to analyze the Eigenfrequencies of different designs, but no direct statements regarding the machining process are possible. By modeling the dynamic behavior based on the Finite Element model, process forces and deflections using different designs can be predicted in the design phase. For the presented setup, process simulations were conducted as shown in Figure 8. A milling tool with two cutting edges, a diameter of $d = 12$ mm, a corner radius of $c_r = 1.5$ mm, and a helical angle of $30°$ was used. The cutting force
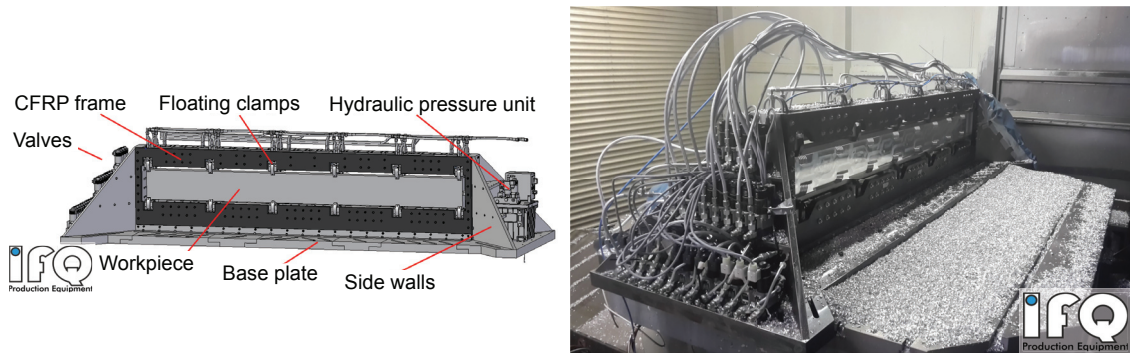
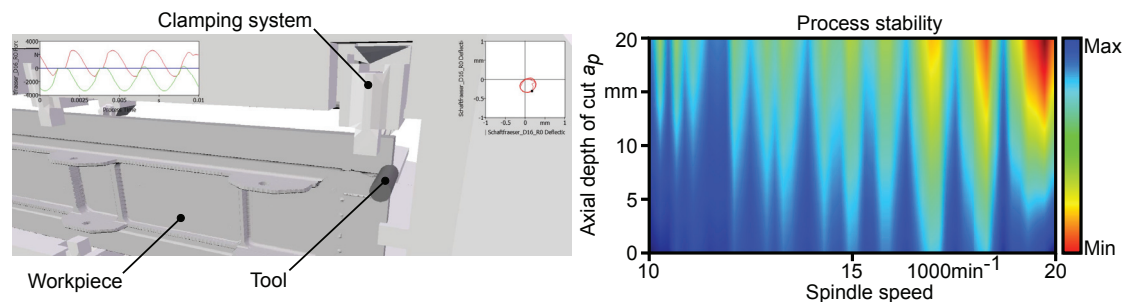Figure 7: Hydraulic clamping system for reducing part distortions (IFQ, Magdeburg).

Figure 8: Simulation of the process stability using the hydraulic clamping system shown in Figure 7.

coefficients were $k_c = 1450\,\mathrm{N/mm^2}$, $k_n = 600\,\mathrm{N/mm^2}$, $k_t = 0\,\mathrm{N/mm^2}$, $m_c = 0.2$, $m_n = 0.35$, and $m_t = 0$. In order to find suitable process parameter values, stability charts can be calculated. The depicted results show that stable process conditions can be achieved with an axial depth of cut of 20 mm. The calculation of the process stability corresponds to the diameter of the poincare section of the history of deflections of the tool.

6. Thermo-mechanical deformations

Beside process dynamics leading to chatter vibrations, thermo-mechanical effects can cause deviations of the machined workpiece from the required shape. During the milling process, the workpiece is heated by the thermal energy resulting from the cutting process. Due to the increasing workpiece temperature, deformations can occur. These deformations are influenced by several parameters of the process setup. The amount of thermal energy, which flows into the workpiece for each tooth engagement, varies with the parameter values of the milling process, e. g., the cutting and feed velocity. The milling strategy and the clamping situation influence the heat distribution in the workpiece as well. Therefore, these parameters can be optimized in order to reduce the final surface location errors and shape deviations.

For this optimization, a hybrid simulation system comprising the geometric physically-based approach and a thermo-mechanical model [25,26] is used. Two thermo-mechanical models have been integrated, which can be selected depending on the desired optimization criterion. If only the temperature distribution has to be known, a finite-difference model can be used, where the workpiece is discretized as a hexahedron mesh, which changes due to material removal by the machining process [25]. In each simulation step, a heat-source is defined at the tool engagement. The amount of heat input by this heat-source is calculated based on the process forces.

Dissipation of thermal energy into the clamps and the surrounding air is simulated by defining boundary zones using an adaptive environment temperature. An examplary application of the finite-difference model of the heat distribution in a structural part during a milling simulation is shown in Figure 9.

The described workpiece models, i. e., the CSG model, multi-dexel boards, and the finite difference model, share the limitation that deformations and their influence on the undeformed chip shapes and, thus, the process forces cannot be modeled easily. Therefore, another model based on an hp-adaptive finite-element model with a high-order fictitious domain approach [27], developed at the University of Salzburg, is used [28]. In this case, the workpiece is discretized with a hierarchical mesh of hexahedrons, tetrahedrons, prisms, and pyramids, which is adapativly changed for modeling the material removal process [28].

An exemplary application of the Finite Element model of the thermo-mechanical deformations is shown in Figure 10. In this case, a simple pocket with a reference surface (cf. Figure 10a) was machined and, thus, heated by the process, resulting in
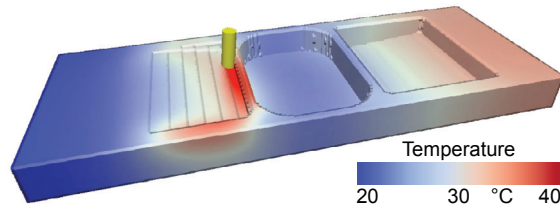
Figure 9: Finite difference model of the heat distribution in a structural part during a milling simulation.

(a) Experiment

(b) Simulation
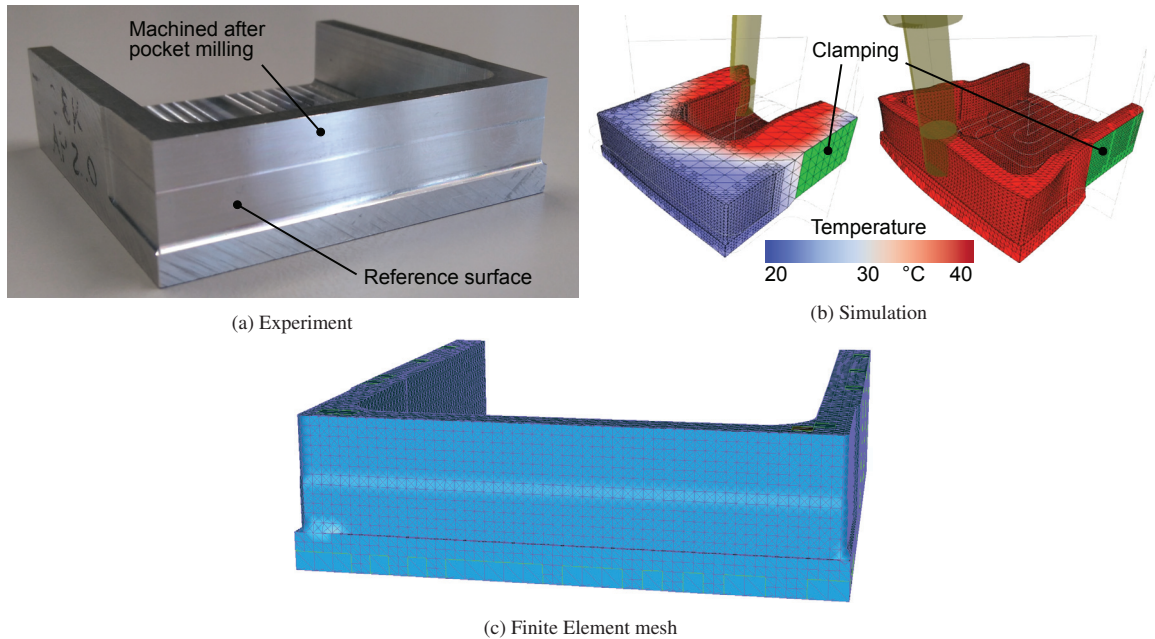

(c) Finite Element mesh

Figure 10: Machined workpiece with shape deviations resulting from thermal deformations (a), the corresponding finite-element-based simulation (b), and the resulting FE mesh (c). The visualization of the displacements is exaggerated.

thermo-mechanical deformations. The size of the initial stock was 70 mm × 70 mm × 20 mm and the workiece material was aluminium EN AW 7075. In the heated state, the reference surface was machined again with a reduced axial depth of cut in order create a step which can be measured to validate the simulated deformations. If no deformations were present, there should be no step between these surfaces. However, the radial depth of cut is increased due to the deformations and a step of 0.15 mm can be measured. The simulation of this milling process is shown in Figure 10b. In the visualization, the deformations of the workpiece are exaggerated to emphasize the effect. The final Finite Element mesh after running the milling simulation is shown in Figure 10c. The step that was measured in the experiments is present as well.

7. Conclusions and outlook

In this paper, a geometric physically-based simulation system, which is being developed at the Institute of Machining Technology, was presented. It could be shown that this system can be applied to analyze and optimize milling processes of the aerospace industry, where the resulting quality of the workpiece is influenced by different process effects. The analyzed problems range from process stabilities resulting from machine tool components, vibrations of thin-walled workpieces to thermo-mechanical deformations.

The range of possibly relevant process effects is not limited to the presented problems. In future research, effects like process damping and tool wear will be integrated into the simulation system.

References

[1] Denkena, B., Schmidt, C.. Experimental investigation and simulation of machining thin-walled workpieces. Production Engineering 2007;1(4):343–350.

[2] Altintas, Y., Weck, M.. Chatter stability of metal cutting and grinding. CIRP Annals-Manufacturing Technology 2004;53(2):619–642.

[3] Altintas, Y., Kersting, P., Biermann, D., Budak, E., Denkena, B., Lazoglu, I.. Virtual process systems for part machining operations. CIRP Annals – Manufacturing Technology 2014;63(2):585–605.

[4] Coffignal, G., Lorong, P., Planchat, J., Yaqub, S., Larue, A.. Virtual Machining: a General Approach to Deal with Flexible Workpieces. In: 10th CIRP International Workshop on Modeling of Machining Operations. Italy; 2007,.

[5] Altintaş, Y., Budak, E.. Analytical prediction of stability lobes in milling. CIRP Annals-Manufacturing Technology 1995;44(1):357–362.

[6] Foley, J., Feiner, S., Hughes, J.. Introduction to computer graphics. Addison-Wesley, Reading, Mass; 1994.

[7] Siebrecht, T., Kersting, P., Biermann, D., Odendahl, S., Bergmann, J.. Modeling of surface location errors in a multi-scale milling simulation system using a tool model based on triangle meshes. vol. 37. 2015, p. 188 – 192.

[8] Kienzle, O.. Die Bestimmung von Kräften und Leistungen an spanenden Werkzeugen und Werkzeugmaschinen. VDI-Z 1952;94(11):299–305.

[9] Hense, R., Surmann, T., Biermann, D.. Korrektur gemessener Zerspankräfte beim Fräsen. wt Werkstatttechnik online 2012;102:789–794.

[10] Muller, H., Surmann, T., Stautner, M., Albersmann, F., Weinert, K.. Online sculpting and visualization of multi-dexel volumes. In: Proceedings of the eighth ACM symposium on solid modeling and applications. ACM; 2003, p. 258–261.

[11] Odendahl, S., Kersting, P.. Higher efficiency modeling of surface location errors by using a multi-scale milling simulation. Procedia CIRP 2013;9:18–22.

[12] Schmitz, T.L., Smith, K.S.. Machining dynamics: frequency response to improved productivity. Springer Science & Business Media; 2008.

[13] Brecher, C., Altstädter, H., Daniels, M.. Axis position dependent dynamics of multi-axis milling machines. Procedia CIRP 2015;31:508–514.

[14] Law, M., Ihlenfeldt, S., Wabner, M., Altintas, Y., Neugebauer, R.. Position-dependent dynamics and stability of serial-parallel kinematic machines. CIRP Annals-Manufacturing Technology 2013;62(1):375–378.

[15] Baumann, J., Siebrecht, T., Wiederkehr, P.. Modelling the dynamic behavior of a machine tool considering the toolposition-dependent change of modal parameters in a geometric-kinematic simulation system. Procedia CIRP 2016;In press.

[16] Biermann, D., Surmann, T., Kehl, G.. Oszillatormodell für Werkzeugmaschinen zur Simulation von Zerspanprozessen. Entkopplung von Schwingungsmoden zur effizienten Berechnung der Prozessstabilität von Fertigungssystemen bei Einwirkung von Prozesskräften wt Werkstatttechnik online 2008;3:185–190.

[17] Wiederkehr, P., Baumann, J., Finkeldey, F., Freiburg, D., Hense, R., Hess, S., et al. Einsatzmöglichkeiten von Prozesssimulationen in der spanenden Fertigung. In: "KMU 4.0" Intelligente Fertigungstechnologie fr kleine und mittelstndische Unternehmen, Fertigungstechnisches Kolloquium Magdeburg. Magdeburg, Germany; 2016,.

[18] Kersting, P., Odendahl, S.. Capabilities of a process simulation for the analysis of five-axis milling processes in the aerospace industry. In: Proceedings of the 18th International Seminar on High Technology. Piracicaba, Brazil; 2013, p. 26–47.

[19] Baumann, J., Hense, R., Wiederkehr, P.. Prozessdynamik und Maschinentemperatur. Werkstatttechnik Online 2016;In press.

[20] Biermann, D., Kersting, P., Surmann, T.. A general approach to simulating workpiece vibrations during five-axis milling of turbine blades. CIRP Annals-Manufacturing Technology 2010;59(1):125–128.

[21] Kersting, P., Biermann, D.. Modeling techniques for simulating workpiece deflections in nc milling. CIRP Journal of Manufacturing Science and Technology 2014;7(1):48–54.

[22] Siebrecht, T., Odendahl, S., Hense, R., Kersting, P.. Interpolation method for the oscillator-based modeling of workpiece vibrations. In: Proceedings of the 3rd International Conference on Virtual Machining Process Technology. Calgary, Canada; 2014,.

[23] Kersting, P., Biermann, D.. Modeling workpiece dynamics using sets of decoupled oscillator models. Machining Science and Technology 2012;16(4):564–579.

[24] Leopold, M., Hense, R., Mhring, H.C., Kersting, P.. Intelligente Werkstückspannsysteme für die verzugsfreie Fertigung dünnwandiger Aluminiumbauteile. In: 12. Magdeburger Maschinenbau-Tage. 2015,.

[25] Schweinoch, M., Joliet, R., Kersting, P., Zabel, A.. Heat input modeling and calibration in dry nc-milling processes. Production Engineering 2015;9(4):495–504.

[26] Schweinoch, M., Joliet, R., Kersting, P.. Predicting thermal loading in nc milling processes. Production Engineering 2015;9(2):179–186.

[27] Schröder, A.. Constraints coefficients in hp-FEM. Springer; 2008.

[28] Joliet, R., Byfut, A., Surmann, T., Schröder, A.. Incremental generation of hierarchical meshes for the thermomechanical simulation of nc-milling processes. Procedia CIRP 2013;12:25–30.

ELSEVIER

CrossMark

16th Machining Innovations Conference for Aerospace Industry - MIC 2016

A New Approach For A Flexible Powder Production For Additive Manufacturing

S. Dietrich*, M. Wunderer, A. Huissel, M. F. Zaeh

"Technical University of Munich, Institute for Machine Tools and Industrial Management, Boltzmannstr. 15, D-85748 Garching, Germany"

Abstract

The technology of Additive Manufacturing (AM) is an enabler for more eco-friendly lightweight aircraft parts due to the possibility to use the freedom of design. Since the process of laser beam melting is powder bed based, there is a huge influence of the powder quality on the building process. The most common process for the AM powder production is the inert gas atomization based on molten material. There are different process types which are mainly used for a large scale powder production. In order to analyze new or expensive alloys for the AM process, small and flexible atomization plants to produce smaller amounts of powder are needed.

This work summarizes the required powder properties for aluminum alloys as well as the different suitable atomization processes. Current challenges concerning AM powder quality will be described and a new atomization plant concept for high-grade powder in small quantities, based on the process of thermal spraying, will be introduced.

Nomenclature

AM   additive manufacturing
SEM   scanning electron microscope

---

* Corresponding author. Tel.: +49 821 568 83 122; fax: +49 821 568 83 50.
  E-mail address: simone.dietrich@iwb.mw.tum.de

1. Introduction

The transport volume in aviation is forecast to increase by 45 % between 2014 and 2035 [1]. In order to reduce the greenhouse gas emission, the efficiency of airplanes has to be increased. One option is to reduce the mass by lightweight constructions. This offers the possibility to carry more load with the same CO_2 emission or the same load with a lower CO_2 emission. Another possibility, besides the use of composite materials, is the implementation of topology optimized structural components. These complex geometries are more frequently produced by additive manufacturing (AM). The most common technology is the powder bed based laser beam melting due to the high freedom of design and the application of aviation relevant metallic materials like titanium, aluminum for structural components and high performance nickel-base alloys for engine parts (e. g. Inconel® Alloy 718). Since aluminum alloys are very common in aerospace industries, in particular in combination with alloying elements like silicon, due to their high specific strength [2], hardness [3] and at the same time light weight, the focus of this paper will be on laser beam melting of aluminum alloys. By the usage of AM and the associated topology optimization, part weight, e. g. of a fuel nozzle or a bracket, can be reduced by about 25 % or 54 % compared to the conventionally manufactured part [4,5]. It is estimated, that the aircraft basic weight could be reduced by 4 to 7 % by replacing conventionally parts with AM optimized lightweight components [6]. In particular aluminum alloy components have the highest mass reduction potential [6]. Besides the weight savings, assembly efforts could be decreased by functional integration and part consolidation. An exemplary traditional fuel nozzle consists of 18 individual parts. After design optimization, it can be manufactured in one piece [4].

2. Aluminum powder production for additive manufacturing

The possibilities to produce function integrated parts and one piece solutions instead of assemblies, are due to the layer wise build up of the additive manufacturing process. A laser beam melts up a thin powder layer on a building platform. This powder layer is usually 20 to 60 μm thick, in dependence of the required part quality and the affordable process time [7]. The eligible process parameters must be well adapted to the relevant material. Otherwise, objectionable effects such as a lack of fusion, balling, high porosity [8] and evaporation of alloying elements may occur [9]. Especially for aerospace industries, reliable processes are mandatory. Besides the influence of the process parameters, the initial powder material has an important influence on the resulting part and its surface finish and becomes increasingly important [10,11]. Due to this strong influence, the AM process cannot only be viewed separately, but upstream process steps, e. g. powder production, powder handling and transport, have to be considered.

Aluminum alloys have, compared to stainless steel, a higher reflectivity for laser radiation and a higher thermal conductivity, which makes process improvements more complicated [12]. In order to increase the build rate, a higher scan velocity and thus a higher laser power is necessary [13]. Furthermore, spherically shaped particles are recommended because they are beneficial for flowability and are more likely to result in a uniform powder bed [14].

A variation of the particle size will lead to a different distribution and packing density in the powder bed which influences the heat balance and affects the part density [15,16]. Oxide formations on the particles may result in oxide residues in the part since aluminum oxide has a higher melting temperature than pure aluminum [17]. The upper oxide film of the melt pool evaporates under the laser beam, the oxide films below remain intact or are disrupted by Marangoni forces that stir the melt pool [17]. A different effect is the explosion of the oxide layer due to the thermal gradient and the thermal expansion between the aluminum and the oxide layer [18]. The hydrogen content of the powder can produce hydrogen pores, if the melt pool solidifies faster than the gas evaporates [19].

Table 1 summarizes the influences of the powder particles and possible defects during the AM build up process and in the manufactured part. This information emphasizes the need for high quality powders and reliable processes for powder handling-, storage- and transport-conditions. The impact of the powder quality and the question of how much variation can be tolerated in the powder bed are areas of research [20].

Table 1. Powder characteristics and their influences on the additive manufacturing process

Powder characteristics	Description	Influence on process and part
particle size distribution	maximum particle size determines minimal powder layer thickness [16]	Process: minimal powder layer thickness, heat balance of the powder bed, consistency in melt pool, packing density, compactibility, spatter
	balanced particle size distribution has a positive effect on packing density (small particles fill in small voids) [15,21] and powder compactibility [22]	
	small particles are light and get easily thrown out of the process zone, furthermore due to their surface to volume ratio they are more likely to inflame or explode if making contact to reactive gas [16]	Part: density
	small particle size and narrow particle size distribution leads to uniformity in the melt pool, and results in a higher part density [15,16,21]	
	powder bed density influences the resulting heat transportation and thus the heat balance [16]	
flowability	affects the layer deposition and layer quality (e. g. homogeneous layers) [12,23]	Process: layer deposition
reflectivity, absorptivity	laser energy is absorbed (absorptivity) or reflected in the process chamber (reflectivity) by the powder bed [16]	Process: variations in energy input, required laser power and wavelength
	absorptivity of a powder depends on the wavelength of the laser and the condition of the powder bed [16]	
	high reflectivity of the powder bed (> 91 % for aluminum) requires an increase in laser power [17,24,25]	
thermal conductivity	high thermal conductivity increases the required laser power [24,25], this leads to a rapid dissipation of heat away from the melt pool [17]	Process: required laser power, melt pool temperature
oxidation	oxides form during the process (oxygen level 0.1 to 0.2 %) [17]	Process: obstacle for effective melting, adherent thin oxide films on molten Aluminum reduce wettability, powder flowability
	theory: most predominant factor controlling the flowability is the amount of surface oxides on particle surface [26]	
	rupture of the oxide layer of small powder particles is more difficult [27]	Part: entrapped oxide: region of weakness
humidity, hydrogen	single or multiple molecular layers can form on the particle surface, leading to hydrogen bonding [28,29]	Process: powder flowability
	increased interparticular forces lead to a decrease in flowability [21,29,30] and the metal microstructure of the part [15]	Part: metal microstructure, hydrogen pores
	on the particle surface and in the powder material can lead to hydrogen porosity [19]	
particle shape, morphology	typical powder defects are irregular shapes e. g. elongated particles, satellites, hollow or porous particles [14]	Process: layer deposition, absorptivity
	affects flowability [21], spherical particle morphology is beneficial for powder flowability and helps to form uniform powder layers [14]	Part: material properties
	excessive amounts of large pores or pores with entrapped gas can affect material properties [14]	
	stacking density is a function of the powder morphology [16]	
	surface roughness affects the absorptivity [16]	

Additive manufacturing is very demanding on the powder properties, especially for the manufacturing of aluminum based parts for the aerospace industry. Contaminations e. g. high fractions of aluminum oxide, potential residues of

ceramic material from the crucible or other foreign material during the powder production, reduce the material properties of the part, e. g. strength, fatigue performance and ductility, significantly [18].

Metal powder material is typically produced in one of the following four ways: chemically, through electrolysis, mechanically or through atomization [30]. Powders for additive manufacturing are most commonly produced using gas atomization in an inert gas atmosphere. A high energy flow of gas atomizes the liquid metal upon impact [31]. The atomized liquid metal forms into spherical droplets and turns solid when cooling below the melting temperature. The solid particles are screened and sorted by their size. For reactive materials (e. g. aluminum) atomization and packaging is performed in a protective atmosphere. In all known processes for the production of aluminum powder, inert gas is used to preserve the spherical shape of the particles. Atomization in air leads to an immediate partial oxidation of the liquid material and prevents the liquid metal from transforming into spherical shape [32] making the powder unsuitable for additive manufacturing processes.

Atomization processes can be grouped by the method of melting the material, with or without the use of a crucible (Fig. 1), and by the type and geometry of the nozzle used (Fig. 2). When the material is melted in a crucible, inductive heating or a plasma torch are used. Subsequently, the melt is led through the nozzle into the atomization chamber.
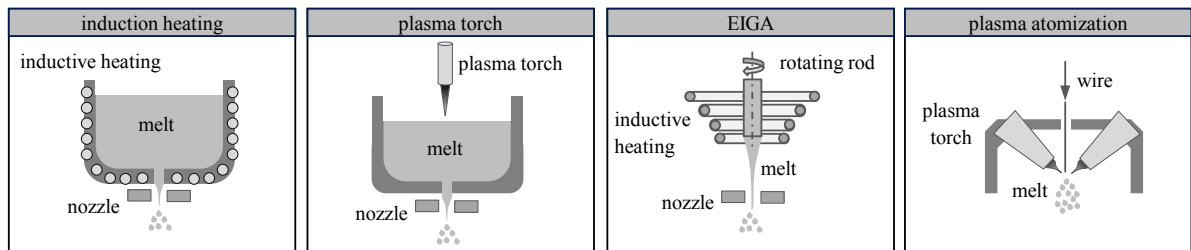
Fig. 1. Melting mechanisms for gas atomization [33–35]

The most common atomizer types are the free fall nozzle, the close coupled nozzle and the De Laval nozzle (Fig. 2). In the free fall nozzle, gravitation drives the melt into the atomization chamber, where it is atomized. The limited flow rate of the melt is a major disadvantage of the free fall nozzle. The diameters of the particles are typically higher than 50 µm [36], which is too large for additive manufacturing processes. In a closed coupled nozzle the atomization gas pulls the melt from the nozzle. In this configuration, the melt flow can be adjusted through a change in the atomization gas flow. In comparison to the free fall nozzle process, significantly higher flow rates and smaller particle sizes of approximately 10 µm [36] can be achieved.

In the De Laval nozzle a laminar gas flow is accelerated to supersonic speed [36]. Compared to the close coupled nozzle atomizer type, less gas is needed [36] and the resulting particle diameter is typically between 15 and 45 µm [37] with a narrow distribution of the particle diameter. A disadvantage of the free fall nozzle and the close couple nozzle is the possibility that a freezing of the melt inside the nozzle can occur and the process aborts.
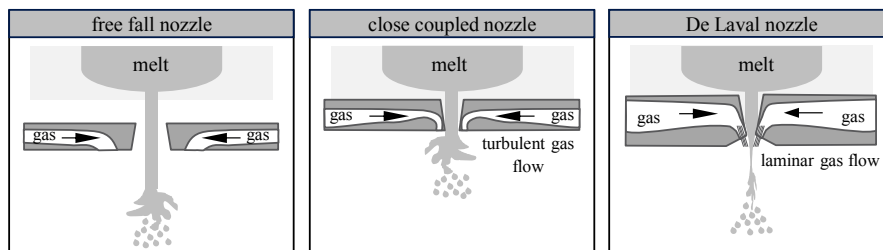

Fig. 2. Common gas atomization nozzle designs [36,38]

In the EIGA (Electrode Induction Melting Gas Atomization) process and in the plasma atomization process (Fig. 1) the material is not melted in a crucible and therefore contaminations by ceramic material or remains of foreign material from earlier process batches should not arise [39]. In the EIGA process, the metal is melted from an induction heated rod, from which the liquid metal drops into the atomization nozzle without any contact to the surrounding parts [34]. Despite the absence of a crucible in the EIGA process, Yablokova et al. describe a contamination of powder with residues from the previously atomized material [40]. In the plasma atomization process, a wire with a diameter of 3 mm is melted using three plasma torches [34], and directly atomized, using the heat and kinetic energy of the plasma. From this process, particles from 5 to 250 µm [39] with a particularly spherical shape are obtained.

Special AM applications demand for high and constant quality powders in relatively small amounts. Aerospace applications are especially demanding, not only on the powder quality, but also on transparency of processes and supply chains as well as storage condition monitoring. Current large powder production plants are optimized for high output of standard material, e. g. up to 300 kg per batch and also require lots of space. Common dimensions of such plants are 4.5 m in height and 1.5 m in diameter [41]. For the demand oriented production of powder from new tailored alloys, small but flexible powder atomization plants are needed. These smaller machines could be placed close to the respective additive manufacturing machine, allowing for quick reaction and short ways when new alloys for improved properties in the additive manufacturing process and the final part are developed.

3. A new approach based on thermal spraying

The process of thermal spraying is similar to the gas atomization process, due to the use of a gas flow for melt atomization, but it is more compact. Molten materials are dispersed on to a surface for coating. There are many process variations, which are listed in DIN EN 657:2005-06 e. g. according to their energy sources or spraying consumables [42]. Considering thermal efficiency, ease of maintenance, material and equipment costs, the process which is most preferable for the powder production is arc spraying. Arc Spraying is a wire based process which transfers the heat of the arc directly into the material [43]. In order to get the same temperature at anode and cathode, recent developments use fast commutating alternating current so that there are almost constant spatter sizes [44]. The particle velocity and the process temperature are lower compared to plasma spraying and reach about 3700 to 4700 °C and 100 to 150 m/s, depending on the process parameters. The coating performance is for aluminum about 6 to 8 kg per hour [45]. Comparing the properties of the arc spray process to the derived requirements of the AM powder, it can be assumed, that arc spraying is suitable for small volume AM powder production.

For a better understanding of the process of arc spraying for powder production, preliminary experiments were carried out. Samples were investigated using laser microscopy and scanning electron microscopy (SEM). Spraying was performed by a TAFA CoArc 9910 console in combination with an arc spray gun Model 9935. Aluminum alloy AlSi$_5$Mg with a wire diameter of 1.6 mm was processed with common spray parameters for coatings, consisting of a voltage of 28 V, an amperage of 100 A, and a process gas pressure of 0.28 MPa (40 psi). In order to produce particles for AM, an adaption of the spray parameters is necessary. According to the conclusions of Krebs [46], the usage of low voltage, low amperage and a high process gas pressure generally lead the way to the production of small particle sizes under 63 µm, which are favorable for AM.

In the experiments conducted, compressed air (O$_2$ ≈ 21 vol.-%) and Argon 4.6 (O$_2$ ≤ 4*10^{-4} vol.-%) [47] were used as atomizer medium. Spraying was performed into a thermal spray cabin and powder samples were collected directly out of the spray cone and sieved to the relevant size fraction ≤ 63 µm. When it comes to principal suitability of the produced powder for AM, the influences of the process gas are especially important. Fig. 3 (left side) shows SEM images of particles produced by the use of air and argon as atomization medium. An irregular particle shape of the air-sprayed powder can clearly be seen. The Argon-sprayed powder particles, however, show a more spheroidal shape. Occasionally rounded oblong (nodular) particles are present. The particle surface is considerably smother. The micro section images of the probes in Fig. 3 (right side) show a highly refined microstructure with a fine dispersed silicon phase at the grain boundaries. The formation of such fine microstructures, which is comparable to the one of industrial inert gas atomized particles, is supported by high cooling rates of the molten particles with cooling rates of 10^3 to

10^5 K/s [39,48]. Air sprayed particles show lots of two-dimensional and punctual structural defects. Argon sprayed particles, shown in Fig. 3 (right side), contain fewer punctual and no two-dimensional defects.
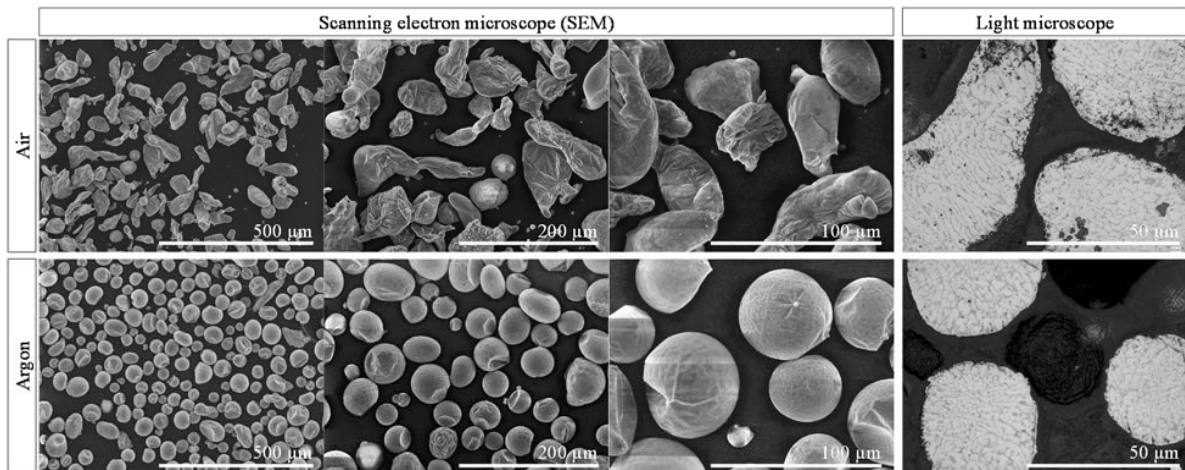

Fig. 3. Comparison of particles produced with air and argon as process gas, SEM images on the left and micro sections on the right side.

Concerning powder production by gas atomization or rather arc spraying, the use of compressed air leads to chemical reactions with molten particles [32]. Due to the strong oxygen affinity of aluminum, an oxide layer arises very quickly on the droplet surface and the surface tension of the molten material is insufficient to form spherical particles resulting in irregular particle shapes [49]. Assuming air is being swirled into the argon shielded spray cone, experimental results confirm that the influence of reactive air is being reduced, but not completely prevented. The appearance of structural defects is somehow similar. Thermal spraying into an inert gas atmosphere yields high powder quality, which could be comparable to inert gas atomized powders.

In the next step of these research activities, the spray cone from the arc spraying process will be inserted into a process chamber that is currently being developed. A schematic representation of the concept is shown in Fig. 4.
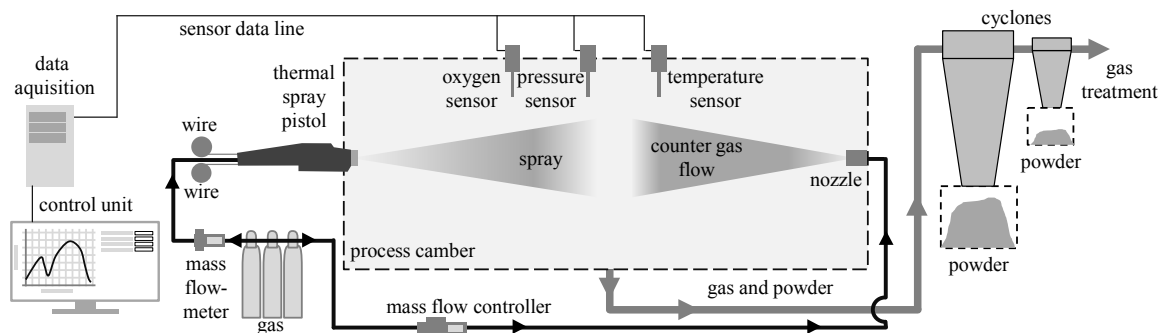
Fig. 4. Schematic representation of the planned process

The dimension of the chamber must be chosen with respect to the cooling distance and the spray cone width, so that the droplets will not hit the chamber walls or the bottom in liquid state and deform. Additionally the chamber dimension has to be minimized in order to save inert gas and space. There are two basic orientations for atomization

chambers, a vertical and a horizontal layout. In industrial atomization plants the vertical layout is common, because the particles will fall with the gravity and the powder can be collected and forwarded at the bottom of the chamber. If the walls are even, the powder can settle harder and is more easily transported with the gas flow. A vertical concept has more preferable characteristics, but requires high ceilings. The concept of the arc spray atomization chamber for preliminary experiments has to be designed for a minimum space, therefore a horizontal concept will be realized. In order to cool down the droplets by a minimum distance, a counter flow will be integrated in the chamber to reduce the particle speed and to increase the cooling rate. The particles in the gas-particle atmosphere will be separated in cyclones. Due to the small dimensions and the wire based process, the atomization chamber can be used flexibly for new materials and located in close proximity to the AM process chain. This avoids unknown influences through handling and storage of the powder. Thereby the user knows the powder history of every single batch and can consider the previous influences while processing.

4. Conclusion

Due to AM, there is a variety of new challenges concerning powder production and the powder quality. Parameters such as the oxygen or hydrogen content of the powder can have a huge influence on the AM process and the resulting part quality, particularly when processing aluminum alloys. Therefore the powder production, handling and transport must be considered. A new small scale atomization chamber, based on arc spraying, shall help to get a better understanding of the process chain. First experiments with an arc spraying system showed, that the process is feasible for powder production, although the particle size and shape are not yet fully comparable to the already established powders for AM. These properties will be improved in further experiments with an adjustment of the thermal spray process parameters and a new experimental setup for atomization in an inert gas atmosphere with less than 3.0 vol.-% oxygen.

Acknowledgements

References

[1]   European Aviation Safety Agency EASA, European Aviation Environmental Report 2016, 2016.
[2]   A. Canakci, T. Varol, A novel method for the production of metal powders without conventional atomization process, Journal of Cleaner Production 99 (2015) 312–319.
[3]   H.E. Friedrich, Leichtbau in der Fahrzeugtechnik, Imprint: Springer Vieweg, Wiesbaden, 2013.
[4]   General Electric Company, These scientists are writing the 3D-printing cookbook for GE.
[5]   M. Seabra, et al., Selective laser melting (SLM) and topology optimization for lighter aerospace components, XV Portuguese Conference on Fracture, PCF 2016, 10-12 February 2016, Paco de Arcos, Portugal 1 (2016) 289–296.
[6]   R. Huang, et al., Energy and emissions saving potential of additive manufacturing: the case of lightweight aircraft components, Journal of Cleaner Production.
[7]   V. Schmidt, M.R. Belegratis (Eds.), Laser technology in biomimetics: Basics and applications, Springer, Heidelberg, 2013.
[8]   J. Kruth, et al., Binding mechanisms in selective laser sintering and selective laser melting, Rapid Prototyping Journal 11 (2005) 26–36.
[9]   M. Simonelli, et al., A study on the laser spatter and the oxidation reactions during selective laser melting of 316L stainless steel, Al-Si10-Mg, and Ti-6Al-4V, Metallurgical and Materials Transactions 46 (2015) 3842–3851.
[10]   T.G. Spears, S.A. Gold, In-process sensing in selective laser melting (SLM) additive manufacturing, Integrating Materials and Manufacturing Innovation 5 (2016) 683.
[11]   M. Qian, Metal powder for additive manufacturing, JOM 67 (2015) 536–537.
[12]   K. Kempena, et al., Process optimization and microstructural analysis for selective laser melting of AlSi10Mg, 2011.
[13]   D. Buchbinder, et al., High power selective laser melting (HP SLM) of aluminum parts, Physics Procedia 12 (2011) 271–278.
[14]   European Powder Metallurgy Association, Introduction to additive manufacturing technology: A guide for Designers and Engineers, 2015.

[15]   E. Uhlmann, et al., Additive manufacturing of titanium alloy for aircraft components, MIC2015 – 15th Machining Innovations Conference for Aerospace Industry 35 (2015) 55–60.
[16]   M. Van Elsen, Complexity of selective laser melting: a new optimisation approach, 2007.
[17]   E. Louvis, et al., Selective laser melting of aluminium components, Journal of Materials Processing Technology 211 (2011) 275–284.
[18]   E.O. Olakanmi, Selective laser sintering/melting (SLS/SLM) of pure Al, Al–Mg, and Al–Si powders: Effect of processing conditions and powder properties, Journal of Materials Processing Technology 213 (2013) 1387–1405.
[19]   C. Weingarten, et al., Formation and reduction of hydrogen porosity during selective laser melting of AlSi10Mg, Journal of Materials Processing Technology 221 (2015) 112–120.
[20]   S. Richter, S. Wischmann, Additive Fertigungsmethoden – Entwicklungsstand, Marktperspektiven für den industriellen Einsatz und IKT-spezifische Herausforderungen bei Forschung und Entwicklung, Berlin, 2016.
[21]   K.G. Prashanth, Selective laser melting of Al-12Si, 2014, Dresden 2014.
[22]   Z. Cai, et al., Effect of Particle Size on microstructure and cold compaction of gas-atomized hypereutectic Al-Si alloy powder, Metallurgical and Materials Transactions 46 (2015) 824–830.
[23]   A.B. Spierings, et al., Powder flowability characterisation methodology for powder-bed-based metal additive manufacturing, Progress in Additive Manufacturing 1–12.
[24]   D.D. Gu, et al., Laser additive manufacturing of metallic components: Materials, processes and mechanisms, International Materials Reviews 57 (2013) 133–164.
[25]   N.T. Aboulkhair, et al., On the formation of AlSi10Mg single tracks and layers in selective laser melting: Microstructure and nano-mechanical properties, Journal of Materials Processing Technology 230 (2016) 88–98.
[26]   E.O. Olakanmi, Direct selective laser sintering of aluminium alloy powders. PhD thesis, Leeds, 2008.
[27]   E. O. Olakanmi, et al., Laser sintering of blended Al‑Si powders, Rapid Prototyping Journal 18 (2012) 109‑119.
[28]   M. Lutter-Guenther, et al., Effects on properties of metal powders for laser beam melting along the powder process chain, in: Fraunhofer Additive Manufacturing Alliance (Ed.), DDMC 2016: Fraunhofer Direct Digital Manufacturing Conference, 2016.
[29]   D. Schulze, Pulver und Schüttgüter: Fließeigenschaften und Handhabung, Springer Vieweg, Berlin, 2014.
[30]   R.J. Hebert, Viewpoint: metallurgical aspects of powder bed metal additive manufacturing, Journal of Materials Science 51 (2016) 1165–1175.
[31]   A. Lawley, Preparation of metal powders, Annual Review of Materials Science. 8 (1978) 49–71.
[32]   J.F. Flumerfelt, Aluminum powder metallurgy processing, Iowa, 1998.
[33]   ALD Vacuum Technologies GmbH, Metal powder technology: Vacuum induction melting and inert gas atomization ceramic-free metal powder production inert gas recycling.
[34]   W. Schatt, et al., Pulvermetallurgie: Technologien und Werkstoffe, 2nd ed., Springer, Berlin, 2007.
[35]   M. Entezarian ,et al., Plasma atomization: A new process for the production of fine, spherical powders, JOM 48 (1996) 53–55.
[36]   ASM Handbook Powder metallurgy. Powder Metallurgy, ASM International, Materials Park, Ohio, 2015.
[37]   IPMD, Nanoval offers extensive range of alloys to metal Additive Manufacturing market, 2016, http://www.metal-am.com/news/003912.html, accessed 17 May 2016.
[38]   A.J. Yule, J.J. Dunkley, Atomization of melts for powder production and spray deposition, Clarendon Press; Oxford University Press, Oxford, New York, 1994.
[39]   O.D. Neikov, Handbook of non-ferrous metal powders: Technologies and applications, 1st ed., Elsevier, Amsterdam, 2009.
[40]   G. Yablokova, et al., Rheological behavior of β-Ti and NiTi powders produced by atomization for SLM production of open porous orthopedic implants, Powder Technology 283 (2015) 199–209.
[41]   ASM Handbook Volume 5A - Thermal spray technology, 2013.
[42]   Deutsches Institut für Normung, DIN EN 657:2005-06, Thermisches Spritzen - Begriffe, Einteilung; 2005th ed., Beuth, Berlin 01.040.25; 25.220.20.
[43]   V. Boronenkov, Y. Korobov, Fundamentals of arc spraying, Springer International Publishing, Cham, 2016.
[44]   H.J. Fahrenwaldt, et al., Praxiswissen Schweißtechnik: Werkstoffe, Prozesse, Fertigung, 5th ed., Imprint: Springer Vieweg, Wiesbaden, 2014.
[45]   E. Lugscheider, F.-W. Bach, Handbuch der thermischen Spritztechnik: Technologien -Werkstoffe -Fertigen, DVS-Verlag, Düsseldorf, 2002.
[46]   B. Krebs, Konturgenaue Bauteilbeschichtung für den Verschleißschutz mittels atmosphärischen Plasmaspritzens und Lichtbogenspritzens. Dissertation, Vulkan-Verl., Dortmund, 2011.
[47]   Linde AG, Argon 4.6, http://produkte.linde-gase.de/gase_in_der_schweisstechnik/argon.html, accessed 6 June 2016.
[48]   G. Wolf, Prozessrelevante Pulvereigenschaften und deren Beeinflussung bei der Herstellung, 19. Augsburger Seminar für additive Fertigung, 2015.
[49]   P. Beiss, Pulvermetallurgische Fertigungstechnik, Springer Vieweg, Berlin, Heidelberg, 2013.

16th Machining Innovations Conference for Aerospace Industry - MIC 2016

Automated Fiber Placement Head for Manufacturing of Innovative Aerospace Stiffening Structures

Berend Denkena[a], Carsten Schmidt[b], Patricc Weber[b]*

[a]Institute of Production Engineering and Maschine Tools, An der Universität 2, 30823 Garbsen, Germany
[b]Institute of Production Engineering and Maschine Tools, Ottenbecker Damm 12, 21684 Stade, Germany

Abstract

In the research project "High-performance Production of CFRP Structures" (HP CFK) a new automated fiber placement (AFP) system for laying thermoset CFRP (carbon fiber-reinforced plastic) slit tapes was developed. Its novel, modular designed laying head faces current industrial needs and challenges of prospective carbon light weight applications, e. g. future aerospace stiffening structures. Thus, its compaction unit is optimized for producing complex-curved structures. To allow approximating slopes on curved geometries, it consists of several height-adjustable rollers which, in addition, are each pressure controlled to enable an individual compacting pressure for the lay-up on materials with different compression strength (e. g. foams, metals). Furthermore, the design of the laying heads cutting unit aided the manufacturing of complex structures while being located as near as possible to the nip point to allow very short minimum placement paths. This paper introduces into the general design of the modular laying head as well as preliminary results of validation studies regarding several process limits.

Keywords: Automated Fiber Placement; Modular laying head; CFRP; Stiffening structure

1. Introduction

Especially in civil aviation, CFRP becomes more and more important to achieve lighter and hence more ecological and efficient airplanes. Today, the global market leaders use CFRP to produce large airplane parts, such as the skin of fuselage and wing covers. Automated Tape Laying (ATL) and Automated Fiber Placement (AFP) are two manufacturing processes used for such parts. MTorres, Electroimpact, Coriolis, BA Composites and the Fives Group are commercial manufacturers of AFP and ATL machines. In the AFP process, small CFRP slit tapes up to 1 inch of width are placed on molds. To achieve a high production rate, AFP machines simultaneously place multiple slit tapes. Machines with up to 32 slit tapes are currently available [1]. New developments of AFP machines build upon robot-

based systems to increase flexibility and decrease the size of the production systems [2]. In addition, the costs can be reduced by using industrial robots. The laying heads of AFP production systems are highly integrated and obsolesce sub units cannot easily be replaced with newly developed and more competitive ones. Therefore, a new AFP head is needed, which offers the possibility to integrate innovative units that improve the AFP process straightforward.

2. Requirements and constraints

To define the requirements for the AFP head, a process analysis of a series production of fuselage panels was conducted. The results show that a big fraction of process time in AFP is non-productive. The floor-to-floor time of the investigated panel is 24 h. Only 46 % of the time is spent with placing slit tapes while it takes 54 % for manually inspecting every ply and correcting placement defects, setting up or cleaning the machine etc.. Furthermore it was determined that 85 % of the placing time were spent for cutting the slit tapes, accelerating and decelerating the fiber placement head and not optimally set placement speeds.. Thus, two foci areas are identified: improving acceleration and speeding up the cutting process. Therefore, one focus is on weight reduction of the laying head especially for usage on an industrial robot and the predominate use of lightweight material such as high-strength aluminum alloys and fiber-reinforced plastics. The other focus is on maximizing the velocity the placement head is allowed to move during the cutting process. The best case is cutting at maximum laying speed of 1 m/s.

Other requirements came from a new structural design for fuselage panels developed in the research project [3]. This panel consists of a skin produced by AFP and local stiffening structures with a supporting foam core also manufactured by AFP. The surface of the structure has a three-dimensionally curved geometry (see Fig. 1). To follow the surface by the compaction unit, a roller with a flexible outer layer and adjustable positioning is necessary. As a restriction from the structural design of the local stiffening structures, the width of slit tapes is 6.35 mm (1/4 "). For the manufacturing, the stiffening structure needs short lengths of slit tapes placed by the AFP head. To insure a better adhesion on surfaces, the laying head needs a pressure control. Especially for mold materials with low compressive strength, a pressure controlled compaction unit is necessary to prevent damages of the molds (e. g. foam cores). These requirements lead to following foci in the mechanical design: flexible compaction roller, manufacturing with short lengths of slit tapes and pressure controlled compaction unit.
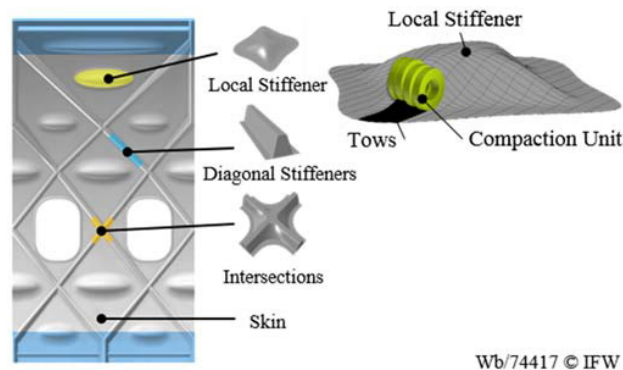

Fig. 1. Fuselage panel design developed by research project HP CFK.

Bridging is one process-induced error, which occurs especially during lay up in concavely shaped molds. It is critical because the tow detaches from the mold and creates a cavity underneath. One possibility to avoid this is to reduce laying speed or to reduce tow tension. In order to maximize the production rate and to avoid derated laying speeds, a continuous feeding synchronous to the laying speed has to be implemented to reduce tow tension during the placement process. High temperatures during the placement process cause increasing tack of slit tapes, especially in the summer with temperatures up to 30 °C. This leads to more adhesion between slit tape and parts of the laying head. For constant climate conditions in a production hall without conditioned environment, the laying head has to be encased and air-conditioned to a constant holding temperature of 21 °C.

3. Experimental manufacturing cell for AFP processes

For the development of innovative AFP heads, a manufacturing cell for experimental studies and processes was needed. To decrease cost and increase flexibility, the AFP machine concept is based on a six axis industrial robot with a linear positioning axis (see Fig. 2). This linear axis is also integrated in the robots positioning interpolation. To allow different end effectors for various applications, a tool changing system is applied. The robot within the manufacturing cell has two operating areas. To its right side different types of molds and other tools can be placed. To its left side a linear high-speed axis is installed, which allows maximum tow-placing speeds of up to 3 m/s and a maximum acceleration of 10 m/s². It can optionally be equipped with a rotation axis, which is also integrated in the robots positioning interpolation and reaches up to 60 revolutions per minute. The core of the fiber placement heads control system is a Beckhoff PLC working synchronously to the KUKA robot control system by master-master communication. This control system is accessible for implementation of new components and axis and thus offers high flexibility for future applications and further developments of fiber placement applications.
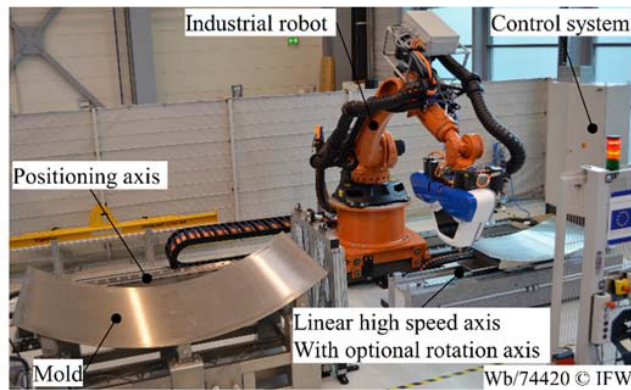
Fig. 2. Layout of the experimental manufacturing cell.

4. Modular AFP head

4.1. General structure of the laying head

The AFP head is designed as a modular system subdivided into eight modules and mounted on an industrial robot (see Fig. 3). There are six functional modules, called air conditioning unit, material supply unit, feeding unit, cutting unit, heating unit and compaction unit, and two passive modules, called module carrier unit and tow guiding unit.
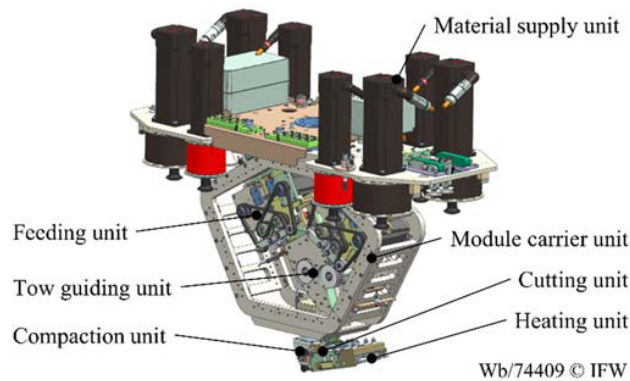
Fig. 3. Design of the modular AFP head.

Furthermore, several sensors are integrated for monitoring temperature, humidity, tow tension and approximating the amount of the material left in the supply unit. The temperature and humidity is measured and recorded during manufacturing process inside the laying head in the material supply unit and to find out the ambient conditions near the nip point. Pyrometer are used for measuring the temperature of the tow inside the laying head and for the temperature control of the heating unit. For the latter one pyrometer measures the temperature of the mold or, later, of the placed tows, and another one the temperature directly in front of the compaction roller. The tow tension is measured by pressure measurement and ultrasonic distance sensors detect the material in the supply unit. In addition, the modularity of the AFP head opens the possibility to integrate sensors for process monitoring. Fig. 4 shows e. g. an infrared camera installed on the module carrier unit. It was developed within a new project called "Therm-O-Plan" [4] and is able to monitor the placement process and to detect defects (gaps, overlaps, foreign bodies, etc.) and the position of the tows. Other sensors can be installed as well, e. g. laser line scanner for the detection of tow edges.
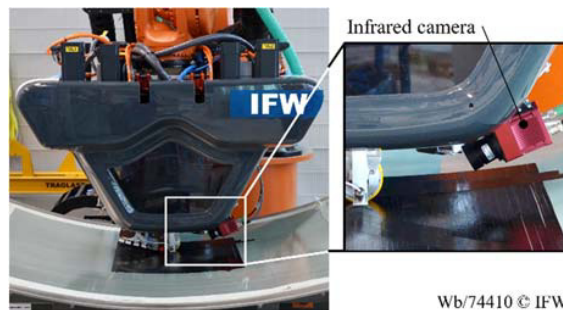
Fig. 4. Integration of an infrared camera for process monitoring.

The modular structure of the laying head makes it possible to replace existing units by newly developed ones and do reference analysis on different approaches. Commercially available machines do not offer this possibility. With this approach, it is easy to replace for example the subdivided compaction roller by a continuous compaction roller.

As mentioned before, the AFP head is primarily designed for placing four 6.35 mm wide tows. However, all units are designed to possibly extent the system to more than four tows as well as the use of wider tows in mind.

4.2. Material supply unit

The first module presented in this paper is the material supply unit. It consists of two identical units with two bobbins of material each. By locating this unit directly in the laying head, the tow guiding from creel (here called

material supply unit) to compaction unit is much shorter than in designs with external creels. This reduces problems related to long distances between these two units such as fuzzball formation and twisting tows.
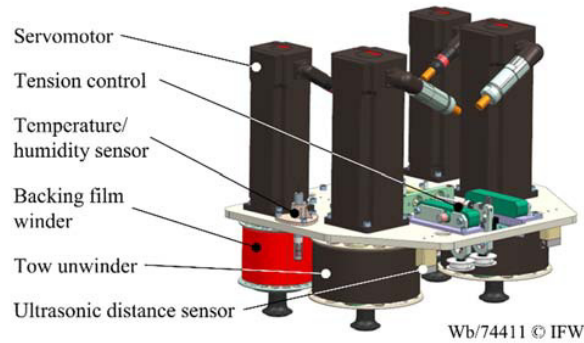

Fig. 5. Design of the material supply unit.

The current material supply unit is dimensioned for research application with a capacity of CFRP slit tapes of about 150 m per tow. This concept of material storage is, however, also possible for the usage of commercial material bobbins. The backing film of the slit tapes is removed directly after unwinding it from the bobbin. A tension control on the one hand generates the necessary tension for slit tapes and on the other hand compensates for the different dynamic behavior of the servomotors located in the AFP head (see Fig. 5). The material supply unit is designed for a maximum speed of 3 m/s and a maximum acceleration of 10 m/s². In combination with the feeding unit, a continuous feeding of the tows is possible.

4.3. Feeding unit

The feeding unit gives a continuous feed rate up to 3 m/s to the tows during the manufacturing process. Hence, the feeding unit is not only used for the restart process after cutting the tows. The continuous feeding leads to less tension in the CFRP tows before placing them on the mold. This is particularly important to prevent bridging. Between feeding and cutting unit, the tow guiding unit is located, as displayed in Fig. 6, and guarantees a direct guidance of the tows towards the nip point.
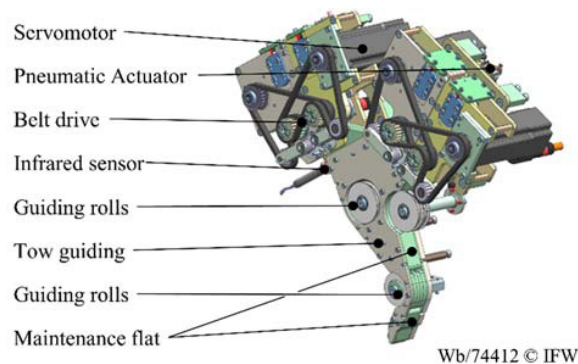
Fig. 6. Design of feeding and tow guiding unit.

4.4. Cutting and heating unit

Among others, the development of the cutting unit focused on reducing the minimum length of a tow, which can be placed (minimum placement length). The cutting mechanism of the cutting unit is knife-edge cutting on an anvil (see Fig. 7a).
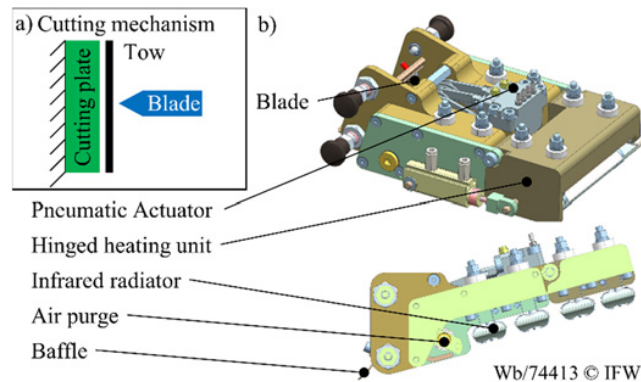
Fig. 7. (a) Cutting mechanism of the cutting process, (b) Design of the cutting unit with integrated infrared radiators.

The anvil, here called cutting plate, is made of a self-healing and flexible material. This combination guaranties a reliable cutting process. In order to describe not only straight laminate boundaries also curved and bevel boundaries, one blade for each tow is required to approximate the outer geometry. For the cutting process, pneumatic actuators actuate the blades and with fast switching valves and a short travel of the piston, the time for cutting can be reduced to a few milliseconds. In Fig. 7b, the assembly of the cutting unit is displayed.

To realize a compact design and high flexibility in the area of the nip point, the heating unit with its four infrared radiators is integrated in the cutting unit. An air purge cools the assemblies because of the thermal radiation of the infrared radiators. They heat up the mold or the already placed CFRP layers, respectively, before placing tows (see Fig. 8). Each infrared radiator has a maximum heating power of 500 W. Therefore, with four implemented infrared radiators, a heating power of 2000 W is available. This corresponds to a surface power density of 15.77 W/cm².
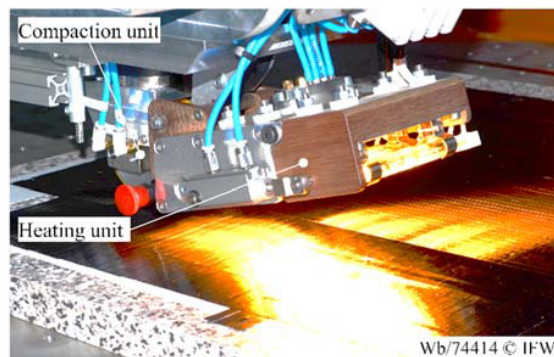
Fig. 8. Using infrared radiators in the heating process.

4.5. Compaction unit

As mentioned in chapter 4.1, the compaction unit consists of four rollers, each having a width of 6.3 mm with a tolerance of +0.05 mm. By design there is a gap of 0.2 mm between the rollers. In total, the compaction roller therefore

has a width of 25.8 mm. The diameter of the rollers is 68 mm, allowing for a maximum curvature of 0.015 1/mm to be followed. Each segment of the roller is height-adjustable by 4 mm. In Fig. 9 important geometric boundary conditions are displayed. These parameters define the limits in manufacture of curved stiffening structures.
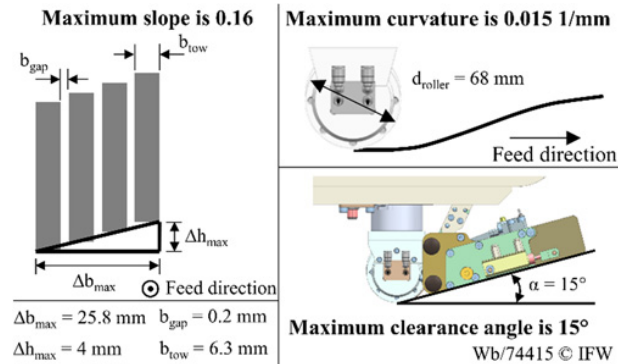

Fig. 9. Geometric boundary conditions of the AFP head.

The mechanical design of the compaction unit is shown in Fig. 10. Each of its segments consists of a roller with a flexible outer layer and a pneumatic actuator within the bearing. The actuator allows for realizing different grades of compaction and surface pressures. A force/torque sensor measures the forces and torques in the nip point and controls the pressure of the pneumatic actuators. The data from the force/torque sensor can be used to analyze the actual pressure applied by the compaction unit and estimate compaction of each placed tows.
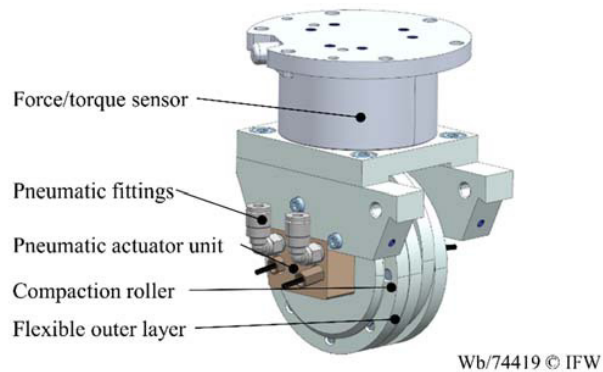
Fig. 10. Design of the compaction unit.

4.6. Process monitoring

Process monitoring becomes more and more important in the manufacturing process of CFRP parts in the aerospace industry. Analyzing the fiber placement process makes direct feedback regarding process failures possible. Such monitoring of the placement process is implemented by using thermographic imaging to detect the temperature difference between the heated mold or placed CFRP layers and the slit tapes in the laying head. When placing slit tapes, the temperature of the placed slit tapes is lower than the temperature of the mold or the CFRP layers. The measured temperature differences are analyzed to detect edges as well as to determine relative positioning of the tows. Furthermore, defects and foreign bodies in or on the laminate can be detected. More information about the thermal process monitoring are published in [4].

5. Validation of placement quality

In first experiments to validate the requirements of the AFP head the characteristics of gaps in flat placement processes were investigated. The gap width varies between 0 mm and 0.4 mm for planar fiber placement. Due to the mechanical design, the gap between the compaction rollers is 0.2 mm. Thanks to the pressure control of the compaction roller and the high-power heating unit, good adhesion of the first ply to mold surface was achieved. While placing the second ply, the regions with low first-ply adhesion were compacted again and a perfect adhesion was reached. In Fig. 11a, the results of the first and second ply placement are displayed.
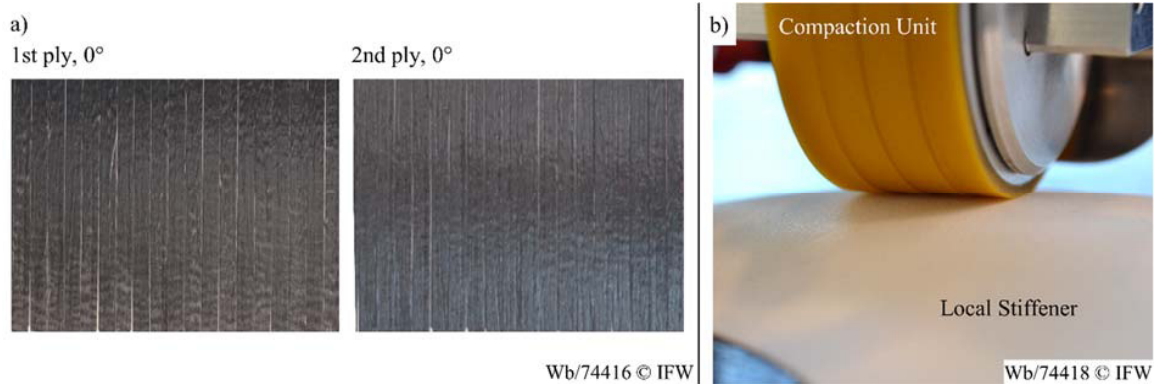
Fig. 11. (a) First and second ply placement in flat manufacturing process; (b) Adjustment of the compaction unit to the shape of the local stiffener.

For manufacturing, it is important to reach a short minimum placing length for tows. Thanks to its design, the AFP head achieves 68 mm. Due to the parallel cutting of tows, this length is constant at any time.

In experiments for validating the flexibility of the compaction unit, the local stiffener was placed on CFRP layers on a metal mold. The local stiffeners are designed with the geometric boundary conditions of the AFP head with respect to the optimal ratio between mass and stability. Within a first test, the rollers are able to follow the surface of the local stiffener during drive over (see Fig. 11b).

6. Conclusion and outlook

The AFP head presented in this paper exhibits an approach for a modular AFP production system. Especially in R&D environments, this system opens the opportunity to test new assemblies for AFP heads without comprehensive changes to the rest of the production system. For research purposes it has only four compaction roller segments, but can easily be enhanced to industrial standards due to its scalable design approach. The heads design and especially the design of the compaction unit allows in particular the manufacturing of stiffening structures with curved surfaces. Thus, design-wise the area of application for AFP processes could be broadened to complex curved structures. First experimental investigations in flat placement processes show the potential of the new laying head. The next step will be to investigate its capabilities on laying on complex curved parts, like the local stiffener. In addition to increase the process complexity, laying tests with maximum laying speed up to 3 m/s will be carried out. The goal is to determine the influence of higher laying speeds to laying qualities and process failures.

References

[1] Izco L, Isturiz J, Moltiva M. High speed tow placement system for complex surfaces with cut / clamp / & restart capabilites at 85m/min (3350IPM). SAE Aerospace manufacturing and automated fastening conference and exhibition Toulouse, France; 2006.
[2] Jeffries K. Enhanced Robotic Automated Fiber Placement with Accurate Robot Technology and Modular Fiber Placement Head. SAE Int. J. Aerosp. 6 (2); 2013.
[3] Schmidt C, Weber P, Völtzer K, Deniz O. Self-Configurable Production of CFRP Aerospace Components Based on Multi-Criteria Structural Optimization, CFK-Valley Convention; 2015.
[4] Denkena B, Schmidt C, Völtzer K, Hocke T. Thermographic online monitoring system for Automated Fiber Placement processes, Composites Part B: Engineering, Volume 97, 15 July 2016, Pages 239-243.

16th Machining Innovations Conference for Aerospace Industry - MIC 2016

Graphical evaluation method for void distribution in direct energy deposition

Ryo Koike[a],*, Ryo Ashida[a], Keiichi Yamazaki[a], Yasuhiro Kakinuma[a], Tojiro Aoyama[a], Yohei Oda[b], Tatsuhiko Kuriya[b], Makoto Fujishima[b]*

[a]Department of System Design Engineering Keio University, 3-14-1 Hiyoshi, Kouhoku, Yokohama, 223-8522, Japan
[b]DMG MORI CO., LTD. 201 Midai, Iga, Mie, 519-1414, Japan

Abstract

Direct energy deposition (DED) process attracts attention from industries because of its applicability to production of complex shape parts. However, technical challenges still remain in DED, such as void evolution inside of the produced object. This paper provides a new graphical evaluation method of void distribution. Binarizing a cross-sectional image of the cladded object and applying a 2-dimensional Gaussian window, the void distribution rate is separately evaluated in each local area on the cross section. To clarify the relation between void evolution and deposition condition in Inconel 625, the void distribution is experimentally evaluated through the various tests.

1. Introduction

In additive manufacturing, direct energy deposition (DED) process recently attracts attention from automotive and aerospace industries. Compared with selective laser melting, the DED does not require a strict seal structure and can be performed continuously without intervals to put a thin layer of powder. Furthermore, the produced objects with DED attain a high density because the process involves deposition, melting and solidification of powdered material using a traveling melt pool [1]. On the other hand, the DED process is difficult to control due to the dynamic movement

* Corresponding author. Tel.: +81-45-566-1825; fax: +81-45-566-1657.
  E-mail address: koike@sd.keio.ac.jp

of material powder, thus, various technical problems still remain in the DED such as shape accuracy and powder efficiency. The porosity rate is comparably smaller than other additive processes but not ignorable to ensure the strength of resulting parts.

The void formation inside the produced object has been focused on as one of the important issues in additive manufacturing. Several researchers analyzed mechanisms of void formation in selective laser melting by evaluating the void distribution in the produced object under various scanning conditions [2,3]. These reports mention that void forms due to the non-molten powder and the gases trapped in the melt pool. On the other hand, the voids hardly appear due to non-molten powder in DED process because the powders are sufficiently molten with high laser power. Some researchers have already evaluated the void formation in DED process and showed that only circular voids are observed on the cross-section of deposited objects [4,5], though the void shape is unsteady when the powder is not molten enough. These researches calculate the porosity rate to evaluate and optimize the parameters for the DED process on Inconel 718.

From the viewpoint of applicability to the metal powder for DED, Inconel 625 is also a suitable material. Inconel 625 is a nickel-based superalloy employed to aerospace, chemical and marine industries because of its heat and corrosion resistances, and demanded to be used for complex shape parts [6,7]. To reduce the voids and ensure the mechanical strength of deposited products, the void formation in Inconel 625 also should be investigated. Furthermore, to clarify the void formation mechanism more, analytical approach to evaluate the distribution of void in the deposited object also should be established. Although porosity rate is calculated in the past researches, a bias in the void distribution is hardly investigated, though the position of void would have a strong relation with its evolution mechanism.

Hence, this paper evaluates the porosity of Inconel 625 by proposing a new graphical evaluation method for void distribution in deposited object with DED. Binarizing a cross-sectional image of the deposited object and applying a 2-dimensional Gaussian window, the local porosity rate is evaluated for each section. To clarify the relation between the void evolution and the deposition condition in DED process for Inconel 625, the void distribution is experimentally evaluated through various deposition tests.

2. Methodology

2.1. Observation for cross section of deposited objects

To evaluate the void distribution in the deposited object, the cross section is observed in this study. After cutting the deposited tracks with an abrasive water jet machine, the cross section is polished to eliminate scratches by using 4 kinds of polishing papers and 2 kinds of diamond slurries (Fig. 1). The polished cross section is observed with a digital microscope to obtain the image data. To emphasize and distinguish a void on the cross-sectional surface, the image data is binarized. As a result, voids can be clearly observed as black pixel areas on the analyzed image.
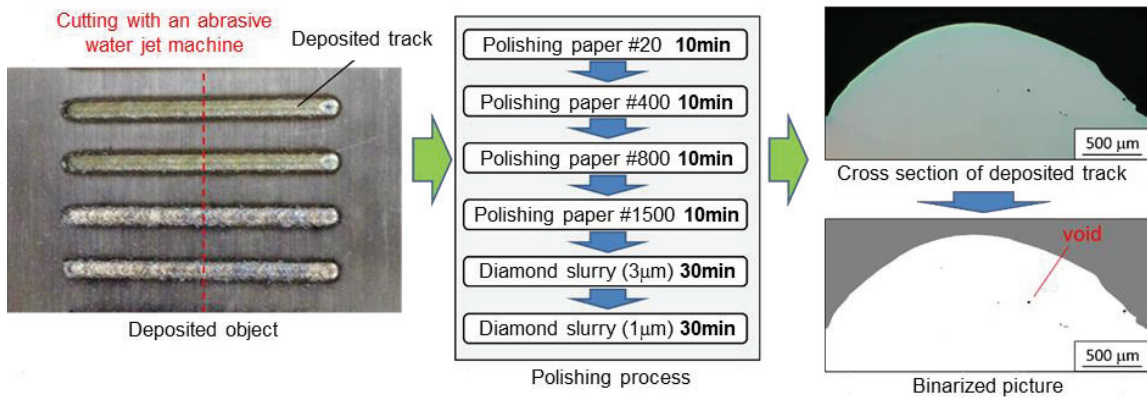

Fig. 1. Procedures for taking cross-sectional images of deposited objects.

2.2. Evaluation of Void distribution

Although porosity rate can be calculated by counting the black and white pixels respectively in the cross-sectional picture, void distribution in each section also should be evaluated to analyze the difference in porosity rate between layers. In this study, a graphical calculation method with 2-dimensional Gaussian window is employed to separate the evaluation section.

Assuming that distributions of x and y components are independent, the Gaussian distribution w on an x-y plane is generally represented as follows:

$$w(x,y) = \frac{1}{2\pi\sigma_x\sigma_y} e^{-\frac{1}{2\sigma_x\sigma_y}((x-\mu_x)^2+(y-\mu_y)^2)} \tag{1}$$

where σ_x and σ_y are the standard deviations, and μ_x and μ_y are the averages in each component. For example, the Gaussian distribution is represented as Fig. 2, where $\sigma_x = \sigma_y = 1, \mu_x = \mu_y = 0$. The central point and the spread of the distribution are easily modified by changing the averages and the standard deviations.
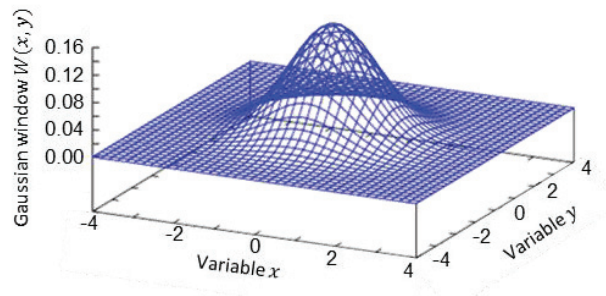
Fig. 2. 2-dimensional Gaussian distribution on an x-y plane ($\sigma_x = \sigma_x = 1, \mu_x = \mu_y = 0$).

The 2-dimensional Gaussian distribution is available as a window function to limit a section on the obtained cross section image. By convoluting the image data and the window function, the evaluated area can be limited. Furthermore, the variation in local porosity rate can be smoothly captured with the 2-dimentional Gaussian widow, comparing with an equal weighting. The local porosity rate P_v at (x, y) is defined as follows:

$$P_v(x,y) = \iint_{-\infty}^{\infty} p(x',y') \cdot w(x - x', y - y')dx'dy' \tag{2}$$

where

$$p(x,y) = \begin{cases} 1 & \cdots \text{ if } (x,y) \text{ is in a void} \\ 0 & \cdots \text{ if } (x,y) \text{ is not in any void} \end{cases}$$

However, the image data is discrete data which is expressed by arranging enormous number of pixels. In discrete domain, Eq. 2 can be represented as follows:

$$P_v[x,y] = \sum_{m=0}^{M} \sum_{n=0}^{N} p[m,n] \cdot w(x - m, y - n) \tag{3}$$

where M and N are the numbers of pixels in the horizontal and vertical directions, and $p[m,n]$ is binary data at the (m,n)th pixel in the binarized cross section image. When the (m,n)th pixel color is black in the binarized cross section image, $p[m,n] = 1$. Conversely, $p[m,n] = 0$ when the (m,n)th pixel is white.

Conducting the calculation of Eq. 3 for each pixel in the binarized image, the local porosity rate for each pixel can be obtained. By giving color corresponding to the local porosity rate for each pixel, a color map of void distribution can be drawn as Fig. 3(b). Not only the influence of large voids but also that of small voids are captured and shown as blue regions in the color map, even if the void is so small to find on the binarized picture as shown in Fig. 3(a). In this study, both porosity rates for the whole cross section is also utilized to evaluate the parameters for DED process.
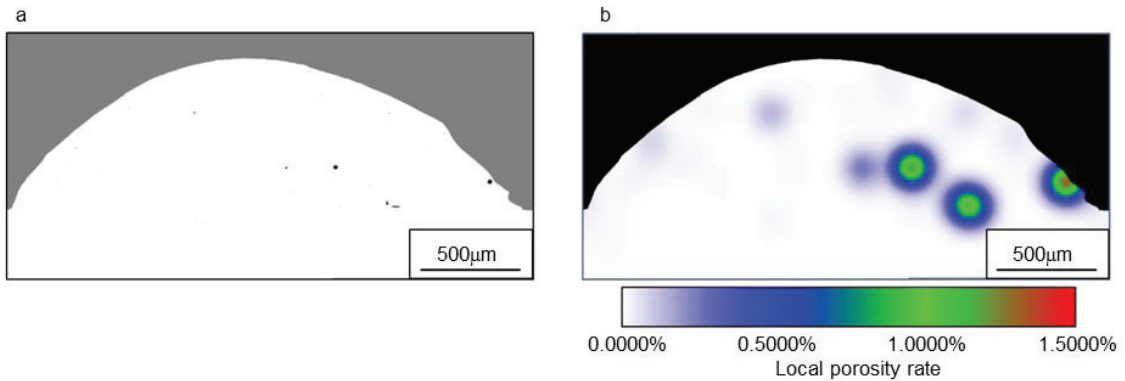
Fig. 3. Proposed graphical evaluation method for void distribution; (a) analyzed original picture, (b) color map of local porosity rate.

2.3. Experimental Setup

DED is a process that uses laser to melt and deposit the material powder as shown in Fig. 4. In this study, the DED test are conducted with an additive/subtractive hybrid machine which employs a high-power fiber-coupled diode laser that can output a tophat beam up to 2000 W to supply the thermal energy (Fig. 5). The laser wavelength is 1020 nm and the melting spot diameter is 3 mm. The material powder is supplied from the powder jet nozzle to the melting spot with carrier Argon gas. The shielding Argon gas is also supplied to avoid oxidation during built-up process. Inconel 625 is used as the material powder for DED.

The void distribution in the resulting parts produced with DED strongly depends on the deposition conditions. In order to find a suitable deposition condition for reducing the voids, single-layer deposition experiments with 36 kinds of difference conditions are carried out by changing laser power, carrier gas supply, and powder flow rate. Furthermore, a multi-layer deposition test is also conducted to evaluate the void distribution in wall-shape deposited objects.

The window size for proposed graphical analysis method can be modified by changing the standard deviations in Eq. 2. To evaluate the local porosity rate, the window size should be small but sufficiently larger than the void size. Thus, defining the radius of the window as the distance between the central point of the window and the distant point at which the value of Gaussian function is 1 % of the central point, 200-pixel-diameter window is employed which corresponds to 200-μm-diameter window because the diameters of observed voids were less than 50 μm.

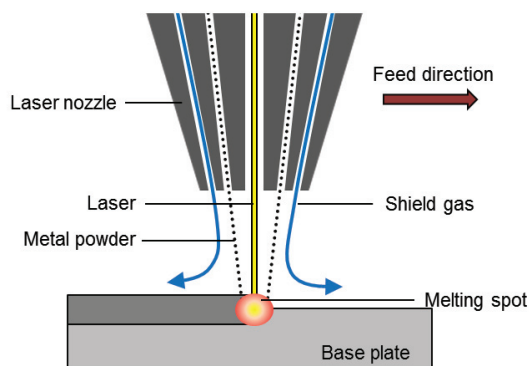The detail of the parameters for DED in this test are summarized in Table 1.
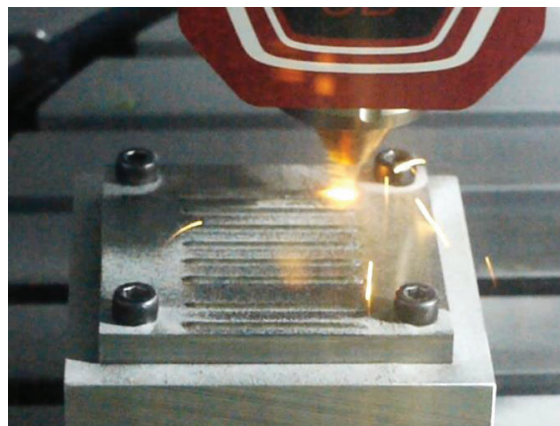

Fig. 4. DED process model.

Fig. 5. Appearance of DED process.

Table 1. Deposition conditions

Parameter	Single-layer deposition	Multilayer deposition
Laser power W	1200, 1600, 2000	1200
Metal powder supply g/min	16, 18, 20	11
Carrier gas supply l/min	4, 6, 8, 10	6
Shield gas supply l/min	4	4
Feed rate mm/min	1000	800
Deposit length mm	50	30
Number of layers	1,	54
Size distribution of metal powder μm	45 – 125	
Material of base plate	Stainless alloy (SUS303)	

2.4. Evaluation of deposited object

Firstly, single-layer deposition tests are conducted. Figures 6 and 7 show the color maps of void distribution when the laser power is set to 2000 and 1200 W respectively. Compared with the results with the laser power of 2000 W, the local porosity rate clearly gets high at some spots in the results of 1200 W. Although each deposition test is repeated 2 times to confirm the repeatability of the void evolution, the void randomly appears in the deposited object. For example, in Figs. 6 and 7, (a) and (b) are the results under the same deposition conditions and show similar porosity rates, but the high porosity areas irregularly appear and the repeatability cannot be confirmed.
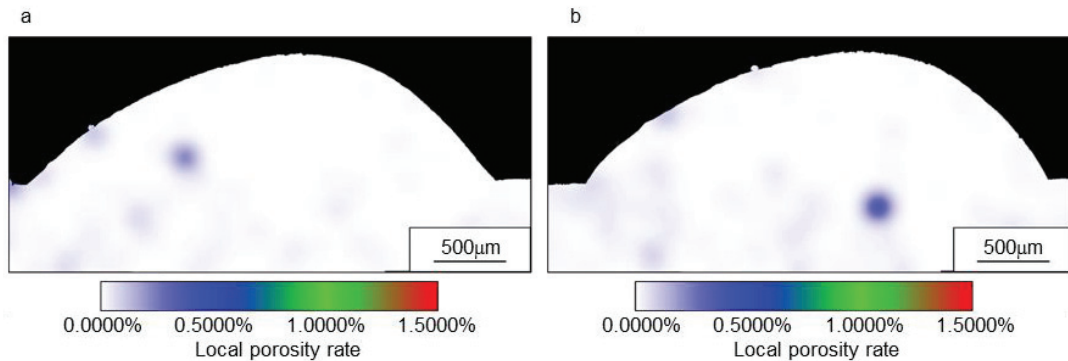

Fig. 6. Color map of local porosity rate under the condition as follows: 2000 W laser power, 20 g/min metal powder supply, and 10 l/min carrier gas supply. (a) result of first test, (b) result of second test.
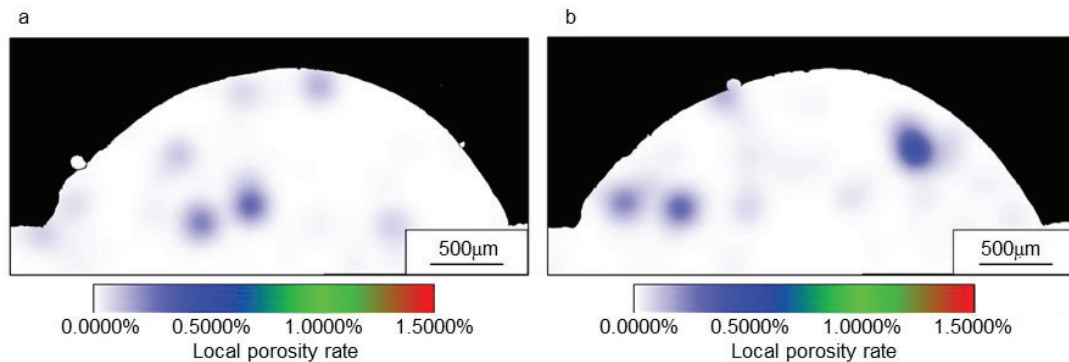

Fig. 7. Color map of local porosity rate under the condition as follows: 1200 W laser power, 20 g/min metal powder supply, and 10 l/min carrier gas supply. (a) result of first test, (b) result of second test.

The average porosity rates of whole cross section under each condition are summarized in Tables 2 – 4. The experimental results clearly show that higher laser power and lower carrier gas supply leads to void reduction in single-layer deposition in the conditions used in this study. In particular, low laser power leads to generation of large voids which drastically enlarges porosity rate. Regarding a single-layer deposition, Zhong et al. also showed that high laser power decreases the porosity rate in a deposited object of Inconel 718 [4]. Though Zhong indicated that the porosity rate does not remarkably change according to the carrier gas supply from 7.3 l/min to 33 l/min, the increase in porosity rate is confirmed in the range of 4 l/min to 10 l/min in this study. The experimental results indicate that the metal powder should be molten sufficiently with high heat supply to avoid the void generation.

Table 2. Porosity rate for whole cross section with laser power of 2000 W.

Laser power 2000 W		Carrier gas supply			
		4 l/min	6 l/min	8 l/min	10 l/min
Metal powder supply	16 g/min	0.0085% (±0.0035%)	0.0069% (±0.0015%)	**0.0029%** (±0.0001%)	0.0070% (±0.0022%)
	18 g/min	0.0080% (±0.0012%)	**0.0039%** (±0.0020%)	0.0108% (±0.0007%)	0.0111% (±0.0007%)
	20 g/min	**0.0029%** (±0.0020%)	0.0069% (±0.0003%)	0.0064% (±0.0004%)	0.0082% (±0.0010%)

Table 3. Porosity rate for whole cross section with laser power of 1600 W.

Laser power 1600 W		Carrier gas supply			
		4 l/min	6 l/min	8 l/min	10 l/min
Metal powder supply	16 g/min	0.0051% (±0.0002%)	0.0057% (±0.0019%)	0.0062% (±0.0003%)	0.0087% (±0.0011%)
	18 g/min	0.0064% (±0.0002%)	0.0073% (±0.0007%)	0.0228% (±0.0146%)	0.0224% (±0.0141%)
	20 g/min	0.0144% (±0.0018%)	0.0103% (±0.0005%)	0.0125% (±0.0041%)	0.0262% (±0.0030%)

Table 4. Porosity rate for whole cross section with laser power of 1200 W.

Laser power 1200 W		Carrier gas supply			
		4 l/min	6 l/min	8 l/min	10 l/min
Metal powder supply	16 g/min	0.0068% (±0.0003%)	0.0138% (±0.0032%)	0.0124% (±0.0040%)	**0.0330%** (±0.0093%)
	18 g/min	0.0149% (±0.0077%)	**0.0397%** (±0.0224%)	0.0141% (±0.0031%)	0.0144% (±0.0025%)
	20 g/min	0.0152% (±0.0069%)	0.0154% (±0.0047%)	0.0268% (±0.0055%)	**0.0316%** (±0.0105%)

The void distribution is also evaluated in the cross section of the multilayer deposition. Figure 8 shows the cross section and void distribution map of multilayer deposition with 1200 W laser power, 6 l/min carrier gas supply, and 11 g/min powder supply. Excepting the analysis result around large voids, the local porosity rate clearly gets large on the bottom of wall. This is because the temperature in the melting spot varies between the bottom and top of the wall due to the difference in the thermal conductive condition. The supplied heat is easily transferred to the base plate during building bottom layers, on the other hand, the heat stays in the deposited parts during building up the top layers because the heat transfer is small when the cross section is small, like a thin wall. Therefore, the temperature of bottom layers would not get high enough to eliminate the void. This result indicates that the deposition condition has to be changed according to the heat transfer conditions at each point in the deposited object.
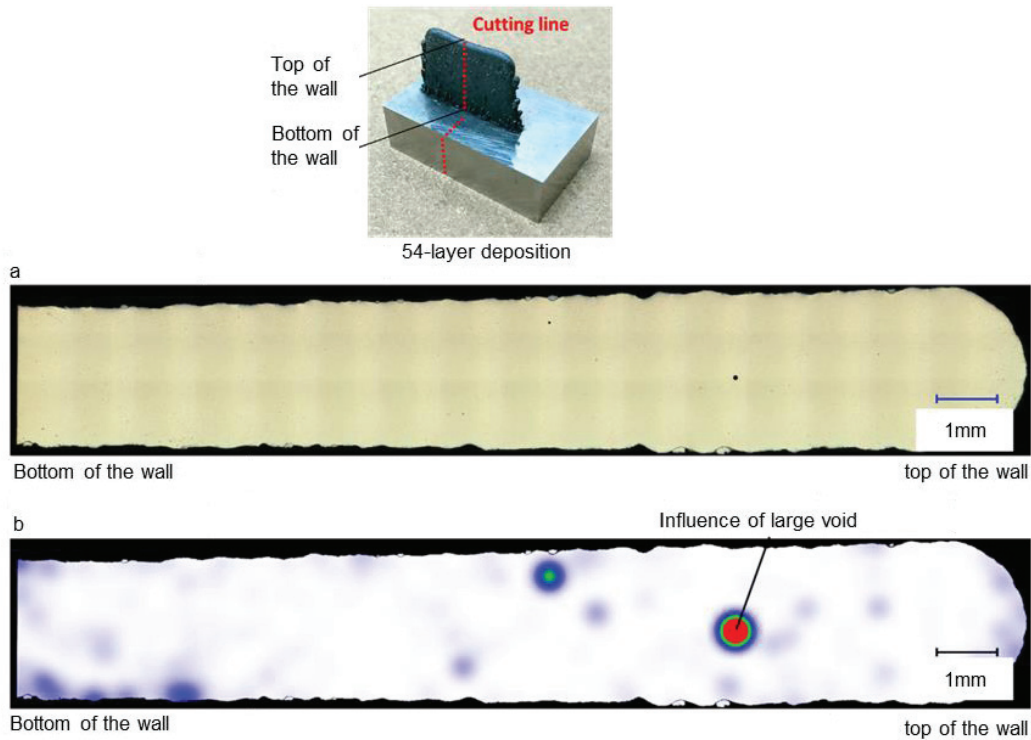
Fig. 8. 54-layer deposited object; (a) cross-sectional view taken with a digital microscope, (b) color void distribution map.

Although the proposed graphical evaluation method certainly captures the difference in the local porosity rates among each section, the local porosity rate suddenly gets large at the area including a large void. However, as shown in Fig. 9, various sizes of voids are observed even in the same samples. Though small voids may have a tendency to appear near the surface of deposited object, the presented evaluation method is not suitable to investigate this tendency because the influence of large void is dominant in the evaluation result. In our future works, a color map for void distribution will be improved to separately evaluate the local porosity rate according to the void size.
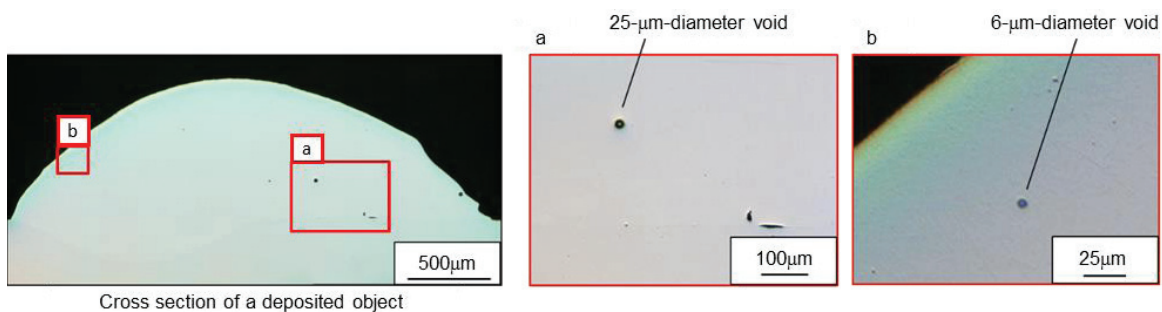
Fig. 9. Size difference among voids; (a) a large void with 25-μm diameter, (b) a small void with 6-μm diameter.

4. Conclusion

This paper proposes a graphical evaluation method for void distribution to investigate the porosity rate in a produced object of Inconel 625 with direct energy deposition (DED). By applying 2-dimensional Gaussian distribution as a window function, porosity rate is separately evaluated in each area on the cross section of deposited object. At the same time, the porosity rate of whole cross section is also calculated to evaluate the DED parameters and find a proper condition to reduce the void. Experimental results clearly show that higher laser power and lower carrier gas supply leads to lower porosity rate in the deposition conditions used in this study. Although no clear tendency of the void distribution is confirmed in single-layer deposition tests, the local porosity rate obviously gets high at the bottom of the wall in a multilayer deposition test. In our future works, the graphical evaluation method will be improved to separately investigate the local porosity rate along with the void size. Furthermore, the obtained results will be utilized to clarify the mechanism of void evolution and optimize the DED parameters.

References

[1] I. Gibson, D.W. Rosen, B. Stucker, Additive Manufacturing Technologies, Springer, New York, 2010, pp. 238.
[2] N.T. Aboulkhair, N.M. Everitt, I. Ashcroft, C. Tuck, Reducing porosity in AlSi10Mg parts processed by selective laser melting, Additive Manufacturing 1-4 (2014) 77-86.
[3] X.J. Wang, L.C. Zhang, M.H. Fang, T.B. Sercombe, The effect of atmosphere on structure and properties of a selective laser melted Al-12Si alloy, Mater. Sci. Eng. A 597 (2014) 370-375.
[4] C. Zhong, A. Gasser, T. Schopphoven, R. Poprawe, Experimental study of porosity reduction in high deposition-rate laser material deposition, Optics & Laser Technology 75 (2015) 87-92.
[5] G.K.L. Ng, A.E.W. Jarfors, G. Bi, H.Y. Zheng, Porosity formation and gas bubble retention in laser metal deposition, Appl. Phys. A 97 (2009) 641-649.
[6] S. Cao, D. Gu, Laser metal deposition additive manufacturing of TiC/Inconel 625 nanocomposites: Relation of densification, microstructures and performance, J. Mater. Res. 30(23) (2015) 3616-3628.
[7] G.P. Dinda, A.K. Dasgupta, J. Mazumder, Laser aided direct metal deposition of Inconel 625 superalloy: Microstructural evaluation and thermal stability, Mater. Sci. Eng. A 509 (2009) 98-104.

16th Machining Innovations Conference for Aerospace Industry - MIC 2016

High Speed Cutting of carbon fibre reinforced plastics

Eckart Uhlmann[a], Sebastian Richarz[a], Fiona Sammler[a],*, Ralph Hufschmied[b]

[a]*Institute for Machine Tools and Factory Management (IWF), Technical University Berlin, Pascalstr. 8-9, 10587 Berlin, Germany*
[b]*Hufschmied Zerspanungssysteme GmbH, Edisonstr. 11 d, 86399 Bobingen, Germany*

Abstract

The effects of high speed cutting (HSC) on metallic workpiece materials have been widely studied and the benefits are commonly employed in the machining industry. However, in the machining of composite materials, these effects have not yet been a focus of significant research work and core questions such as what impact HSC cutting parameters have on tool wear, process forces and workpiece quality remain open. As such, the work described in this paper shall focus on the use of HSC cutting parameters with spindle speeds up to 60000 rpm for the machining of carbon fibre reinforced composites. Workpiece quality and tool wear are quantified in dependence of cutting speed and feed rate and the known phenomena of reduced cutting forces at high cutting speeds are examined in the case of CFRP machining.

1. Introduction

Sustainable manufacturing from an environmental, economical and social point of view is key for the continued growth of the automotive and aeronautical industries. Cars and airplanes of the future must be quieter, lighter and more efficient. One way of achieving this is the use of innovative composite materials such as carbon or glas fibre reinforced composites (CFRP, GFRP), which are significantly lighter whilst exhibiting comparable or higher strength and wear resistance. CFRPs have been used in the manufacturing of airplanes for a number of decades, however their further development in recent years, for example in relation to the strength of the carbon fibres, plays

---

* Corresponding author. Tel.: +0-000-000-0000 ; fax: +0-000-000-0000 .
  E-mail address: fiona.sammler@iwf.tu-berlin.de

a significant role for their increased use [1]. As such, large proportions of airplane structural components are now made of composite materials, for example the Airbus model A400M (Figure 1). In the automotive industry the use of CFRPs and GFRPs is relatively recent in series production, and is expected to increase dramatically in the coming years.

With few exceptions, CFRP/GFRP components are not produced as near-net shape, meaning machining is almost always required. Commonly this is done using milling, drilling and water jet cutting. Due to the continuous development of cutting tools, machining centres, robot-based machining and control systems, a significant productivity increase is expected, and also required in order to allow series production of CFRP components. In particular, the processing times and part qualities must be improved upon to achieve an economically viable production process of these parts.

Fig. 1. Airbus A400M - The wings (over 20 m long and 4 m wide) consist mainly of CFRP

In recent years research work has focused on the mechanisms of material removal in the machining of CFRPs using conventional machining parameters, with few studies on the use of high cutting speeds and feed rates [1, 2, 3, 4, 5]. Of course, the machinability of fibre reinforced composites depend on the selected materials of the matrix and the reinforcement, the cohesion between the two, the orientation of the fibres in the matrix, the volume fraction of fibres and matrix and the ratio of fibre length to fibre diameter [6]. A number of authors [1, 5, 7, 8, 9, 10] show that when milling fibre reinforced plastics, the type and orientation of the fibre, cutting parameters, and tool geometry have an essential influence on the machinability. When speaking about fibre orientation, it must be differentiated between the fibre orientation and the fibre orientation with respect to the cutting direction $\theta = 0°$, 45°, 90°, 135° [7, 10, 11]. Everstine and Rogers [12] presented the first theoretical work on the machining of FRPs in 1971, since then the research carried out in this area has been based on experimental investigations. Hashin and Rotem [13], Koplev et al. [14] and Kaneeda [15] established that the principal cutting mechanisms are strongly related to fibre arrangement and tool geometry. Colligan and Ramulu [16, 17] carried out studies on machining of polymeric composites and concluded that an increasing of the cutting speed leads to a better surface finish.

Depending on the fibre orientation with respect to the cutting direction, different fundamental failure modes commonly occur in composite machining: fiber-tensile failure, fiber-compression failure, matrix-tensile failure and matrix-compression failure [7, 11, 13, 18, 19, 20, 21].

These fundamental failure modes usually occur in combination with one another and determine the chip formation modes in CFRP machining, with fibre buckling, fibre cutting, fibre delamination, fibre deformation, shearing and macrofacture being the main modes of chip formation [7, 10, 20]. Figure 2 shows the fundamental correlations between rake angle and chip formation modes with fibre orientations $\theta = 0°$ and 90°. The different chip formation mechanisms strongly influence the tool loading situation, thus defining the tool wear and lifetime as well as the machined part quality.

Teti et al. [10] showed that at fibre orientations between $\theta = 0°$ and 30° it is possible to achieve high part qualities, as the cutting forces are low. With rising fibre orientations, for example between $\theta = 90°$ and 135°,

achieving high part qualities becomes more difficult. It should be noted that the tests were undertaken at a relatively low cutting speed of $v_c = 77$ m/min.

The influence of the cutting parameters has been studied by Alexandraki et al. [6] and Xu et al. [22], where it was shown that the feed rate affects the surface quality obtained, with highest feed rates causing local cracks and delamination, particularly when the cutting plane is parallel to material layers ($\theta = 0°$). A number of authors show that the use of higher cutting speeds led to a reduction of cutting forces and a higher part quality [1, 3, 10, 22, 23, 24, 25, 26].
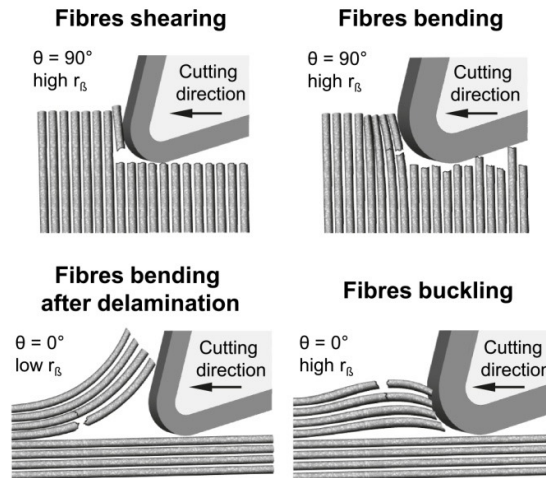
Fig. 2. Dominant chip formation modes and cutting mechanisms in CFRP machining according to [7]

It can be concluded that currently only few publications related to high speed cutting of CFRPs exist. An analysis of the fundamental effects, such as chip formation mechanisms and failure modes using HSC parameters has to date not been undertaken. Furthermore, most of the experimental activities in the literature on composite materials machining have been carried out in laboratory settings with simple analogy tests, without testing of milling processes. Previous work has shown that the use of high speed cutting parameters has led to substantial improvements in the machining result [1, 3, 10, 23, 24, 25, 26]. In those studies, the surface quality and tool wear were mostly focused on, whilst the complex chip formation mechanisms remain to be analysed.

As such, the aim of this work is to analyse the influence of high speed milling of carbon fibre reinforced plastics with a high fibre content on cutting forces, to investigate the relationship between the cutting forces and the part quality a function of the cutting parameters, such as the cutting speed, axial depth of cut, and the feed rate. Finally, an analysis of the failure modes and chip formation mechanisms is undertaken.

2. Experimental setup and materials

In order to study the influence of high speed cutting parameters on fundamental failure and chip formation mechanism CFRP workpieces were face milled in an orbital milling path. The orbital milling path was oriented at a relative fibre orientation with respect to the cutting direction $\theta = 0°$. Tungsten carbide milling tools with eight cutting teeth were used, of which four cutting teeth had a fine tooth pitch. The tools were prepared by Hufschmied Zerspanungssysteme GmbH especially for high speed cutting of CFRP, particularly in relation to the macro- and micro geometries and the concentricity. For tool preparation, a new patented method was used, the Internal Combined External Experience (ICE-X). For the analysis of the chip formation mechanisms the tools were used in

an uncoated state, to allow for an extremely high cutting edge quality with low cutting edge radii. Preparatory testing showed that the uncoated tools wear in a controlled, abrasive manner with a slight, continuous increase of the process forces with increasing wear. Cutting edge break-outs were not observed.

In a second test row, the focus lay on the economical analysis of the HSC process in comparison to conventional CFRP machining processes. For these tests, CVD diamond coated cutting tools were used in the trimming of CFRP. Details of the tools and the workpiece material are given in Figure 3. To allow a comparison with conventional milling processes, process parameters commonly used in the aeronautical industry were chosen as a benchmark. As such, cutting speeds between v_c = 250 m/min and 300 m/min and feed rates of f = 3 m/min and 4.5 m/min were used [4].

a) Analysis of performance

Trimming, down-cut

Tool:
Carbide end mill
CVD-diamond coating
d = 10 mm, z = 4
Helix angle λ = 0°

HSC-milling machine
Röders RXP600

b) Analysis of fundamental chip formation mechanism

Up-cut face milling of circular pockets

Tool:
Carbide end mill
Uncoated
d = 8 mm, z = 8 (4)
Helix angle λ = 30°

Workpiece, milling path
and orientation of forces
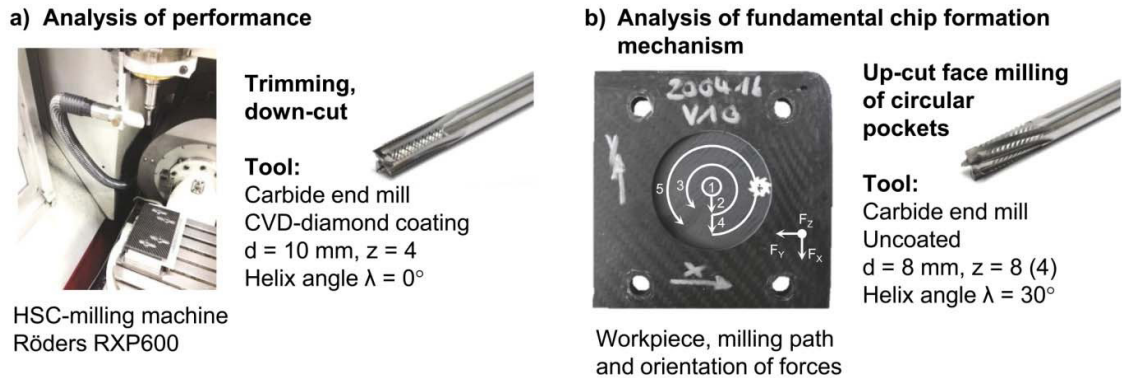
Fig. 3. Setup - Machine tool with external dust extraction system and force dynamometer,
cutting tools as well as CFRP workpiece and milling path

The CFRP workpieces were t_p = 6 mm thick panels with eleven inner layers of unidirectional prepreg with the fibre type SGL CARBON SIGRAFIL C30 T050 and epoxy resin content of 35 %. The two outer layers consist of the woven fibre SIGRATEX PREPREG CE 8201-200-45/ 1200 MM/ 3K with an epoxy resin content of 45 %. The milling processes were undertaken using a RÖDERS RXP600 HSC-milling machine with a maximum rotational speed of n = 60000 rpm. In order to allow sufficient dust extraction, a NA35-D1-Type III Zone 22 extraction system from RUWAC, Melle-Riemsloh, Germany was used. The cutting force measurements were taken by fixing the CFRP plates over large screws directly onto the force measurement device type 9257B from KISTLER. The directions F_X, F_Y and F_Z are defined in Figure 3b.

3. Results and discussion

It has been previously shown by the authors in milling of CFRP with 60 % fibre content that the process forces can be reduced significantly due to the use of high speed cutting parameters. A 40 % reduction of the process forces could be achieved by increasing the cutting speed from v_c = 250 to v_c = 600 m/min. The workpieces machined with higher cutting speeds showed better surface qualities, with no delamination, fibre protrusion or thermal effects on the workpiece surface being observed [24, 25].

With the goal to increase the productivity further and to determine the limit between conventional machining and high speed machining phenomena, the cutting speed was then further increased to v_c = 1800 m/min, with a maximum spindle rotational speed of n = 60000 rpm. In Figure 4 the feed forces F_f and the tool life at different feed rates v_f and radial cutting depths ae are illustrated. At relatively low cutting depths and feed rates, the tools machined $L_{c,max}$ = 40 m without the wear criterion of VB_{max} = 0.2 mm being reached. It can thus be concluded that

longer tool lifetimes are possible, as a number of milling tools showed a width of flank wear land of $VB_{max} = 50\ \mu m$ after a cutting distance of $L_c = 40$ m.

It was also observed that the increase in the feed rate and radial depth of cut led to increased feed forces and reduced tool lifetimes. Besides the higher loading on the cutting edge at higher feed rates, which leads to higher tool wear rates, issues in relation to the capacity of chip and dust evacuation were also evident.
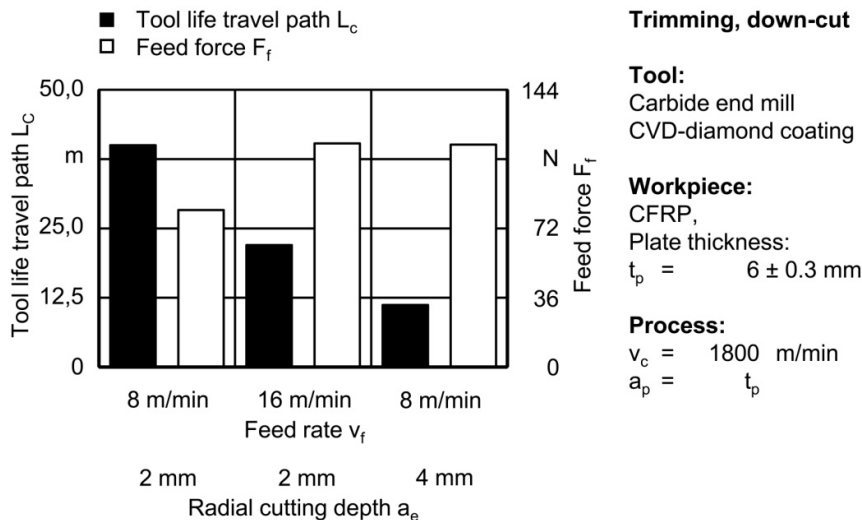

Fig. 4. Tool lifetimes at different HSC process parameters

Optical analyses of the milling process using a high-speed camera showed that the CFRP chips exit the flute periodically if end mills with a low helix angle are used and that the volume of the flutes are a limiting factor at high removal rates, as described in previously published articles [23, 25, 26]. If the dust evacuation is not sufficient, adhesion of CFRP material on the tool occurs, which leads to increased process forces and reduced tool lifetimes.

Current research and development goals are therefore the development of HSC cutting tool geometries with optimised geometries for chip and dust evacuation. At the same time, new technologies for extraction systems are also being developed. Within this work, a prototype extraction system with rotational speeds of up to n = 15000 rpm has been tested. The enormous potential of internal tool dust extraction could be shown at relatively low rotational speeds. It was observed that efficient dust extraction can be achieved with optimized internal extraction channels in the tool, which significantly reduces process forces (Figure 5).

In order to allow the effect of high speed cutting on the fundamental failure modes and chip formation mechanisms to be analysed, the influence of dust extraction and tool wear must be kept to a minimum. For that reason, circular pockets were milled using a relatively low radial depth of cut $a_e = 2$ mm. The process forces in dependence of the cutting speed and feed rate were determined and the machined surface quality analysed. Due to the circular milling path and force measurement on the workpiece, the maximum forces in the x-, y- and z-direction oriented on the machine/workpiece coordinate system are analysed.
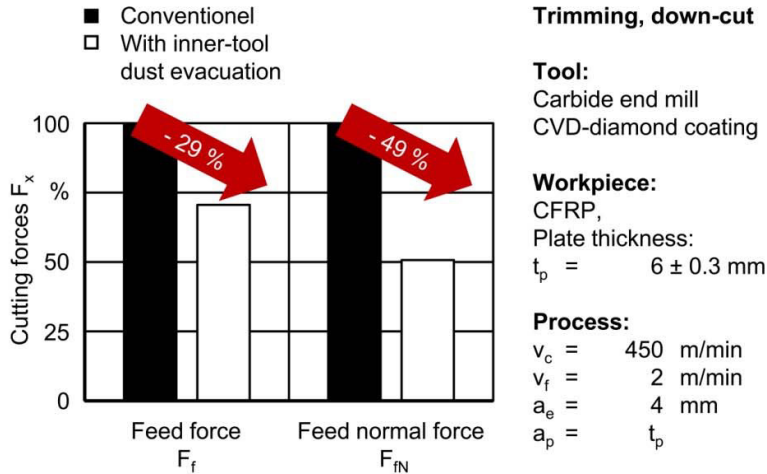
Fig. 5. Reduction of process forces by chip and dust extraction through internal tool extraction system

The measured forces in the y-direction and z-direction at difference cutting speeds and feed rates are shown in Figure 6. In comparison to conventional cutting parameters of v_c = 276 m/min and v_f = 5.3 m/min, all tested HSC process parameters led to a significant reduction of the cutting forces. The direct comparison between HSC cutting speed and conventional cutting speed at constant feed rate showed a reduction of 400 %. An increase in the feed rate has a lower influence on the cutting forces, although higher feed rates generally cause higher process forces.

With the goal of productivity increase in mind, the use of high cutting speeds in combination with high feed rates is of course most interesting. Results, as shown in Figure 6, show that an increase of the feed rate of 230 % in combination with high cutting speeds still leads to a reduction of cutting forces by 50 %. The reduction of the axial force component F_Z is particularly relevant in the milling of pockets, as high axial forces can lead to chatter and tool deflection and thus reduced component quality.
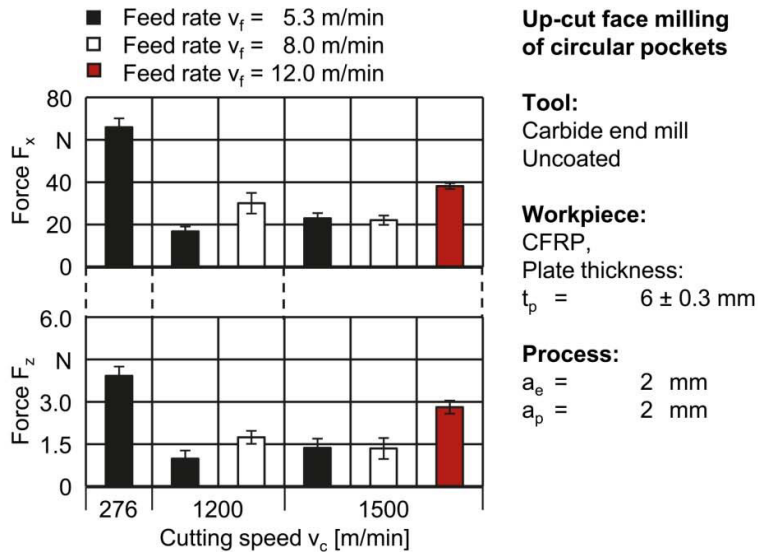
Fig. 6. Process forces using conventional parameters and HSC parameters

The guarantee of high quality workpieces is a second important factor besides productivity increase. Often, fibre delamination and protrusion occure. The machined surfaces at a fibre orientation with respect to the cutting direction $\theta = 0°$ were thus analysed using SEM images. Figure 7 shows the machined surfaces of the pockets. The pockets milled using HSC parameters with high material removal rates exhibit a high surface quality, with uniform fibre orientation without delamination or protrusions. Those pockets machined with conventional cutting parameters ($v_c = 276$ m/min and $v_f = 5.3$ m/min) have comparatively low part qualities. The structure of the fibres in the matrix materials is less uniform, with fibre protrusion of single fibres and fibre bundles. In both cases the tool´s geometry is identical and the fibre orientation with respect to the cutting direction was $\theta = 0°$. It can therefore be assumed that the use of high speed cutting parameters changes the fundamental failure modes and chip formation mechanisms.
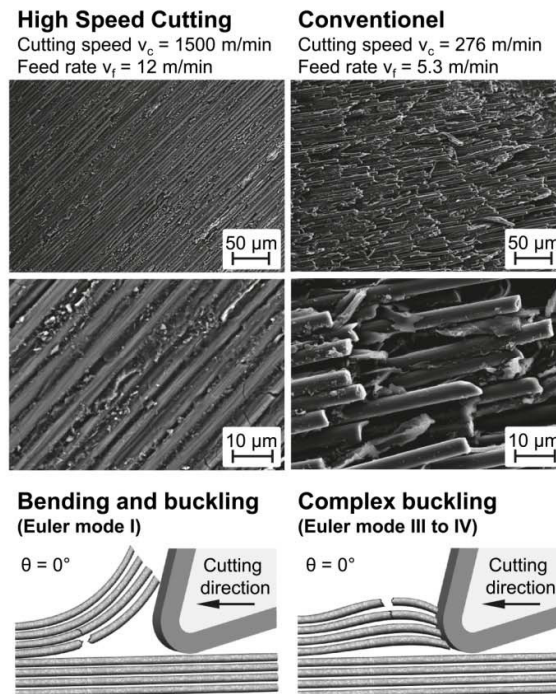
Fig. 7. Surface quality as result of changes in chip formation mechanisms at high speed cutting parameters for fibre orientation $\theta = 0°$

At conventional cutting parameters the chip formation can be described as a multistage looping process comprising of a periodical decrease of compressive stress in the tool material contact zone followed by progressive split propagation in the matrix material parallel to the fibre direction and finally ending in „brooming“ failure with multiple random spaced fibre splits after extensive fibre buckling and progressive fibre bending. The different failure mechanisms act together, although fibre buckling can be described as the main chip formation mechanism [10, 21].

With identical tool geometries with sharp and unused cutting edges as well as identical fibre orientation with respect to the cutting direction θ the chip formation mechanism changes due to the high speed cutting parameters applied. The SEM-analysis of machined surfaces with HSC-parameters allows the conclusion to be drawn, that the main chip formation mechanism changes into fibre bending, resulting in fibre cracking and "well-defined" splitting if the critical bending stress of the fibres is reached. These effects take place in a defined direction, mainly spaced in

the direction of the radial depth of cut, and produce a high surface quality with less damage of the subsurface, as depicted in Figure 7.

Similar changes in the chip formation mechanisms through an alteration of the cutting edge radii are described by a number of authors [7, 10, 11, 13, 18, 19, 20, 21]. These results showed that best surface qualities can be achieved using small cutting edge radii, as this allows for a more defined fibre failure. When cutting with higher cutting edge radii, fibre bending and particularly undefined fibre buckling become more dominant, which results in higher process forces and tool wear as well as lower surface qualities, as shown in Figure 2. In machining CFRPs, ideally sharp cutting edges should therefore be used. It must be noted however that extremely sharp cutting edges with radii $r_B < 5$ µm can only be produced with significant additional costs, and coatings of course lead to an increase in the cutting edge radius.

The approach followed here, to avoid extensive fibre and fibre bundles buckling through the use of HSC parameters, is independent of the cutting edge radius however. As exact description of the failure modes and cutting mechanisms at HSC parameters is currently being developed, a possible explanation is given by Xu and Zhang [20, 27, 28], who researched the mechanics of fibre deformation and fracture of unidirectional fibre-reinforced polymer composites in vibration-assisted cutting. It is described, that the use of high frequency vibrations, comparable to high dynamic accelerations due to the use of high speed cutting, is advantageous for achieving high surface integrity. The high frequency vibrations lead to a rapid increase of tensile stresses and the critical tensile stress, required for fibre fracture and defined cutting of fibres, is reached faster than without ultrasonic assistance.

The failure mechanisms observed in the SEM analysis can also be explained theoretically. Through a combination of technical mechanics and strength theory, a stress hypothesis according to the acting load type can be made. At a fibre orientation with respect to the cutting direction of $\theta = 0°$, the main loading direction is a compressive loading in the fibre direction, which leads to Euler buckling. According to Euler, four different relevant buckling cases can be differentiated between. Using this for the analysis of CFRP chip formation mechanisms at high speeds, allows a classification of fibre orientation with respect to the cutting direction $\theta = 0°$ as buckling case I, in which the compressive loading leads to bending of the fibres. Conventional speeds presumably lead to the complex buckling cases Type III and Type IV, which lead to complex buckling with bending of fibres in different planes and directions. Euler's theory states that in a load situation of Type IV, approx. 16 times the buckling load is necessary compared to Type I in order to cause a fibre breakage. This may explain the significant reductions in the cutting forces at higher cutting speeds, which allow a Type I buckling to occur.

This theoretical explanation is supported through analyses of CFRP workpieces. Finnegan et al. [29] studied the compressive response of carbon fiber composite parts and showed that the two main failure modes were delamination and Euler buckling. The measured peak stress occurs before any visible failure such as cracking or shearing is observed, associated with large bending deformation that precedes the onset of Euler buckling. The experimental studies confirmed that complex Euler buckling cause higher forces compared to other failure modes.

The discussed results and explanations relate to one CFRP material and only a fibre orientation with respect to the cutting direction of $\theta = 0°$ was studied in this case. Of course, the loading situation is impacted by both the mechanical and thermal loads. In order to allow a first estimation of the influence of thermal conditions, additional process cooling using a vortex tube was used. Results showed that when using uncoated milling tools with HSC process parameters, cooling led to increased feed forces but lower tool wear rates (Figure 8).

It is known from literature, that cooling the machining process leads to an embrittlement of the CFRP matrix material and thus may lead to better chip formation mechanisms. However, a higher alteration in the thermal load may lead to higher tool wear [30, 31]. The results of the work described here showed that the use of process cooling in HSC machining of CFRP can have significant advantages in relation to tool life. Detailed analysis of the impact of cooling on the chip formation mechanisms and failure modes is a current research topic at the IWF.
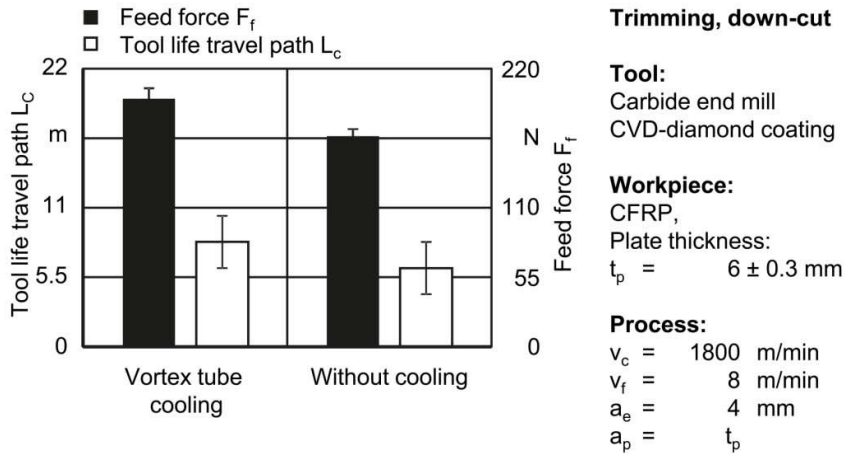
Fig. 8. Impact of vortex cooling on process forces and tool wear in HSC milling of CFRP

4. Economical assessment

An important criterion for the evaluation of productivity in CFRP machining is the material removal rate Q_W. In order to allow a direct comparison of the maximum material removal rates using HSC parameters, industrially used process parameters for conventional milling (cM) and of alternative processes were calculated, as shown in Figure 9. Within the described tests using HSC parameters, material removal rates of $Q_W = 288$ to 384 cm^3/min were validated, with CVD diamond coated tools reaching high tool lifetimes at such high material removal rates (see Figure 4). The increase of the material removal rate compared to conventional milling is therefore more than +300 %.

The typical removal rates for the alternative processes were taken from literature, with ablation rates for laser machining of CFRP ranging from $Q_W = 0.03$ to 0.04 cm^3/min [32, 33]. New results from Onu et al. [34] showed that through a further development of the process strategy and the laser parameters, higher ablation rates of $Q_W = 0.06$ cm^3/min could be reached.
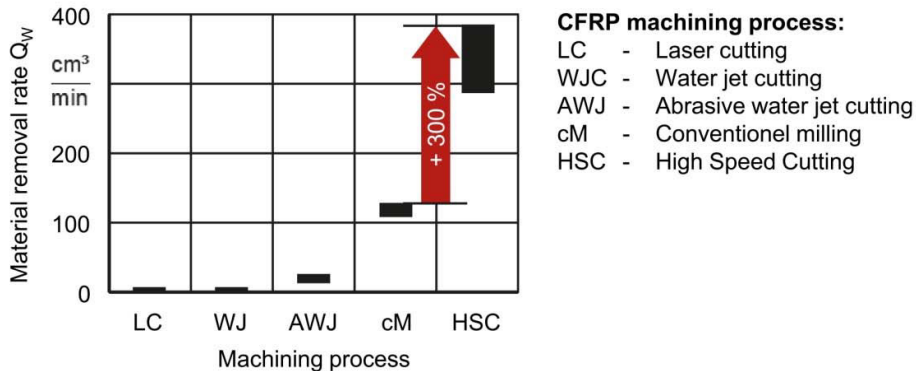
Fig. 9. Productivity of HSC milling compared to conventional milling and alternative processes [32, 33, 34, 35, 36]

The material removal rates for laser cutting shown in Figure 9 are for the maximum thickness which can be machined, $a_p = 2$ mm and a typical width of kerf $a_e = 0.2$ mm. For waterjet-based processes, feed rates $v_f = 0.1$ to

0.6 m/min (water jet cutting - WJC) and v_f = 2.1 to 4 m/min (abrasive water jet cutting - AWJ) are recommended for CFRP machining, with a plate thickness of a_p = 6 mm and a radial depth of cut a_e = 1 mm [35, 36].

It can be concluded that using HSC milling allows for a significant productivity increase compared to conventional milling and current alternative processes. Of course it must be noted that the material removal rate is only one indicator for productivity, as the required workpiece quality and the tool wear rates also play important roles in relation to tool costs and idle times. Finally, investment costs for machine tools and periphery must also be considered.

5. Conclusions

Milling of CFRPs with high cutting speed allows a productivity increase and thus has enormous cost saving potential. HSC milling of CFRPs can also positively influence the workpiece quality and as such reduce waste and necessary post-machining work.

It is however not as trivial as simply increasing the cutting speed. HSC of CFRPs must be understood as a complete system of cutting tool geometry, machine tool conditions and process parameters. Key factors for successful HSC milling are tool geometries with low tolerances, with macro and micro geometries that have been adapted to the requirements of CFRP milling. Furthermore, the machine tool, clamping of tool and workpiece and the dust extraction system must all be adapted for HSC milling. The mechanisms of HSC machining of metallic materials have been the focus of research work for a long time. The effects of force and temperature decreases as well as the influence of HSC parameters on the chip formation are therefore largely known. However, in CFRP machining, these effects have thus far not been analysed, and due to the complex nature of the matrix and fibre composite, pose questions which remain to be answered.

Within this work the authors showed, for the first time, that the use of HSC parameters in comparison to conventional cuttings speeds leads to a fundamental change in the chip formation mechanisms in CFRP machining. A correlation between reduced process forces, workpiece qualities and higher cutting speeds was identified.

When evaluating the productivity of a process, the feed rate is of particular importance, as this largely defines the time required to produce a component. Higher feed rates generally lead to higher cutting forces and thus have a negative impact on tool lifetimes and workpiece quality [22]. Within the work presented here it could be shown that the significant increase in cutting speed led to a reduction in process forces. This reduction in forces can be used to increase tool life or to increase the feed rate whilst keeping tool life at a similar level. Results shown here demonstrated that high feed rates could be successfully used in combination with high cutting speeds, thus resulting in a drastic improvement in productivity.

Acknowledgements

References

[1] R. M'Saoubi, D. Axinte, L. Soo, C. Nobel, H. Attia, G. Kappmeyer, S. Engin, W. Sim, High performance cutting of advanced aerospace alloys and composite materials, CIRP Annals - Manufacturing Technology 64 (2015) 557-580.
[2] J. C. C. Rubio, A. M. Abrao, P. E. Faria, A. E. Correia, J. P. Davim, Delamination in High Speed Drilling of Carbon Fiber Reinforced Plastic (CFRP), Journal of Composite Materials 15 (2008) 1523-1532.
[3] S. Rawat, H. Attia, Characterization of the dry high speed drilling process of woven composites using Machinability Maps approach, CIRP Annals - Manufacturing Technology 58 (2009) 105-108.
[4] T. Geisa, C. Klingelhöllera, W. Hintze, Constant depth scoring of fibre reinforced plastic structures to prevent delamination, Procedia CIRP 14 (2014) 205-210.
[5] L. Sorrentino, S. Turchetta, Cutting Forces in Milling of Carbon Fibre Reinforced Plastics, Hindawi Publishing Corporation, International Journal of Manufacturing Engineering Volume 2014 (2014) 1-8.
[6] S. Alexandrakis, P. Benardos, G. C. Vosniakos, N. G. Tsouvalis, Neural surface roughness models of CNC machined Glass Fibre Reinforced Composites, International Journal of Materials and Product Technology (2008) 276-294.
[7] D. H. Wang, M. Ramulu, D. Arola, Orthogonal cutting mechanisms of graphite/epoxy composite. Part I-unidirectional laminate, ln. J. Mach. Tools Manufact. 35 (1995) 12, 1623-1638.

[8] S. Gordon, M. T. Hillery, A Review of The Cutting Of Composites Materials, Proceedings of the Institution of Mechanical Engineers, Part L: Journal of Materials Design and Applications, 217 (1) (2003) 35-45.

[9] J. P. Davim, P. Reis, Damage and dimensional precision on milling carbon fiber-reinforced plastics using design experiments, Journal of Materials Processing Technology 160 (2005) 160-167.

[10] R. Teti, V. Lopresto, A. Caggiano, High performance cutting of fibre reinforced plastic composite materials, Procedia CIRP 46 (2016) 71-82.

[11] D. Arola, M. Ramulu, D. Wang, Chip formation in orthogonal trimming of graphite/epoxy composite, Composites, 27A (1996) 2, 121-133.

[12] G. Everstine, T. Rogers, A theory of machining of Fiber-Reinforced Materials, J. Comp. Mater., 5 (1971) 94-106.

[13] Z. Hashin, A. Rotem, A Fatigue Failure Criterion for Fiber Reinforced Materials, Journal of Composite Materials 7 (1973) 448-464.

[14] A. Koplev, A. Lystrup, T. Vorm, Cutting process, chips and cutting forces in machining CFRP, Composites, 14 (1983) 4, 371-376.

[15] T. Kaneeda, CFRP Cutting mechanism, Proceeding of the 16th North American Manufacturing Research Conference, 1989, 216- 221.

[16] K. Colligan, M. Ramulu, The Effect of Edge Trimming on Composite Surface Plies, Manufacturing Review 5 (1992) 4, 274-283.

[17] M. Ramulu, Machining and surface integrity of fibre-reinforced plastic composites, Sadhana 3 (1997) 449-472.

[18] D. Purslow, Some fundamental aspects of composites fractography, Composites 12 (1981) 4, 241-247.

[19] A. Puck, Festigkeitsanalyse von Faser-Matrix-Laminaten: Modelle für die Praxis, Hanser, Wien, 1996.

[20] W. Xu, L. Zhang, Mechanics of fibre deformation and fracture in vibration-assisted cutting of cutting of unidirectional fibre-reinforced polymer composites, International Journal of Machine Tools & Manufacture 103 (2016) 40-52.

[21] D. Iliescu, D. Gehin, I. Iordanoff, F. Girot, M. E. Gutiérrez, A discrete element method for the simulation of CFRP cutting, Composites Science and Technology 70 (2010) 73-80.

[22] J. Xu, M. E. Mansori, Cutting Modeling of Hybrid CFRP/Ti Composite with Induced Damage Analysis, Materials 9 (2016) 1, 67-70.

[23] R. Hufschmied, S. Richarz, Hochgeschwindigkeitsbearbeitung von carbonfaserverstärkten Kunststoffen, VDI-Z Integrierte Produktion, Spezial Werkzeuge II 8 (2015) 32-33.

[24] E. Uhlmann, F. Sammler, S. Richarz, Machining of Carbon Fibre Reinforced Plastics, Procedia CIRP Volume 24 (2014) 19-24.

[25] E. Uhlmann, I. Rieck, Advanced machining processes for CFRP, Advanced Materials Research 1018 (2014) 67-74.

[26] E. Uhlmann, F. Sammler, S. Richarz, G. Reucher, R. Hufschmied, A. Frank, B. Stawiszynski, F. Protz, Machining of carbon and glass fibre reinforced composites. Procedia CIRP 46 (2016) 63-66.

[27] W. Xu, L. Zhang, A finite element analysis of fibre fracture in a polymer composite during vibration-assisted cutting, Proceedings of 8th Australasian Congress on Applied Mechanics, Engineers Australia, 2014, s1-s8.

[28] W. Xu, L. Zhang, Y. Wu, Elliptic vibration-assisted cutting of fibre-reinforced polymer composites: Understanding the material removal mechanisms, Composites Science and Technology 92 (2014) 103-111.

[29] K. Finnegan, G. Kooistra, H. N. G. Wadley, V. S. Deshpande, The compressive response of carbon fiber composite pyramidal truss sandwich cores, Int. J. Mat. Res. 98 (2007) 12, 1264-1272.

[30] N. Sorbo, J. Dionne, Dry Drilling of Stackup Composite: Benefits of CO2 Cooling, SAE Int. J. Aerosp. 7 (2014) 1, 156-163.

[31] Y. Yildiz, M. Nalbant, A review of cryogenic cooling in machining processes, International Journal of Machine Tools & Manufacture 48 (2008) 947-964.

[32] K. W. Jung, Y. Kawahito, S. Katayama, Ultra High Speed Laser Cutting of CFRP Using a Scanner Head, Transactions of JWRI, 42 (2013) 2, 9-14.

[33] V. Onuseit, R. Weber, M. Wiedenmann, C. Freitag, T. Graf, Efficient Laser Processing of CFRP. 8th International Conference on Photonic Technologies LANE 2014.

[34] V. Onuseit , C. Freitag , M. Wiedenmann, R. Weber, J.-P. Negel , A. Löscher, M. Abdou Ahmed , T. Graf, Efficient processing of CFRP with a picosecond laser with up to 1.4 kW average power, Proc. SPIE 9350, Laser Applications in Microelectronic and Optoelectronic Manufacturing (LAMOM) XX, 935012 (2015).

[35] K. Lange, M. Liewald, Umformtechnik: Handbuch für Industrie und Wissenschaft, Springer-Verlag, 2013.

[36] E. Uhlmann, M. Manthei, S. Motschmann, M. Bilz, Marktstudie Wasserstrahlschneiden 2011. Berlin: Fraunhofer IPK, 2011.

16th Machining Innovations Conference for Aerospace Industry - MIC 2016

Investigation of chip formation and workpiece load when machining carbon-fiber-reinforced-polymer (CFRP)

Marco Zimmermann[a]*, Lukas Heberger[a], Frank Schneider[a], Christian Effgen[b], Jan C. Aurich[a]

[a]University of Kaiserslautern, Institute for Manufacturing Technology and Production Systems, D-67663 Kaiserslautern, Germany
[b]Guenter Effgen GmbH, D-55756 Herrstein, Germany

Abstract

Carbon-fiber-reinforced-polymers (CFRP) are increasingly used in aerospace industry due to their superior material properties in comparison to non-reinforced materials. In order to manufacture components made of CFRP, cutting processes are often required. These are challenging and different from metal cutting because of the heterogeneous structure (matrix and reinforcement) and the material properties of CFRP. In this paper, the chip formation and the workpiece load are investigated regarding the cutting condition used when orthogonal cutting CFRP with fiber orientations of 45° and 135°. The workpiece temperature significantly decreases using a smaller cutting speed or feed for cutting. The cutting speed is the most important cutting parameter for chip formation. At low cutting speeds (e.g. v_c = 5 m/min), chips are formed. Concerning a cutting speed of v_c = 100 m/min, the CFRP is removed by material fracture.

Keywords: Cutting; Chip formation; Carbon-fiber-reinforced polymer

1. Introduction

Carbon-fiber-reinforced-polymers (CFRP) have a high strength and low density. Therefore, CFRP is beneficial - especially in fields where reducing weight and increasing stiffness are needed. CFRP is already used in current aircrafts, like the Airbus A380 that is made of almost 25 weight percent CFRP [1] or the A350 that is made of 53 weight percent CFRP [15]. In the future, an increasing application of CFRP is also expected in the automotive industry

---

* Corresponding author. Tel.: +49-631-205-2872; fax: +49-631-205-3238.
  E-mail address: marco.zimmermann@mv.uni-kl.de

[2]. Although components of CFRP can be manufactured near net shaped, machining is often required in order to achieve demanded workpiece geometries [3]. However, the knowledge in machining of metal, e.g. regarding the chip formation or tool wear, cannot be transferred to the cutting of CFRP, because CFRP is anistropic, inhomogeneous and barely plastically deformable [4]. Many investigations focus on the enhancement of the tool, the determination of an optimal cutting condition, and the detection of workpiece damages when machining CFRP. Typical damages of the workpiece are delamination, fiber fracture or fiber pullout, and the thermal overload of the matrix [5].

The chip formation and the thermal and mechanical workpiece and tool load play an important role in terms of the machining quality and the tool life [6]. The loads determine the deformation of the workpiece during cutting and thus the accuracy of machining. Moreover, the material properties and the damage of the workpiece are affected by the thermal and mechanical workpiece load. Measurements of the tool temperature and the workpiece temperature during milling of CFRP plates with layers of a different fiber orientation were presented by KERRIGAN ET AL. [7] and YASHIRO ET AL. [8]. They showed that the cutting condition significantly affects the temperature distribution in the workpiece and the tool and the magnitude of their thermal load. Investigations of chip roots with e.g. the quick-stop-method or the investigation of chip formation using a high speed camera are appropriate methods to evaluate the (mechanisms of) chip formation. This is well documented when machining metal, but less in machining of CFRP particularly with respect to CFRP with multiple fiber orientations. KOPLEV ET AL. [9] revealed that the cutting of unidirectional CFRP is a series of material fractures, which result in chips. Several researchers carried out orthogonal cutting tests on unidirectional CFRP in order to investigate the mechanisms of chip formation. They found that the cutting mechanism is affected by the fiber orientation [10], the tool geometry [1], and the cutting condition [14]. The fiber orientation, the cutting edge radius, and the feed were assessed as the most important parameters for chip formation.

In this paper, the influence of the cutting condition on the process forces, the temperature of the workpiece, and the chip formation is investigated in orthogonal turning of CFRP with fiber orientations of 45° and 135°.

2. Experimental design

Orthogonal cutting investigations were carried out on a five-axis machining center without the use of a cutting fluid (Fig. 1). The geometry of the cemented carbide (90 % tungsten carbide, grain size: 0.2 - 0.5 µm; 10 % cobalt) tools used is listed in Table 1. A new cutting edge was applied for each investigation. The results are thus not affected by tool wear. The workpiece material used was a carbon-fiber-reinforced-polymer with an epoxy resin matrix (60 % fiber volume content; fiber diameter: 7 µm). The orientation Θ of the fibers on a workpiece was $\Theta = 45°$ and $\Theta = 135°$, i.e. the fibers are crossed (Fig. 1c). The fiber orientation is defined counterclockwise with regard to the direction of primary motion, i.e. a fiber orientation of 0° specifies a parallel orientation of the fibers to the direction of primary motion. The values of the cutting parameters are depicted in Table 1. A cutting speed of 5 m/min is low and appears to be beyond of an industrially relevant range. However, such a cutting speed is of scientific interest. Moreover, the cutting speed in drilling significantly decreases from the maximum at the outer diameter of the drill to the minimum in the center. The cutting speed in drilling thus is at least in a part of the cutting edge in accordance with the considered cutting speed of 5 m/min. The removed material volume (approximately 500 mm³) was the same for each cutting condition in order to ensure the comparability of the results.

Table 1. Tool geometry and cutting conditions.

Tool geometry (ISO-code ODMW 050408)		Cutting parameters
Clearance angle: $\alpha = 15°$	Tool cutting edge angle: $\kappa = 0°$	Cutting speed v_c [m/min]: 5, 20, 40, 60, 80, 100
Rake angle: $\gamma = 0°$	Tool cutting edge inclination: $\lambda = 0°$	Depth of cut a_p [mm]: 2 (wall thickness of the tubes used)
Cutting edge radius: $r_\beta = 5$ µm	Cutting edge form factor $K = 1.0$	Feed f [mm/rev]: 0.025, 0.05, 0.075, 0.1, 0.4

The forces were measured by means of a dynamometer (sampling rate 10 kHz) and evaluated without filtering. Each cutting force and thrust force, shown in the results, is calculated from the mean over the time of cutting. A commercial thermographic camera was used to detect the temperature of the workpiece during orthogonal cutting (Fig. 1b). The thermographic camera operates with wavelengths from 1.5 µm to 5.1 µm (infrared). The frame rate applied was 100 frames per second. The coefficient of emission ε of the CFRP-tubes (workpiece, Fig. 1c) was

determined to $\varepsilon = 0.75$. Each image was evaluated directly before the process end. Beside the workpiece, further objects, such as the tool or the tool holder, are included in the images. However, the images were evaluated using the coefficient of emission of the CFRP-tube. Thus, the temperature of the further objects in the images does not depict the actual temperature of the respective object. The chip formation was recorded by means of a high speed camera using a frame rate of 4,000 frames per second for each investigation. In order to achieve appropriate images, two high power light sources were used (Fig. 1b). From the images captured, characteristic images were selected for the chip formation using a specific cutting condition. These selected images are illustrated in the Figures 2 and 3 in a consecutive order with respect to the process time.
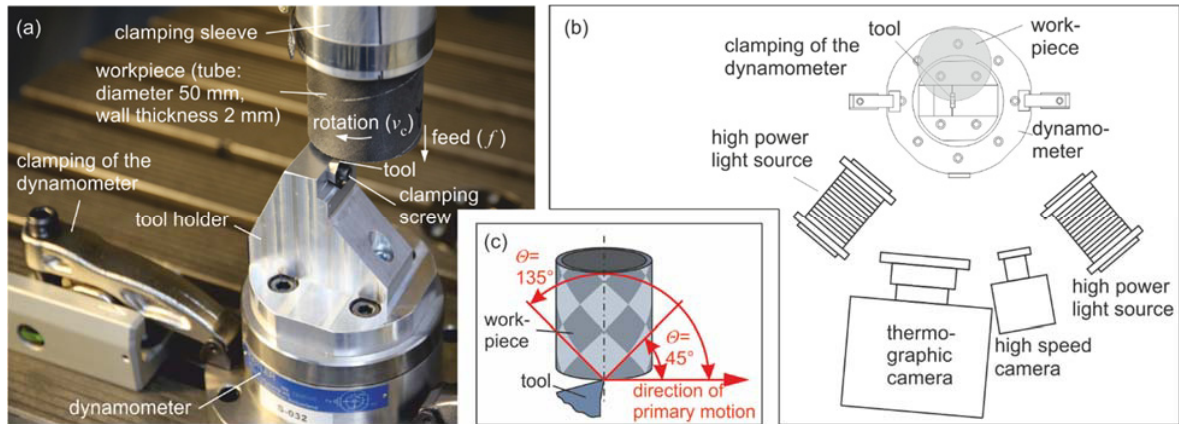
Fig. 1. (a) Experimental setup; (b) Top view experimental setup; (c) Workpiece.

3. Results

3.1. Chip formation

The cutting speed influences the removal of the material (Fig. 2). At the minimum cutting speed of 5 m/min, comparatively large chips are formed. The formation of these chips is occasionally accompanied with a partial fracture of the CFRP material. The fracture of the material causes the formation of small chips or "dust" like chips. The latter have very small dimensions in comparison to the cross-section of undeformed chip. Concerning cutting speeds of 60 and 100 m/min, the removed material is, contrary to a cutting speed of 5 m/min, completely fractured (Fig. 2).

In order to investigate a possible influence of the feed on the chip formation, feeds of 0.1 mm/rev and 0.4 mm/rev were used for orthogonal turning. A significant impact of the feed on the chip formation is not ascertainable (Fig. 3). With a rise of the process time, the chip length considerably increases at both feeds until chip breakage occurs.

CFRP consists of brittle carbon fibers and a more ductile matrix material. The carbon fibers determine the material removal mechanisms. During the cutting process, the carbon fibers undergo only a very small plastic deformation; they exhibit a brittle behavior with a very little strain to fracture [1]. In the present case, the fiber orientations are $\Theta = 45°$ and $\Theta = 135°$ (Fig. 1c). RUMMENHÖLLER [10] and LI [11] found that the material removal mechanism for the fiber orientation of $\Theta = 45°$ often is a combination of buckling, bending, and peeling when machining unidirectional CFRP. Peeling is due to the formation of cracks in the CFRP ahead of the cutting edge. The fibers of the orientation $\Theta = 135°$ are oriented in the direction of primary motion. As a result, these fibers undergo a smaller bending in comparison to $\Theta = 45°$ [13]. They fracture via a compression-induced shearing [1]. The described material removal mechanisms for the fiber orientations of $\Theta = 45°$ and $\Theta = 135°$ when machining unidirectional CFRP overlap in the present case of a CFRP with two different fiber orientations. An increase of the cutting speed leads to a higher relative velocity between the tool and the workpiece material ahead of the cutting edge, i.e. a larger impulse on the carbon fibers. Moreover, higher cutting speeds are accompanied with an embrittlement of the CFRP [6]. As a result, material fracture is facilitated at higher cutting speeds and smaller chips or even "dust" like chips are formed (Fig. 2).
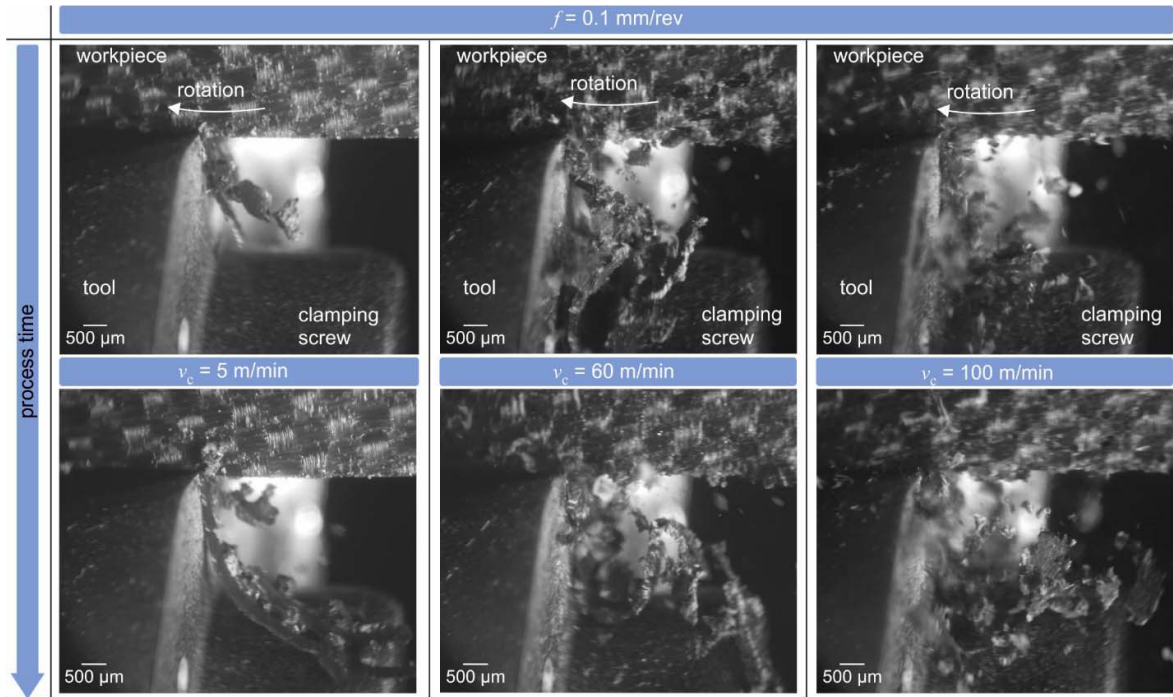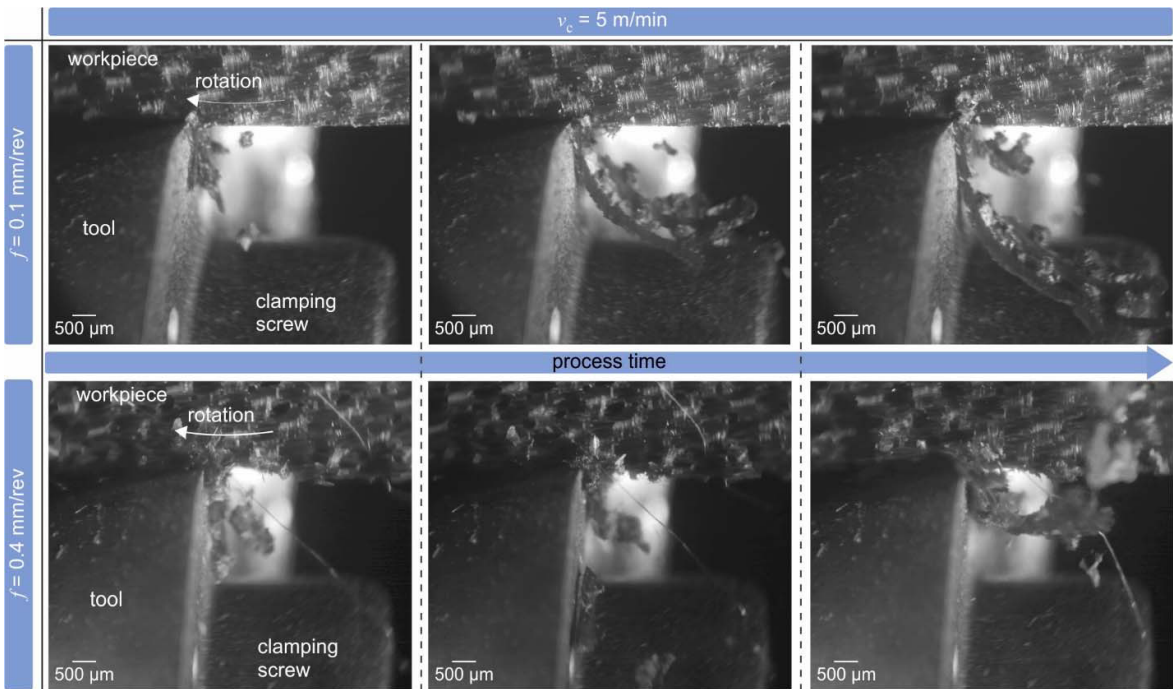
Fig. 2. Impact of the cutting speed on chip formation.

Fig. 3. Chip formation with regard to the feed and the process time.

3.2. Process forces

The cutting forces and the thrust forces are depicted in Figure 4 with regard to the cutting speed and feed used for orthogonal turning. The cutting forces are larger compared to the thrust forces, particular at high feeds and cutting speeds. An increase of feed causes larger cutting forces. The effect of the feed on the thrust force is indifferent at the given cutting conditions. The rise of feed does not generally lead to larger thrust forces. A significant impact of the cutting speed on the cutting force can only be observed when comparing the cutting force at a cutting speed of 5 m/min with the cutting forces at the higher cutting speeds investigated. The least cutting speed results in the minimum cutting force. Moreover, also the lowest thrust force was observed using a cutting speed of 5 m/min. The maximum cutting speed causes the highest thrust force.

The forces occurring during the machining of CFRP are determined by

- The energy required for the material separation.
- The energy required for the material deformation, chip fracture, and chip deflection.
- The pushing of material (e.g. particles of the fractured CFRP) under the cutting edge, and thus ploughing of this material in the newly generated workpiece surface.
- The friction at the flank face.
- The friction between the chips and the cutting material on the rake face.
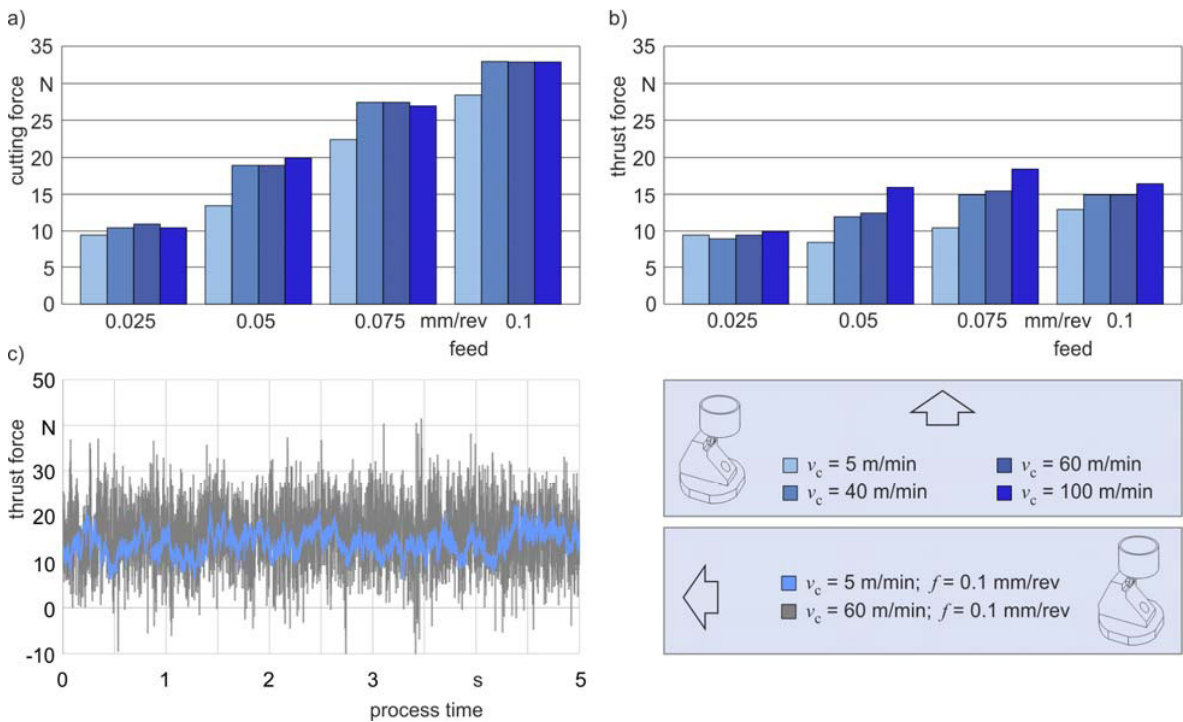
Fig. 4 (a) Cutting forces; (b) Thrust forces; (c) Raw signal of the thrust force regarding the cutting speed used.

The material removal mechanism differs between the minimum considered cutting speed and the other investigated cutting speeds, as already described in section 3.1. We believe that this difference in the material removal mechanism is the reason for the least cutting force when using a cutting speed of 5 m/min for turning. The large chips at the minimum cutting speed indicate that the material is separated from the bulk by peeling. On the contrary, the CFRP is completely fractured at the other cutting speeds. This leads to higher cutting forces in comparison to the peeling. The

oscillation width of the signal of the thrust force considerably rises at higher cutting speeds (Fig. 4c). Possible reasons are the pushing of material under the cutting edge, the stimulation of the unknown eigenfrequency of the setup, or the turning at a fractured position, i.e. sudden changes of the amount of removed material along the circumference of the workpiece. However, our images captured did not indicate the pushing of material under the cutting edge.

The greater the feed, the larger the undeformed chip thickness and thus the required energy for the material deformation, chip fracture, and chip deflection. Moreover, the contact length of the workpiece material with the rake face, and hence the friction work increases in orthogonal turning using higher feeds. Therefore, larger cutting forces and thrust forces arise when raising the feed.

3.3. Workpiece temperature

An increase of cutting speed (Fig. 5) or feed (Fig. 6) causes a rise of the workpiece temperature. Concerning a low cutting speed of 5 m/min, an elevated temperature of the workpiece due to turning is approximately only visible in the area of chip formation. The greater the cutting speed, the larger the heated volume of the workpiece material and the temperature values of the workpiece are. The effect of the feed on the workpiece temperature is in accordance to the described impact of the cutting speed. However, the cutting speed has within the investigated cutting conditions a superior influence on the workpiece temperature in comparison to the feed. The material removal rate increases with a rise of cutting speed or feed, i.e. more material is cut in a specific time-period. As a result, more fractured material is visible in the thermal images at higher feeds or cutting speeds than at the lower values of the cutting parameters.
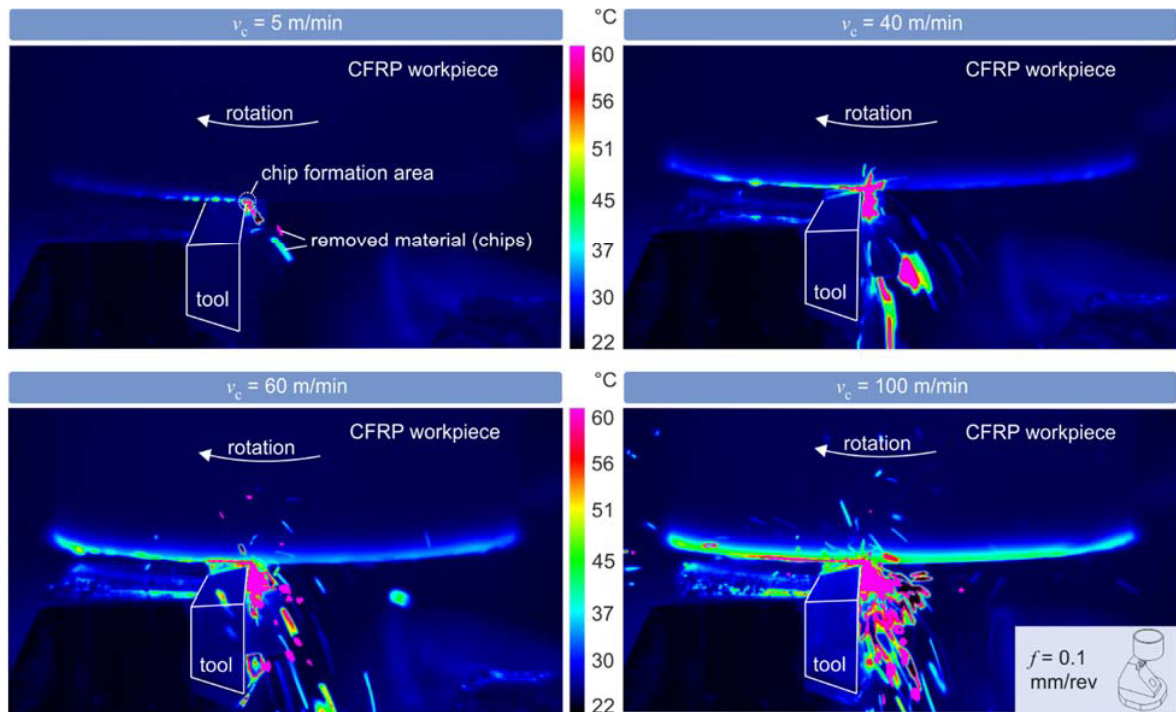

Fig. 5. Workpiece temperature in terms of the cutting speed.

For the evaluation of the thermal images, the maximum temperature was set to 60 °C because we were only interested in the temperature of the workpiece and not in the more elevated temperature of the chips. The use of the low maximum temperature for the evaluation facilitates the analysis of both the temperature change of the workpiece and the temperature distribution due to the precisely differentiated color scale. Tool and workpiece are stationary. The distance of a particular pixel (size 14 µm) of the detector to the heat source, i.e. the chip formation area, is the same

for all cutting conditions considered. The amount of mechanical energy dissipated into heat in the shear zones does not change with respect to the process time. Fuzziness inside of a pixel when measuring at different cutting speeds can thus only arise via a significant change of the material temperature during the aperture time (1.4 ms). Thus, we believe that the measurements are not influenced by fuzziness.
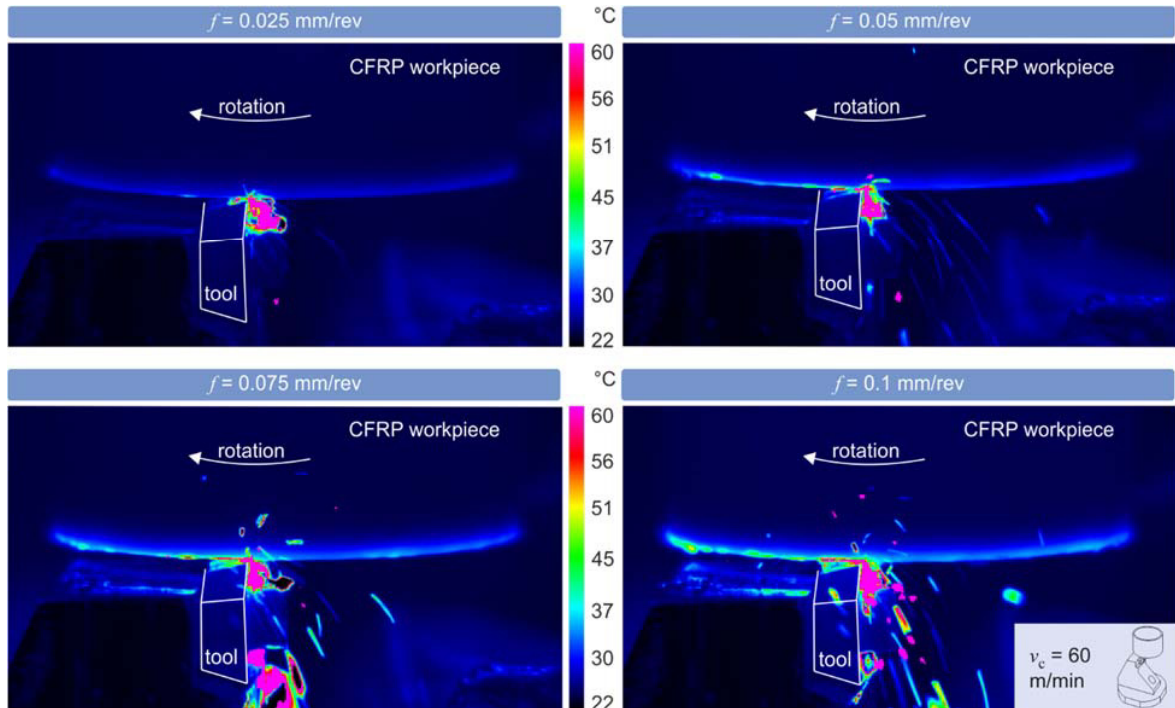

Fig. 6. Workpiece temperature with regard to the feed.

The thermal load of the workpiece is the result of the sum of the heat flow into the workpiece due to turning and the heat flow from the workpiece to the environment owing to forced convection. The longer the time of turning and the higher the temperature or the rotational speed of the workpiece, the larger the heat flow to the environment. The product of the cutting force, the cutting speed, and the time of turning approximately determines the mechanical energy required for turning. The mechanical energy is during the cutting of metal mostly converted into heat by the plastic deformation of the workpiece material and friction [12]. In turning CFRP, the workpiece material is only slightly deformed plastically. However, the thermal images revealed that the workpiece is subjected to a considerable temperature increase during turning. The heating of the workpiece is concentrated to a comparatively small material volume because of the low thermal conductivity of the CFRP. Taking the cutting speed of 5 m/min into account, the minimum thermal load of the workpiece is due to the smallest generated quantity of heat (overcompensation of the greatest time of turning through the least cutting force and cutting speed) and the significant heat flow to the environment owing to the long time of turning. The thermal image of the workpiece using a cutting speed of 5 m/min shows that the heated material volume of the workpiece is approximately cooled down to ambient temperature during a single workpiece rotation. The effective increase of the temperature, i.e. the difference of the workpiece temperature directly after chip formation and directly prior to chip formation, of a specific area along the circumference of the workpiece between consecutive rotations of the workpiece thus is, contrary to larger cutting speeds, negligible. At higher cutting speeds than 5 m/min, the temperature of a specific area increases with each rotation of the workpiece because the heat flow into the workpiece is at these cutting speeds superior compared to the heat flow to the environment. The generated quantity of heat is approximately the same at cutting speeds of 40, 60, and 100 m/min since the cutting forces are identical and the change in cutting speed and cutting time neutralize each other. Thus, the

difference in the workpiece temperature at cutting speeds greater than 5 m/min is primarily due to the varying heat flow to the environment. The rise of the workpiece temperature using higher feeds for turning is due to the larger generated quantity of heat in comparison to low feeds and the difference, in analogy to the cutting speed, in terms of the magnitude of the heat flow to the environment.

4. Conclusion

In this paper, the chip formation when orthogonal turning a carbon-fiber-reinforced-polymer (CFRP) and the mechanical and thermal loads of the workpiece were experimentally investigated with regard to the cutting condition used. The most important cutting parameter for the chip formation is the cutting speed. At low cutting speeds (v_c = 5 m/min), comparatively large chips are formed. At higher cutting speeds on the contrary, significantly smaller or even dust like chips arise. The feed has a non-significant impact on the chip formation. However, the feed affects the thermal and particularly the mechanical load of the workpiece. The greater the feed, the larger the mechanical and the thermal load of the CFRP workpiece. An increase of the cutting speed causes a considerable rise of the workpiece temperature. The forces measured revealed that the cutting speed primarily affects the thrust force, while the cutting force is within the cutting speeds considered approximately the same when using greater cutting speeds than 5 m/min.

Acknowledgement

References

[1] J.Y. Sheikh-Ahmad, Machining of polymer composites, Springer, Abu Dhabi, 2009.
[2] H. Jaeger, Carbonfaserverstaerkte Werkstoffe im Automobilbau, VCI Forum ''Chemie macht Elektromobil'', Berlin, 2011.
[3] Y. Karpat, B. Deger, O. Bahtiyar, Milling force modeling of multidirectional CFRP laminates, *Procedia CIRP* 1 (2012) 460-465.
[4] R. Teti, Machining of Composite Materials, *CIRP Ann - Manuf Techn* 51/2 (2002) 611-634.
[5] M. Henerichs, R. Voß, F. Kuster, K. Wegener, Machining of carbon fiber reinforced plastics: Influence of tool geometry and fiber orientation on the machining forces, *CIRP J Manuf Sci Techn* 9 (2015) 136-145.
[6] R. Voß, M. Henerichs, F. Kuster, K. Wegener, Chip root analysis after machining carbon fiber reinforced plastics (CFRP) at different fiber orientations, *Procedia CIRP* 14 (2014) 217-222.
[7] K. Kerrigan, J. Thil, R. Hewison, G.E. O`Donnell, An integrated telemetric thermocouple sensor for process monitoring of CFRP milling operations, *Procedia CIRP* 1 (2012) 449-454.
[8] T. Yashiro, T. Ogawa, H. Sasahara, Temperature measurement of cutting tool and machined surface layer in milling of CFRP, *Int J Mach Tool Manu* 70 (2013) 63-69.
[9] A. Koplev, A. Lystrup, T. Vorm, The cutting process, chips, and cutting forces in machining CFRP, *Composites* 14/4 (1983) 371-376.
[10] S. Rummenhöller, Werkstofforientierte Prozessauslegung für das Fräsen von kohlenstoffbasierten Kunststoffen, Dissertation, RWTH Aachen, 1996.
[11] H. Li, X. Qin, G. He, Y. Jin, D. Sun, M. Price, Investigation of chip formation and fracture toughness in orthogonal cutting of UD-CFRP, *Int J Adv Manuf Tech* 82/5 (2016) 1079-1088.
[12] J.C. Aurich, M. Zimmermann, S. Schindler, P. Steinmann, Effect of the cutting condition and the reinforcement phase on the thermal load of the workpiece when dry turning aluminum metal matrix composites, *Int J Adv Manuf Tech* 82/5 (2016) 1317-1334.
[13] X.M. Wang, L.C. Zhang, An experimental investigation into the orthogonal cutting of unidirectional fibre reinforced plastics, Int J Mach Tool Manu 43/11 (2003) 1015-1022.
[14] N. Bhatnagar, N. Ramakrishnan, N.K. Naik, R. Komanduri, On the machining of fiber reinforced plastic (FRP) composite laminates, Int J Mach Tool Manu 35/5 (1995) 701-716.
[15] Airbus S.A.S.: A350 MSN2 rolls out of paint hangar with special 'Carbon' livery. <http://www.airbus.com/presscentre/pressreleases/press-release-detail/detail/a350-msn2-rolls-out-of-paint-hangar-with-special-carbon-livery/> - 09.08.2016.

16th Machining Innovations Conference for Aerospace Industry - MIC 2016

Automated and cost-efficient Production of Hybrid Sheet Moulding Compound Aircraft Components

M. Fette[a,b]*, M. Hentschel[a,b], F. Köhler[b], J. Wulfsberg[a], A. Herrmann[b]

[a] Helmut-Schmidt-University, Institute of Production Engineering, Holstenhofweg 85, 21129 Hamburg,
[b] CTC GmbH, Airbusstrasse 1, 21684 Stade, Germany

* Corresponding author. Tel.: +49(0) 40 / 6541 2610; *E-mail address:* marc.fette@hsu-hh.de   *and*   marc.fette@airbus.com

Abstract

Nowadays, innovative lightweight structures and highly complex aircraft components are made of modern lightweight materials such as carbon fibre reinforced plastics (CFRP). In this context current production technologies for fibre composite parts in aviation industry are generally characterised by long cycle times, sub-optimal material usage and a huge effort for reworking or finishing. A promising technology for the cost-efficient and time-saving manufacturing of lightweight, geometrically complex and functional components is the combination of thermoset Sheet Moulding Compounds (SMC) with chopped fibre reinforcements and pre-impregnated, tailored continuous fibre reinforcements in a single-stage compression moulding process. In comparison to conventional production technologies for composite materials this hybrid material and process technology obtains short cycle times, functional integration, a high freedom of design, an optimum material usage and less rework. For the manufacturing of cabin, cargo and also secondary structure aircraft components a direct implementation of metallic elements, such as inserts, and the use of recycled carbon fibres can be realised. Furthermore, this process technology can be fully automated to yield an increased economic efficiency.

Hence, this paper deals with the potentials of this new technology, especially regarding to cost reduction and saving of time, by analysing and simulating the holistic process chain for the production of appropriate reference parts. In addition, different production concepts, with various grades of automation, are considered in detail and compared to each other in reference to determined criteria.

1. Introduction and motivation

The aviation industry is a rapidly growing branch due to the increasing demand on passenger aircraft. About 36,800 orders for commercial aircraft are expected by the leading aircraft manufacturers until 2034 due to a rise of the passenger number of 4.7 percent per year [1, 2]. To improve the efficiency by reducing the total weight of future aircraft, the use of modern lightweight materials, such as CFRP, and appropriate design approaches are becoming increasingly important. Against this background, the development of highly productive and cost-efficient production technologies for carbon composite components and structures is one of the main objectives of the aviation industry. Nevertheless, most of the manufacturing processes for the production of fibre composite aircraft parts are expensive, time-consuming and not automated.

The combination of tailored, pre-impregnated continuous fibre reinforcements and Sheet Moulding Compounds reinforced by chopped fibres in a single-stage compression and curing process is a promising technology for the cost-efficient and time-saving production of fibre composite components. This hybrid material and process technology can be used to produce geometric complex, highly functional and lightweight cabin, cargo and also secondary structural parts for aerospace applications in an industrial way. In this context, the determination of the Level of Automation, related to economic and time aspects, has great relevance.

This publication deals with the development and potentials of the combination of SMC and pre-impregnated, tailored carbon fibre reinforcements for cabin, cargo and secondary structure applications in aerospace industry. Furthermore, the methodical determination of the level of automation for using this technology for the production of future aircraft components is another main objective of the current work. Considered criteria are the part complexity, the number of pieces, the rate of variant diversity and the required lead time.

Nomenclature

CFRP   Carbon Fibre Reinforced Plastics
FST   Fire, Smoke and Toxicity
GFRP   Glass Fibre Reinforced Plastics
LoA   Level of Automation
NC   Numerical Control
SCARA Selective Compliance Assembly Robot Arm
SMC   Sheet Moulding Compound
SoPI   Square of Possible Improvements
TFP   Tailored Fabricated Patch

---

2. State of the Art

Aircraft cabin and cargo components require various properties which limit the range of possible materials. Especially requirements concerning fire resistance, smoke density, toxicity, temperature resistance, compatibility to media and abrasion of the part surface lead to only a few applicable materials. At the same time, the materials have to enable adequate mechanical properties at a low weight and low material costs, see Fig. 1. [3, 4]
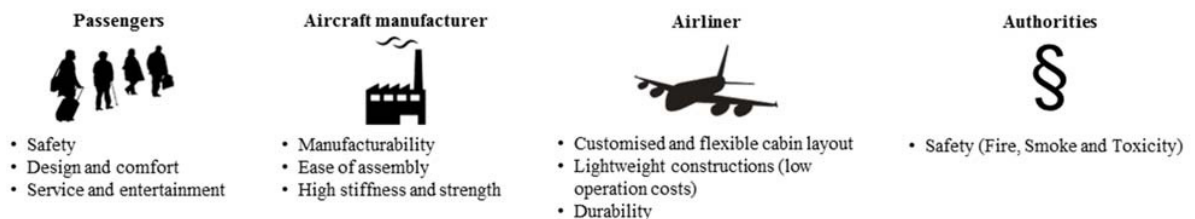

Fig. 1. Requirements on aircraft interior components.

All these and further requirements are fulfilled amongst others by sandwich structures. In general, these sandwich structures consist of aramid honeycomb cores and phenolic prepreg systems, reinforced by woven glass fibre fabrics as top layers. For that reason, cabin and cargo sandwich structures can meet the strict FST and lightweight requirements. [4]

2.1 Manufacturing of composite cabin and cargo components

Most of the aircraft interior components are made out of sandwich structures. The manufacturing of those components is characterised by numerous steps of manual work for several decades. Either the delivered sandwich plates have to be trimmed to the final contour or the honeycomb cores and the uncured top layers prepreg are formed, bonded and cured. Manual laminating methods and the crush core technology are exemplary state-of-the-art composite manufacturing processes for cabin and cargo components. After the curing step, holes are drilled where attachments, such as screens, mirrors or newspaper holders, are mounted later on. In those holes, connecting elements, such as metallic inserts, have to be positioned. By the use of core filler, the inserts and the sandwich structure are bonded. Depending on the part, the positioning of the inserts is manually or partly automated. In order to manufacture three dimensional components out of sandwich plates, all necessary sub-components have to be assembled. For this purpose and in order to protect the sandwich core against humidity and water, the sandwich edges are sealed by core filler. The sub-components are bonded afterwards. Both, filling the holes and sealing the cores, is done manually and cause insufficient reproducibility. [5]

Due to limited mechanical properties of the core filler the joint areas of the sub-components are reinforced by additional GFRP layers which are applied manually. As a consequence, the components mass varies in a comparatively wide range and the surface quality is often not sufficient. Many manual trowel and sand steps prepare the surface for painting and reduce the weight tolerances. All these necessary manufacturing steps make each part to a single piece, increase the lead time and raise the manufacturing costs.

2.2. Sheet Moulding Compound technology

The SMC technology is a process that is used to produce fibre reinforced plastic parts with chopped long fibres as reinforcement. For SMC semi-finished products, various fibre types, thermosets and additives are combined, depending on the required properties. Usually, they consist of unsaturated polyester, vinyl ester or epoxy resins that are reinforced by chopped carbon or glass fibres. Especially the additives influence the processability and the properties of the cured product significantly. For example, SMC for aircraft interior applications have to have a high content of flame retardants in order to fulfil all FST requirements. [6, 7]

Advantages of the SMC technology, compared to other technologies for producing fibre reinforced plastic parts, are low material costs, the opportunity of a fully automated process, short manufacturing times, a high material usage of almost 95%, the opportunity of complex three dimensional structures and the opportunity of functional integration of metallic components. Disadvantages of SMC components are comparatively low mechanical properties and the insufficient prediction of stress and material behaviour due to the flowability of the SMC during the compression moulding and a lack of adequate simulation methods. [7]

Currently, a few applications in the field of primary aircraft structures were already realised. Applications in the field of interior components are not developed yet. New improvements in the field of material development led to a qualified SMC by the Polynt Composites Germany GmbH and the Airbus Operations GmbH. With this SMC it is possible to establish the SMC technology in aircraft interior components in the future. [8]

3. Hybrid SMC

The combination of chopped fibre SMC and pre-impregnated, continuous fibre reinforcements in a single-stage compression moulding process, is a promising manufacturing technology for future cabin, cargo and also structural aircraft parts, illustrated in Fig. 2. This thermoset composite material and process technology combines the advantages of discontinuous and continuous fibre reinforcements to produce geometric complex, highly functional as well as load

path optimised lightweight components in a cost-efficient and quick way. The complexity and functional integration of these parts can be realised in particular by the excellent flowability of the SMC material during the compression moulding procedure and the direct integration of metallic elements, such as inserts. On the one hand, the high freedom of design can be useful for functional integration. On the other hand, lightweight design can be realised by new design approaches and high variety of stiffening elements. Furthermore, the lightweight potential can be increased by the load path optimised implementation of pre-impregnated continuous fibre reinforcements, such as woven fabrics, unidirectional fibres or tailored fibre placement patches. In comparison to current composite processes in aerospace industry, this new manufacturing method obtains a high productivity due to short curing cycle times in a range of 120 to 180 seconds, its ability to be fully automated and less time for finishing and assembly of the part. In addition to the mentioned facts, relatively low material costs and an excellent material usage of almost 90% make this hybrid technology very cost-efficient. [9]

Depending on the part requirements and surrounding thermoset matrix systems based on unsaturated polyester, vinyl ester or epoxy resins can be used. Moreover, the possibility of using recycled carbon fibre veils as reinforcements for special SMC formulations can increase the resource and energy efficiency of the production method. The carbon fibre veil can be made of dry chopped fibres from production waste or long carbon fibres from cured production waste or end-of-life aircraft components that are processed in a pyrolysis process. [10]

For cabin and cargo applications, the SMC matrix systems are based on unsaturated polyester resin with a high percentage on flame retardant additives, especially aluminium hydroxide due to the strict fire, smoke and toxicity requirements. Possible future applications in this area can be load carrying cabin monuments, highly functional overhead storage systems and complex linings. Apart from that clips cleats and brackets are possible exemplary applications for structural components which require epoxy-based resin systems. [11]
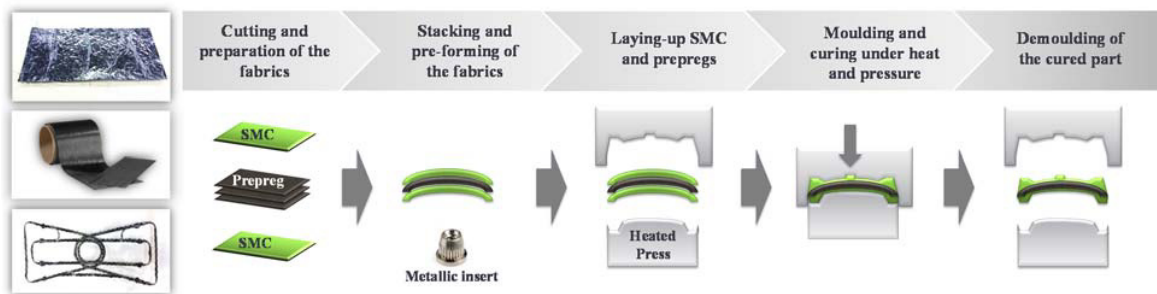

Fig. 2. Schematic process cycle for the production of hybrid SMC parts [11].

4. Estimation of LoA

The distinction between manual, semi-automated and fully automated systems is not enough to establish a cost-efficient production system. Such a system requires both an advanced technical system and skilled human workers and thus one needs a deep understanding of automation and ways to approach it to decide upon an appropriate LoA. Aspects, such as sharing of tasks, control and authority between humans and machines, are in the spotlight, especially when it comes to human-machine integration. The LoA concept is based on the assumption that a manual work task is performed without any tool or support simply by the human operator. With an increasing level, the support is increased or the operator gets tools as an aid. The highest level is reached when full automation is in place. Thus automation is not an "all or nothing" decision but should rather be seen as a continuum from manual to fully automated processes. Furthermore, automation is classified in physical and cognitive automation as a replacement for the respective human task. While physical automation refers to the mechanisation of tasks, such as replacing human operators with machines or robots, cognitive automation is defined as a computerised system that provides relevant information to operators. [12]

Frohm et. al. suggested a classification that takes the interaction between the two types of tasks into account; physical tasks and cognitive tasks and is applicable in all kinds of manufacturing contexts [12]. Each task can be

assigned to one of seven steps, from totally manual control to fully automatic and both scales (physical and cognitive) are independent from each other. The developed LoA scale is shown in Table 1.

Table 1. Level of Automation defined by Frohm et. al. [12]

LoA	Mechanical and Equipment (Physical)	Information and Control (Cognitive)
1	Totally manual - Totally manual work, no tools are used, only the users own muscle power	Totally manual - The user creates his/her own understanding for the situation, and develops his/her course of action based on his/her earlier experience and knowledge.
2	Static hand tool - Manual work with support of static tool, e.g. screwdriver	Decision giving - The user gets information on what to do, or proposal on how the task can be achieved, e.g. work order
3	Flexible hand tool - Manual work with support of flexible tool, e.g. adjustable spanner	Teaching - The user gets instruction on how the task can be achieved, e.g. checklists, manuals
4	Automated hand tool - Manual work with support of automated tool, e.g. hydraulic bolt driver	Questioning - The technology questions the execution, if the execution deviates from what the technology considers being suitable, e.g. verification before action
5	Static machine/workstation - Automatic work by machine that is designed for a specific task.	Supervision - The technology calls for the users' attention, and direct it to the present task, e.g. alarms
6	Flexible machine/workstation - Automatic work by machine that can be reconfigured for different tasks, e.g. CNC-machine	Intervene - The technology takes over and corrects the action, if the executions deviate from what the technology considers being suitable, e.g. thermostat
7	Totally automatic - Totally automatic work, the machine solves all deviations or problems that occur by itself, e.g. autonomous systems	Totally automatic - All information and control are handled by the technology. The user is never involved, e.g. autonomous systems

The presented scale is used in the DYNAMO++ methodology to assess the current LoA and decide upon relevant min- and max values of a possible future state. The methodology consists of four stages: Pre-study, measurement, analysis and implementation. [13]

Starting point is the process flow. All necessary process steps are identified and brought into a logical order, resulting in a flow chart. The process chain of an interior part, manufactured in SMC technology, is shown in Fig. 3. In the following analysis, the operations "Cutting", "Stacking" and "Press" and "Mechanical processing" are in the focus of interest as they are the characteristic steps of the SMC technology. In the subsequent phase, the current LoA of the tasks within the process chain is measured. Afterwards, in the analysis phase, the relevant min- and max levels are defined. Those reveal the potential for process automation and set the frame for possible future improvements. The relevant minimum LoA is equal to a solution where the work can be carried out at a sufficient speed, acceptable costs and working environment while the relevant maximum LoA is a possible technical solution without exceeding cost limits. It is important to keep in mind that automation should only be considered to a degree where it is justifiable regarding investment costs, rigidity and manual backup in case of fatal breakdowns. [14]
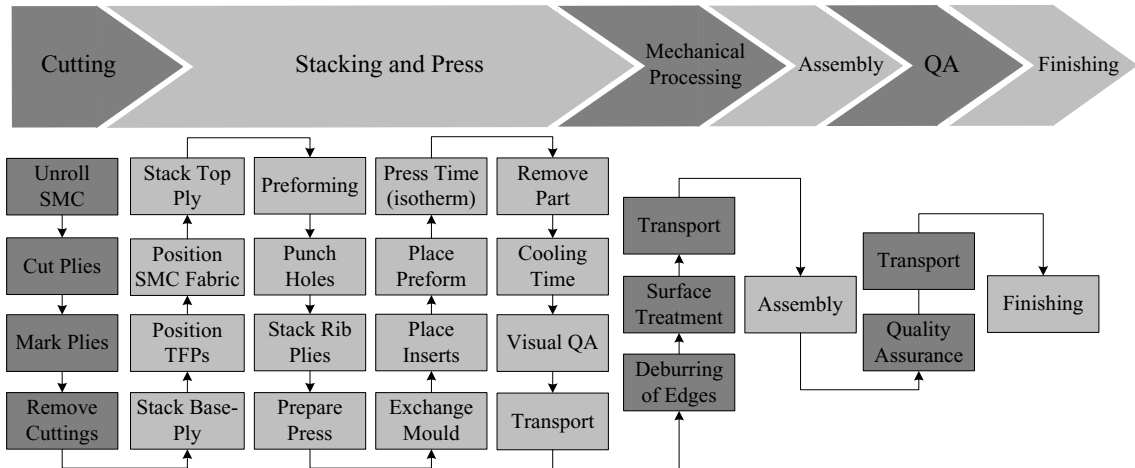
Fig. 3. Flowchart of the manufacturing of an aircraft interior component.

The outcome of the analysis is the Square of Possible Improvements, a two dimensional matrix that contains the range of possible cognitive and physical LoA for each task. Inside the obtained area, there are several possible solutions. The most time-consuming tasks are investigated further to obtain significant time savings. Thus, the results of "Cut the SMC plies", "Position TFPs and rib plies", and "Mount inserts in mould" are plotted in the SoPI below (see Fig. 4). Their percentage contribution to the total lead time is 28%, 14% and 8%, respectively. All other 16 tasks make up for the other 50%.
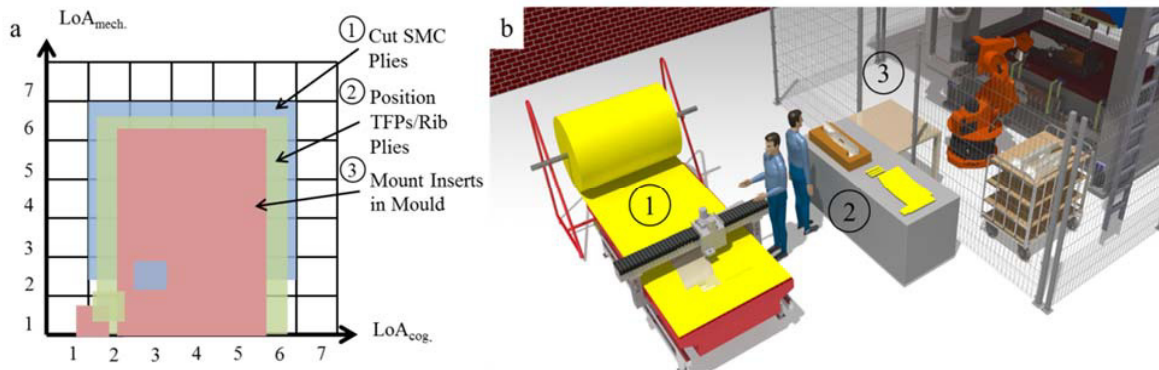
Fig. 4. (a) SoPI showing the automation potential and the current level of automation; (b) suitable man-machine concept.

The matrix shows a great potential to automate as the current levels are very low and the solution space in contrast is very wide. As the SMC technology obtains the possibility of functional integration the complexity of lay-up and preforming activities increases with the degree of functional integration. This calls for a higher cognitive automation to provide the operator with information and guidance. In this way, cycle times and errors are reduced. They would otherwise lead to costly rework or high scrap rates. Solutions include the use of template or laser projection systems, in combination with hand devices or screens. They show the operator which step has to be performed next and which ply and insert are needed to complete the task.

In the example of the manufacturing of a functional cabin lining used in a single aisle aircraft with a production rate of 50 aircraft per month, a combination of cognitive and mechanical automation is necessary to achieve the required lead time. The component appears in two variants with a total production volume of 4,600 parts per year.

Before determining the appropriate levels, a pairwise comparison is done considering cycle time, costs (non-recurring and recurring costs), ergonomics, safety and reproducibility, while the first two of them turn out to be most crucial criteria. Furthermore, several concepts are developed and a cost-utility-analysis performed to evaluate the most suitable concept. One of the most preferable concepts is visualised in Figure 4b. Special attention is turned to the previously identified, most time consuming process steps. To evaluate the relevant cycle times, different scenarios are simulated to achieve robust results.

In case of cutting the SMC plies the use of a NC-cutter is most favourable realising time savings up to 70% due to a 10 times higher cutting speed. The use of a NC-cutter reflects a LoA_{mech} of 6 and a LoA_{cog} of 5 to 6, depending on the use of a visionary system. The stacking and preforming require a lot of crafting skills and experience. Additionally, several automation concepts are imaginable. The use of a SCARA or parallel kinematic robot (LoA_{mech} of 6) would reveal the greatest time savings. But the costs for such a system are not justifiable considering the desired production volume and complexity of the preforming step. Instead, a rather low mechanical level is chosen. The operator uses specially designed templates to assure reproducible results and adequate cycle times at moderate costs. This represents a LoA_{cog} of 4 to 5, while LoA_{mech} of 1 to 2 is kept rather low.

The task of "Mount the inserts in the mould" is not only characterised by long cycle times but by ergonomic issues as well. The operator has to work very close to the hot tool (circa 145°C) and needs to wear safety equipment which makes the handling of the inserts more complicated. The use of a manipulator, such as an articulated robot (LoA_{mech} of 6) would reduce the cycle time and at the same time avoid bad ergonomics. Another option is to equip the operator with a handling tool to avoid working too close to the mould and use scratch marks or laser projection systems to assure a reproducible placement. This scenario would generate less investments costs and is characterised by a lower mechanical LoA of 2 to 3 and a higher cognitive level of up to 5. The great potential of the first scenario is that once the robot is installed to perform the insert mounting. Other tasks such as placing the preform and demoulding can be performed as well. This enables further time savings, avoids safety issues and frees up the operator for other tasks like stacking while the part is cured. If the robotic system is further developed, it can take over quality assurance tasks, e.g. by using a camera system to perform a visual check. This would otherwise be done by a human operator. If a human-machine system is chosen, it needs to be considered that appropriate safety equipment is necessary which increases the investment costs. Furthermore, the work space of human operator and robot needs to be separated.

5. Conclusion and outlook

The hybrid SMC technology obtains a lot of advantages in the field of aircraft applications, compared with current composite materials and manufacturing processes, especially for interior components. The main benefits of the SMC technology are cost-efficient processes and materials, the opportunity for parts with complex 3D shapes, a high reproducibility, tailored mechanical properties and short lead times. In order to exploit the maximum potentials of SMC for such aircraft parts, it is necessary to deeply analyse the boundary conditions for the manufacturing of those parts, e.g. part design including geometrical complexity and functional components or number of units per year, before planning the process chain and evaluating and adjusting the LoA for each station. As a result, the presented preforming step requires a higher level of cognitive automation with an increasing complexity of preforms in order to keep the manufacturing time and the reproducibility within reasonable limits. A low production volume of SMC components requires high cognitive aids but no fully automated manufacturing systems whereas fully automated solutions become necessary for very high production rates. Also ergonomic and industrial safety issues have to be considered for the adjustment of the LoA. Finally, defining the LoA influences further processes, like the quality assurance and documentation. Hence, choosing the most suitable automation concept requires detailed planning and considering the complete process chain. Consequently, in-line process monitoring during the SMC production and other automated quality assurance measures may create great benefits and adds to the overall system performance.

References

[1] I. Hartbrich, Airbus geht neue Wege in der Flugzeugproduktion, in: VDI-Nachrichten, ed. 21, 2014.
[2] HAR, Boeing prognostiziert Nachfrage nach 36800 neuen Flugzeugen, in: VDI-Nachrichten, ed. 29/30, 2014.

[3]   C.-C. Rossow et al., Handbuch der Luftfahrzeugtechnik, Hanser, Munich, 2014.
[4]   Airbus S.A.S., ABD0100.1.6 - Equipment - Design - General Requirements For Suppliers, Airbus S.A.S., Toulouse, 1998.
[5]   H.-D. Berg, Processing and Manufacturing of Interior Components, in Proceedings: Improved Fire- and Smoke-Resistant Materials for
      Commercial Aircraft Interiors, National Research Council Staff, Washington, DC, USA, National Academies Press, 1995.
[6]   H. Schürmann, Konstruieren mit Faser-Kunststoff-Verbunden, 4th ed., Springer, Berlin, 2014.
[7]   H.G. Kia, Sheet Molding Compound Materials: Science and Technology, Hanser Gardner Publications, Cincinnati (OH), 1993.
[8]   N. Stoess et al., New flame-retardant SMC for Aerospace Applications, in: Proceedings of the 15th European Meeting on Flame Retardancy
      and Protection of Materials (FRPM) 2015, BAM, Berlin, Germany, 2015, T31.
[9]   M. Fette et al., Combination of carbon fibre sheet moulding compound and prepreg compression moulding in aerospace industry, in:
      Procedia Engineering, Volume 81, 2014, pp. 1601-1607.
[10] M. Fette et al., Resource Efficient and Sustainable Production of Secondary Structure Aircraft Components by Using Carbon Fibers for
      Sheet Molding Compounds, in: Proceedings of the 10th SAMPE CHINA 2015 Conference, Beijing, China, 2015, pp. 124-129.
[11] M. Fette et al., Hybrid Sheet Molding Compound Technologies for a New Generation of Cabin and Cargo Aircraft Components, in:
      Proceedings of the SAMPE Long Beach 2016 Conference, Long Beach, CA, USA, 2016, LB15-0096.
[12] J. Frohm, V. Lindström, J. Stahre, M. Winroth, Levels of Automation in Manufacturing, in: Ergonomia – International Journal of
      Ergonomics and Human Factors, Vol. 30, Issue 3, 2008.
[13] A. Fasth, J. Stahre, K. Dencker, Measuring and Analysing Levels of Automation in an Assembly System, in: 41st CIRP Conference on
      Manufacturing Systems, Tokyo, Japan, 2008.
[14] A. Fasth, J. Stahre, Does Level of Automation Need to Be Changed in an Assembly System? – A Case Study, in: 2nd Swedish
      Production Symposium (SPS), Stockholm, Sweden, 2008.

16th Machining Innovations Conference for Aerospace Industry - MIC 2016

Influence of the quality of rivet holes in carbon-fiber-reinforced-polymer (CFRP) on the connection stability

Lukas Heberger[a],*, Benjamin Kirsch[a], Tobias Donhauser[b], Sebastian Nissle[b], Martin Gurka[b], Sebastian Schmeer[b], Jan C. Aurich[a]

aUniversity of Kaiserslautern, Institute for Manufacturing Technology and Production Systems, Gottlieb-Daimler-Str., 67663 Kaiserslautern, Germany
bInstitut für Verbundwerkstoffe GmbH, Erwin-Schrödinger-Straße, Building 58, 67663 Kaiserslautern, Germany

Abstract

Components made of carbon-fiber-reinforced-polymer (CFRP) are frequently linked together via rivet connections. The machining of the holes of the rivet connections can cause damages such as delamination (layer separation) or fiber protrusion (non-cut fibers). Those damages affect the strength of the connections, since they weaken the structure and thus reduce the quality of the connection. In this paper three manufacturing strategies – conventional drilling, industrial state-of-the-art drilling , and circular milling – are compared with respect to the machining quality and the resulting connection strength with respect to trigger force (to initiate the rivet connection failure case) achieved.

The study revealed a direct relationship between the hole quality and the trigger force. The hole manufactured via circular milling resulted in the smallest variation in the cylindricity and the lowest delamination and fiber protrusion. The trigger force required to initiate failure was highest for the rivet connections manufactured via circular milling.

Keywords: drilling; milling; carbon-fiber-reinforced-polymers

* Corresponding author. Tel.: +49-631-205-5482; fax: +49-631-205-3238.
    E-mail address: lukas.heberger@mv.uni-kl.de

1. Introduction

Carbon-fiber-reinforced-polymers (CFRP) are composite materials with inhomogeneous and anisotropic properties with respect to the fiber orientation [1]. Because of its good mass-stiffness-ratio, CFRP is becoming increasingly popular in aerospace and automotive applications [2]. Thus, the Boing 787 or the Airbus A 350 already consist of 50 % CFRP [3]. The structures used are assembled of several CFRP components. The assembly is often implemented by means of rivet connections. A high-quality structure is (beside other criteria) characterized by a high strength to mass ratio, which implies a high quality for the riveted connections as they are load bearing elements in the structure. Occurring imperfections while machining rivet holes in CFRP are inter alia fiber protrusion and delamination. These imperfections at the rivet hole have a strong influence on the rivet hole connections as they weaken the material [4]. Compared to a hole without imperfections, holes with lower quality can lead to significantly lower strengths (about 11%) [16]. If the CFRP structure fails through external energy, the CFRP has excellent energy absorption properties especially when continuous fiber-reinforced [5]. Therefore CFRP is superior to metals at crushing [6] and thus, CFRP is used in energy absorbing structures.

Different machining strategies influence the quality of the rivet hole. Laser machining of CFRP can cause high thermal damage (micro-cracks, voids, and delamination) due to the high process heat [7]. Although recent work successfully investigated possibilities of combined laser machining and drilling [8], chip forming processes are commonly used to produce the holes in CFRP.

In [9] is shown, that the quality of the drilled rivet hole strongly depends on the drill-point angle. A larger drill-point angle leads to lower delamination around the hole entrance but higher delamination at the hole exit. When drilling the rivet hole, the damage can also be reduced by the choice of a suitable clamping [10].

Orbital milling (as shown in [11]) is a promising alternative for machining rivet holes of high quality in CFRP [12]. Also the circular milling (the end mill does not move in the direction of the tool axis) results in a reduction of delamination and fiber protrusion as compared with a drilling process [13].

To evaluate the CFRP's material strength after a drilling operation, different tests can be made as described in [17]. Combinations of these different test setups enable an efficient evaluation of the material strength [17].

In the present paper, the influence of the rivet hole's quality on the strength of the rivet connection is investigated by comparing three different manufacturing strategies: conventional drilling with a twist drill, drilling with a state of the art CFRP-drill and circular milling. The quality, described by the delamination and the fiber protrusion, is compared. Finally, the influence of the quality on the trigger force is compared. The trigger force is the force that is necessary to initiate a progressive hole bearing failure (a measure for the connection strength).

2. Experimental setup

For the experimental characterization bidirectional CFRP plates as tensile specimen with 12 layers [0°,90°,0°,90°,0°,90°,90°,0°,90°,0°,90°,0°] were manufactured from the unidirectional prepreg C100715038 supplied by SGL. The plates were cured for 1 h at 130 °C and 24 bar in an autoclave. Subjected to manufacturing tolerances, the tested plates had a thickness of 1.5-1.85 mm with fiber contents of 60 Vol.-%.

7 rivet holes for each of the three manufacturing strategies were made. 2 of them were cut to investigate the inner damage. 5 of them were used to analyze the influence of the rivet hole quality on the trigger force. The cutting edge radius and the cutting edge form factor of the tools were measured using an optical device based on the phase measuring fringe projection.

2.1. Manufacturing processes

For all three machining strategies, conventional drilling with a twist drill, drilling with a state of the art CFRP-drill, and circular milling (see Fig. 1. c), the CFRP plates were fixed in a fastening device, see Fig. 1. a). The fastening device consisted of a bottom and an upper part. The fastening device was attached on a 5-axis machining centers table, see Fig. 1. b). Dust, produced during the machining processes, was removed by a suction. A 3d-printed suction adapter guaranteed a complete elimination of the dust.
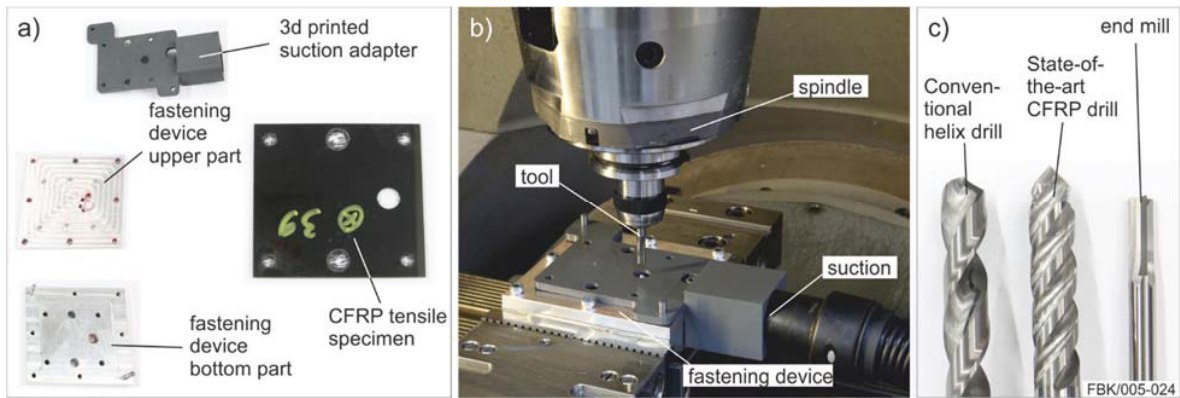
Fig. 1. a) Details fastening device; b) fastening device attached on 5-axis machining center; c) applied tools.

The conventional drilling process was representative for a non-optimized drilling process as a worst-case reference. The uncoated cemented carbide twist drills with a tool orthogonal rake angle $\gamma_0 = 30°$ had a diameter of 10 mm and drill point angle of $\sigma = 118°$. For the cutting edge radius each cutting edge of every tool was measured three times. Each measurement included 100 cross-sections. The average measured cutting edge radius was $r_\beta = 2$ µm (standard deviation was $\sigma_{r\beta} = 0.4$ µm) with a cutting edge form factor $K = 1$ before the machining [14]. The cutting parameters were $f = 0.03$ mm/rev and $v_c = 47$ m/min. The process conditions are listed in table 1.

Table 1. Drilling parameters (conventional drilling with twist drill)

Tool geometry parameters		Cutting parameters	
Tool diameter in mm	10	Feed in mm/rev.	$f = 0.03$
No. of major cutting edges	2	Cutting speed in m/min	$v_c = 47$
tool orthogonal rake angle in degree	$\gamma_0 = 30$		
drill point angle in degree	$\sigma = 118$		
Cutting edge radius in µm	$r_\beta = 2$		
Cutting edge form factor	$K = 1.0$		

For the state of the art drilling process uncoated cemented carbide step drills with a diameter of 10 mm were used. Those kinds of step drills are used for operation in industrial application and thus represent the prevailing quality of rivet holes. The steps allow the gradual increase of the hole diameter while the drill passes the CFRP. Thus, the load on the CFRP is reduced and hence the hole's damages. The tool orthogonal rake angle was $\gamma_0 = 30°$, the drill point angle $\sigma = 90°$. The radius of the cutting edge was $r_\beta = 3.4$ µm (standard deviation was $\sigma_{r\beta} = 1.0$ µm) and the cutting edge form factor was $K = 1$. The optimal process parameters $f = 0.08$ mm/rev and $v_c = 283$ m/min were specified by the drill manufacturer and are shown in table 2.

Table 2. Drilling parameters (CFRP-step drill)

Tool geometry parameters		Cutting parameters	
Tool diameter in mm	10	Feed in mm/rev.	$f = 0.08$
No. of major cutting edge	2	Cutting speed in m/min	$v_c = 283$
tool orthogonal rake angle in degree	$\gamma_0 = 30$		
drill point angle in degree	$\sigma = 90$		
Cutting edge radius in µm	$r_\beta = 3.4$		
Cutting edge form factor	$K = 1.0$		

The circular milling process was done in two steps. First step was machining a pre-drilled hole to 7 mm diameter with parameters assuring that resulting damages are smaller in diameter than the final diameter of 10 mm. The second step was the actual milling process, done by triple tooth end mills with a diameter of 6 mm. The end mills consisted of uncoated cemented carbide (WC + Cr_3Cr_2 + VC: 90 %; Co: 10 %; grain size: 0.6 µm) and were manufactured at the *Institute for Manufacturing Technology and Production Systems- FBK*. The milling tool's rake angle γ_0 is 10°. A constant helix angle of 0° in combination with the circular movement of the end mill in plate plane prevented forces in axial direction. Before the machining, the average cutting edge radius was $r_\beta = 2.7$ µm (standard deviation was $\sigma_{r\beta} = 0.5$ µm) with a cutting edge form factor $K = 1$ before the machining. The parameters of the milling process are summarized in table 3.

Table 3. Milling parameters.

Tool geometry parameters		Cutting parameters	
Tool diameter in mm	6	Feed in mm/rev.	$f = 0.03$
No. of circumference cutter	3	Width of cut in mm	$a_e = 0.1$
Helix angle in degree	0	Cutting speed in m/min	$v_c = 188$
tool orthogonal rake angle in degree	$\gamma_0 = 10$		
Cutting edge radius in µm	$r_\beta = 2.7$		
Cutting edge form factor	$K = 1.0$		

2.2. Investigation of hole quality / Analyses of hole quality

The investigation of the hole quality was done by analyzing the delamination, the fiber protrusion and the inner damages in the CFRP plates near the rivet hole.

The delamination was determined by the delamination factor F_d, maximum diameter of delamination divided by hole diameter. F_d was measured optically using a light microscope. This light microscope was also used to determine the fiber protrusion, percentage coverage of the circular area of uncut fibers, while this was done by a self-developed MATLAB-routine [13]. F_d and the fiber protrusion were measured on 5 holes per machining strategy. The values shown in the results are the mean values over the 5 holes.

For the analysis of inner damages of the rivet holes a laboratory X-ray micro computed tomography (XCT) device with a 180 kV nano focus tube, a 2300 x 2300 pixel detector and a wolfram target was used. For all scans the pixel distance was 7.5 µm, the tube voltage was 100 kV and the measurement current was 80 µA. 1,800 pictures, each averaged from 5 frames, were taken with a recording time of 500 ms per frame for each scan. Commercial software was used for the reconstruction and analysis of the 3D volume.

2.3. Experimental characterization

The energy absorption during tensile failure of the riveted joint is highly influenced by the laminate layup and the drilling hole quality. The chosen layup is responsible for the occurring failure mechanism. Therefore a layup has been

chosen to prevent shear, cleavage or flank-tension fracture in order to achieve bearing load failure with constant repeat accuracy [15]. To prove the correlation between of the drilling hole quality and the energy absorption capabilities experimental tests have been carried out with a tension testing machine by IVW GmbH. A constant testing speed was used to reduce the influence on the tensile strength of the material through strain rate effects [15]. Therefore, a test jig has been designed and manufactured (see Fig. 2). The CFRP plate with the machined rivet hole was attached between clamping jaws to prevent relative motion during the experiment. This is realized by applying equivalent calming pressure around the pin hole. Furthermore it is necessary to meet a minimum distance between the claming and the measuring region to not influence the test results. FEA tools helped to find a suitable design to solve this problem. A CFRP slipknot was used to pull a steel bolt through the laminate which represents the desired load case. The slipknot allowed an unhindered view on the failure region around the bolt when damage occurred. The longitudinal tension forces were recorded by using a strain-gauge-load cell on the lower mounting point. The movement of the bolt through the laminate was evaluated by using an image based tracking algorithm. For each variation of the drilling hole quality 3 samples have been tested. The amount of the trigger force provided information on the strength of the rivet connection.
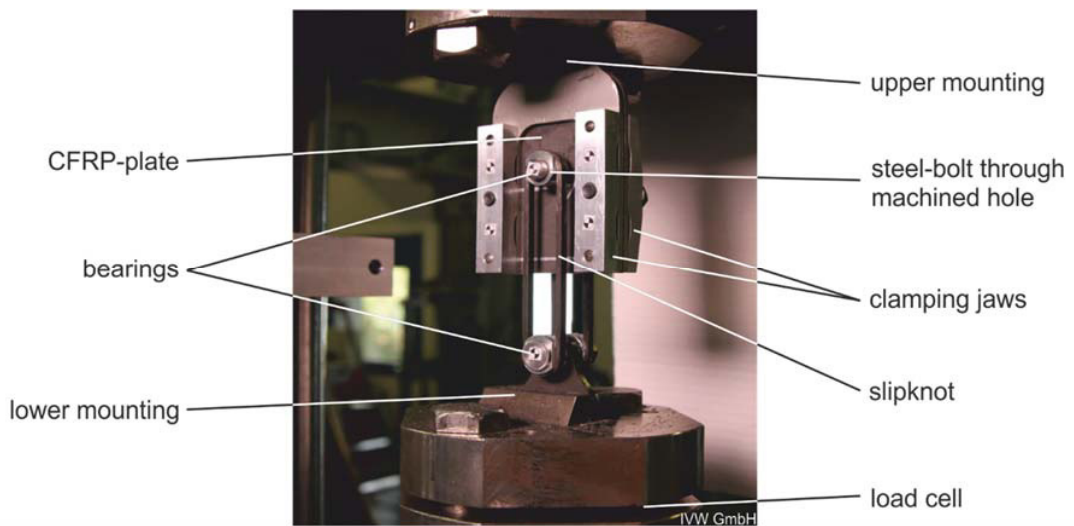
Fig. 2. Tension testing machine with attached test jig.

3. Results

It has been found that the different machining processes - conventional drilling with a twist drill, drilling with a state-of-the-art CFRP-drill, and circular milling - have resulted in different qualities (see Fig. 3) and trigger forces, representing different connection strengths.
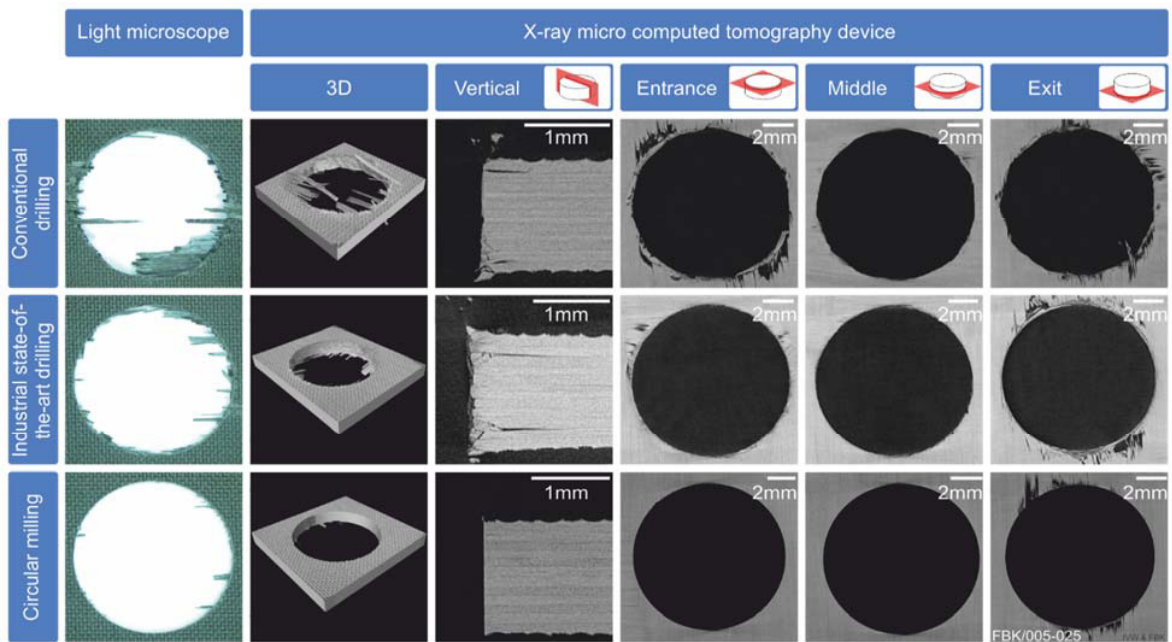
Fig. 3. Overview of the rivet hole qualities machined by different processes.

Drilling with conventional helix drills produced rivet holes which have the highest delamination factor F_d and fiber protrusion (see Fig 4 b). Because of the unfavorable geometry like the tool orthogonal rake angle γ_0, the fibers were pulled up contrary to the feed direction. This caused a flaking of the CFRP plate's uppermost layers $\rightarrow$ peel-up delamination. When the drill point exited the CFRP plate, the feed forces effected a flanking of the lower layers of the CFRP plate $\rightarrow$ push-out delamination. Both effects, peel-up and push-out delamination led to a higher delamination factor F_d compared to the other machining processes investigated in this paper, see Fig. 4 b). The relatively large drill point angle $\sigma = 118$ ° resulted in an unfavorable position from the cutting edge to the fiber. That means the angle between carbon fiber and cutting edge was large and thereby nearly parallel when the drill point angle is large. This fact led to a larger contact length between fiber and cutting edge, which reduced the ability to cut the fiber. Therefore, the fiber protrusion was higher than for the other machining processes.

The rivet holes, machined by a state-of-the-art CFRP-drill, exhibited a lower delamination factor F_d and less fiber protrusion than the rivet holes machined by a conventional helix drill. The smaller drill point angle, the steps and other optimizations (see Fig. 4. b) led to favorable cutting behavior. Moreover, this process was the fastest and thus the most cost-effective process.

The circular milling process needed pre-drilling, whereby it had to be ensured, that the delamination diameter was smaller than the final diameter of the rivet hole. The end mill's constant helix angle of 0° prevented forces in axial direction, thus a delamination could be largely prohibited [13]. Also, the beneficial angle between cutting edge and fiber led to low fiber protrusions, see Fig. 4 b).

The results for the delamination factor measured by light microscope were confirmed by XCT analysis. Fig. 3 shows clearly the peel-up and push-out delamination for the drilled holes. The results of [10] showed that F_d measured by light microscope is sufficient for the evaluation of bore hole quality. But it is clearly visible in the vertical view of Fig. 3 that the bore hole walls of the drilled holes had a poor quality compared to the milled hole.
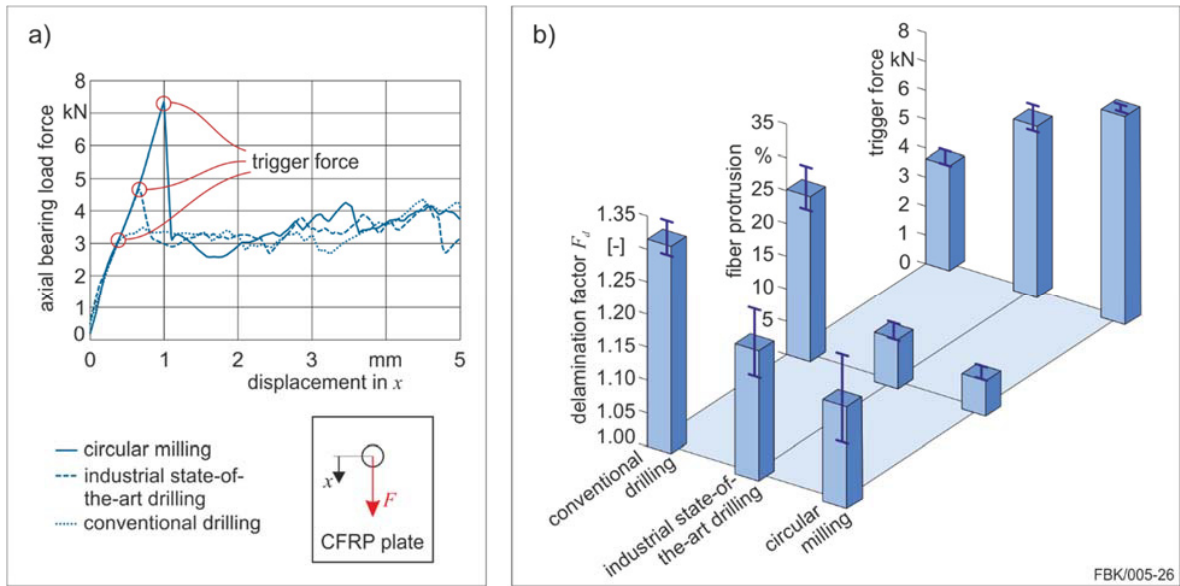
Fig. 4. a) Influence of the machining process on the trigger force (one measurement); b) Delamination factor, fiber protrusion and trigger force based on the machining processes (mean value).

The experimental results show a clear dependence of the drilling hole quality to the trigger force. The shearing and the hole bearing's measured trigger force were influenced by any kind of triggering mechanism. Delamination within the CFRP plate, induced by the drilling process, lowered the axial tensile strength of the hole and implanted an initial crack at the bore edge. This kind of localized damage behaved like a trigger under high bearing stresses.

4. Conclusion and Outlook

In this paper, the influence of three machining strategies on the rivet hole quality and ultimately on the corresponding strength of the rivet connections was examined. The quality of the rivet holes was investigated by means of delamination and fiber protrusion. The strengths of the connections were compared by the trigger force in a tensile test.

For the drilling processes, the delamination factor was high, because of the movement of the drill tools in spindle axis direction which causes feed forces. In addition, the helix angle leads to an up pealing of the fibers. The unfavorable angle between the cutting edge and the fibers resulted in uncut fibers and thus in a higher fiber protrusion. In the milling process there was no movement in spindle axis direction and hence no force in the same. Also the helix angle of 0 ° prevented any force in spindle axis direction. The tensile tests proved that the strength of the rivet connection correlated directly with the rivet hole quality. The trigger force was influenced by the delamination within the CFRP plate, which acted as a triggering mechanism whilst the damages on the hole implanted initial cracks at the rivet hole edge.

In future investigations the influence of different weakening geometries near the rivet hole on the crash behavior will be investigated.

References

[1] R. Voß, M. Henerichs, F. Kuster, K. Wegener, Chip root analysis after machining carbon fiber reinforced plastics (CFRP) at different fiber orientations, *Procedia CIRP* 14 (2014) 217-222.

[2] W. Hufenbach, D. Biermann, G. Seliger, Serientaugliche Bearbeitung und Handhabung moderner faserverstärkter Hochleistungswerkstoffe (sefawe)- Untersuchungen zum Forschungs- und Handlungsbedarf, Institut für Leichtbau und Kusntstofftechnik, Technische Universität Dresden, 2008.

[3] J.Y. Sheikh-Ahmad, Machining of polymer composites, Springer, Abu Dhabi, 2009.

[4] E. Brinksmeier, S. Fangmann, R. Rentsch, Drilling of composites and resulting surface integrity, *CIRP Annals - Manufacturing Technology* 60 (2011) 57-60.

[5] A.G. Mamalis, et al, Crashworthy capability of composite material structures, *Composite Structures 37* (1997) 109-134.

[6] G.L. Farley, R.M. Jones, Crushing characteristics of continuous fiber-reinforced composite tubes, J*ournal of Composite Materials* 26 (1992) 37-50.

[7] D. Herzog, P. Jaeschke, O. Meier, H. Haferkamp, Investigations on the thermal effect caused by laser cutting with respect to static strength of CFRP, *International Journal of Machine Tools & Manufacture* 48 (2008) 1464–1473.

[8] F. Schneider, B. Kirsch, M. Gurka, T. Hermann, J.A. L´huiller, J.C. Aurich, Improved Quality of Drilled Holes in Laminated Carbon Fiber Reinforced Plastics via Laser-Preprocessing, *New Production Technologies in Aerospace Industry - Proceedings of the 4th Machining Innovations Conference* (2013) 27-31.

[9] U. Heisel, T. Pfeifroth, Influence of Point Angle on Drill Hole Quality and Machining Forces when Drilling CFRP, *5th CIRP Conference on High Performance Cutting 2012, Proceedia CIRP 1* (2012) 471-476.

[10] L. Heberger, S. Nissle, M. Gurka, B. Kirsch, J. C. Aurich, Qualitätssteigerung von Bohrungen in Faserkunststoffverbunden - Untersuchung des Einflusses verschiedener Einspannstrategien, *wt Werkstattstechnik online Jahrgang* 105 (2015) 501-507.

[11] E. Brinksmeier, S. Fangmann, I. Meyer, Orbital drilling kinematics, *Production Engineering – Research and Development* 2 (2008) 277-283.

[12] A. Sadek, M. Meshreki, M.H. Attia, Characterization and otimization of orbital drilling of woven carbon fiber reinforced epoxy laminates, *CIRP Annals – Manufacturing Technology* (2012) 123-126.

[13] J.C. Aurich, B. Kirsch, C. Müller, L. Heberger, Quality of drilled and milled rivet holes in carbon fiber reinforced plastics, *Procedia CIRP 24 - Proceedings of the New Production Technologies in Aerospace Industry - 5th Machining Innovations Conference* (2014) 56-61.

[14] B. Denkena, D. Biermann, Cutting edge geometries, *CIRP Annals – Manufacturing Technology 63* (2014) 631-653.

[15] M. Pain, Entwicklungsmethode für Hochleistungswerkstoffe am Beispiel von Energieabsorbern für Flugzeugkabinen, Dissertation TU Hamburg-Harbur, *Hamburger Schriftenreihe Produktentwicklung und Konstruktionstechnik Band 1* (2009).

[16] E. Persson, I. Eriksson and L. Zackrisson, Effects of hole machining defects on strength and fatigue life of composite laminates, *Composites Part A: Applied Science and Manufacturing* 28 (1997) 141-151.

[17] M. Henerichs, R. Voss, H. Tanaka, F. Kuster, K. Wegener, Analysis of Material Weakening in CFRP after a Drilling Operation, *Procedia CIRP 24* (2014) 44-48.

16th Machining Innovations Conference for Aerospace Industry - MIC 2016

Effect of Quench Delay on Subsurface integrity during Machining of Titanium Alloy Ti6Al4V

Swapnil Kekade [*], Sandip Patil, Kamlesh Phapale,Shital Jadhav, Amit Powar, Ashish Supare, Dr.RKP Singh

Kalyani Centre for Technology and Innovation; Bharat Forge Ltd. Pune, 411036,India.

Abstract

Machining of titanium alloys generates enormous amount of heat at the chip-tool interface which leads to poor machinability. The current research investigates the effect of change in alpha and transformed beta phase resulting from different delays during quenching at subsurface level during machining. The change in subsurface deformation was analyzed based on various output response measured such as deformed depth, shear strain in deformed grains, micro-hardness and surface finish, using optical microscopy and SEM. The deformation induced damage detected near the machined edge due to microstructural restructuring was correlated with chip microstructure.

Keywords: Ti6Al4V; subsurface; quench delay; primary alpha; transformed beta.

1. Introduction

In aerospace industry, the surface integrity of machined component is a very critical aspect for maintaining the reliability. The machining process can damage this surface integrity [1, 2]. Due to high strength to weight ratio and excellent corrosion resistance, titanium alloys are the most widely used material for aerospace applications [1-3]. Also, titanium alloys possesses some undesirable properties, like low thermal conductivity, high chemical reactivity, low modulus of elasticity, high hardness and high strength, which leads to poor machinability [3]. The low modulus of elasticity, of titanium alloys, affects its machinability by producing chatter marks on the workpiece during machining [4]. Also, the surface damage and premature tool failure occurs, due to increased cutting temperature at cutting edge, because of low thermal conductivity of titanium alloys [4]. The strong welding of workpiece material to the tool tip affects the machining process, due to high chemical reactivity of titanium alloys [3-4]. Various researchers reported that, the machinability of titanium alloys is strongly affected by the heat treatment process and subsequent microstructure produced [4-6]. Previous researches reported the variations in the surface integrity, in terms of

subsurface grain deformations, subsurface microstructure alteration, white layer formation and residual stresses. The depth and the micro-structure of this deformed layer, depend not only on the machining parameters, but also on the mechanical and physical properties of the material. The subsurface microstructural alteration was reported with the formation of twins [5, 6]. Many researchers have carried out, the analysis of effect of material composition and process parameters, on chip formation mechanism and chip microstructure, during machining of titanium alloys [7]. However, the effect of change in volume fraction of alpha and beta phase, at subsurface level during the machining, has not been investigated. Therefore, the objective of this research is to investigate the effect of change in phase fraction on subsurface deformation, during machining of Ti6Al4V alloy. For this purpose, titanium Ti6Al4V samples were subjected to solution treatment and annealing (STA) process, with introducing various quench delays, to get the combinations of alpha and beta phase fractions. During the analysis, various output parameters, such as surface roughness, subsurface grain deformations and micro-hardness of deformed grains, were measured. An optical microscopy was performed to reveal the subsurface deformations and microstructural alterations.

2. Experimental details

2.1. Heat treatment

Titanium alloy, Ti6Al4V, raw material as per AMS 4928 specification was procured from TIMET UK, in the form of round bar with 70 mm diameter and 150 mm length, in annealed condition. The beta phase transition temperature for this material was assumed to be 995^0C.
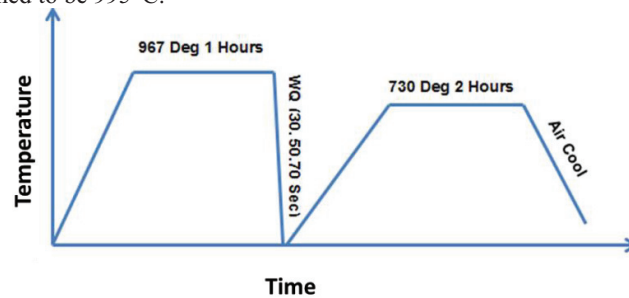
Fig. 1 Schematic representation of solution treatment and annealing (STA) heat treatment cycle

The samples were solution treated at 967°C and hold for an hour and further annealed at 730°C for 2 hours and then air cooled. An increase in quench delay from 30 seconds to 70 seconds resulted into an increased percentage of volume fraction of primary alpha and reduced percentage of transformed beta (refer Table 1). Using the optical microscope (Carl Zeiss make); the optical images of each sample were taken. Then using Image J analysis software, the phase composition was measured.

Table 1 Phase analysis

Quench delay (sec)	Primary α (%)	Transformed β (%)
30	30	70
50	49	51
70	67	33

2.2. Machining

Quench delayed samples of Titanium Ti6Al4V alloy were used as an input for machining. The face turning operation was performed on DMG Turn mill center CTX beta 1250TC as shown in Fig. 2 and 3. All the turning

experiments were performed at room temperature in dry environment and high pressure environment of 50 bar. During machining, a through coolant Tool Holder Capto C6-ASHR-30100-20 with DCLNR-20202-K12 of WALTER make, was used. For high pressure coolant experiments, water soluble Blaser B-COOL 9665 coolant with 6 to 8% concentration was used.
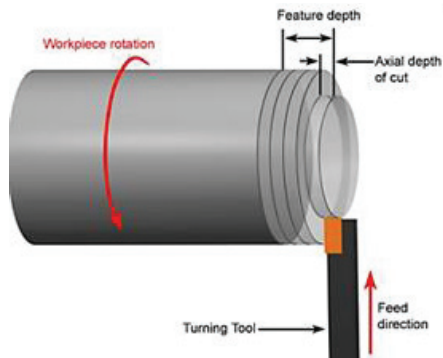
Fig. 2 Face turning setup

Fig. 3 DMG Turn mill center

   Total six sets of experiments were performed with first three experiments as QD 30 – HPC, QD 50-HPC and QD 70- HPC with high pressure coolant application. Then remaining three experiments QD 30 – DRY, QD 50-DRY and QD 70- DRY using dry cutting environment were done. A constant cutting speed of 90 m/min, feed rate of 0.3 mm/rev and depth of cut of 1 mm was used for all the experimentations. Face turning was conducted with a Walter's carbide insert CNMG 120408 with WSM20 geometry. For high pressure coolant experiments, a constant coolant pressure of 50 bar was directed at the chip tool interface near the rake face of the tool through specially designed tool holder. For each experiment a new cutting edge of insert was used. The chips and inserts were collected after each trail with proper identification. The surface finish of the machined surface was measured after each experiment using Mahr Pocket Surf. After each experiment, the surface which undergone the face turning operation was sliced along the periphery (as shown in fig.5). The surface was cut into equal slices such that surface underneath the machined edge could be used as sample for metallurgical observations. The selected samples were subjected to sample preparation and etching procedure for scanning electron microscopy, optical microscopy and micro-hardness testing.
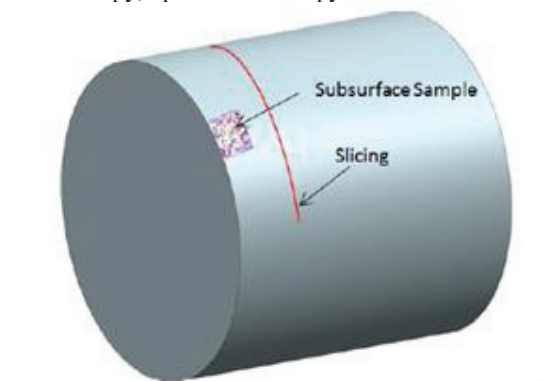
Fig. 4 Subsurface analysis sample preparation

3. Results and discussion

3.1. Surface finish

During machining of titanium alloy, Ti6Al4V, surface finish of the machined workpiece is one of the most critical parameter as there will be a direct effect of any change in microstructure and cutting conditions on the subsequent surface topography [7]. The surface finish was measured along the cutting direction in terms of average surface roughness Ra over the periphery. For each experiment, ten readings were taken and average reading was used for comparative analysis.
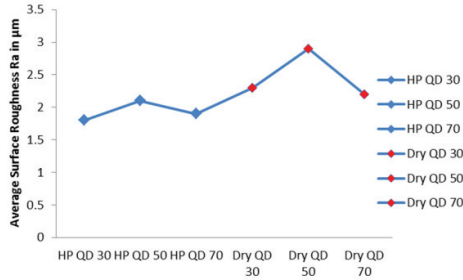
Fig. 5 Effect of quench delay on surface roughness
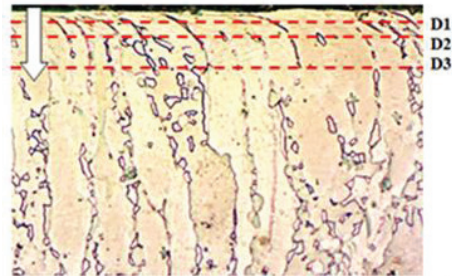
Fig. 6 Regions of subsurface deformation

As shown in fig. 5, trend of surface roughness is increasing for similar cutting parameters. The surface roughness was found to be increased at higher extent in dry environment as compared to HPC environment. This is due to the fact that high pressure coolant eliminates the vapor barrier at the chip tool interface resulting in more effective heat removal and better surface integrity [8]. During machining of QD50- dry, due to equal volume fraction of alpha and beta, alternate soft and hard phase occur which causes higher amount of tool marks and resulted into surface damage on the machined surface.

3.2. Subsurface alterations

The recent studies identified three distinct regions near the machined surface during titanium alloy machining [2]. The three deformed regions D1, D2 and D3 are represented in fig. 6. The region D1 is composed of highly deformed grains and is just beneath the machined surface. The region D2 is beyond region D1 and is composed of moderate deformed grains. Last region D3 is composed of unaffected grains after machining. Fig. 7 shows the effect of different quench delay samples under dry and HPC environment on the deformation of grains, which was measured by measuring the deformation depth and strain in the corresponding grain. The deformation depth and corresponding shear strain values were measured using the image analyzing software and optical microscopy. With the increase in quench delay, the deformation depth as well as shear strain in deformed grain increases. In HPC environment the magnitude of this increase was observed less compared to dry cutting environment.
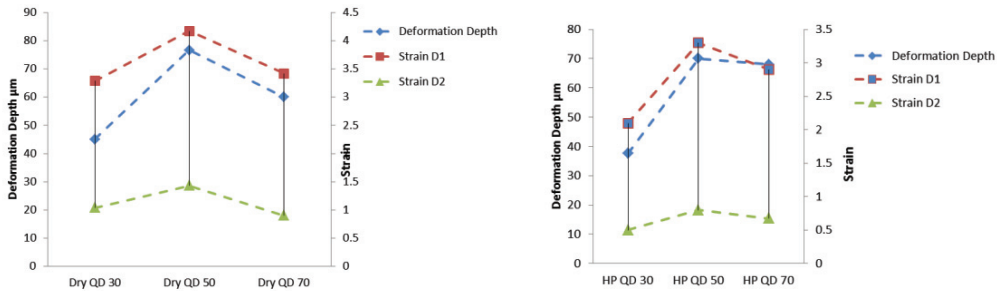
Fig. 7 Effect of quench delay on deformation depth and strain

In the subsurface deformation phenomenon, change in microstructure plays an important role. A change in alpha and beta phase volume fraction resulted into increase in deformation depth beneath the machined surface. Fig. 8-13 shows the optical micrographs of the deformed grains beneath the machined surface.
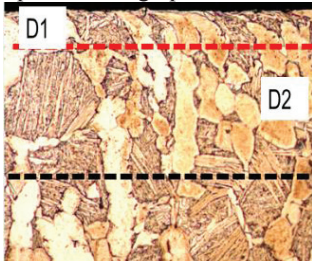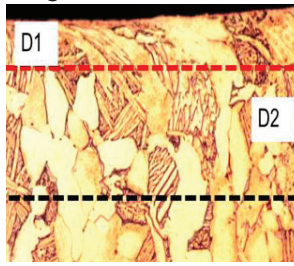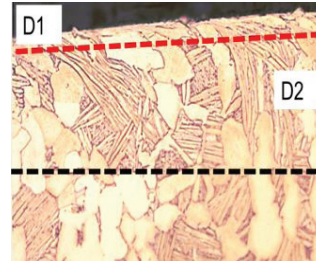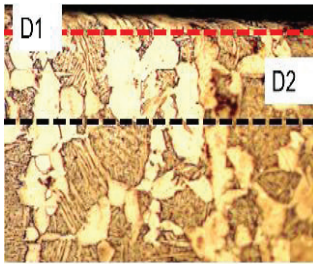

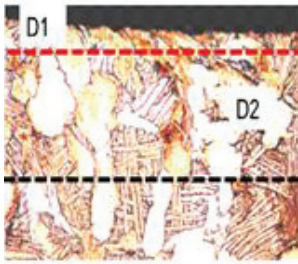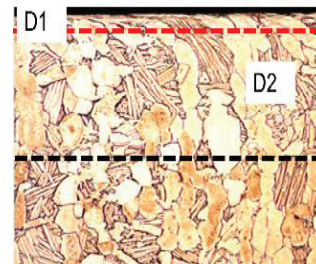| Fig. 8 QD30-Dry | Fig. 9 QD50-Dry | Fig. 10 QD70-Dry |

| Fig. 2 QD30-HPC | Fig. 12 QD50-HPC | Fig. 13 QD70-HPC |

The micrographs reveal the damage with the grains at subsurface level. The said damage was seen with single grain or similar oriented structure unit. It can be seen that the severity of plastic deformation beneath the machined surface can be controlled by varying the alpha and beta phase volume fraction in microstructure. An equal amount of alpha and beta phase volume fraction in QD50 sample, amplifies the subsurface deformations during machining of Ti6Al4V.

Work hardening phenomenon resulting from deformed grains beneath surface area resulted in higher micro-hardness than that of base material [4]. The micro-hardness of the deformed region and undeformed region was measured for each experiment. Fig.14 shows the graph of micro-hardness for each QD specimen. The results show higher micro-hardness for QD50. However, HPC machining reduces the work hardening and thermal softening phenomenon which otherwise was dominant during dry machining, and more particularly during QD 50 Dry machining.
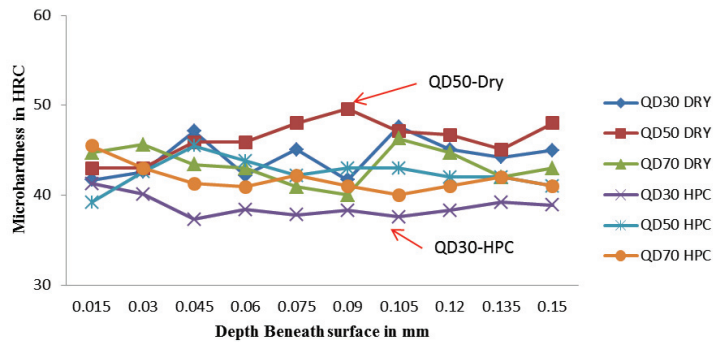
Fig.14 Micro-hardness at the deformed depth

4. Conclusion

The current research investigated that the incorrect industrial practices of delayed quenching for the reason that the transfer time associated with furnace and quench tank, makes significant effect on the volume fraction alpha and beta percentage, during solution treatment and annealing of titanium alloy Ti6Al4V. During machining process this effect of change in volume fraction was clearly visible on the surface roughness, subsurface deformation and micro-hardness. For QD 50, a decrease in difference between the volume percentage of two phases further contributes to an alternate hard and soft cutting which causes thermal and frictional shock at the cutting face leading to higher surface roughness, highly deformed grains, high deformation depth, high shear strain and higher micro-hardness which leads to poor machinability. Use of high pressure coolant generates adequate lubrication at the cutting interface to reduce the overall effect of phase change on machinability.

References

[1] Ginting A and Nouari M. Surface integrity of dry machined titanium alloys. International Journal of Machine Tools & Manufacture 2009; 49:325-332.
[2] Edkins Kyle D, Rensburg Nickey Janse van, Laubscher Rudolph F. Evaluating the subsurface microstructure of machined Ti-6Al-4V. Procedia CIRP 2014 ; 13: 270-275.
[3] Velásquez Puerta J.D., Tidu A, Bolle B, Chevrier P, Fundenberger J. Sub-surface and surface analysis of high speed machined Ti–6Al–4V alloy. Materials Science and Engineering A 2010; 527: 2572–2578.
[4] Che-Haron C.H. Tool life and surface integrity in turning titanium alloy. Journal of Material Processing Technology 2001; 118: 231-237.
[5] Tidu A, De Saever A, Schuman C, Bolle B, Chevrier P. Machining of Pure High Grade Titanium: Effect on the Subsurface Microstructure. International Journal of Metallurgical & Materials Engineering 2015; 1: 108.
[6] Ravi Shankar M, Rao Balkrishna C, Lee Seongeyl, Srinivasan Chandrasekar, King Alexander H, Compton Dale W. Severe plastic deformation (SPD) of titanium at near-ambient temperature. Acta Materilia 2006; 54: 3691-3700.
[7] Joshi Shashikant, Pawar Pravin, Tewari Asim, Joshi Suhas S. Effect of b phase fraction in titanium alloys on chip segmentation in their orthogonal machining. CIRP Journal of Manufacturing Science and Technology 2014; 7: 191-201.
[8] Sandip Patil, Swapnil Kekade, Pravin Pawar et.al. Effect of Coolant Pressure on Machinability of Titanium Alloy Ti6Al4V, Applied Mechanics and Materials, Vol. 826(2015), pp 82-87.

16th Machining Innovations Conference for Aerospace Industry - MIC 2016

Tool Wear Investigation in Dry and High Pressure Coolant Assisted Machining of Titanium Alloy Ti6Al4V with Variable α and β Volume Fraction

Kamlesh Phapale, Sandip Patil , Swapnil Kekade, Shital Jadhav, Amit Powar, Ashish Supare ,Dr. RKP Singh

Kalyani Centre of Technology and Innovation, Bharat Forge Ltd. Pune 411036, India

Abstract

During machining of titanium alloys friction and cutting temperature plays vital role in determining the cutting tool performance. This work investigates the effectiveness of change in volume fraction of alpha and beta phase in the bimodal titanium Ti6Al4V on tool wear phenomenon. A detailed tool wear mechanism and micro structural analysis was performed for dry and high pressure coolant machining of Titanium Ti6Al4V to investigate the role of quench delay on machining performance. The analysis concluded that use of high pressure coolant was useful to overcome the difficulties relating to change in alpha and beta volume fraction during machining of Titanium Ti6Al4V.

Keywords: Titanium alloy, Quench delay, Dry/High pressure coolant, Tool wear, EDAX.

1. Introduction

Titanium alloys Ti6Al4V are the most commonly used material in aerospace industry, due to their excellent properties such as, extremely high strength to weight ratio, corrosion resistance and ability to retain high strength at high temperatures. However, they have poor machinability because of low thermal conductivity, high chemical reactivity, high hardness and low modulus of elasticity, which results into poor machinability [1-3]. The low thermal conductivity and modulus of elasticity of titanium alloys, affects its machinability by producing tool wear which leads to surface damage and premature tool failure occurs [4].Ti6Al4V alloy contains alpha and beta phases in the percentage volume fraction with reference to the heat treatment followed. This volume fraction further determines the deformation behavior and mechanical properties of this alloy under both quasi-static and dynamic loading conditions [2]. Both α and β phases are relatively soft but α – β interface is an effective stoppage to dislocation and crack propagation [2,

3].Various researchers reported that the tungsten carbide WC is the best material for machining of titanium alloys. With these tools, a stable layer of titanium is formed between the rake face of the tool and chip that protects against crater wear. Tool wear mechanism during machining of Ti6Al4V is different than steel or Inconel [4-5].Machining of titanium alloys in the aerospace elements requires high standard of finishing, not only dimensional and geometrical accuracy but also physicochemical surface properties [6]. In dry machining rapid tool wear was recorded when coolants are avoided but it is an environmentally friendly machining process with absence of hazard cutting fluids [7].Multilayer coating on carbide tool in dry machining of titanium alloys increases the productivity relative to single layer. Wear on cutting tools such as, abrasive, adhesive, chipping, coating delamination and built up edge occurred on the rake and flank face [8]. Many researchers have carried out, the analysis of effect of material composition and process parameters, on chip formation mechanism and chip microstructure, during machining of titanium alloys [7]. However, the effect of change in volume fraction of alpha and beta phase, tool wear during the machining, has not been investigated. Therefore, the objective of this work is to investigate the effect of change in phase fraction on tool wear, during machining of Ti6Al4V alloy. For this purpose, titanium Ti6Al4V samples were subjected to solution treatment and annealing (STA) process, with introducing various quench delays, to get the combinations of alpha and beta phase fractions. During the tool wear analysis, such as rake face, flank face and micro composition on tool face, were measured using Scanning Electron Microscopy, Optical Microscopy and Energy Dispersive Spectroscopy.

2. Experimental details

2.1. Heat treatment

Annealed cylindrical specimen of Titanium alloy, Ti6Al4V, raw material having diameter 70 mm and 150 mm length, raw material as per AMS 4928 specification was procured from TIMET, UK. The beta transition temperature for the material was assumed to be 995°C.
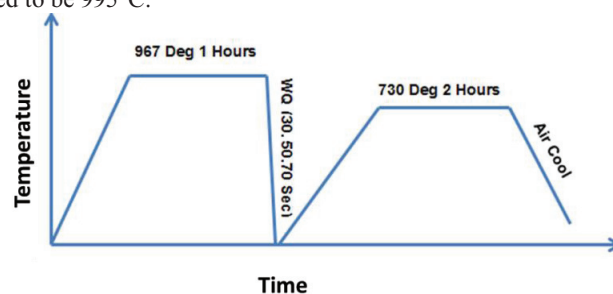

Fig. 1. Schematic representation of solution treatment and annealing (STA) heat treatment cycle.

As shown in Fig. 1, the sample were solution treated at 967°C and hold for an hour and further annealed at 730°C for 2 hours and then air cooled. An increase in quench delay from 30 seconds to 70 seconds resulted into high percentage of volume fraction of primary alpha and reduced percentage of transformed beta as shown in Table 1. Using the optical microscope (Carl Zeiss make); the optical images of each sample were taken. Then using Image J analysis software, the phase composition was measured.

Table 1. Phase analysis.

Quench delay (sec)	Primary α (%)	Transformed β (%)
30	28	66
50	45	50
70	64	32

2.2. Machining

Titanium Ti6Al4V quench delayed samples were used for machining trials using DMG Turn Mill center. All the turning experiments were performed at room temperature using dry cooling environment and high pressure environment.
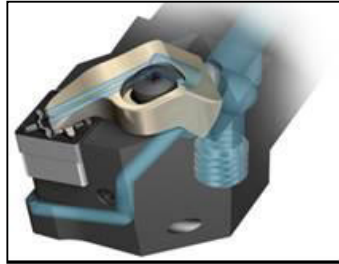

Fig. 2. High pressure coolant set up for rake face of the tool.

The face turning experiments were carried with Walter makes carbide insert CNMG 120408-NFT WSM20 having physical vapour deposition (PVD) coating with chemical composition TiCN of the substrate and through coolant tool holder Capto C6-ASHR-30100-20 with DCLNR-20202-K12 using DMG Turn mill centre CTX beta 1250TC machine. Water soluble Blaser B-COOL 9665 coolant with 6 to 8% concentration was used for high pressure coolant experiments. A constant cutting speed of 90 m/min, feed rate of 0.3 mm/rev and depth of cut of 1 mm was used for all the experimentations. As shown in Fig. 2, for high pressure coolant assisted experiments, a constant coolant pressure of 50 bars was directed at the chip tool interface near the rake face of the tool.

A detailed investigation of the each worn out tool (cutting edge) was carried out using scanning electron microscopy (SEM). Moreover, compositional features of the adhered material to the tool surface and compositional changes of the tool material were analyzed by Energy Dispersive Spectroscopy (EDS) techniques, using an EDAX analyzer.

3. Results and Discussion

3.1. Effect on tool wear

A microanalysis testing with scanning electron microscopy (SEM) was performed on tool wear to observe detailed wear mechanism. Fig. 3 shows some SEM images of tool wear mechanism occurred on rake face and flank face during turning such as, adhesive wear, coating delamination, abrasion, diffusion, chipping and built up edge etc. were discussed and their significance was correlated with different alpha and beta phase volume fraction. Adhesive, abrasive wear and coating wear was observed on the tool rake face which may be as a result of friction between chips and work piece material [8]. Abrasion wear occurred when formation of the built up edge (BUE) on the cutting edge is dominated at the rake and flank face.
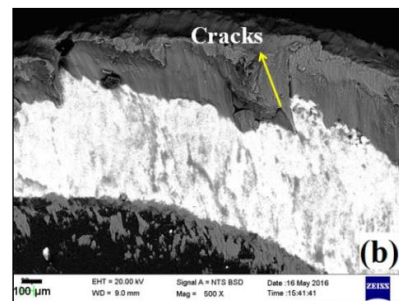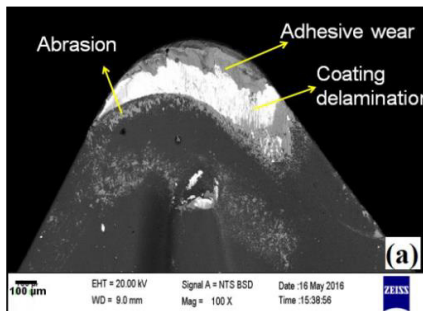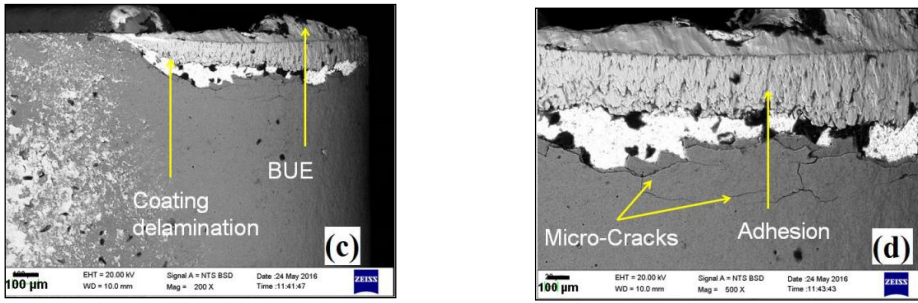
Fig. 3. SEM images of tool wear (a-b) Rake face; (c-d) Flank face.

The adhesion on the rake and flank face due to strong bond at the tool and work piece interface. Ti6Al4V alloys having strong affinity with the substrate resulted in built up edge formation on the cutting edge. Difference in the thermal coefficient of expansion between tool coating and the substrate during machining may cause cracks on the flank face [8]. The adhesion wear, built up edge or coating delamination occurs when the tool coating gets worn out.
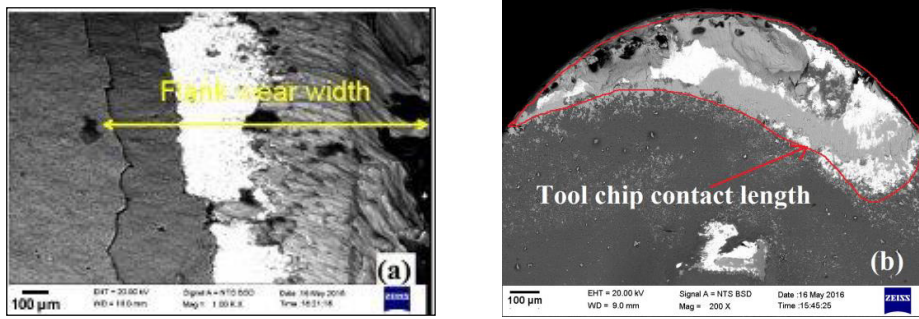

Fig. 4. SEM images (a) flank wear width; (b) tool-chip contact length.

The contact length of the chip with rake face is called tool-chip contact length. This contact length determines the friction at the cutting interface [8]. The SEM image of flank wear width and tool-chip contact length of worn-out inserts as shown in Fig. 4.
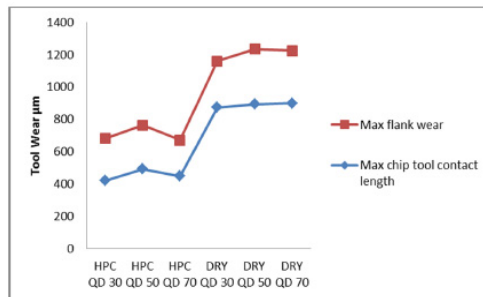

Fig.5. Effect of phase change on tool wear.

Fig. 5 shows that, the effect of change in quench delay and the subsequent phase composition on the tool wear. At high pressure coolant having smaller tool chip contact length ensures less friction at tool chip interface and reduces the quantity of heat transferred to the tool. In dry machining having larger tool chip contact length causes more friction at tool chip interface leading to more amount of heat transfer to the cutting tool. More specifically QD50 shows higher chip tool contact length. The impact of change in phase composition was more critical during dry machining. The

adhesion of titanium causes increased friction between chip and the tool rake face which ultimately produces tool wear [1]. However, with the use of high pressure coolant machining approach, the adhesion and subsequent formation of BUE on the tool surface was reduced. This was mainly because of reduction in contact time between tool and chip [1].

However, with both the machining approach at cutting speed of 90m/min, feed rate of 0.3mm/rev and depth of cut of 1mm, with an increase in quench delay from QD30 to QD70, an increase in tool wear was recorded. However, the specimen with QD50 showed higher tool wear as compared to specimens QD30 and QD70. This shows that as explained in Table 1, phase composition of QD 50, 51% transformed beta and 49% primary alpha has resulted into more amount of friction at the interface. In the current phase composition, none of the phase acts as dominant phase wherein transformed beta carries higher amount of strength and hardness as compared to alpha. This may create an alternate soft and hard cutting leading work hardening and thermal softening counteracting over each other which may create frictional shock.

As shown in Fig. 6, during dry machining the effect of change in volume fraction of α and β phase on the tool wear phenomenon was found to be predominant from QD30 dry to QD70 dry. However, for QD50 more particularly for rake face, higher amount of friction and more chip tool contact length resulted into excessive adhesive and abrasive wear. However, with the use of HPC, this tool chip contact length gets reduced which further minimizes the wear phenomenon as depict in QD50HPC.
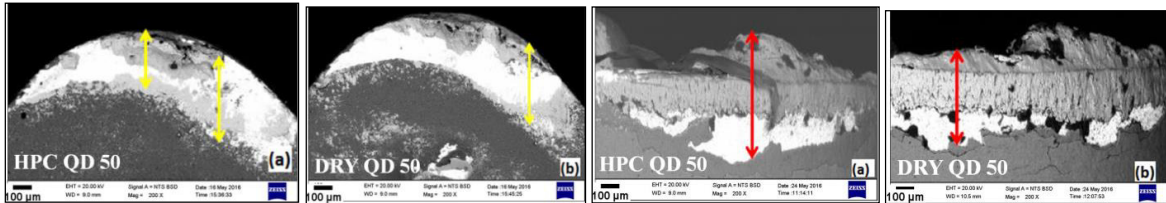

Fig. 6. SEM images rake wear tool (a) HPC QD50; (b) DRY QD50.   Fig. 7. SEM images flank wear tool (a) HPC QD50; (b) DRY QD50.

Similarly, for flank face higher amount of work hardening and excessive thermal softening done, which created thermal shock at the cutting zone, more particularly for QD50 dry which resulted into micro-cracks. However, this effect is minimized by using HPC at QD50HPC as shown in Fig. 7.

3.2. EDAX Analysis

Energy Dispersive Spectroscopy (EDS) microanalysis was used for determining the micro-composition on the tool face. As shown in Fig. 10, during dry machining, specifically for QD 50 more amount of titanium deposition 80.92% was observed at the rake face. Initially, thin layers are formed by titanium oxides, which come from the initial oxidation of Ti. During dry machining, initial properties of the tool changes not only geometrical due to high temperature and they also change the cutting conditions. So, once stratified layers are placed, mechanical adhesion is favored, and the incorporation of work piece material to the tool surfaces is promoted [7].While comparing high pressure coolant cutting, less material deposition occurred on tool face.
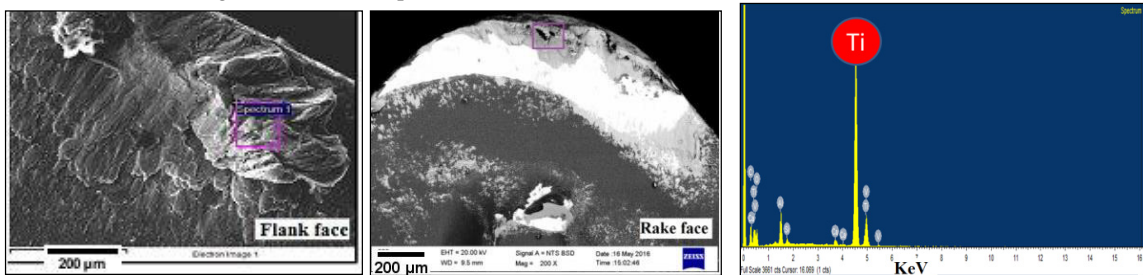

Fig. 8 EDAX analysis. (Dry machining QD50)

At QD50, Micro-composition on tool face as shown in Table 2

Table 2. Micro-composition on tool face.

Element	Dry	HPC
A$_l$ K	5.62	7.53
T$_i$ K	80.92	40.87
V	3.97	2.82

4. Conclusions

The current investigation showed that the volume fraction alpha and beta percentage causes substantial effect on the tool wear phenomenon for QD50 DRY. During dry machining, decrease in difference between the volume percentages of 2 phases further contributes to an alternate thermal softening and work hardening, which causes thermal and frictional shock at the cutting face leading to higher adhesive wear, coating delamination, abrasion, diffusion, built up edge etc. to impair the machinability as compared to that of for QD50 HPC. Use of high pressure coolant generates adequate lubrication at the cutting interface to reduce the overall effect of phase change on machinability compared to dry machining.

References

[1] Sandip Patil, Swapnil Kekade, Pravin Pawar, Effect of Coolant Pressure on Machinability of Titanium Alloy Ti6Al4V, Applied Mechanics and Materials, Vol. 826, pp 82-87,2015.

[2] Berend Denkena, Thilo Grove, Patrick Helmecke, The Effect of Microstructure on the Machinability of Ti6Al4V, Ti-2015: The 13th World Conference on Titanium TMS, 2015.

[3] Shoujin Sun, Milan Brandt, John P.T. Mo, Effect of Microstructure on Cutting Force and Chip Formation during Machining of Ti-6Al-4V Alloy, Advanced Materials Research Vols. 690-693, pp 2437-2441,2013.

[4] Sandip Patil, Pravin Pawar, Shital Jadhav, Ashish Supare, Amit Powar, Kekade S., Dr.RKP Singh, Correlation between heat treatment, microstructure and machinability for Ti6Al4V, International Journal of Mechanical And Production Engineering, Volume- 3, Issue-6, June-2015.

[5] Gil Mur F.X, Rodriguez D. and Planell J.A, "Influence of tempering temperature and time on the α'-Ti-6A1-4V martensite," Journal of Alloys and Compounds 234, pp 287-289,1996.

[6] Yessine Ayed, Guenael Germain, Amine Ammar and Benoit Furet, Experimental study of tool wear mechanisms in conventional and high pressure coolant assisted machining of titanium alloy Ti17, Key Engineering Materials Vols. 554-557, pp 1961-1966,2013.

[7] Alvarez M,Gomez A,salguero J,Batista M,Huerta M, Marcos ,SOM-SEM-EDS Identification of Tool Wear Mechanisms in the Dry-Machining of Aerospace Titanium Alloys, Advanced Materials Research Vol. 107, pp 77-82,2010.

[8] Ibrahim G.A,Che C.H, Haron,Ghani J.A,Tool Wear Mechanism in Continuous Cutting of Difficult-to-Cut Material under Dry Machining,Advanced Materials Reaserch Vols.126-128, pp 195-201,2010.

[9] Shashikant Joshi, Pravin Pawar, Asim Tewari, and Suhas Joshi, "Effect of β-phase fraction in titanium alloy on chip segmentation in their orthogonal machining", CIRP journal of manufacturing science and technology, vol.7, pp 191- 201,2014.